The Role of the Transient Receptor Potential Vanilloid 1 (TRPV1) Channel in Sharp Wave Ripples, Place Cells, and Spatial Memory

Dissertation
for the award of the degree
"Doctor rerum naturalium" (Dr.rer.nat.)

of the Georg-August-Universität Göttingen

within the doctoral program IMPRS Neuroscience of the Georg-August University School of Science (GAUSS)

submitted by
Chrystalleni Vassiliou

from Paphos, Cyprus

Göttingen, 2022

Thesis Committee

Camin Dean, PhD (Reviewer)	Synaptic Dysfunction Group Deutsches Zentrum für Neurodegenerative Erkrankungen (DZNE) Berlin, Germany
Prof. Dr. Hansjörg Scherberger (Reviewer)	Neurobiology Laboratory Deutsches Primatenzentrum (DPZ) Göttingen, Germany
Prof. Dr. Tobias Moser	Institute for Auditory Neuroscience Universitätsmedizin Göttingen (UMG) Göttingen, Germany

Members of the Examination Board

Camin Dean, Ph.D. (Reviewer)	Synaptic Dysfunction Group Deutsches Zentrum für Neurodegenerative Erkrankungen (DZNE) Berlin, Germany
Prof. Dr. Hansjörg Scherberger (Reviewer)	Neurobiology Laboratory Deutsches Primatenzentrum (DPZ) Göttingen, Germany
Prof. Dr. Tobias Moser	Institute for Auditory Neuroscience Universitätsmedizin Göttingen (UMG) Göttingen, Germany

Further members of the Examination Board:

Brett Carter, Ph.D.	Synaptic Physiology and Plasticity European Neuroscience Institute (ENI) Göttingen, Germany
Dr. Caspar M. Schwiedrzik	Neural Circuits and Cognition European Neuroscience Institute (ENI) Göttingen, Germany
Prof. Dr. Dr. Oliver Schlüter	Psychiatry and Psychotherapy Universitätsmedizin Göttingen (UMG) Göttingen, Germany

Date of the oral examination: 9th February 2023

Table of contents

List of abbreviations

Abbreviation	Expansion
ACC	Anterior cingulate cortex
ACh	Acetylcholine
AChR(s)	Acetylcholine receptor(s)
aCSF	Artificial cerebrospinal fluid
AD	Alzheimer's disease
AMPA	α-amino-3-hydroxy-5-methyl-4-isoxazolepropionic acid
ANOVA	Analysis of variance
APV	2-amino-5-phosphonopentanoic acid
ASD(s)	Autism spectrum disorder(s)
ATP	Adenosine triphosphate
Aβ	Amyloid-β
BCA	Bicinchoninic acid
C57BL6/J	C57 black 6J (mouse strain)
CA	Cornu ammonis
Ca^{2+}	Calcium
CCK	Cholecystokinin
CNQX	6-cyano-7-nitroquinoxaline-2,3-dione

CNS	Central nervous system
DG	Dentate gyrus
DMSO	Dimethyl sulfoxide
dNTP	Deoxynucleotide triphosphate
DTT	Dithiothreitol
EA	Epileptiform activity
EC	Entorhinal cortex
ED(s)	Epileptiform discharge(s)
EEG	Electroencephalogram
EPSC(s)	Excitatory postsynaptic current(s)
EPSP(s)	Excitatory postsynaptic potential(s)
fEPSP(s)	Field excitatory postsynaptic potential(s)
fps	Frames per second
FWHM	Full width at half maximum
GABA	γ-aminobutyric acid
GluA	Subunit of AMPA receptors
h	Hour/hours
H_2O	Water
H_2O_2	Hydrogen peroxide

HFS	High frequency stimulation
HSD	Honestly significant difference (referring to Tukey's post-hoc test)
IED(s)	Interictal epileptiform discharge(s)
IPSC(s)	Inhibitory postsynaptic current(s)
IPSP(s)	Inhibitory postsynaptic potential(s)
IQR	Interquartile range
KDa	Kilodalton
KO	Knockout
LFP	Local field potential
LFS	Low frequency stimulation
LIA	Large amplitude irregular activity
LTD	Long-term depression
LTP	Long-term potentiation
mGluR(s)	Metabotropic glutamate receptor(s)
min	Minute/minutes
mRNA	Messenger ribonucleic acid
MWCO	Molecular weight cut off
nAChR(s)	Nicotinic acetylcholine receptor(s)
NMDA	N-methyl-D-aspartic acid

NREM	Non-rapid eye movement (sleep)
ofx	Open field ‘x’, e.g., of1 is open field 1
ohtau40	Oligomeric human tau40
OLM	Oriens lacunosum moleculare
PBS	Phosphate-buffered saline
PCR	Polymerase chain reaction
PFA	Paraformaldehyde
PIP2	Phosphatidylinositol 4,5-bisphosphate
p-ripples	Pathological ripples
PSD	Power spectral density
PV	Parvalbumin
Px	Postnatal rodent age in ‘x’ days, e.g., P0 is day of birth
REM	Rapid eye movement (sleep)
RMANOVA	Repeated measures analysis of variance
RMS	Root mean square
RTX	Resiniferatoxin
SAHA	Suberoylanilide hydroxamic acid
SC	Schaffer collateral
SEM	Standard error of the mean

Shank3	SH3 and multiple ankyrin repeat domains 3
STDP	Spike timing dependent plasticity
SW(s)	Sharp wave(s)
SWR(s)	Sharp wave ripple(s)
SWS	Slow wave sleep
ThioT	Thioflavin-T
TRPV1	Transient receptor potential vanilloid 1
WT	Wild-type

List of figures

List of tables

Summary

Previous research in our lab found impaired long-term potentiation (LTP) of CA3-CA1 synapses, a fundamental process for learning and memory, in transient receptor potential vanilloid 1 (TRPV1) knockout (KO) mice. The TRPV1 channel is specifically expressed in oriens lacunosum moleculare (OLM) interneurons in the hippocampus, where it controls their excitatory innervation. OLM neurons participate in sharp wave ripples (SWRs), another phenomenon known for its importance in memory consolidation. During SWRs, which occur during sleep and rest, neuronal firing sequences representing a previous waking experience are reactivated, leading to consolidation of the memory by strengthening the connections between firing neurons, i.e., LTP. We therefore hypothesized that TRPV1 KO mice will have impaired SWRs, mirroring LTP deficits.

The TRPV1 channel is activated by a multitude of signals, including temperature, which decreases during sleep, when SWRs occur. We therefore first studied SWRs in hippocampal slices at different temperatures. Slices from TRPV1 KO mice had enhanced SWRs, with the most prominent effect being increased duration and rate of occurrence at 36 ^{o}C. We then examined SWRs in vivo in behaving mice during rest periods before and after exploration of two open fields, and saw a similar enhancement of SWRs, this time manifested as increased ripple magnitude and frequency. Theta oscillations, which are involved in memory encoding, had a higher frequency but lower power in TRPV1 KO mice, and delta oscillations were also affected. Spatial tuning was impaired in TRPV1 KO mice, as place cells had larger place fields and were less stable than in wild-type (WT) mice. Memory was examined using the cheeseboard maze task. Both WT and TRPV1 KO mice learned the first reward location at similar rates, but KO mice took longer to reach a new reward when its location was moved. This could hint at an impairment in memory extinction, but further analysis is required to confirm this.

SWRs can transform into epileptiform discharges and pathological ripples. Febrile seizures develop in young children due to fever, and since the TRPV1 channel is temperature sensitive, we hypothesized it might alter susceptibility to seizure induction. Temperature elevation increased epileptiform activity (EA) in a similar percentage of slices from young WT and TRPV1 KO mice. However, a lower percentage of TRPV1 KO slices had EA at 31 ^{o}C, consistent with a protective effect of TRPV1 inhibition in seizure susceptibility.

Another goal of this study was to investigate the relationship between LTP and SWRs. High-frequency stimulation (HFS) that induces LTP increased SW duration, but decreased SW incidence. Anisomycin, which blocks protein synthesis and LTP maintenance, had no effect on SWRs. SAHA, which on the other hand enhances LTP, had only minimal effects on SWRs with short-term application, and decreased SWRs with long-term application, possibly due to excitotoxicity. Our results suggest that SWRs and LTP are therefore not always positively correlated.

LTP and SWRs are impaired in Alzheimer's disease (AD), the most prominent type of dementia. Tau aggregation is a hallmark of AD pathogenesis and tau application on slices causes LTP deficits. We tested SWRs in the presence of tau, and found that tau oligomers only moderately affect SWRs, while larger tau aggregates significantly reduced SWRs in hippocampal slices, consistent with SWR changes in AD mouse models and subsequent learning and memory deficits.

In summary, we provide evidence that the TRPV1 channel is involved in hippocampal SWRs, theta and delta oscillations, place cell spatial tuning, and possibly memory extinction, and expand knowledge of the association between SWRs and LTP in normal and pathological states.

1. Introduction

1.1 Memory

Memory is a fundamental process of the human experience. Through memory we learn, associate experiences, understand the world, and build our own life stories. Memory impairment has indeed detrimental effects on life quality as seen by dementia patients. For these reasons, memory is a process that has been extensively studied. It can be separated into different sub-categories based on a variety of factors.

The first factor is the stage of the memory, which is based on the length of time the information remains available to us and includes sensory, short-term, and long-term types (Stangor & Walinga, 2014). Sensory memory is brief, immediate, automatic, and has a large capacity. It consists of unprocessed sensory information and, despite its short duration, it has broad importance. For example, auditory sensory memory allows us to remember the start of a long sentence (Hall & Stewart, 2010). If paid attention to, sensory memory is transferred to short-term memory for processing. While sensory memory only lasts for a few seconds at maximum, short-term memory can last up to 30 seconds (Atkinson & Shiffrin, 1968). A limited amount of information can be stored in short-term memory and only temporarily, but it makes the information available for processing. This processing is often called working memory, which is not exactly a memory store in itself; it is rather a set of mental operations such as solving sequential mathematical equations and using the output of the first as the input to the second equation. Techniques such as maintenance rehearsal, i.e., repeating information mentally or aloud, and chunking, i.e., separating information into smaller groups, have been shown to increase the duration and amount of information held in short-term memory, respectively (Stangor & Walinga, 2014). Lastly, long-term memories are those that last days, months, or years, or may even be permanent. Long-term memory has a large capacity with unknown limits (Stangor & Walinga, 2014). Different mechanisms support these distinct types of memory (Citri & Malenka, 2008). For example, paired-pulse facilitation, the increased excitatory postsynaptic response to the second of two consecutive stimulations, is a short-term activity-dependent form of synaptic plasticity (Santschi & Stanton, 2003) that might underlie short-term memory. On the other hand, longer lasting changes are required for long-term memory, such as structural changes of synaptic-bouton morphology, cellular activity, and network connectivity and synchrony (Citri & Malenka, 2008; Rao-Ruiz et al., 2021).

The second type of memory categorization concerns long-lasting memories and is based on the type of memory itself. Declarative or explicit memory includes information about one's own life, a subdivision known as episodic memory, as well as general facts and information about the world (e.g., the capital of Germany or historical events), also known as semantic memory. It involves conscious remembering of events after intentional retrieval. Non-declarative or implicit memory, on the other hand, is not consciously recollected. Rather, it shows how current behavior is influenced by past experiences. It includes procedural memory (e.g., playing the piano), priming (e.g., being more likely to use a word that was heard recently), and associative memory such as conditioning (e.g., salivating at the sound of a bell that is associated with food access) (Stangor & Walinga, 2014). These

types of memories emerge due to varied cellular and network mechanisms and depend on different brain structures. The hippocampus is mainly involved in declarative memories, while non-declarative memories depend on structures such as the basal ganglia and the cerebellum (Camina & Güel, 2017). In addition, some types of memories, like association memories, require communication between different brain areas, such as the hippocampus and amygdala in the case of contextual fear conditioning (Kim & Cho, 2020).

Memory is also subdivided based on the processes underlying it: encoding, storage, and retrieval (Stangor & Walinga, 2014). Encoding represents the first stage, during which a memory is formed after an experience. Cells representing different aspects of the event are co-activated, and hence linked to each other, forming memory engrams. The Hebbian theory that is described in the following section provides the suggested framework for how this linking occurs. Some mechanisms involved in memory encoding, such as synaptic potentiation, are also involved in memory consolidation. Consolidation refers to the process of memory storage during which previously formed memory engrams are reactivated. This strengthens the existing connections of the network, while also recruiting new cells and synchronizing activity in other brain areas, allowing the transfer of the memory from initial, temporary stores (in the hippocampus) to permanent stores (in the cortex) (Ortega-de San Luis & Ryan, 2022). Memory retrieval involves accessing these stored memories and is also associated with reactivation of the memory engrams. Importantly, this reinstates the engram's malleability, so new experiences can alter and be linked to old ones (Bisaz et al., 2014).

The converse of memory retrieval (remembering) is memory erasure or forgetting. This can be caused by erasure of the memory itself or the inability to access an existing memory. In the latter case where the memory trace exists but is temporarily unavailable, it might become available again if, for example, cues (cued recall) are given (Frankland et al., 2019). Forgetting involves multiple mechanisms, which differ in terms of reversibility and time course (Ryan & Frankland, 2022). One such mechanism is intrinsic forgetting, which is hypothesized to be the default state of the brain and involves continually active signaling systems that gradually deteriorate memory traces (Davis & Zhong, 2017). Another mechanism is memory extinction, which involves acquiring a new memory that suppresses activation and expression of the original memory trace and associated response (Myers & Davis, 2007; Tovote et al., 2015; Davis & Zhong 2017) and allows behavioral flexibility (Nicholls et al., 2008). Forgetting might be a form of learning with many similarities to extinction, whereby memories that are no longer needed are replaced by more relevant memories (Ryan & Frankland, 2022).

1.2 The hippocampus

1.2.1 Anatomy and connectivity

The hippocampus is one of the most extensively studied brain areas, mainly for its importance in memory processes (Knierim, 2015). It was first described in 1587 by Julius Caesar Aranzi, a pioneer anatomist and surgeon (Bir et al., 2015). The name comes from the Greek word for seahorse (ιπποκαμπος), due to the resemblance of the human hippocampus to the animal. In mice, it has a

C-shape and occupies a large part of the rodent brain. The hippocampus is conserved across mammals (Manns & Eichenbaum, 2006), which have one in each temporal lobe. It is part of the archicortex and the limbic system, which supports memory and emotional regulation.

The hippocampus includes the dentate gyrus (DG) and the cornu ammonis (which is roughly subdivided into CA1, CA2, and CA3, with CA2 often omitted due to its small size). The cornu ammonis consists of the layers stratum oriens, stratum pyramidale, stratum radiatum, and stratum lacunosum moleculare, from most superficial to the deepest (Li & Pleasure, 2013). A large variety of inhibitory cells are found in the hippocampus across all layers. The pyramidal cells are the principal cells of the hippocampus and have their somata in the pyramidal layer. Their dendrites extend into all layers of the hippocampus (Pelkey et al., 2017), while their axons make both intra- and extra-hippocampal connections, as described below.

The major input and output region of the hippocampus is the entorhinal cortex (EC). The EC targets all hippocampal subregions through the perforant path. EC layer II cells project to the DG and then through mossy fibers to CA3. CA3 pyramidal cells are reciprocally connected and also receive direct input from pyramidal cells of EC layer II. After local processing, the signal is transmitted from CA3 to CA1 stratum radiatum through axons called Schaffer collaterals (van Strien et al., 2009). EC layer III cells, on the other hand, project to the distal apical dendrites of CA1 in stratum lacunosum moleculare and to the subiculum; this input is called the temporoammonic pathway. Interestingly, temporoammonic axons also target hippocampal interneurons (Dvorak-Carbone & Schuman, 1999). Input to the hippocampus comes from additional sources such as the contralateral hippocampus (Finnerty & Jefferys, 1993), cortical areas such as the anterior cingulate cortex (Rajasethupathy et al., 2015) and retrosplenial cortex (Wyss & van Groen, 1992), and subcortical areas such as the thalamus (Bertram & Zhang, 1999; Jankowski et al., 2013), the hypothalamus (Robert et al., 2021), and the amygdala (Felix-Ortiz et al., 2013). CA1 pyramidal cells are the major output of the hippocampus. They innervate the subiculum and deeper layers of the EC, as well as the amygdala, hypothalamus, nucleus accumbens, olfactory regions, visual cortex, auditory cortex, cingulate cortex, and more (Arszovszki et al., 2014; van Groen & Wyss, 1990; Cenquizca & Swanson, 2007). Some also consider the subiculum as part of the hippocampal formation (O'Mara et al., 2001), establishing it as another main hippocampal output source. The subiculum has extensive projections, some shared with CA1 (e.g., to the EC, prefrontal cortex, and amygdala) and some unique (e.g., to the retrosplenial cortex, anterior thalamic nuclei, and mammillary bodies; Aggleton & Christiansen, 2015). Figure 1 shows a diagram of hippocampal anatomy and connectivity.

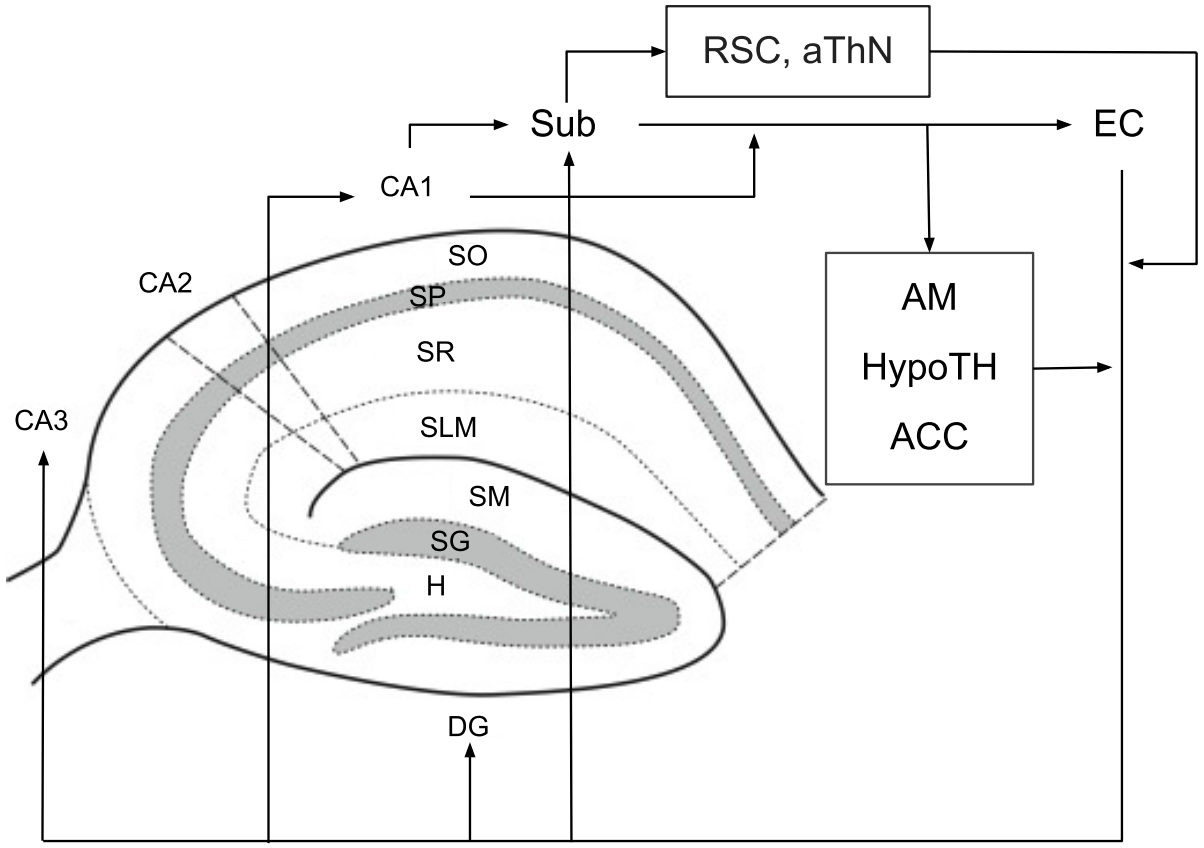

Figure 1: The hippocampal circuitry. The hippocampus includes the dentate gyrus (DG) and cornu ammonis (CA3, CA2, CA1). The DG consists of the hilus (H), stratum moleculare (SM), and stratum granulosum (SG). The CA consists of stratum oriens (SO), stratum pyramidale (SP), stratum radiatum (SR), and stratum lacunosum-moleculare (SLM). The main input to the hippocampus comes from the entorhinal cortex (EC). Hippocampal output projects from CA1 and the subiculum (Sub). These regions both project to the EC, the amygdala (AM), the hypothalamus (hypoTH), and the anterior cingulate cortex (ACC), but only the subiculum projects to the retrosplenial cortex (RSC) and the anterior thalamic nuclei (aThN). The RSC, aThN, AM, HypoTh, and ACC also send direct projections back to the hippocampus. Figure adapted from Li & Pleasure, 2013.

1.2.2 Function

The involvement of the hippocampus in memory formation became apparent after assessment of patient H.M., whose hippocampi and surrounding structures were removed bilaterally as a treatment for severe epilepsy. Even though seizures improved, patient H.M. experienced anterograde amnesia after the surgery, the inability to form new episodic memories, and temporally-graded retrograde amnesia, the inability to remember recent memories, while remote memories were relatively intact. The procedure, however, spared short-term memory, motor learning, and intellectual abilities (Penfield & Milner, 1958; Kensinger et al., 2001; Corkin, 2002). Work with other patients revealed that the hippocampus is not only important for past actions, but is also involved in planning and imagining future experiences (Addis & Schacter, 2012; Schacter et al., 2008).

Later studies further investigated the importance of the hippocampus in memory formation, consolidation, and retrieval (Frankland et al., 1998; Brasted et al., 2003; Girardeau et al., 2009; Roux et al., 2017; Kim & Fanselow, 1992; Squire et al., 2001; Moser & Moser & Andersen, 1993). It is often challenging to differentiate whether the effect of hippocampal inactivation is due to a failure of memory retention or failure to access the memory, as retrograde amnesia due to post-learning hippocampal lesions could be attributed to a defect of either process. It is generally accepted though that memory consolidation is hippocampal dependent (Buzsáki, 2015), and that memory retrieval is hippocampal dependent for at least some time after an initial experience (Fortin et al., 2004; Carr et al., 2011). Two different models emerged for the involvement of the hippocampus in memory consolidation and subsequent retrieval. The "standard model" postulates that memories become independent of the hippocampus once they are transferred to the neocortex, while the "multiple-trace theory" posits that the hippocampus remains involved (Moscovitch et al, 2005).

A vast number of electrophysiological studies revealed that pyramidal cells in the hippocampus respond to spatial features of the environment. Most well-known are "place cells", termed as such after the discovery that they fire action potentials when the animal occupies a specific location in space, making the hippocampus important for forming an internal representation of one's own environment (O'Keefe & Dostrovsky, 1971; O'Keefe & Nadel, 1978). This is in agreement with impaired spatial learning in rodents after hippocampal lesions (Moser & Moser & Andersen, 1993). Interestingly, place cells were also found in humans during exploration of virtual space (Miller et al., 2013). The familiarity of an environment seems to affect place fields, as they tend to be more diffuse during exploration of a novel environment and tend to become smaller, carrying more spatial information during familiarization (Cacucci et al., 2007). Following the discovery of place cells, other spatially modulated cells have been discovered in the hippocampal formation, such as grid cells, head-direction cells, border cells, and cells encoding the animal's speed (Hafting et al., 2005; Rubin et al., 2014; Lever et al., 2009; Kropff et al., 2015).

Some studies also suggest that the function of the hippocampus varies across its dorsoventral (also known as the septotemporal or longitudinal) axis. This is supported by both anatomical and behavioral data. For example, while both the dorsal (posterior in primates) and ventral (anterior in primates) part of the hippocampus is populated by place fields, their size becomes gradually larger along the axis towards the ventral part, suggesting that they might be involved in spatial orientation and navigation at different scales (Harland et al., 2017). A topographical connection between the EC and the hippocampus exists, with the caudolateral band of the EC, which receives most visuospatial information, targeting the dorsal hippocampus, while the medial band of the EC, which receives olfactory, gustatory, and visceral inputs, projects to the ventral hippocampus (Fanselow & Dong, 2010). Moreover, Tao and colleagues (2021) report that the amygdala, olfactory area, and thalamic nuclei such as the paraventricular nucleus, target ventral but not dorsal CA1. A similar topographic organization is seen in the output projections from the hippocampus to the EC (Fanselow & Dong, 2010). Dorsal projections target the retrosplenial and anterior cingulate cortices, which carry visuospatial information, but also selectively target the mammillary nuclei and anterior thalamic cortex. Conversely, the ventral hippocampus sends direct projections to the olfactory area, amygdala, insular cortex, and hypothalamus (Fanselow & Dong, 2010). The distinct connectivity patterns of the two areas is reflected in their function. Results from lesion, gene expression, and fMRI studies

suggest that the dorsal hippocampus is more important for spatial navigation and contextual association memory (e.g., contextual fear conditioning), while the ventral hippocampus is important for both contextual (Kim & Cho, 2020; Jimenez et al. 2020) and cued (Herbst et al., 2022) fear conditioning, as well as emotional processing as shown by decreased anxiety and altered stress responses after ventral-hippocampal lesions (Bannerman et al., 2003; McHugh et al., 2004; Chang & Gean, 2019; Scopinho et al., 2013).

1.2.3 Alzheimer's disease and the tau protein

Memory impairment is a hallmark of a vast repertoire of pathologies. Alzheimer's disease (AD) is the most prevalent kind of dementia, affecting 6% of the population over the age of 65 (Burns & Iliffe, 2009). The hippocampus is one of the first and most affected brain areas in AD (Coupé et al., 2019). Two histological hallmarks characterize the pathology: extracellular deposition of amyloid-β (Aβ) plaques and intracellular tau-containing neurofibrillary tangles (Bloom, 2014). However, various oligomeric forms of the two proteins contribute to neurodegeneration (Verma et al., 2015; Shafiei et al., 2017).

Although they only represent a minority of AD cases, some forms of the disease are hereditary and are characterized by early onset (Wu et al., 2012). In these familial AD patients, mutations were identified and used to develop animal models. The first group of mutations targets Aβ, for example by causing overproduction, increased aggregation, or altered cleavage of Aβ. The second family replicates tau pathophysiology by increasing tau phosphorylation or aggregation. Some models combine Aβ and tau related mutations to replicate more features of AD (Yokoyama et al., 2022; Myers & McGonigle, 2019). Contrary to familial AD cases, the third group of mouse models targets the apolipoprotein-E (APOE) gene, which is the strongest risk factor associated with AD. Even a single copy of the ε4 allele increases AD risk 4-fold (Hall & Roberson, 2012).

Abnormal tau protein deposition is associated with a large cluster of neurodegenerative disorders called tauopathies, with a major clinical symptom being frontotemporal dementia (Kovacs, 2017). Tau is a microtubule-associated protein, which under physiological conditions plays a role in microtubule assembly and stabilization (Mandelkow & Mandelkow, 2012). Exogenously applied tau is uptaken into cells and can seed intracellular inclusions of endogenous tau (Jiang et al., 2020), which can further propagate the pathology.

1.3 Synaptic transmission

The brain is made up of a complex network of neurons that transmit electrical signals. This neuronal communication is essential for the function of the network, including memory formation, and takes place at synapses, connections between the presynaptic and the postsynaptic cell. Inputs from multiple neurons arrive at axonal presynaptic boutons connecting to the postsynaptic dendrites of a neuron. Signals are then integrated in the axon initial segment of this postsynaptic neuron and, if a threshold is surpassed, an electrical signal (action potential) is transmitted along the axon of the

neuron. When an action potential reaches a presynaptic bouton, it activates the release of chemicals, called neurotransmitters, that are stored there in vesicles, which then travel across the synaptic cleft and activate receptors on dendrites of postsynaptic cells. These chemical synapses form the basis of synaptic transmission in the central nervous system (CNS). In response to an action potential, a large number of synaptic vesicles release neurotransmitters synchronously from the presynaptic terminal (Hammond & Esclapez, 2015). However, neurotransmitters can also be released spontaneously in the absence of an action potential due to stochastic fusion of single synaptic vesicles (Ramirez & Kavalali, 2011).

There is a large number of neurotransmitter molecules and neurotransmitter receptors in the CNS. The most common excitatory neurotransmitter is L-glutamic acid or glutamate (Zhou & Danbolt, 2014), while the main inhibitory neurotransmitter is γ-aminobutyric acid (GABA; Allen & Sabir & Sharma, 2022). Both of these neurotransmitters activate ionotropic and metabotropic receptors. Ionotropic receptors are membrane proteins that change conformation after neurotransmitter binding, leading to the opening of a pore that allows ions to flow in and out of the cell. Some receptors are non-selective, while others only allow specific ions to pass through. Glutamate activates two types of ionotropic receptors, α-amino-3-hydroxy-5-methyl-4- isoxazolepropionic acid (AMPA), and N-methyl-D-aspartic acid (NMDA) receptors. These are formed by different subunits, and subunit composition affects receptor function. For example, most AMPA receptors are only permeable to sodium and potassium cations, but those lacking the edited form of the GluA2 subunit are also permeable to calcium (Henley & Wilkinson, 2016; Traynelis et al., 2010). NMDA receptors, on the other hand, allow calcium to pass through, but at resting membrane potentials their pore is blocked by magnesium ions. Therefore, NMDA receptor activation is only achieved when glutamate binding coincides with a depolarized membrane potential (e.g., due to previous AMPA receptor activation), hence acting as a coincidence detector (Collingridge et al., 1983; Lee et al., 2014). Conversely, metabotropic receptors do not directly permit ionic flow, but upon activation they initiate a cascade of intracellular events in the postsynaptic cell. Metabotropic glutamate receptors (mGluRs) comprise a large and diverse family with a variety of functions in the CNS (Ferraguti & Shigemoto, 2006). GABA also exerts its function through ionotropic and metabotropic receptors, called $GABA_A$ and $GABA_B$ receptors, respectively. Many other neurotransmitters exist, such as dopamine, serotonin, adrenaline, and more, which can in turn modulate glutamatergic and GABAergic transmission.

An alternative type of synaptic transmission through electrical synapses also exists. These synapses are formed by gap junctions, channels that directly connect the cytoplasm of two neurons, allowing direct flow of ions between them. While this is useful in synchronizing neuronal activity (Pereda, 2014), it doesn't allow synaptic integration and reduces flexibility of response. The main form of neuronal communication in the CNS is therefore chemical synapses.

1.4 Hebbian theory and synaptic plasticity

A mammalian neuron makes roughly 8,000 connections with other neurons in the brain (Schüz & Palm, 1989), but not all are equally strong. A strong synapse would be more likely to initiate an action

potential in the postsynaptic cell after firing of the presynaptic cell, while probabilities would be lower for a weak connection. Synapses are able to modulate their strength in a specific and activity-dependent manner, which is termed synaptic plasticity. Stronger synapses have more neurotransmitter release and/or more postsynaptic receptors. Some connections of one neuron might get stronger (synaptic potentiation) while others get weaker (synaptic depression) as a consequence of network activity. This is believed to be the synaptic correlate of learning and memory.

Donald Hebb, a Canadian psychologist, was the first to suggest that if a neuron fires at the same time as another neuron, then either a new synapse is created or the strength of an already existing synapse is enhanced. If the activities of a presynaptic and a postsynaptic cell do not match, the synapse should in turn be weakened (Hebb, 1949). Long-term synaptic strengthening was first demonstrated in rabbits (Bliss & Lomo, 1973), where high-frequency stimulation of presynaptic fibers increased postsynaptic potentials for hours and was therefore called long-term potentiation (LTP). Later studies stressed the importance of the precise timing of activation for such potentiation to occur (Taylor, 1973). Long-term depression (LTD), the weakening of synapses caused by low-frequency stimulation, was first shown in the cerebellum (Ito & Kano, 1982). Many forms of synaptic plasticity depend on the coincidence of activity of the pre- and the postsynaptic cells. Since the NMDA receptors act as coincidence detectors (Collingridge et al., 1983; Lee et al., 2014), they are often critical in the process (Lüscher & Malenka, 2012). Several types of synaptic plasticity are now known, some of which will be outlined below.

1.4.1 LTP, LTD, and depotentiation

In the hippocampus, if an electric pulse is delivered extracellularly to axonal presynaptic afferents, it leads to activation of a population of postsynaptic cells, and such a field excitatory postsynaptic potential (fEPSP) can be measured extracellularly by a recording electrode. A series of such pulses given at one to two minute intervals determines the baseline postsynaptic response to presynaptic stimulation. Following an LTP induction protocol (a train of 100 Hz stimulation, for example), LTP is seen as an increased fEPSP compared to baseline fEPSP in response to a pulse of the same strength, while a decreased fEPSP is seen after an LTD protocol (a train of 1 Hz stimulation, for example).

If LTP lasts more than 1-2 hours, it is called strong- or late-LTP, which has been found both in vitro and in vivo. It requires activation of NMDA receptors for its initiation and de novo protein synthesis for its stability and longevity (Park et al., 2013). LTP cellular mechanisms include increased presynaptic neurotransmitter release after an action potential, for example through increasing release probability from synaptic vesicles (Schulz, 1997), or increased number of postsynaptic receptors through insertion of new receptors into the plasma membrane (Bliss & Collingridge, 2013). Similarly, decreased probability of neurotransmitter release (Choi & Lovinger, 1997) and decreased number of postsynaptic receptors (Granger & Nicoll, 2014) are mechanisms of LTD. The most common LTP protocols, at least for potentiation of Schaffer collateral-CA1 synapses, are high frequency stimulation (HFS), which usually involves 3 trains of 100 pulses at 100 Hz with 10-minutes between trains, and theta burst stimulation (TBS), for example 4 pulses at 100 Hz repeated 10 times

at 5 Hz (Park et al., 2013). In weak- or early-LTP on the other hand, the fEPSP returns to baseline levels after 1-2 hours. Weak-LTP induction protocols employ fewer trains or pulses per train of stimulation. Weak-LTP is believed to be the early phase of strong-LTP, so it is also NMDA receptor dependent, but without de novo protein synthesis it decays. LTD is also NMDA receptor and protein synthesis dependent (Dong et al., 2015; Park et al., 2013; Raymond, 2007). A common LTD protocol is low frequency stimulation (LFS), which uses pulses delivered at 1 Hz for 15 minutes (Collingridge et al., 2010). Depotentiation is induced by similar protocols and has similar mechanisms to LTD, but it refers to LTP reversal, when fEPSPs return back to baseline levels after first having been enhanced (Fujii et al., 1991).

1.4.2 Homeostatic plasticity

The forms of plasticity above are synapse-specific. Homeostatic plasticity, also known as metaplasticity or synaptic scaling, on the other hand, is a form of homeostatic regulation, where a neuron modulates the strength of all or multiple connections simultaneously. This allows the neuron to maintain and stabilize its activity, preventing uncontrolled potentiation. First described in the primary visual cortex, the Bienenstock Cooper Munro (BCM; Bienenstock & Cooper & Munro, 1982) theory of sliding plasticity thresholds posits that the threshold for potentiation and depression of a synapse changes based on the overall activity of a network. For instance, the threshold for LTP is higher in a more active network, hence stronger stimuli are needed to induce it. This can be achieved through mechanisms including changing the number or composition of postsynaptic NMDA receptors (Philpot et al., 2007).

1.5 Memory engrams and place cells

When a new experience is acquired, populations of cells representing it are simultaneously active. Such populations are called neuronal ensembles, neural assemblies, or engrams. Engram formation and synaptic plasticity are associated with each other, as synaptic density and spine size between CA3-CA1 engram cells are increased after memory formation (Choi et al., 2018). By labeling proteins whose expression is activity dependent (e.g., c-fos), scientists are able to identify, label, and modulate memory engrams (Liu et al., 2012). As a proof of concept for neural ensembles being the cellular signature of memories, Ramirez and colleagues (2013) labeled DG cells active in context-A (context-A engram cells) and reactivated them during fear conditioning in another context (context-B). This led to the creation of a false association of fear memory with context-A, as shown by increased freezing in context-A.

Memory engrams have been studied particularly using hippocampal place cells. Neural ensembles of such cells are believed to map the environment, hence forming a place code or a cognitive map (O'Keefe & Dostrovsky, 1971; O'Keefe & Nadel, 1978). Place cells often change the position (or firing rate) of their place fields to a different location when recorded in different rooms or environments. This phenomenon is called remapping, and impaired remapping is seen in animal models of AD (Jun et al., 2020), which may lead to poor discrimination between environments.

Activation of one neuronal assembly can propagate and activate other populations, leading to creation of phase sequences and association between different concepts (Hebb, 1949; Almeida-Filho et al., 2014). It is also widely accepted that engram reactivation represents the mechanism behind memory consolidation and recall (Wilson & McNaughton, 1994; Lee & Wilson, 2002; Diba & Buzsáki, 2007; Carr et al., 2011; Foster & Wilson, 2006; Ecker et al., 2022; Wikenheiser & Redish, 2013). Engram formation and reactivation occurs during hippocampal oscillations of different frequencies, which are the focus of the next section.

1.6 Oscillations of the hippocampus

Brain oscillations are generally thought to reflect synchronized network activity and are closely associated with different behavioral states. Various types are seen in the hippocampus and have been studied for their role in memory processes. Sharp wave ripples are the focus of this study, so they will be extensively discussed below, with a shorter introduction for other hippocampal oscillations.

It is important to mention that the cortex also exhibits different types of oscillatory network activity. Simultaneous recordings from the hippocampus and various cortical areas suggest that the two can be coupled in time through synchronized oscillatory activity, leading to the hippocampal-cortical communication that is essential for memory consolidation (Todorova & Zugaro, 2019; Colgin, 2011; Çalışkan & Stork, 2019).

1.6.1 Sharp wave ripples

1.6.1.1 History and characterization

Sharp wave ripples (SWRs) were first observed by Jouvet and Michel in 1959 (Jouvet & Michel, 1959; Buzsáki, 1986) in cats as electroencephalogram (EEG) spikes and were regarded as a subcortical electrophysiological correlate of slow wave sleep (SWS). Cornelius Vanderwolf (1969) recorded EEGs from rats and described large amplitude irregular activity (LIA) in the hippocampus during awake immobility and consummatory behaviors such as drinking, grooming, and chewing. Many studies since have investigated SWRs in both awake and sleep states. It is now known that SWRs exist in humans (Bragin et al., 1999a; Axmacher et al., 2008b), non-human primates (Kaplan et al., 2016), rodents (Vanderwolf, 1969), zebrafish (Vargas et al., 2012), and lizards (Shein-Idelson et al., 2016), but not in birds (Vorster & Born, 2015).

In vitro, SWRs spontaneously occur in slices from the ventral hippocampus, while stimulation is necessary to elicit them in dorsal hippocampal slices (Buzsáki, 2015). They are found by local field potential (LFP) recordings. Sharp waves (SWs) have a relatively large amplitude and their occurrence is non-periodic. They have a slow frequency, which in some cases is reported as 5-15 Hz (Oliva et al., 2018) or even as low as 0.01-3 Hz (Colgin, 2016) and duration of 40-100 ms (Buzsáki et al., 1983). SWs are thought to reflect synchronous activity of the network and their polarity changes across different layers of the hippocampus; they are positive in stratum oriens and pyramidale of CA3 and

CA1, the hilus of the DG, and layers II-IV of the subiculum, while negative polarity is seen in stratum radiatum of CA1, stratum lucidum of CA3, layer I of the subiculum, and the molecular layer of the DG (Buzsáki, 1986).

SWs usually occur simultaneously with fast 120-250 Hz (Pangalos et al., 2013) oscillations called ripples. Even though SWs and ripples are coupled in time, they are considered separate events, as the mechanisms and networks responsible for their generation differ and one may exist without the other (Colgin, 2016; Buzsáki, 2015). During SWRs 50,000-100,000 neurons discharge together, making SWRs one of the most synchronous neuronal signals (Buzsáki, 2006). According to Ylinen and colleagues, the number of simultaneously firing units during SWRs varies from 0-40%, with an average of 10% of the recorded neurons firing. Different neurons have different probability of participation in SWRs; some pyramidal cells discharged in up to 40% of consecutive SWRs while others are only seldom associated with SWRs. Furthermore, pyramidal cell firing is phase locked to the negative peaks of the ripples recorded from the CA1 pyramidal layer (Ylinen et al, 1995).

1.6.1.2 Mechanisms of generation, propagation, and termination

A lot remains unknown about the mechanisms behind SWRs. SWRs appear to be the default, intrinsic state of the hippocampus, as they emerge spontaneously in hippocampal slices (Buzsáki, 2015). Therefore, some models suggest that SWRs are "released" rather than triggered. This release comes in the form of disinhibition, where extrahippocampal input that suppresses SWRs is removed (Buzsáki, 2015). SWs are believed to originate in CA3 (Csicsvari et al., 2000) by the dense recurrent excitation circuit there that synchronizes hippocampal activity (Buzsáki, 2015; Wittner & Miles, 2007). Accordingly, SWs in CA1 follow SWs in CA3 on average 4.0 ± 0.2 ms later and are eliminated when the connection between the two areas is surgically removed (Colgin et al., 2004). This procedure does not affect baseline responses in CA1, LTP induction, or CA3 SWs. Contrary to this, a different study reports the presence of CA1 SWs in CA1 minislices, suggesting that SWs can be locally generated in CA1, albeit at a much lower frequency of occurrence (Maier et al., 2003). In the same study, it has been demonstrated that application of the AMPA/kainate receptor antagonist 6-cyano-7-nitroquinoxaline-2,3-dione (CNQX), but not the NMDA receptor antagonist 2-amino-5-phosphonopentanoic acid (APV), blocks SWRs, suggesting a differential dependance of SWR generation on different types of glutamate receptors. However, NMDA receptors are involved in SWR modulation, as is seen by suppression of clusters of SWs in the presence of NMDA receptor antagonists (Papatheodoropoulos, 2010).

When it comes to inhibitory transmission, gabazine, a $GABA_A$ receptor antagonist, transforms SWRs to epileptiform discharges (Maier et al., 2003), indicating the importance of a balance between excitation and inhibition for physiological SWRs. Conversely, low concentrations of bicuculline, a different $GABA_A$ receptor antagonist, do not elicit epileptiform activity and result in suppression of secondary SWs (and hence SW clusters) to a greater extent compared to primary SWs (Papatheodoropoulos, 2010). Interestingly, enhanced GABAergic transmission by the use of allosteric $GABA_A$ receptor modulators thiopental and diazepam also decreases the occurrence of SW clusters (Papatheodoropoulos, 2010), pointing to a precise regulation of SWRs by GABAergic transmission.

During in vivo SWRs, inhibition dominates over excitation in terms of peak conductance, the amplitude of IPSCs but not EPSCs is correlated with SWR magnitude, and IPSCs but not EPSCs are phase-locked to ripples, supporting an even bigger role for inhibition compared to excitation in shaping SWRs (Gan et al., 2017).

While CA3 input is critical for SW generation, CA1 ripples are preserved after CA3 silencing. However, intrinsic ripple frequency decreases, as well as the ripple-associated reactivation of CA1 cell pairs, which is crucial for memory consolidation (Nakashiba et al., 2009). Moreover, CA1 ripples have a higher frequency than CA3 ripples (Sullivan et al., 2011). Ripples are therefore believed to not only be transmitted from CA3, but also to be locally generated in CA1 (Csicsvari et al., 1999; Nakashiba et al., 2009; Buzsáki, 2015; Sullivan et al., 2011). Pyramidal cell depolarization is sufficient to elicit ripples, while silencing pyramidal cells abolishes ripples (Stark et al., 2014). The negative peaks of the ripple seem to represent the superimposed action potentials of synchronously discharging cells, while the positive peaks emerge from the outward membrane currents of pyramidal cell somata, which are hyperpolarized due to interneuron firing (Buzsáki, 2015).

The hippocampus includes different types of interneurons with varied participation in SWRs. Bistratified cells fire with high frequency during the ascending phase of ripples (Klausberger et al., 2004). Parvalbumin (PV)-positive basket cells fire at the troughs of ripples, while PV-positive axo-axonic cells fire at the beginning of the ripple event and are silent afterwards (Klausberger et al., 2003). To further stress the importance of inhibitory cells in SWR initiation, optogenetic activation of PV-positive interneurons is sufficient to generate SWRs even in the absence of excitation (Schlingloff et al., 2014). Silencing these cells interrupts or inhibits SWRs (Schlingloff et al., 2014), similar to the effects of pharmacological blockade of $GABA_A$ receptors (Stark et al., 2014). However, activation of PV or somatostatin expressing cells during an ongoing spontaneous SWR event interrupts SWRs, highlighting the significance of temporally precise interactions between excitatory and inhibitory cells for SWR generation (Stark et al., 2014). Cholecystokinin (CCK)-expressing interneurons, on the other hand, participate only in some ripple events, which might be affected by the recent history of the network. Thus, it is suggested that CCK-expressing cells may be involved in selecting which pyramidal cells will participate in a specific SWR event and which not, so that only cells that are part of the same memory engram are co-activated (Klausberger et al., 2005). Contrary to these cell types, calbindin-expressing interneurons (Lasztóczi et al., 2011) and axo-axonic interneurons (Viney et al., 2013) seem to be silent during SWRs. The silencing of the axo-axonic cells is due to input from medial septal GABAergic cells, leading to disinhibition of pyramidal cells (Viney et al., 2013). While the precise network underlying SWRs remains elusive, evidence seems to agree that transient silencing of inhibitory cells leads to a buildup of synchronized excitation, which in turn activates different classes of interneurons that block excitatory transmission in a feedback loop, leading to the appearance of SWRs.

In addition to synaptic transmission, gap junctions have been suggested to be crucial for the synchrony underlying SWRs. Carbenoxolone and octanol, two gap junction blockers, decrease SWR occurrence in both CA1 and CA3, while also decreasing the percentage of SWs with superimposed ripples (Maier et al., 2003). In addition to these agents, halothane, a third gap junction blocker, abolishes ripples, while NH_4Cl, a drug that enhances gap junction coupling through intracellular

alkalinization, prolongs and increases the occurrence of ripples (Draguhn et al., 1998). Connexin-36, a gap junction subunit, has been studied in terms of SWR involvement, but results from knockout mice remain controversial (Maier et al., 2002; Hormuzdi et al., 2001; Buhl et al., 2003).

While SWRs are present during sleep and consummatory behaviors, they are absent during theta-associated preparatory behaviors such as active exploration. The cholinergic system is involved in theta oscillations, as optogenetic activation of septal cholinergic neurons abolishes SWRs while increasing the power and coherence of theta waves (Vandecasteele et al., 2014). In vitro studies suggest that both muscarinic and nicotinic acetylcholine receptors (AChRs) are involved in the balance between theta oscillations and SWRs (Fischer et al., 2014; Norimoto et al., 2012). Indeed, ACh levels are high during active wakefulness and low during quiet wakefulness and slow-wave-sleep (Hasselmo, 1999). ACh is therefore hypothesized to gate the oscillatory activity of the hippocampus, with ACh enhancing theta oscillations and suppressing SWRs during wakefulness, and SWRs taking over in the absence of ACh during sleep.

1.6.1.3 Functional significance of sharp wave ripples

Various lines of evidence implicate SWRs in memory consolidation. Firstly, rats that learned successfully a discrimination task have increased SWR incidence, ripple magnitude, and ripple duration in subsequent resting periods (Eschenko et al., 2008; Fernández-Ruiz et al., 2019), while in an AD mouse model the opposite SWR changes are seen (Prince et al., 2021). Moreover, electrical disruption of SWRs impairs memory performance (Girardeau et al., 2009; Ego-Stengel & Wilson, 2010).

During both awake and sleep SWRs, theta sequences that were formed during active exploration are reactivated, although 20-fold temporally compressed, in both forward and reverse directions. This replay is thought to be the foundation of memory consolidation (Wilson & McNaughton, 1994; Lee & Wilson, 2002; Diba & Buzsáki, 2007; Carr et al., 2011; Foster & Wilson, 2006; Ecker et al., 2022; Wikenheiser & Redish, 2013). Accordingly, disruption of SWR-associated place cell reactivation prevents refinement and stabilization of place maps (Roux et al., 2017; van de Ven et al., 2016). Awake SWR-associated reactivation may reflect both recent (Foster & Wilson, 2006) and remote (Karlsson & Frank, 2009) experiences. This is particularly important for making associations (Lewis & Durrant, 2011), as it allows neural ensembles representing past experiences to be reactivated and coupled to present experiences, and is theorized to be important for creativity (Buzsáki, 2015). Some researchers suggest that the same mechanism is involved in memory retrieval (Carr et al., 2011), while others believe that theta are primarily responsible for conscious recollection of past experiences and SWRs for involuntary recall such as subconscious priming (Buzsáki, 2015). Reactivation of neuronal ensembles during SWRs makes established memories malleable, which is also important for inhibitory learning. A new neural ensemble is formed that blocks activation of the original memory trace in a competitive manner, leading to memory extinction (Çalışkan & Stork, 2019). Sierra and colleagues (2022) activated the medial forebrain bundle during SWRs and found accelerated extinction, further supporting SWR involvement in the process. SWR-associated replay is also critical for emotional memory (Girardeau et al., 2017), spatial-working memory, and

memory-guided action (Jadhav et al., 2012). SWR-associated replay might thus represent a general mechanism not just for learning and memory, but also for cognitive processes such as planning (Pfeiffer & Foster, 2013; Ólafsdóttir et al., 2018), decision making (Yu & Frank, 2015), and imagination (Joo & Frank, 2018). Replay in the ventral CA1 in particular has been linked to social cognition. There, cells responding to memorized individuals, termed social memory neurons, are co-activated during SWRs if they share social representations (Tao et al., 2022).

Replay of cell assemblies can couple cellular representations of events that were separated in time. Their co-activation during off-states allows synaptic plasticity to take place. In a compelling experiment, Sadowski and colleagues (2016) recorded SWR-associated place cell activity in vivo and then replayed that activity in vitro. This stimulation led to LTP between CA3-CA1 synapses only in the presence of SWRs. Interestingly, one method for LTP induction in slices is through tetanic stimulation, which could be thought of as mimicking physiological SWRs (Buzsáki, 2015; Buzsáki, 1989). The process might be bidirectional, as LTP-inducing stimuli can also generate SWRs (Behrens et al., 2005).

SWRs were also studied for their relationship with synaptic depotentiation. SWR facilitation through increased gap junction coupling or $GABA_A$ receptor activation led to decreased synaptic strength and widespread, long-lasting synaptic depression (Bukalo et al., 2013). In agreement, Norimoto and colleagues (2018) showed that silencing SWRs during slow-wave sleep states prevents spontaneous synaptic depression and impairs memory encoding.

The involvement of SWRs in both potentiation and depotentiation processes reveals a dual role for these oscillations. Synaptic downscaling may function to erase older or irrelevant memories, preventing network saturation and resetting it to a naïve state that can participate in later memory formation. When this is combined with synaptic potentiation, the signal-to-noise ratio is increased such that synapses that are part of memory engrams are specifically targeted.

1.6.1.4 Sharp wave ripples as a therapeutic target

Since strong evidence connects SWRs and memory, it is expected that they have been studied for their involvement in Alzheimer's disease (AD), a progressive neurodegenerative disease that causes memory loss. Various alterations in SWRs were observed in different AD models, for example a decrease in SWR abundance (Gillespie et al., 2016; Ciupek et al., 2015), SWR-associated slow-gamma power (Gillespie et al., 2016; Iaccarino et al., 2016), or SWR amplitude (Witton et al., 2016), or altered SWR temporal structure and SWR-associated spike dynamics (Witton et al., 2016), as well as absence of a learning-induced increase in SWR occurrence (Nicole et al., 2016). Additionally, it has been suggested that decreased SWR-associated slow-gamma power in young APOE4 (an AD associated gene) knockin mice can be used as a predictor for later learning impairment (Jones et al., 2019). This has potential diagnostic value, but the origin and behavioral relevance of such SWR-associated gamma oscillations remains controversial (Oliva et al., 2018). A role for SWRs in memory problems associated with normal aging has also been suggested, as sequence reactivation was impaired in aged animals and the degree of reactivation correlated with spatial memory scores (Gerrard et al., 2008).

The hippocampus is a highly epileptogenic structure and is involved in temporal lobe epilepsy, the most common variant of epilepsy in adults (Avoli, 2007). The synchronized network activity underlying SWRs might therefore be involved in seizures, as the same anatomical substrates and physiological mechanism might account for the generation of both SWRs and epileptic activity (Buzsáki, 2015). As previously mentioned, pharmacological inactivation of the $GABA_A$ receptor transforms SWRs in slices into epileptiform discharges (Maier et al., 2003). The similarities between SWRs and epileptic activity are intriguing. Like SWRs, interictal epileptiform discharges (IEDs) and pathological ripples (p-ripples) are usually coupled in time, but they can also occur independently (Buzsáki, 2015). In some cases, IEDs also share the depth profile of SW polarity across hippocampal layers (Buzsáki et al., 1989), and due to their often larger amplitude, they are described as "exaggerated SWs" (Buzsáki, 2015). However, despite amplitude, duration, and frequency often being used to distinguish between physiological and pathological oscillations, there is an overlap between the two that makes straightforward separation challenging (Buzsáki, 2015). Additionally, p-ripples might co-exist with normal SWRs (Buzsáki, 2015). P-ripples have been well documented in both epileptic humans (Jacobs et al., 2012; Bragin et al., 1999b) and animal models such as the kainic acid model (Bragin et al., 1999b), the pilocarpine model (Lévesque et al., 2012), and the tetanus toxin model (Jiruska et al., 2010) of epilepsy. SWR impairment is also found in a mouse model of Dravet syndrome, a severe early onset epilepsy caused by loss of function mutations in the SCN1 gene (Cheah et al., 2019). Importantly, the faster the p-ripples that are detected, the higher the rate of spontaneous seizures and the faster their development after kainic acid injection (Bragin et al., 2004). P-ripples might be useful in identifying the seizure locus in the brain, which can then inform surgical intervention in drug-resistant patients (Buzsáki, 2015). On the other hand, IEDs might be involved in the cognitive impairments often accompanying epilepsy, such as memory deficits, reaction time deficits, and visual perception deficits (Holmes & Lenck-Santini, 2006; Shewmon & Erwin, 1988; Buzsáki, 2015). It is important to mention, however, that IEDs and p-ripples might occur in the absence of seizures, or they might act as a predictor of seizures rather than being identical (Buzsáki, 2015).

SWR involvement in social memory could also suggest an impairment in autism spectrum disorders (ASDs). One mouse model of ASD is SH3 and multiple ankyrin repeat domains 3 (Shank3) KO mice. Shank3, a gene encoding for a scaffolding protein, is identified as an ASD-susceptibility gene in humans (Durand et al., 2007) and Shank3 KO mice show deficits in social novelty recognition and decreased social interaction (Peça et al., 2011). Shank3 KO mice not only show a decreased proportion of social memory neurons in the ventral hippocampus, but they also have disrupted ripple phase locking and SWR-associated reactivation of sequences (Tao et al., 2022). The contacting-associated protein like 2 (CNTNAP2) gene, encoding for a synaptic cell adhesion molecule, is also an ASD-susceptibility gene, as its polymorphism has been associated with increased ASD risk (Arking et al., 2008) and CNTNAP2 KO mice show autism-related abnormalities (Peñagarikano et al., 2011). Spatial memory is also affected in CNTNAP2 KO mice, which could result from reduced SWR incidence and ripple power (Paterno et al., 2021) Interestingly, CNTNAP2 is also involved in epilepsy (Peñagarikano et al., 2011), further suggesting a role for the gene in both physiological and pathological ripples.

Sharp wave ripples have been implicated in other conditions, for example chronic stress which was shown to increase neuronal synchrony during SWRs (Tomar et al., 2021). Chronic stress is associated with memory deficits and mood disorders (Grizzell et al., 2014). Accordingly, SWR reinforcement by neuronal stimulation is absent in stress or depression mouse models, an effect that is rescued with the antidepressant fluoxetine (Ishikawa et al., 2014). Additionally, hippocampal oscillations and their coordination with oscillations in the amygdala and prefrontal cortex are implicated in innate anxiety and generalized disorders, such as post-traumatic stress disorder (Çalışkan & Stork, 2019). Specific SWR dysfunction is also seen in schizophrenia mouse models. For example, the DN-DISC1 transgenic model, in which a dominant-negative DISC1 gene, which is associated with depression and schizophrenia in humans (Blackwood et al., 2001), is expressed, shows increased incidence of SWRs while other hippocampal oscillations are spared (Altimus et al., 2015). Similar findings are reported in the calcineurin KO mouse model, where KO mice also lack the SWR-associated replay of place cell activity (Suh et al., 2013). Lastly, a rat neurodevelopmental model of schizophrenia shows fragmented NREM sleep and disrupted coordination between hippocampal SWRs and cortical spindles, suggesting impaired cortico-hippocampal communication as an additional disease mechanism (Phillips et al., 2012).

1.6.2 Theta waves

In the hippocampus, theta (4-12 Hz) oscillations dominate during active behavior and are hence hypothesized to be important for memory encoding (Hasselmo & Stern, 2014). When an animal moves across a place field of a given place cell, the firing of this cell shifts to earlier phases of the theta cycle, a process called theta phase precession. This phenomenon is believed to contribute to the emergence of theta sequences, as sequential place cells along a path will precess and maintain their temporal firing relationship within each theta cycle (Foster & Wilson, 2007). Interestingly, the past, present, and future location of an animal can be predicted by the place cell spiking sequence within individual theta cycles (Chadwick et al., 2015). This relative timing of cell firing with respect to the network oscillation might therefore also be used to carry information about the environment (temporal code) in addition to the firing rate code. Theta phase precession can act as a bridge between the different time scales of synaptic plasticity (milliseconds to tens of milliseconds) and behavior (seconds). Theta oscillations have also been implicated in synaptic plasticity, since theta burst stimulation can induce LTP in slices (Sheridan et al., 2014). Moreover, a single burst stimulation (4 pulses, 100 Hz) can lead to potentiation, if given at the peak of cholinergically induced theta, and to depotentiation, if given at the trough (Huerta & Lisman, 1995).

While theta oscillations are mostly studied during active exploration, they are also present during rapid-eye movement (REM) sleep. Less is known about this type of theta, but it has been hypothesized that it is involved in memory consolidation in a similar fashion to SWRs and NREM sleep (Çalışkan & Stork, 2019). Some suggest a special role for REM sleep and associated theta oscillations in strengthening and modulation of emotional memories (Hutchison & Rathore, 2015).

Based on pharmacological sensitivity, two types of theta oscillations are reported: type 1, which are atropine-resistant but sensitive to anesthesia by urethane or ether, and type 2, which are

atropine-sensitive and resistant to anesthesia. Type 1 theta (7-12 Hz) have a slightly higher frequency than type 2 (4-7 Hz) and are associated with exploration and voluntary movement, while type 2 are seen during immobility and are linked to emotionally laden contexts like the presence of a predator (Kramis et al., 1975; Mikulovic et al., 2018). Lesion of the EC renders the remaining hippocampal theta oscillations atropine-sensitive, suggesting that entorhinal inputs are necessary for atropine-resistant theta (Montoya & Sainsbury, 1985). This indicates that awake and sleep theta might have different functions, generators, and pharmacology.

It should be noted that while theta oscillations and phase-locked neuronal discharge are seen in other structures such as the EC, the cingulate cortex, and the amygdala, these brain areas are not capable of generating theta independently (Buzsáki, 2002). Theta oscillations are abolished after inactivation of the medial septum, the area traditionally thought of as the theta pacemaker. Such abolishment spares place fields but disrupts theta phase precession, thus leading to impaired performance in memory tasks. Indeed, septal glutamatergic, cholinergic, and GABAergic projections reach the hippocampus and are hypothesized to be involved in theta generation (Nuñez & Buño, 2021).

It remains unclear how septal inputs and ACh lead to generation of theta oscillations, but direct excitatory activation of hippocampal pyramidal cells seems unlikely. Rather, tonic cholinergic excitation and phasic septal GABAergic inhibition of hippocampal interneurons leads to their rhythmic discharge, which subsequently leads to rhythmic IPSPs on pyramidal cells (Buzsáki, 2002). The recurrent network of CA3 has also been suggested as a rhythm generator, since after lesion of the EC, remaining theta depends on CA3 integrity and theta activity becomes highly coherent across all hippocampal layers. Thus, it is possible to study this EC independent, ACh-dependent form of theta in hippocampal slices after their pharmacological induction, for example by the cholinomimetic carbachol (Bland et al., 1988). Using this method, theta are generated in CA3, are attenuated by AMPA receptor inhibitors, and do not require interneurons for their maintenance, an important difference from the in vivo condition. In vitro theta oscillations also differ in that they consist of only a limited number of cycles and the induced synchrony is larger than that seen in vivo (Buzsáki, 2002). NMDA application, tetanic stimulation of Schaffer collaterals, and microiontophoresis of glutamate at apical dendrites of CA1 pyramidal cells also evoke theta-like oscillations in hippocampal slices (Nuñez & Buño, 2021), further demonstrating the importance of the hippocampal circuitry in theta generation.

1.6.3 Gamma waves

Gamma oscillations (25-100 Hz) are also seen during awake state and REM sleep (Nuñez & Buño, 2021). They are often nested into theta and the theta phase has been shown to modulate gamma amplitude (Lisman & Jensen, 2013). Similar interactions have been reported between gamma and SWRs (Sullivan et al., 2011) or gamma and delta (Furtunato et al., 2022). Gamma oscillations are very diverse in terms of frequency and amplitude. They are often subdivided into categories such as high- or fast-gamma and low- or slow-gamma, which are suggested to support different functions, are coupled to different inputs, and dominate different areas of the hippocampus (Nuñez & Buño, 2021).

For example, fast-gamma are suggested to support memory encoding (Zheng et al., 2016) and are coupled to EC inputs, while slow-gamma are coupled to CA3 input and promote memory retrieval (Nuñez & Buño, 2021). Impaired gamma oscillations have been reported in diseases such as AD and Fragile X syndrome, suggesting that they might constitute a therapeutic target (Mably & Colgin, 2018). Iaccarino et al., (2016) went a step further, showing that driving fast spiking parvalbumin positive interneurons at gamma frequency (40 Hz) specifically, leads to decreased levels of Aβ, which could have therapeutic potential. Gamma oscillations can originate locally; in the hippocampus both DG and CA3-CA1 were reported as generators (Csicsvari et al., 2003), and inhibitory networks seem to have a prominent role in the process (Colgin, 2016).

1.6.4 Delta waves

Delta oscillations have a high amplitude, frequency up to 4 Hz, and are most commonly associated with deep sleep (delta power has been used to infer sleep quality; Johnson & Durrant, 2021), even though other functions in the awake state, such as mental calculation and semantic tasks, have been reported to involve delta waves (Malik & Amin, 2017; Harmony, 2013). Research on the function and importance of delta oscillations usually concerns cortical areas; hippocampal delta oscillations have not been studied extensively. SWRs are locked to the phase of hippocampal delta oscillations, which might be important for the subsequent phase-locking to neocortical delta and memory consolidation (Axmacher et al., 2008b). Similar to theta, awake hippocampal delta oscillations are modulated by speed. They are most prominent when rats are moving slowly or are stationary, with high delta coherence during stationary bouts and high theta coherence between the hippocampus and the medial prefrontal cortex during running (Schultheiss et al., 2020). The relationship between delta oscillations and velocity appears to be different on the stationary treadmill compared to normal movement, since delta power and peak frequency on a treadmill are higher at faster speeds. Delta oscillations co-occur with but are independent from theta, and delta oscillations phase modulate the amplitude of slow-gamma waves (Furtunato et al., 2022). In hyperglycemic animals, which have increased cortical and hippocampal phosphorylated tau and perform worse on long delay trials in a spatial delayed alternation task, hippocampal delta power is increased while theta power is decreased, leading to altered theta/delta ratios and implicating delta oscillations in memory (Wirt et al., 2021). Interestingly, some researchers propose that during REM sleep, delta frequencies are the human analog of rodent theta oscillations, as delta-gamma rather than theta-gamma coupling is observed (Ferrara et al., 2012).

1.7 Brain temperature fluctuations

Drops in core and brain temperature have been observed during NREM sleep (Harding et al., 2019), when delta oscillations and SWRs occur. In the rat hippocampus, temperatures between 36-38 ^{o}C have been reported (Andersen & Moser, 1995). The exact magnitude of brain temperature change depends on various factors, such as ambient temperature (Alfoeldi et al., 1990), time of day (DeBow & Colbourne, 2003), the location the temperature was recorded from, or presence of arousing

stimuli like social interaction (Kiyatkin, 2019). Additionally, external warming is associated with improved sleep quality (Raymann et al., 2008) and decreased latency to sleep onset (Raymann et al., 2005), while sleep-wake states can be predictive of brain temperature (Sela et al., 2021).

In awake subjects, increased temperature is associated with improved working memory, visual attention, subjective awareness, and slower reaction time (Wright et al., 2002). The function of such fluctuations in sleep is less well understood, but a role in energy consumption, metabolism, and facilitation of immune defense has been suggested (McGinty & Szymusiak, 1990). Brain temperature was found to be correlated with frequency of sleep spindles, while negatively correlated to their duration (Csernai et al., 2019). Andersen and Moser (1995) report multiple electrophysiological changes in hippocampal response to stimulation upon temperature fluctuations. Furthermore, temperature has been shown to influence SWRs in vitro. Ripple frequency increases at 37 °C and decreases at 27 °C, while the time between SWs increases at 27 °C compared to 32 °C. At 37 °C, SW clusters appear, consisting of consecutive SWs at short intervals, with longer time between clusters (Papatheodoropoulos et al., 2007). Cheah and colleagues (2021) also report increased ripple frequency from 36 °C to 38 °C, with no change in SW amplitude. Theta oscillations are also modulated by temperature, as cooling of the medial septum decreased hippocampal theta power and frequency and increased the number of errors in a spatial task (Petersen & Buzsáki, 2020).

Given these correlations and the importance of NREM sleep and SWRs in memory consolidation, it is possible that temperature might also influence memory consolidation. Supporting this hypothesis, distorted thermoregulation has been linked to AD-like pathology, and increasing body temperature of AD mice via exposure to a thermoneutral environment improved memory performance (Vandal et al., 2016).

1.8 The transient receptor potential vanilloid 1 (TRPV1) channel

1.8.1 Structure and regulation of channel activity

The TRPV1 channel is a non-specific cation channel that senses temperature. It is a tetramer, with each subunit consisting of six transmembrane alpha-helices (TM1-6) and a loop between TM5 and TM6. The pore is made of TM5, TM6, and the loop from each of the four subunits (Liao et al., 2013). TRPV1 receptors have similarities in 3D structure to voltage-gated ion channels, despite dissimilar gating mechanisms (Cao et al., 2013b). It is activated by heat (> 43 °C, but lipids modulate the channel's temperature sensitivity so that activation at physiological ranges is observed; Cao et al., 2013a), protons, and vanilloids such as capsaicin (Tominaga et al., 1998). It is part of a larger family of TRP channels found in many vertebrates and invertebrates. In mammals, birds, amphibians, and teleost fishes, the heat sensitivity of the TRPV1 channel is conserved, although it might be less in some species. In contrast, the capsaicin sensitivity of the channel varies widely among vertebrates and evolutionary diversification of channel properties is suggested (Saito & Tominaga, 2017). Moreover, human TRPV1 has 86% amino-acid homology with rat TRPV1, is similarly activated by capsaicin, temperature, and low pH (Hayes et al., 2000), and shows similar expression profiles across

species (Hayes et al., 2000; Cavanaugh et al., 2011a), indicating that results and possible therapeutic interventions identified in rodent models might hold translational value.

TRPV1 activation is not straightforward. For example, low pH not only activates the channel directly, but it also decreases the temperature threshold leading to channel activation even at room temperature (Tominaga et al., 1998) and sensitizes the channel to capsaicin (Ryu et al., 2003). In addition, the channel gets desensitized after activation, a state that may be both acute and long-term (Sanz-Salvador et al., 2012). Many endogenous TRPV1 agonists have been found, including products from polyunsaturated fatty acids, endocannabinoids, N-acyl amides, N-acylethanolamines, oxytocin, hydrogen sulfide, glycerophospholipids (Benítez-Angeles et al., 2020), histamine, and cyclic phosphatidic acid (Morales-Lázaro et al., 2016), with varied potencies. In the brain, the main endovanilloid ligands of TRPV1 appear to be unsaturated N-acyldopamines, lipoxygenase products of arachidonic acid, and the endocannabinoid anandamide (Van Der Stelt & Di Marzo, 2004). Omega-3 fatty acids, of which docosahexaenoic acid is particularly interesting due to its abundance in the brain, are especially intriguing, as they are shown to act both as direct agonists of the channel and inhibitors of channel activation by vanilloids (Matta et al., 2007). Endovanilloids are not released by classical chemical vesicular transmission; they are rather believed to act locally in a paracrine/autocrine or intracellular fashion (Edwards, 2014). The activation of the channel by multiple stimuli and the ability of different agonists to enhance the action of other agonists suggest that the channel might integrate multiple stimuli and act as a coincidence detector.

Of note here is that many endovanilloids such as anandamide also act on cannabinoid receptors (Scherma et al., 2019), thus suggesting an interplay between the two systems. The same molecules might therefore exert opposing functions through activation of TRPV1 or cannabinoid receptors. For instance, synaptic plasticity is enhanced by TRPV1 and reduced by CB1 activation in the hypothalamus (Jamieson et al., 2022).

In addition to multiple agonists, there is a vast repertoire of TRPV1 modulators. Phosphatidylinositol 4,5-bisphosphate (PIP2), for example, regulates the thermal threshold and the dynamic sensitivity range of the channel (Prescott & Julius, 2003). Moreover, TRPV1 Ca^{2+}-calmodulin dependent desensitization might be regulated by PIP2 and adenosine triphosphate (ATP) (Lishko et al., 2007). Other modulators include the $GABA_{B1}$ receptor subunit (Hanack et al., 2015), $GABA_A$ receptor associated protein (Laínez et al., 2010), kinases such as protein kinase A (De Petrocellis et al., 2001), protein kinase C (Bhave et al., 2003), and c-Src kinase (Jin et al., 2004), pro-algesic agents such as bradykinin and nerve growth factor (Chuang et al., 2001), enzymes such as phospholipase C (Chuang et al., 2001), and polyamines (Ahern et al., 2006). Various endogenous TRPV1 antagonists also exist, including indole alkaloids (Dessaint et al., 2004), *N*-arachidonoyl-serotonin (Maione et al., 2007), and omega-9 fatty acids (Morales-Lázaro et al., 2016). Many synthetic TRPV1 antagonists have been developed, some of which exhibit brain penetration (Brito et al., 2014) and might hence hold potential therapeutic value. This broad modulation of TRPV1 activity further highlights TRPV1 involvement in multiple pathways and functions.

1.8.2 TRPV1 expression in the brain and hippocampus

TRPV1 expression in the peripheral nervous system and involvement in nociception and inflammation is well documented (Tognetto et al., 2001; Szallasi & Blumberg, 1991; Michael & Priestley, 1999; Helliwell et al., 1998; Caterina et al., 2000; Ji et al., 2002; Malin et al., 2006; Schwartz et al., 2011). Brain expression, however, has been particularly controversial. Originally, TRPV1 was thought to be widespread in the brain. A 1996 study used [3H]resiniferatoxin (RTX), which is thought to specifically bind TRPV1, to indirectly infer TRPV1 expression in the preoptic area, locus coeruleus, thalamus, and reticular formation, but not in midbrain central gray matter, somatosensory cortex, or cerebellum (Acs et al., 1996). Later studies used immunohistochemistry and documented TRPV1 expression in the hippocampus, cortex, cerebellum, olfactory bulb, mesencephalon, and hindbrain, where TRPV1 was found in synapses but also astrocytes and pericytes (Tóth et al., 2005). Additionally, mRNA for the TRPV1 receptor has been reported in layers 3 and 5 of the cortex, the hippocampus, amygdala, habenula, striatum, hypothalamus, thalamus, substantia nigra, cerebellum, inferior olive, reticular formation, and locus coeruleus (Mezey et al., 2000). Cristino et al. (2006) reported TRPV1 expression in the hippocampus, basal ganglia, thalamus, hypothalamus, cerebral peduncle, pontine nuclei, periaqueductal gray matter, cerebellar cortex, and dentate cerebellar nucleus. Despite many papers suggesting a broad TRPV1 expression in the brain, later studies found only limited expression, restricted to the hypothalamus, accessory olfactory bulb, and only a small fraction of hippocampal neurons (Cavanaugh et al., 2011a). Here, the authors argue that TRPV1 is transiently expressed widely in the brain during development, but the high expression is gone in adults. A similar developmental downregulation of TRPV1 is seen in the peripheral nervous system (Cavanaugh et al., 2011b). Interestingly, TRPV1 expression was also reported in hippocampal Cajal-Retzius cells, suggesting a possible developmental role for the channel (Anstötz et al., 2018).

Hippocampal expression of TRPV1 has likewise been a topic of debate. While Cristino and colleagues (2006) originally found a broad expression of TRPV1 across CA1-CA3 pyramidal neurons and the molecular layer of the DG, more recent evidence pointed towards a more restricted expression only in a subset of nonpyramidal neurons (Cavanaugh et al., 2011a). Our lab combined qPCR, immunohistochemistry, calcium imaging, and electrophysiology comparing wild-type (WT) and TRPV1 KO mice, and found a subpopulation of hippocampal neurons with their somata in stratum oriens that were TRPV1 positive. Their co-expression of somatostatin, GAD-65, and reelin and innervation by presynaptic terminals expressing the metabotropic glutamate receptor 7 (mGluR7) further identified these TRPV1-positive cells as oriens lacunosum moleculare (OLM) interneurons (Hurtado-Zavala et al., 2017). These results also point towards a restricted expression of TRPV1 in the hippocampus.

1.8.3 Functional significance of the TRPV1 channel

The TRPV1 channel was first identified and extensively studied in the peripheral nervous system for its involvement in nociception, especially noxious heat (Caterina et al., 2000), and as a possible target for analgesia (Brederson et al., 2013). Many neurogenic and non-neurogenic functions of the TRPV1 channel have been studied, such as synaptic plasticity, astrocyte mobilization, microglia activation,

muscle constriction, metabolism, and T-cell activation (Shuba, 2021). This has made TRPV1 a target for drug development with possible therapeutic effect in many disorders (Carnevale & Rohacs, 2016). Here, we focus on possible TRPV1 functions in the brain in physiology and disease.

Brain TRPV1 is reported to affect synaptic transmission and plasticity with both presynaptic and postsynaptic mechanisms. In the locus coeruleus, presynaptic TRPV1 activation by capsaicin enhances glutamate and adrenaline/noradrenaline release (Marinelli et al., 2002). A similar facilitation of glutamatergic transmission by TRPV1 activation is reported in the striatum (Musella et al., 2009). Additionally, a role in spike-timing-dependent LTP has been found in the pyramidal cells of the cortex (Cui et al., 2018). In the amygdala, TRPV1 activation has been reported as being able to both enhance and reduce LTP, an effect that is influenced by the type of anesthetic used (Zschenderlein et al., 2011). Dopaminergic signaling is also affected by TRPV1 activation. In the ventral tegmental area it activates dopaminergic cells, leading to increased dopamine release in the nucleus accumbens (Marinelli et al., 2005). On the other hand, also in the nucleus accumbens, postsynaptic TRPV1 activation leads to AMPA receptor internalization and synaptic LTD via an mGluR5-dependent mechanism (Grueter et al., 2010). Moreover, a TRPV1-dependent LTD has been found in neurons from the bed nucleus of the stria terminalis, whereby anandamide activates postsynaptic TRPV1 after mGluR5 receptor activation (Puente et al., 2011). TRPV1 also participates in superior colliculus LTD, which is absent after P25, indicating that TRPV1 might be involved in synaptic refinement during development (Maione et al., 2009).

TRPV1 has been specifically implicated in synaptic transmission and plasticity in the hippocampus. An increase in pair-pulsed depression of CA1 population responses has been reported after TRPV1 activation with exogenous and endogenous agonists (Al-Hayani et al., 2001), while Marsch and colleagues (2007) have found reduced CA1 LTP in TRPV1 KO mice. A role in synaptic depression in the DG has also been demonstrated, as postsynaptic TRPV1 activation leads to LTD of excitatory transmission through Ca^{2+}-calcineurin and clathrin-dependent AMPA receptor internalization (Chávez et al., 2010). TRPV1 has also been found to be involved in LTD of excitatory synapses on CA1 stratum radiatum hippocampal interneurons (Gibson et al., 2008). The authors demonstrate dependance of this process on group I mGluRs, whose postsynaptic activation has previously been shown to generate endocannabinoids and eicosanoid metabolites of arachidonic acid, which in turn act as retrograde messengers by activating presynaptic TRPV1. Another study supports TRPV1 involvement in both synaptic potentiation and depotentiation, as TRPV1 activation facilitated LTP, decreased the threshold for LTP, and reduced LTD (Li et al., 2008). It is therefore evident that TRPV1 is associated with both LTP and LTD in different structures, including the hippocampus.

Besides glutamatergic transmission, TRPV1 has also been studied regarding inhibitory currents. Drebot and colleagues (2006) have shown that capsaicin in hippocampal cultures decreases the frequency and amplitude of spontaneous IPSCs, although they haven't ruled out potential TRPV1-independent effects. A role for TRPV1 in GABAergic transmission has also been reported in the DG, where TRPV1 activation reduces inhibitory transmission postsynaptically, in a mGluR and Ca^{2+}-calmodulin dependent manner. Here, the authors predict that the mechanism is clathrin-dependent internalization of GABA receptors (Chávez et al., 2014). Moreover, Brown and coauthors (2013) have found that decreased pyramidal LTP in CA1 of TRPV1 KOs is rescued by

blocking $GABA_A$ receptors with picrotoxin, in agreement with Bennion et al., 2011, who have shown that LTP enhancement of CA1 pyramidal cells induced by TRPV1 activation is absent after picrotoxin application. These further point to an interplay between TRPV1-mediated and GABAergic signals.

Our lab has also reported LTP deficits in CA3-CA1 synapses of the hippocampus in TRPV1 KO mice. This was due to decreased excitatory innervation of OLM cells (in which the TRPV1 channel was found to be expressed) and was rescued by specific OLM cell activation through alpha2 nicotinic acetylcholine receptors (α2nAChRs) (Hurtado-Zavala et al., 2017). Therefore, TRPV1 plays a role not only in synaptic plasticity, but also synaptogenesis - specifically in excitatory innervation of OLM cells.

While most studies focus on TRPV1 expression in neurons, it is worth mentioning that TRPV1 in the brain might exert several different functions through microglia. In the anterior cingulate cortex, for example, microglial TRPV1 activation indirectly enhances glutamatergic transmission, hence participating in microglial-neuron communication. The authors of this study also demonstrate a proinflammatory role of TRPV1 in the brain (Marrone et al., 2017).

In a lot of studies reported here, capsaicin was used to activate TRPV1 and infer its function. It should therefore be mentioned that TRPV1-independent effects of capsaicin have been documented (Zhang et al., 2022a). For example, Benninger and colleagues (2008) suggest that the effects of capsaicin on excitatory synaptic transmission of the DG are TRPV1-independent. In most cases, confidence in attributing effects of capsaicin application on TRPV1 activation is gained by preventing the effect of capsaicin with TRPV1 antagonists or showing that the effect is absent in TRPV1 KOs.

1.8.4 TRPV1 in behavior and CNS diseases

1.8.4.1 Memory and Alzheimer's disease

The importance of the TRPV1 channel in memory formation, consolidation, and recall is not well understood, but it has been suggested by a few lines of evidence. TRPV1 KO mice freeze less in the auditory fear conditioning test compared to WTs, while for contextual fear conditioning assessed 1 day or 1 month after training, freezing is less in TRPV1 KOs after a strong conditioning protocol, but not after a weak one (Marsch et al., 2007). The importance of the aversiveness of the conditioning procedure on TRPV1 KO memory has also been demonstrated by Genro and colleagues (2012). While Marsch et al. attribute these effects to deficits of hippocampal LTP, these tests mainly assess amygdala function, with partial hippocampal dependence in the case of contextual fear memory. Interestingly, Li et al., 2008, suggest that TRPV1 activation rescues memory performance after stress, but has no effect under baseline conditions. Riera and colleagues (2014), who were studying the effect of TRPV1 KO on metabolism and longevity, used the Barnes maze to assess memory of TRPV1 KO mice and found improved performance. They note, however, that TRPV1 KO mice had decreased motivation to hide, hence the result could also be attributed to reduced anxiety. A different study reports reduced short-term memory but normal long-term memory of TRPV1 KO mice as assessed in the novel object recognition test and the passive avoidance test (You et al., 2012). Here, many other alterations in behavior have been reported. Therefore, while a role for the channel is suggested in memory processes, it is challenging to separate it from other effects in behavior; and hence, its

precise function is unclear. Lastly, since endocannabinoids also act as TRPV1 ligands (Li et al., 2021) and the endocannabinoid system is implicated in memory extinction (de Oliveira Alvares et al., 2008), the TRPV1 channel might also be important for inhibitory learning and behavioral flexibility, but fear memory extinction is not impaired in TRPV1 KO mice (Marsch et al., 2007).

A functional role for the TRPV1 channel in memory is suggested by disease models. In a mouse model of AD, TRPV1 expression in the brain is significantly decreased and genetically upregulating TRPV1 reduced Aβ generation and rescued CA1 LTP and memory decline (Du et al., 2020). The TRPV1 channel has been associated with brain oscillations, as TRPV1 activation with capsaicin rescued gamma power reduction, as well as CA3 pyramidal cell desynchronization caused by incubation of hippocampal slices with Aβ (Balleza-Tapia et al., 2018). These data indicate that the TRPV1 channel might constitute a potential therapeutic target for AD. Interestingly, as mentioned before, impaired thermoregulation has been reported in AD mice (Vandal et al., 2016) and the temperature dependance of the TRPV1 channel might play a role in this.

1.8.4.2 Anxiety and stress

The TRPV1 channel has been described as a CNS stress protein (Ho et al., 2012). Slices from stressed rats show impairments in LTP and enhanced LTD in hippocampal slices, which are associated with decreased memory performance; and TRPV1 activation ameliorated effects of stress in both behavior and synaptic plasticity (Li et al., 2008). Marsch and colleagues (2007) describe decreased anxiety in TRPV1 KOs as shown by performance in the light-dark test and elevated plus maze. The latter was also used to assess anxiety by Hakimizadeh and coauthors (2012), who show reduced anxiety in mice after intra-CA1 injection of TRPV1 antagonist and increased anxiety when capsaicin is used. The same has been found when a TRPV1 antagonist was infused in the ventral hippocampus (Santos et al., 2008). Other tests, such as the novelty-suppressed feeding test used for anxiety-like and depression-like responses, also suggest an anxiolytic function for TRPV1 inactivation (You et al., 2012). The effect of hippocampal TRPV1 activation in rescuing effects of stress is somehow in opposition with findings of decreased anxiety in KOs or after TRPV1 inhibition, which might be due to the effect of TRPV1 in different brain areas (in the case of KO), TRPV1 desensitization by capsaicin leading to TRPV1 inhibition, or different TRPV1 function in baseline emotional regulation compared to emotional regulation after stressful events. Fear memory is also impaired in TRPV1 KO mice (Marsch et al., 2007), which might be due to deficits in memory or emotional processing. TRPV1 in other brain areas has also been implicated in anxiety. Microinjections of TRPV1 antagonist in the medial prefrontal cortex, for example, also have an anxiolytic effect as assessed by the elevated plus maze and the Vogel conflict test (Aguiar et al., 2009).

1.8.4.3 Epilepsy

TRPV1 expression is increased in the cortex and hippocampus from mesial temporal lobe epilepsy patients (Sun et al., 2013). The same is seen in the DG of mice after pilocarpine-induced status epilepticus, and capsaicin in this model enhanced spontaneous miniature EPSC frequency (Bhaskaran

& Smith, 2010). In agreement, TRPV1 activation increases the duration of loss of equilibrium and decreases the onset of bilateral forelimb clonus in mice injected with subconvulsive doses of pentylenetetrazole, suggesting a facilitation of seizure activity (Shirazi et al., 2014). TRPV1 inhibition reduces duration of loss of equilibrium and after-discharge duration in rats with amygdala-induced kindling (Shirazi et al., 2014), and increases the threshold for myoclonic twitches and generalized clonic seizures (Socała et al., 2015), pointing to a possible anticonvulsive role. Similarly, intraperitoneal injection of TRPV1 antagonists reduces seizure severity in male and completely suppresses seizure susceptibility in female GERP-3 rats that are genetically prone to epilepsy (Cho et al., 2018).

Contrary to the results mentioned above, Lee and colleagues (2011) found a protective effect of capsaicin against kainic-acid induced epileptogenesis, with the capsaicin-treated group experiencing less behavioral seizure activity, high-frequency seizure discharges, oxidant activity, and apoptotic cell death. Similar anti-seizure properties have been reported for piperine, another TRPV1 agonist, which delays the onset of myoclonic jerks and generalized clonic seizures (Chen et al., 2013). This effect is absent if TRPV1 receptor antagonists are applied, so it cannot be attributed to receptor desensitization. Results by Suemaru and coauthors (2018) also support an anticonvulsive effect of TRPV1 activation, as the protective effect of acetaminophen against seizures was blocked by TRPV1 antagonists. Thus, it remains unclear whether protective effects come from TRPV1 activation or inhibition. It is possible that differences are due to actions of TRPV1 agonists and antagonists on different areas or due to homeostatic mechanisms taking effect after prolonged alteration of neuronal activity (Storozhuk et al., 2019).

A special mention should be made here about febrile seizures. These are convulsions initiated by fever in children between 6 months and 5 years old (Leung et al., 2018). In rodents aged 8-11 days, seizures can be induced by increasing ambient temperature to 48 °C for 1 hour, with latency to seizures around 30 minutes (Schuchmann et al., 2006). TRPV1 KO mice have longer latency and decreased duration and severity of febrile seizures in vivo through mechanisms suggested to involve cytokines and microglia (Huang et al., 2015; Kong et al., 2019), but effects on hippocampal circuitry were not tested in these studies.

1.8.4.4 Autism spectrum disorders (ASD)

Altered social behavior has been reported in TRPV1 KO mice. You et al., 2012, report enhanced aggressiveness in a social dominance test and decreased social interactions within TRPV1 KOs. ASD is also frequently associated with abnormal pain sensitivity involving SHANK3 deficiency. TRPV1 interacts with SHANK3 and partial SHANK3 knockdown impairs TRPV1 signaling in human dorsal root ganglion neurons, indicating that TRPV1 might be involved in different symptoms of ASD (Han et al., 2016).

1.8.4.5 Addiction

The TRPV1 channel is believed to be involved in mechanisms underlying addiction to diverse substances, which are often similar to mechanisms underlying learning and memory. TRPV1 inhibition in rat nucleus accumbens blocks expression of persistent morphine conditioned place preference (Heng et al., 2014) and decreases morphine-induced c-fos expression (Ma et al., 2017). In addition, repeated morphine administration increases TRPV1 expression in the dorsal striatum, where TRPV1 inhibition also blocks morphine conditioned place preference and morphine-induced gene expression changes (Nguyen et al., 2014). Moreover, systemic injection of TRPV1 antagonists reduces morphine self-administration as well (Ma et al., 2017).

Repeated daily administration of cocaine leads to increased behavioral sensitization, a form of drug-induced behavioral plasticity, in TRPV1 KOs (Grueter et al., 2010). Intraperitoneal injections of a TRPV1 antagonist decreases cocaine-induced reinstatement of cocaine-seeking behavior (Adamczyk et al., 2012).

Alcohol consumption is also altered in TRPV1 KOs, which have higher preference for and consumption of ethanol. TRPV1 KO mice and WT mice treated with a TRPV1 antagonist recover faster from ethanol-induced motor incoordination and loss of righting reflex (Blednov & Harris, 2009). Furthermore, ethanol avoidance is reduced in TRPV1 KO mice (Ellingson et al., 2009).

Repeated exposure to methamphetamine also increases TRPV1 mRNA expression in the frontal cortex (Tian et al., 2010).

Since many substances can activate both vanilloid and cannabinoid receptors, it is not surprising that TRPV1 is implicated in both negative effects of cannabis consumption, such as apathetic and impulsive patterns of choice (Fatahi et al., 2018), as well as positive outcomes, such as anxiolytic effects (Campos & Guimarães, 2009) and antihyperalgesia (Anand et al., 2020; Costa et al., 2004).

1.9 Oriens lacunosum moleculare interneurons

Our lab found that in the hippocampus, the TRPV1 channel is specifically expressed in OLM interneurons (Hurtado-Zavala et al., 2017). OLM cells represent 4.3% of CA1 interneurons (Bezaire & Soltesz, 2013). They express somatostatin and in CA1 they selectively express the nicotinic acetylcholine receptor 5 α2 subunit (α2nAChR) (Leão et al., 2012). Their cell bodies are found in stratum oriens, with axons projecting to stratum lacunosum moleculare, which is where their name comes from. Their dendrites project horizontally across stratum oriens without entering other CA1 layers. The main input to OLM interneurons comes from CA1 pyramidal cells. Their GABAergic connections remain obscure, but they seem to be innervated by other OLM cells, bistratified cells, and interneurons that innervate other interneurons. They are also hypothesized as direct targets for medial septum afferents (Müller & Remy, 2014; Haam et al., 2018; Bell et al., 2013).

89% of OLM axons target pyramidal cells (Bezaire & Soltesz, 2013). In CA1, OLM axons mainly project to distal pyramidal apical dendrites, which is where input from the entorhinal cortex arrives into the hippocampus (Leão et al., 2012). Since CA1 pyramidal cells are both the main input and output

population of OLM signals, OLM neurons might promote feedback inhibition, decreasing the effectiveness of EC input in activating CA1 excitatory cells. This in turn decreases CA1 output on the EC (Haam et al., 2018). OLM cells also target bistratified cells, disinhibiting CA3 input on CA1 pyramidal cells (Müller & Remy, 2014; Leão et al., 2012; Figure 2). Because OLM activation suppresses the influence of extrahippocampal while promoting the influence of intrahippocampal activity in eliciting firing in CA1, it is said that they gate the flow of information in the hippocampal circuit (Leão et al., 2012).

OLM cells are involved in memory processes. Activation of OLM neurons in the intermediate (between dorsal and ventral) hippocampus has been found to cause deficits in encoding of object and fear memories, while their inhibition specifically during training enhances object recognition (Siwani et al., 2018). Others report impaired performance in the object-location task but intact object-recognition after OLM cell ablation in the ventral hippocampus (Haam et al., 2018). This suggests differential function of OLM neurons across the dorsoventral axis of the hippocampus or compensatory mechanisms after long-term OLM inactivation. Additionally, in a mouse model of AD, ACh-dependent learning-induced synaptic rewiring of OLM neurons is impaired (Schmid et al., 2016). Because cholinergic signaling is particularly affected in AD and is the main target of current treatments (Davies & Maloney, 1976; Weller & Budson, 2018), it is possible that disrupted ACh regulation of OLM neuron plasticity accounts for some aspects of the pathology.

The involvement of OLM interneurons in theta waves is well established. Not only do OLM cells fire rhythmically on the trough of theta oscillations (Klausberger et al., 2003), but CA1 OLM activation in the ventral hippocampus of anesthetized mice can generate theta. This generation was absent in the presence of atropine, a muscarinic receptor antagonist, suggesting that these are type 2 theta oscillations, which are ACh-dependent and associated with emotional states like anxiety and responses to predator odor. The authors found that OLM activation and generation of theta 2 reduces anxiety and increases risk-taking behavior, as mice approached the zone with the predator odor more frequently and for longer times compared to controls (Mikulovic et al., 2018).

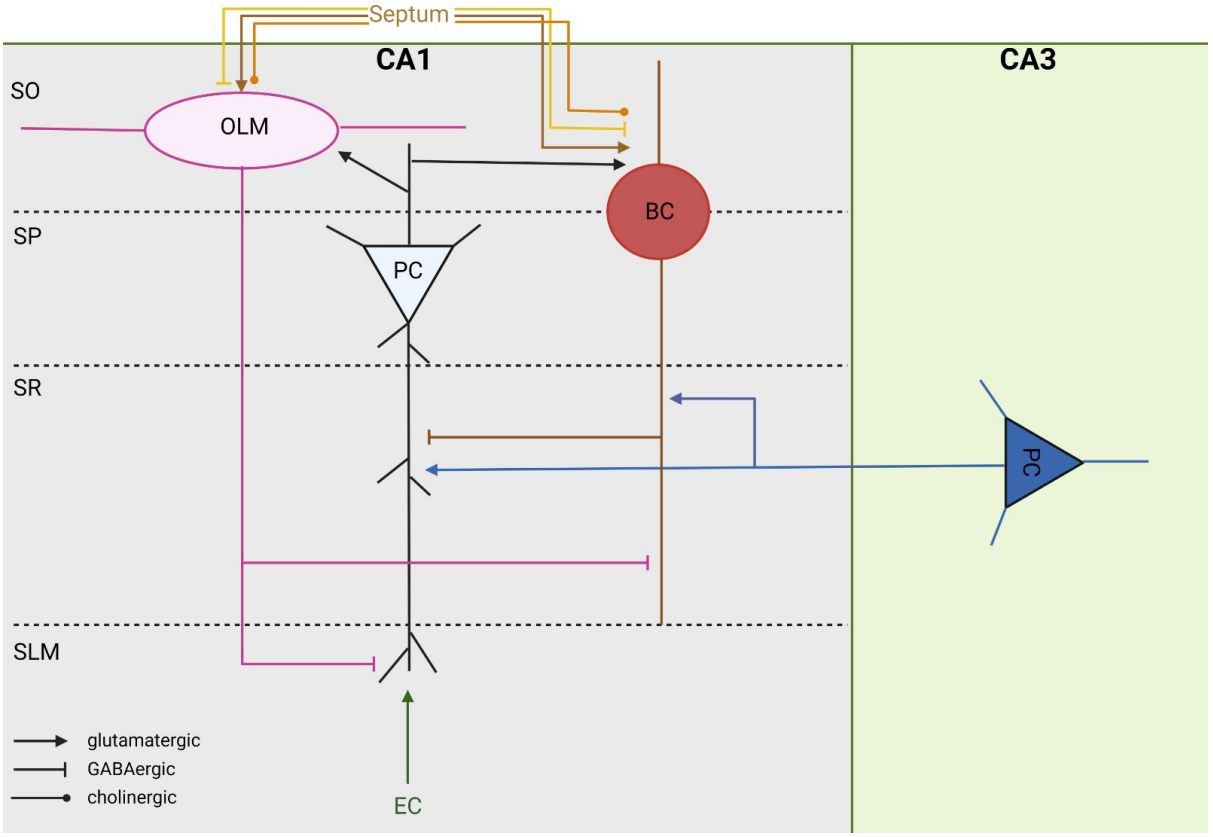

Figure 2: OLM interneurons gate the flow of information in the hippocampus. OLM cells project to the distal apical dendrites of CA1 pyramidal cells. This is where input from the EC arrives. OLM interneurons also project to PV-positive bistratified cells (BC), which inhibit pyramidal cells in stratum radiatum (Sik et al., 1995; Maccaferri et al., 2000), where CA3 input arrives. PC = pyramidal cell, BC = bistratified cell, EC = entorhinal cortex, SO = stratum oriens, SP = stratum pyramidale, SR = stratum radiatum, SLM = stratum lacunosum moleculare.

OLM cell participation in SWRs is controversial. Earlier studies in anesthetized mice suggested that OLM cells are silenced during SWRs (Klausberger et al., 2003), while a later study in awake, head-fixed animals showed that OLM neurons fired during half of the recorded SWR events (Varga et al., 2012). In agreement with these later findings, it has been shown in vitro that OLM cells receive phasic, ripple-associated input. 59% of recorded OLM cells fired during SWRs, with peak spike probability at 6.5 ms after the maximum ripple peak in the ascending ripple phase (Pangalos et al., 2013). This suggests that OLM cells are involved in SWRs in addition to theta.

OLM interneurons are also present in CA3, but their morphology differs. In CA3, OLM dendrites span all layers of the hippocampus except stratum lacunosum moleculare. Interestingly, the dendritic laminar distribution of OLM cells in both CA1 and CA3 mirrors that of recurrent collaterals of local pyramidal cells (Freund & Buzsáki, 1996).

1.10 Scope and hypothesis

In the present thesis, SWRs in TRPV1 KO and WT mice were studied in vivo and in vitro. We hypothesized that TRPV1 KO mice, which show impaired hippocampal LTP, would have decreased SWRs, as the two processes are both positively correlated with memory consolidation. First, we compared SWRs from TRPV1 KO and WT slices at different temperatures to test the temperature sensitivity of the TRPV1 channel's potential involvement in SWRs. This could be relevant to brain temperature fluctuations observed during sleep, when SWRs occur to consolidate memory formation. We also recorded SWRs in vivo from mice during sleep and exploration of two environments under both novel and familiar conditions. Cellular activity and place fields were compared between the two genotypes, as well as the remapping of place fields in different environments. From these recordings, theta and delta activity was also analyzed. We anticipated impaired remapping or decreased place field stability in TRPV1 KOs, as well as altered LFP oscillation patterns, which would indicate compromised spatial navigation and memory. The cheeseboard maze task, a dry land version of the water maze with a decreased anxiety component, was therefore employed to study spatial learning, while an open field test was performed to assess anxiety levels in WT and KO mice. We expected impaired performance in the memory task and decreased anxiety levels in TRPV1 KOs.

Under epileptic conditions, SWRs change into p-ripples and/or epileptiform discharges. The TRPV1 channel is temperature sensitive and hence might be involved in febrile seizures caused by fever. After confirming that increased temperature could lead to epileptiform activity in hippocampal slices, we compared TRPV1 KO and WT slices for relative susceptibility to such induction of pathologic activity. We expected decreased temperature-dependent generation of epileptiform activity in the KOs if the TRPV1 channel is involved in febrile seizure generation, or increased susceptibility if TRPV1 has a protective role.

It has been previously shown that TRPV1 KO mice have LTP deficits. Both SWRs and LTP are important in memory consolidation and a connection between the two has been suggested, but their exact relationship and mechanistic correlates remain elusive. We therefore investigated this pharmacologically, by recording SWRs from WT slices exposed to drugs known to affect LTP such as anisomycin and SAHA. Additionally, we studied the effect of LTP induction by high-frequency stimulation on spontaneously occurring SWRs. Lastly, the effect of bath-applied tau oligomers, a hallmark in AD that has been shown to decrease LTP (Acquarone et al., 2019; Fá et al., 2016), on SWRs was also examined.

2. Methods

2.1 Mice

All procedures described here were in accordance with the German animal welfare laws (Tierschutzgesetz), the directive 2010/63/EU of the European Parliament and of the council of 22 September 2010 on the protection of animals used for scientific purposes, as well as the ethic committee of the Charité under the guidelines of the Berlin state authorities (T-CH 0013/20 for in vitro, G-0047/21 for in vivo experiments).

TRPV1 KO mice on the C57BL6/J background were acquired from Jackson Laboratories and bred at the European Neuroscience Institute animal facility in Göttingen, Germany. They were later crossed with C57BL6/J from Janvier laboratories, Germany, to generate heterozygous parents to produce TRPV1 KO and WT littermates. When our lab moved to Berlin, the TRPV1 KO line was re-derived and TRPV1 KO founders crossed again with C57BL6/J mice from Charles River, Germany, to propagate the mouse line at the Forschungseinrichtungen für Experimentelle Medizin (FEM) at the Charité University Medical School in Berlin. For pharmacological experiments where only WT mice were used, C57BL6/J mice were acquired either internally from Charité-FEM or externally from Charles River.

Exact information on mouse number, age, and sex used in each experiment can be found in Table 1. Animals were kept on a 12-hour light-dark cycle with *ad libitum* access to food and water, except mice that participated in the cheeseboard maze and open field tests, which were under food restriction (2-3 g per day per mouse, so that body weight decreased to no less than 90% of the original body weight) until the end of the behavioral experiments. Adult mice for in vitro electrophysiology were 4-11 weeks old, while P18-P25 mice were used for in vitro induction of febrile seizures. During behavioral tests and in vivo electrophysiology, mice were 9-15 weeks old and 15-26 weeks old, respectively. The same mice were used in both behavioral and in vivo experiments, but three WT mice could not be recorded (mice either died or lost the microdrive implant) and two KO mice were excluded from analysis after histological examination of tetrode location (see below), resulting in different sample sizes. Tails from these mice were kept and used for genotyping after experiments, during which it was found that two WT females were actually heterozygous, and were therefore excluded from analysis. Mice were group housed, except those used for in vivo electrophysiology that were single-housed after tetrode implantation. Both male and female mice were used in most experiments (Table 1).

Table 1: Mouse information per experiment. Mouse genotype, background, age, sex, and number for each experiment.

Experiment	Genotype and background	Age	Sex and number

In vitro: TRPV1 KO and WT SWRs at different temperatures - sleep simulation	TRPV1 KO and WT (C57BL6J)	6-9 weeks	WT: 4 male, 3 female KO: 4 male, 4 female
In vivo: Cheeseboard maze and open field	TRPV1 KO and WT (C57BL6J)	9-15 weeks	WT: 3 male, 3 female KO: 4 male, 4 female
In vivo: LFP and single-unit recordings	TRPV1 KO and WT (C57BL6J)	15-26 weeks	WT: 1 male, 2 female KO: 2 male, 4 female
In vitro: susceptibility to induction of febrile seizures	TRPV1 KO and WT (C57BL6J)	P18-P25	WT: 3 male, 5 female KO: 4 male, 4 female
In vitro: SWR recordings before and after LTP protocol	WT, C57BL6J	7-10 weeks	8 male
In vitro: SWRs after incubation with anisomycin	WT, C57BL6J	7 weeks	2 male, 1 female
In vitro: anisomycin application after spontaneous SWR generation and recording	WT, C57BL6J	5-6 weeks	2 male, 3 female
In vitro: SWRs after incubation with SAHA	WT, C57BL6J	5-7 weeks	2 male, 3 female
In vitro: SAHA application after spontaneous SWR generation and recording	WT, C57BL6J	5-6 weeks	2 female
In vitro: SWRs after incubation with ohtau40-H_2O_2	WT, C57BL6J	9-11 weeks	2 female
In vitro: ohtau40-H_2O_2 application after spontaneous SWR generation and recording	WT, C57BL6J	8-10 weeks	3 male, 3 female
In vitro: ohtau40-heparin application after spontaneous SWR generation and recording	WT, C57BL6J	8 weeks	4 male, 4 female

2.2 Genotyping

Genotyping was originally performed in our lab using the protocol detailed below. Tissue from mice used in experiments was kept and samples were later sent to GVG Genetic Monitoring GmbH, which confirmed genotypes. The procedure has been widely used since its discovery (Mullis, 1990; Davis & Dibner & Battey, 1986; Shehadul Islam et al., 2017).

2.2.1 Tissue lysis and DNA extraction

The tissue (ear punch or tail sample) was incubated while shaking for at least 6 hours or overnight at 55 °C in lysis solution (100 mM Tris-HCl (pH 8.5), 5 mM EDTA (pH 8.0), 0.2% or 2% (w/v) SDS and 200 mM NaCl) containing 3.5 µL of 20 mg/ml Proteinase K (Thermo Fisher Scientific cat. #AM2546). DNA extraction started the following day with 10 minutes of centrifugation at maximum speed, so that the tissue remained stuck at the bottom and the supernatant transferred to a new tube. There, 500 µL of > 98% isopropanol were added and the mixture centrifuged for another 10 minutes at maximum speed, allowing the DNA to precipitate at the bottom. The supernatant was then removed and the tube washed with 1 mL 70% ethanol during a last 10 minute centrifugation. Ethanol was then removed from the tube, which was left to dry for 10-20 minutes. The DNA pellet was then dissolved in 100 µL distilled H_2O.

2.2.2. Polymerase chain reaction (PCR) and gel electrophoresis

The polymerase chain reaction (PCR) mixture contained, in µL: 1.5 WT forward primer, 1.5 KO forward primer, 1.5 reverse primer, 0.75 10 mM dNTP mixture (Thermo Fisher Scientific cat. #R0192), 0.75 Phire Hot Start II DNA Polymerase (Thermo Fisher Scientific cat. #F122), 7.5 Phire green reaction buffer (Thermo Fisher Scientific cat. #F527L), 23.5 H_2O, and 3 DNA extracted as described above. The primers used were synthesized and ordered from Sigma-Aldrich and their sequences were:

WT forward, VR1-For-MC: 5'- TGG CTC ATA TTT GCC TTC AG

KO forward, VR1-TA1-MC: 5'- CTG TCC ATC TGC ACG AGA CT

Common reverse, VR1-Rev-MC: 5'- CAG AAT CTC TTT CAG CCC CTG

The PCR protocol used is outlined below:

95 °C	5 min	
95 °C	45 s	x34
57 °C	40 min	
72 °C	45 min	
72 °C	10 min	
10 °C	hold	

The PCR product was loaded in gels that were made from 1.8 g Agarose (Invitrogen cat. #16500) and 10 µL Roti-Safe (Carl Roth cat. #3865) per 100 mL 1x TAE buffer (40 mM Tris, 20 mM acetic acid, 1

mM EDTA). GeneRuler 1 kb Plus DNA Ladder (Thermo Fisher Scientific cat. #SM1333) was used as a reference. Gels were run until bands were separated and visualized using UV-light. WT mice were identified by having a single band at 400 bp, TRPV1 KO a single band at 500 bp, and heterozygous mice by having both 400 bp and 500 bp bands.

2.3 In vitro electrophysiology

2.3.1 Slice preparation

Hippocampal slice preparation and SWR recordings were performed similar to previous descriptions (Schneiderman, 1986; Papatheodoropoulos & Kostopoulos, 2002). Mice were anesthetized using isoflurane (Forene, AbbVie cat. #B506) inhalation before being decapitated and having their brains extracted. The brains were then moved to a cold plate with ice-cold (0.5-2 ^{o}C) artificial cerebrospinal fluid (aCSF). Three types of aCSF were used.

F4, in mM: 119 NaCl, 2.5 KCl, 1 NaH_2PO_4, 1.3 $MgSO_4$, 2.5 $CaCl_2$, 26 $NaHCO_3$, and 10 D-glucose.

F1, in mM: 124 NaCl, 4.9 KCl, 1.2 KH_2PO_4, 2 $MgSO_4$, 2 $CaCl_2$, 25.6 $NaHCO_3$, and 10 D-glucose.

LTP-aCSF, in mM: 124 NaCl, 4.8 KCl, 1.2 KH_2PO_4, 2 $MgSO_4$, 2 $CaCl_2$, 25.6 $NaHCO_3$, and 10 D-glucose.

Due to the higher concentration of potassium, F1 promotes slice excitability while F4 is closer to physiological conditions (basal level ~ 3 mM; Larsen et al., 2016). Therefore, F4 was used in all experiments except those investigating febrile seizures, where F1 was used to increase susceptibility. The LTP-aCSF was used in experiments where SWRs were recorded before and after HFS, as it was found to be better for synaptic potentiation compared to F4 and had been used successfully in our lab before for LTP induction.

Once the hippocampus was excised free, the ventral part was placed perpendicular to the blade of the tissue chopper (Stoelting cat. #51425) and four slices were taken. Both left and right hippocampi were used and slice thickness was 450 µm. They were then transferred to an interface chamber where they were left to incubate at 31 +/- 1 ^{o}C for at least two hours before recordings. The aCSF was oxygenated by bubbling with 95% oxygen and 5% CO_2, at 31-33 L/h, with pH under these conditions being 7.3-7.4.

2.3.2 SWR recordings

Spontaneously evoked SWRs were recorded from CA1 stratum pyramidale, where SW polarity is positive. Unless stated otherwise (e.g., in temperature or febrile seizure induction experiments) slices were kept at 30-32 ^{o}C during recordings. SPIKE 2v8.18 (Cambridge Electronic Design Limited) was used for signal acquisition. The microelectrodes used were Platinum/Iridium with 0.1 MΩ impedance (Microprobes cat. #PI20030.1A3 and #PI2PT30.1H5) and were inserted into glass tubes for better isolation. Both the incubation aCSF and the recording chamber aCSF were oxygenated by bubbling 95% oxygen and 5% CO_2 at 32 +/- 1 L/h. The bath-applied aCSF was flowing at a rate of 1.3-1.5 ml per

minute in all experiments except those where the effect of LTP induction protocol on SWRs was studied, for which flow rate was 1.1-1.3 ml/min. The CA1 pyramidal layer was identified using a light microscope (Leica). After SWRs were found in a slice and the location in the CA1 pyramidal layer where SWs had the highest amplitude was selected, the electrode was inserted roughly in the middle of the section. The recording time used for analysis was always at least 20 minutes after electrode insertion, except in experiments in which epileptiform activity was induced by increased temperature where recordings were made from the surface of the slices; see section below. The signal was amplified 10,000-fold using a differential AC amplifier (A-M Systems cat. #1700) and frequencies between 0.1 Hz and 5000 Hz were recorded. A data acquisition board (micro3 1401, Cambridge Electronic Design Limited) was used to digitize the signal at 10 kHz.

2.3.3 In vitro temperature experiments

Slices from TRPV1 KO and WT adult mice were prepared and incubated for at least two hours in F4 aCSF at 31 ^{o}C. Afterwards, slices with SWRs were identified and recorded at 31 ^{o}C baseline temperature for at least 25 minutes. Temperature variation during sleep is between 36 ^{o}C and 38 ^{o}C, so two "wake-sleep-cycles" followed, in which the temperature was increased to 36 ^{o}C, then to 38 ^{o}C, then back to 36 ^{o}C, and finally to 38 ^{o}C again. After the end of the two 36-38 ^{o}C cycles, the temperature was increased to an extreme of 40 ^{o}C (simulating high fever), before being returned to 31 ^{o}C for potential recovery effects. Temperature varied by +/- 1 ^{o}C and slices were kept in each temperature for at least 22 minutes and no more than 35 minutes. Two two-minute recording sections were extracted for analysis - one at the beginning (maximum 7 minutes after the temperature was reached) and another at the end (after at least 18 minutes at a given temperature) of each temperature step.

2.3.4 Pharmacological experiments

2.3.4.1 Experiments where slices were pre-incubated with drugs

Slices were prepared in F4 aCSF in the absence of drugs. They were then separated into 2 groups, one in which slices were incubated in normal aCSF and one in which slices were incubated in aCSF containing the pharmacological agent. After at least two hours of incubation, slices with SWRs were found and recorded for 35 minutes each in the presence of normal aCSF or aCSF containing the pharmacological agent. Two minutes of the last 27-35 minutes were used for analysis, so the results indicate a minimum total incubation of 2.5 hours in the drug. The aCSF (control: DMSO-aCSF or tau-free aCSF, and experimental: SAHA-aCSF or tau-aCSF) was reused during the first day of experiments involving pre-incubation with SAHA and for all experimental days involving pre-incubation with tau.

2.3.4.2 Experiments where drugs were applied after baseline recording of SWRs

Slices were prepared and incubated for at least two hours in F4 aCSF in the absence of drugs. After incubation, slices with SWRs were found, the electrode was inserted in the middle of the slices, and a 35 minute baseline recording was taken. Then, aCSF was switched to F4 aCSF containing the drugs and a second recording was taken for 35 minutes. Lastly, aCSF was switched back to drug-free aCSF for a final 35 minute recording. This protocol means that for every pharmacological agent there were three conditions: baseline, drug application (for which 2 time points were analyzed, the first at the beginning of drug application (2 minutes selected from the first 3-12 minutes of application) and the other at the end of drug application (2 minutes selected between 27-35 minutes of application)) and wash.

2.3.5 Sharp wave ripple recordings after LTP

These experiments were performed in collaboration with my colleague, Dmytro Nesterenko, in Camin Dean's lab. Slices from the ventral hippocampus were prepared as described above and incubated in LTP-aCSF for 2 h. Slices with spontaneously occurring SWRs were then identified and baseline recordings were taken for 35 minutes, after a bipolar stimulation electrode was inserted between stratum radiatum and stratum pyramidale in CA1. Slices were then stimulated with a single 10 ms pulse every minute with an increasing current, starting at 20 µA and increasing by 20 µA in each step until the fEPSP slope reached a plateau (which equals to maximum response) to record an input-output curve of fEPSP responses to stimulation. Then, SWRs were recorded again for at least 10 minutes. To establish a baseline for fEPSP responses to stimulation, slices were then stimulated with a single 10 ms pulse every two minutes for 20 minutes, with a current corresponding to 40% of the maximum fEPSP of the input-output curve. SWRs were recorded again for at least 10 minutes following baseline, before proceeding with a compressed LTP induction protocol (3 trains of 100 pulses at 100 Hz, with 10 s between trains; Yamazaki et al., 2012). Early-LTP was then confirmed by again giving a single pulse every 2 minutes and recording fEPSP responses for 1 hour. Only slices where LTP induction was successful (fEPSP slope was increased by 115-235% for at least 1 hour after HFS compared to baseline) were included in the analysis. Following LTP, SWRs were again recorded for at least 10 minutes. Temperature was 30-32 ^{o}C and flow rate of perfused, bubbled aCSF was 1.2 ± 0.1 mL/min.

2.3.6 Analysis of SWR properties

Two minutes from each recording were extracted for analysis using SPIKE 2v8.11. These were then analyzed on MATLAB version 2020b (The Mathworks, Inc., Massachusetts, USA) using a custom written code available at request. All filtering was done using the *eegfilt* function (Makeig et al., 1997). Initially, raw data were high-pass filtered at 0.5 Hz. Then, for SWs, the signal was low-pass filtered at 40 Hz, while a bandpass filter between 140-250 Hz was used for ripples. A histogram of the amplitude of each point from the SW filtered channel was plotted and the mode of the distribution taken. This mode was then subtracted from all points to correct the baseline of SWs to zero. All

points with amplitude less than or equal to zero, which is the new mode, were taken and the standard deviation of this distribution, called leftbranch, was calculated. Points smaller than four times the standard deviation of leftbranch were removed from the leftbranch population to exclude extreme values. All points from the SW filtered channel with amplitude between -3.5*std(leftbranch) and +3.5*std(leftbranch) were then taken as baseline noise (b_noise) and SW-amplitude threshold was defined as 3, 3.5, or 4 (see Table 2) times the standard deviation of the b_noise population. The full width at half maximum (FWHM) for each possible SW was calculated using an adapted version of the *fwhm* function (Egan, 2022). Possible SWs with FWHM less than 15 ms and more than 150 ms were excluded from further analysis. SW start and end was found by finding the closest minimum before and after each SW peak that was either the last minimum before another SW, or had an amplitude less than 2*std(b_noise). A maximum of three minima before each peak and 5 minima after each peak were checked, if none satisfied these conditions then the closest minimum to the peak was selected. If a SW was cut at the start or the end of the recording snippet, the start or end of the recording were taken as SW start and end respectively. SW peak, start, and end detection was visually confirmed. If the difference between the starting time of a SW and the ending time of the previous SW was less than 50 ms, they were defined as clusters (consisting of 1 primary and 1 or more secondary SWs). Single SWs were also defined as primary SWs. For each SW event, the amplitude and duration (SW end time - SW start time) were taken and averaged for each slice. The probability of cluster occurrence (number of clusters / number of primary SWs) and the number of SWs per minute were also measured. If there were no SWs in a recording, the slice was excluded from analysis of all SW parameters except number of SWs per minute.

Analysis of ripples was performed similarly. The distribution of amplitude for all points in the ripple filtered channel was plotted and the mode and standard deviation of the distribution taken. All points with amplitude larger than the mode minus two times the standard deviation and smaller than the mode plus two times the standard deviation were taken as baseline noise in the ripple channel. Then, the threshold for ripple peaks was set at 3 or 3.5 (see Table 2) times the standard deviation of the baseline noise in the ripple channel. Ripple peaks were detected after rectification of the ripple filtered channel. Peaks less than 10 ms apart were attributed to the same ripple event and events with less than 4 peaks were excluded from further analysis. Ripple duration was found by subtracting the time of the last peak of each event from the time of the first peak of that event. For power analysis, 130 ms sweeps were taken from the ripple-filtered channel, each centered at the middle of one ripple event. Wavelet transformation for each sweep took place using the *wavelet* function by Torrence and Compo (1998) with parameters set as follows: amount of time between each Y value (dt) = 1/sampling frequency, zero padding on, spacing between discrete scales (dj) = 0.01, smallest scale of the wavelet = 10*dt, number of scales minus one = 10/dj, and mother wavelet function set to “Morlet”. Power was calculated by taking the square of the absolute value of the wave output. Peak frequency for each ripple event was defined as the frequency in the ripple range (140-250 Hz) with the highest power (= peak power). Ripple events were excluded from analysis of peak frequency and peak power if the time of the maximum power was more than 15 ms from the middle of the event and more than 15 ms from the maximum ripple peak of the event or if the event had a duration longer than 110ms. Peak frequency, peak power, duration, and number of peaks of each ripple event were taken and averaged for each 2-minute recording. Average ripple amplitude

was calculated as the mean amplitude of all ripple peaks of a recording. If a recording had no ripples, the slice was excluded from analysis of all ripple variables except for the number of ripple events per minute.

During one day of the ohtau40-H_2O_2 application experiment after naive SWRs were recorded, a high number of artifacts were present in all four recorded slices simultaneously (ensuring these were artifacts and making their identification obvious). These started appearing around 20 minutes after beginning of tau application and persisted until near the end of wash, making it impossible to select two minutes that were artifact-free for the tau-end condition. In this case, the MergeFiles Spike2 script was used to cut snippets with artifacts out and merge the remaining sections of the recording.

Statistical analysis was performed in MATLAB. For drug experiments where the drug was applied after SWRs were recorded in drug-free aCSF and for the LTP experiment, a repeated measures analysis of variance (RMANOVA) was used with condition ("baseline", "start of drug application", "end of drug application", "wash", or "baseline", "after input/output curve", "after fEPSP baseline", "after LTP", respectively) as within subjects factor. For the temperature experiment, a RMANOVA was again used, with temperature ("31 °C baseline", "36 °C","38 °C","36 °C 2nd", "38 °C 2nd", "40 °C", "31 °C recovery") as within subjects factor and genotype ("WT", "KO") as between subjects factor. If the sphericity assumption of the RMANOVA was violated, the Greenhouse-Geissner correction was applied. Tukey's honestly significant difference (HSD) post-hoc test with multiple comparisons correction was used to determine which specific conditions were significantly different from each other. In drug experiments where slices were pre-incubated with the drug, a Mann-Whitney U-test was performed.

Table 2: SW and ripple detection threshold details per experiment. Values by which the respective standard deviation (as described above) was multiplied in each in vitro experiment for SW and ripple detection thresholds.

Experiment	**SW threshold**	**Ripple threshold**
Temperature	4	3.5
HFS	3	3
Anisomycin pre-incubation	3.5	3.5
Anisomycin application after SWR generation	3.5	3.5
SAHA pre-incubation	3	3.5
SAHA application after SWR generation	3.5	3.5

ohtau40-H_2O_2 pre-incubation	3	3.5
ohtau40-H_2O_2 application after SWR generation	4	3.5
ohtau40-heparin application after SWR generation	4	3

2.3.7 In vitro induction of febrile seizures

Hippocampal slices from eight P18-P25 WT and eight P18-P25 KO mice from WT and TRPV1 KO parents, respectively, were prepared as described above and incubated for at least two hours in F1 aCSF at 1.4 ml/min flow rate and 30-32 ^{o}C temperature. Recordings were made from two slices simultaneously. Each recording was 10 minutes long and consisted of 5 min recording LFP from different areas of CA1, changing location every 10-30 seconds, followed by 5 min stable recording in mid CA1 near the pyramidal layer. Recordings were made from the surface of the slice to avoid damaging the slices by multiple punctures. After the first two slices were recorded, the second pair followed until all eight slices were recorded. Then, the temperature was increased to 38.2 +/- 0.6 ^{o}C. Two to five minutes after the desired temperature was reached, high temperature LFP recordings were made in a similar manner to baseline recordings (5 min recording from different areas followed by 5 min stable recording in mid CA1). Two slices were recorded at a time, until all eight slices were recorded for 10 minutes each pair. In one experiment, only seven slices were used as one slice was destroyed. Analysis was done manually, by examining each 10 minute recording and noting the number and type of epileptiform events found. The following types of events were included as epileptiform activity:

- Continuous epileptiform discharges (EDs)
- Groups or bursts of EDs or SWs and EDs

EDs were defined as SW-like events in terms of shape, but with amplitude more than 0.5 mV. A group of such events would consist of at least 3 SW-like events, of which at least one passes the amplitude criterion (Figure 3A). A burst was similar to a group, but events followed each other directly (Figure 3B). If EDs or SWs and EDs were seen continuously before moving to a new location, they were considered continuous EDs (Figure 3C). When quantifying whether epileptiform responses were present, and increased, decreased, or stayed the same in response to the temperature change, continuous EDs counted as higher epileptiform activity (EA) than a single ED or SW/ED group or burst, but were considered equal to more than one group or burst present in a 10-minute recording. Similarly, two ED bursts were counted as higher EA than a single burst. Groups and bursts were considered equal. The percentage of slices with EA at baseline and at high temperature was calculated for each mouse, as well as the percentage of slices where EA increased (either because there was EA at high temperature and not at baseline, or there was EA in both conditions but more EA events at high temperature compared to baseline). Statistical analysis was performed in GraphPad Prism 9 (GraphPad Software, USA). The percentage of slices with EA at 31 ^{o}C and 38.2 ^{o}C was compared between WT and TRPV1 KO mice using RMANOVA, with genotype as between subjects

factor and temperature as within subjects factor, followed by Šidák's post-hoc test. The percentage of slices where EA increased from 31 °C to 38.2 °C was compared between genotypes using a chi-square test, and after averaging per animal using a Mann-Whitney U-test. Lastly, all slices per genotype were pooled together to show the total percentage of slices that increased, decreased, or had no change in their EA with increased temperature.

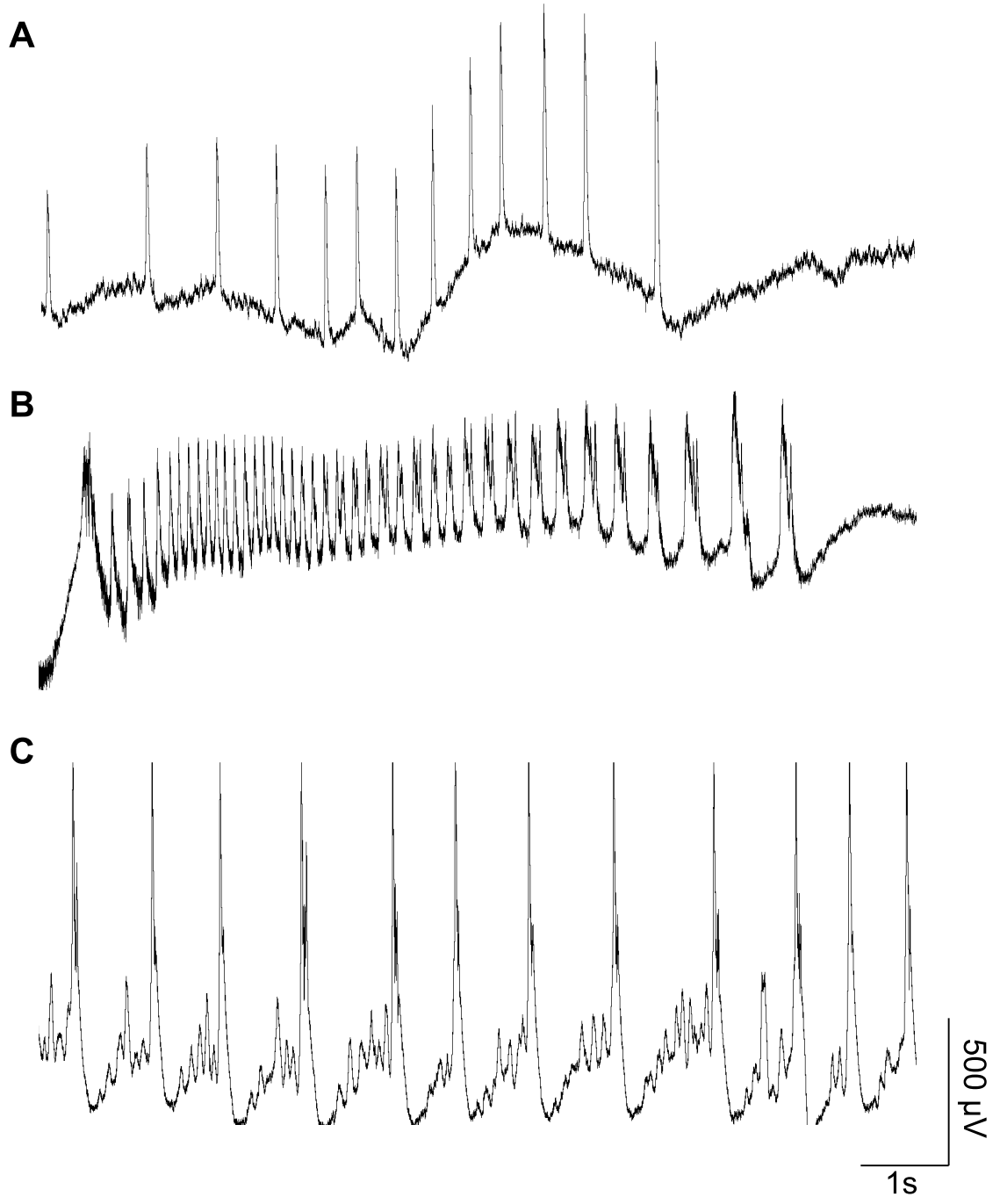

Figure 3: Examples of epileptiform activity (EA) included in our experiment. (A) SW/ED group, **(B)** SW/ED burst, and **(C)** ED continuous.

2.4 Drugs

2.4.1 Anisomycin

Anisomycin was purchased from Sigma-Aldrich (cat. #A9789) and dissolved in water at a concentration of 1 mM. This was used to make a solution of 20 µM anisomycin final concentration in aCSF, which was used in our experiments.

2.4.2 Suberoylanilide hydroxamic acid (SAHA)

SAHA (also known as Vorinostat and Zolinza) was obtained from Cayman Chemical Co. (cat. #10009929) and was dissolved in dimethyl sulfoxide (DMSO, Sigma-Aldrich cat. #276855). This was then used to make a solution of 10 µM SAHA in aCSF. The same amount of DMSO was added in control aCSF and in SAHA-aCSF to account for DMSO effects. The amount of DMSO used in aCSF was no more than 1:1000.

2.4.3 Human tau oligomers

2.4.3.1 Preparation

Human tau (htau40) oligomers were prepared and assessed by Susanne Wegmann's lab. Two types of tau-oligomer preparations were used, one using H_2O_2 following Acquarone et al. (2019), which reported impaired LTP after tau application (see also Fá et al., 2016) and another using heparin, which increases aggregation (see Figure 4). We will call the first ohtau40-H_2O_2 and the second ohtau40-heparin for simplicity.

The ohtau40-H_2O_2 was prepared in two batches. In short, htau40 monomers in phosphate-buffered saline (PBS), 1 mM dithiothreitol (DTT) were used and buffer was exchanged with sterile PBS to remove DTT at least 2 x 2 h at 4 °C, with a 12 kDa molecular weight cut off (MWCO) (Dialyse devices-Pur-A-Lyzer, Sigma-Aldrich) and further concentrated with a filter device (Pierce protein concentrators, Thermo Fisher Scientific) at 3 kDa MWCO (at 10,000 x g 4 °C) if needed. Next, 1 mM H_2O_2, 1x Halt Protease inhibitor mix (Thermo Fisher Scientific cat. #78429), and 0.01% NaN3 were added to 8.5 mg/ml htau40. The mixture was incubated at 25 °C in a Thermoblock, at 250 rpm for 20 hours. Buffer was then exchanged as before and the sample was centrifuged for 20 minutes at 10,000 x g, after which the supernatant containing the tau oligomers was taken. The seeds were sonicated for 15 minutes in a water bath and final stock protein concentration was determined by a bicinchoninic acid (BCA; Smith et al., 1985) assay (198.4 µM = 9.1 mg/ml and 87 µM = 4 mg/ml). The aliquots were stored at -80 °C.

For ohtau40-heparin, 60 µM = 2.75 mg/ml of tau monomers were mixed with 0.7 mg/ml heparin (Applichem; MW= 8-25 kDa) in PBS, 2 mM DTT and incubated at 37 °C for 6 days. Every second day, fresh 2 mM DTT was added. The buffer was exchanged by dialysis using a 10 kDa MWCO and sterile PBS. Then, the samples were sonicated for 30 minutes and a BCA assay was used to determine protein concentration, here 56.7 µM = 2.6 mg/ml. The aliquots were flash frozen with liquid nitrogen

and stored at -80 °C. Experiments with ohtau40-heparin were done with Ana Carolina Odebrecht Vergne de Abreu as part of her lab rotation.

The presence of oligomers was confirmed by SDS-PAGE and semi-native-PAGE. Increased fluorescence intensity of ohtau40-heparin compared to tau monomers and ohtau40-H_2O_2 in the Thioflavin-T aggregation endpoint assay showed the presence of tau β-sheets in ohtau40-heparin only (Figure 4). For all tau experiments, the htau40 stocks described above were diluted in aCSF at a concentration of 25 nM = 1.15 µg/ml and bath applied to the slices.

2.4.3.2 SDS-PAGE and semi-native-PAGE

These two procedures were performed according to Hochmair et al., 2022, by Susanne Wegmann's lab. For SDS-PAGE, 6X reducing SDS-containing loading buffer was added to the protein samples, which were then boiled at 95 °C for 5 minutes and separated by SDS-PAGE (NuPAGE 4-12% Bis-Tris, Thermo Fisher Scientific). For semi-native-PAGE, 6X loading buffer without SDS and reducing agents (BioLabs cat. #B7025S) was used. The samples were not boiled and instead loaded directly onto Native-PAGE gels (NativePAGE, Thermo Fisher Scientific). For both preparations, MES-buffer was used as running buffer (additionally containing 0.1% SDS (Thermo Fisher Scientific) and 1 µg tau was loaded per well. After separation, protein bands were stained with SYPRO Ruby (Thermo Fisher Scientific) and visualized with a Typhoon scanner (Trio, GE Healthcare) using the 532 nm laser and a 610 nm bandpass filter.

2.4.3.3 Thioflavin-T aggregation endpoint assay

The aggregation state of tau was monitored by adding 50 µM Thioflavin-T (ThioT, Sigma-Aldrich) to 4 µM (0.18 mg/ml) of htau40. Samples were prepared in triplicates in clear bottom 384-well µClear plates (Greiner) and ThioT fluorescence (λEx = 440 nm, λEm = 485 nm) was recorded at 37 °C in a plate reader (Infinite M Plex, Tecan) after a 5 s shake. The procedure was performed by Susanne Wegmann's lab (Hochmair et al., 2022).

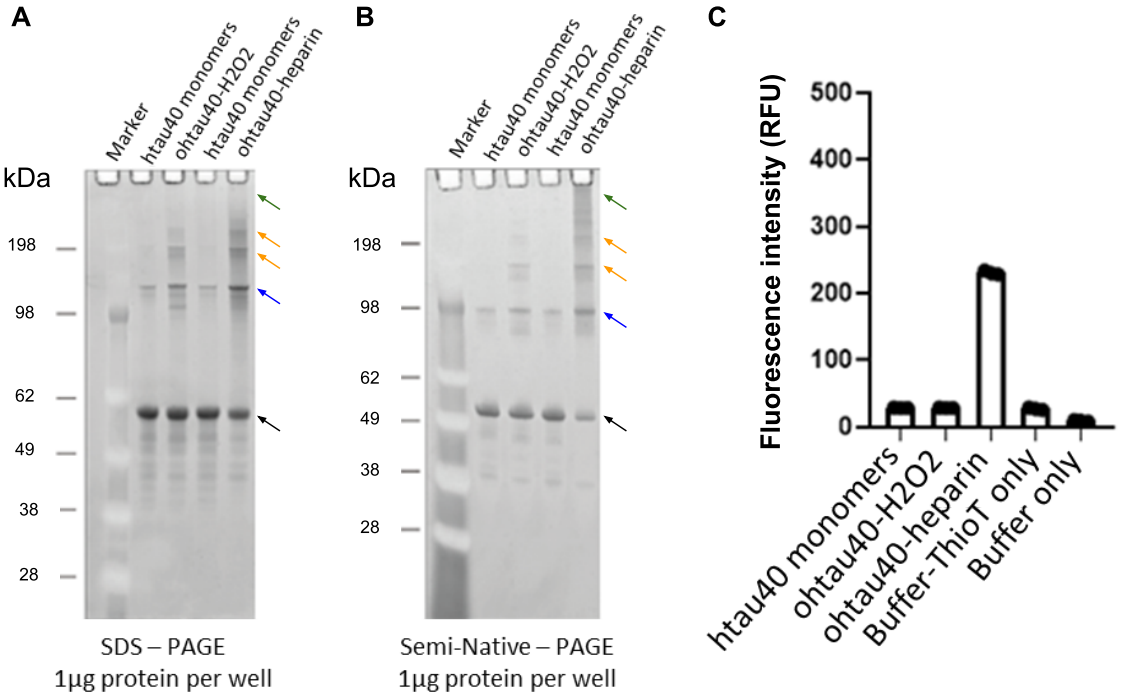

Figure 4: Presence of oligomers and β-sheets in the two ohtau40 preparations. Results from **(A)** SDS-PAGE and **(B)** semi-native-PAGE showing the presence of htau40 monomers (black arrows), dimers (blue arrows), oligomers (orange arrows), and higher order aggregates (green arrows) in the different preparations. Notice that ohtau40-heparin had less monomers and more oligomers and higher order aggregates compared to ohtau40-H_2O_2. **(C)** Thioflavin-T aggregation endpoint assay showing presence of tau β-sheets only in ohtau40-heparin. Figure was provided by Janine Hochmair from Susanne Wegmann's lab and subsequently adapted.

2.5 Behavioral tests

2.5.1 Cheeseboard maze

This is a dry land version of the water maze task (Morris, 1981; Vorhees & Williams, 2006). It lacks the aversive component of the water maze, but requires mild food restriction to motivate the mice to look for the reward. Llano Lopez and colleagues (2010) have compared the two before. Our protocol was similar to the one used by Kesner and colleagues (1991).

2.5.1.1 Platform

The apparatus used for the cheeseboard maze task was custom-made by the Viana da Silva lab. The maze was comprised of a plastic, circular, black arena of 80 cm diameter and 1.5 cm thickness, standing 51.5 cm above the floor in the recording room at the Neurowissenschaftliches Forschungszentrum (NWFZ) at the Campus Charité Mitte in Berlin. The platform had a total of 140

plastic wells, each being 5.3 mm deep, with 12.5 mm external and 7.5 mm internal diameter. These wells were placed in evenly spaced rows (5.5 cm from row to row, 6 cm from well to well in the same row). The start location for each trial was constant and consisted of a 10 cm x 10 cm square area on one side of the maze (Figure 5).

2.5.1.2 Experimental protocol

2.5.1.2.1 Habituation and training

Before training, mice were habituated to the platform for two days. This was done by placing each mouse alone on the platform, in the absence of any rewards, for 10 minutes. Food restriction began on habituation day 1, with mice losing no more than 10% of their original body weight. During the training phase, a liquid reward (diluted chocolate oat milk: ~ 25% chocolate oat milk, 12.5% soy milk, 62.5% tap water) was placed in 30 of the 140 wells. The reward-containing wells changed between different training days; a diagram of the combinations used can be found in Figure 6. Mice were placed on the start location of the platform and had 10 minutes to find and consume the rewards. The training phase was completed when a mouse ate the rewards from at least 21 out of the 30 wells (70% criterion) for two days in a row. Mice took 3-6 days to pass the criterion.

2.5.1.2.2 Learning phase

The learning phase followed, which lasted fourteen days. For the first seven of these, mice were learning the first reward location, which was well 25 for half of the mice and 116 for the other half (Figure 5). Mice were assigned in groups as follows: well 25 = 2 male and 2 female TRPV1 KOs, 1 male and 2 female WTs; well 116 = 2 male and 2 female TRPV1 KOs, 2 male and 1 female WTs. During the following seven days, the reward location was changed to the opposite well (well 116 for mice whose original reward location was well 25 and vice versa) and reverse learning took place. Each day, each animal had four trials, with 60-80 seconds inter-trial interval. Each trial lasted for a maximum of 3.5 minutes; if a mouse didn't find the reward during this time, it was guided to it using a glass beaker and taken out of the platform after the reward was consumed or after the mouse licked the reward and moved away. In trials where the mouse successfully found the reward, the mouse was removed from the maze after consumption or after the mouse walked away from the reward. The trial ended when the mouse was removed from the maze. The first trial of day 6 and of day 13 (day 6 of reverse learning) were probe trials. During a probe trial, no reward was present and the mouse was allowed to explore the platform for 3.5 minutes. For each trial, the position of the animal was recorded by a camera (15 frames per second (fps), acA1300-75gc, operated using pylon Viewer, Basler AG) placed on the ceiling above the platform, and performance was assessed offline using the animal's tracking data (see below). To prevent the use of odor cues, the same milk that was used as reward was spread evenly across the surface of the platform using a wet tissue after each trial. Ethanol was used to clean the maze from other possible odor cues between different mice, but not between different trials of the same mouse. We considered features of the room, such as a small lamp, a computer, and a Scantainer, as distal cues. No proximal cues were used in this task. We did not differentiate

between allocentric and egocentric navigation. Trials took place during the light phase, but dim light was used to ensure low levels of anxiety.

2.5.1.2.3 Markerless tracking of subject's body parts

This step was performed by Dejana Mitrovic from the Viana da Silva lab. Behavioral experiments on the cheeseboard maze were recorded with one video per trial. The videos were recorded at 15 fps. Some of these video recordings were processed post-experimentally to adjust for orientation of the open field and cheeseboard maze such that it was the same throughout all the trials, which was important later on for the analysis.

The body parts used for locating the animals were the nose, left and right ears, and tail base. This was done using a markerless tracking method called DeepLabCut (DLC; Mathis et al., 2018). DLC was run on a computer with Windows 10 operating system with the GTX 3070 founders edition GPU.

Two different DLC projects were used for tracking in open field and cheeseboard maze recordings. One video per mouse was used in both projects for selection of frames. The frames used for labeling the body parts of interest were extracted by clustering based on visual appearance (k-means). 250-300 frames per DLC project were used for training the deep neural network to recognize the body parts. Additionally, the neural network for both projects was refined twice by extracting outliers, where a particular body part or all body parts jumped more than the pixel threshold defined by DeepLabCut compared to the last frame. ResNet50 was used for training with 500,000 iterations. After the deep neural networks were trained, the videos were analyzed by extracting all body parts' coordinates for each frame and saved for each video in an .h5 file. To make sure the deep neural networks were trained well enough, one random video was chosen for creating labeled video to visually assess the quality of the tracking. If during analysis it appeared that the tracking was not good enough, the network was refined and retrained.

The commands for executing all the steps described above can be found at DeepLabCut's GitHub documentation page:

https://deeplabcut.github.io/DeepLabCut/docs/standardDeepLabCut_UserGuide.html .

The files were organized in a manner that is compatible with the BikiPy Python package (https://pypi.org/project/bikipy/) which provides results for various parameters.

For the cheeseboard maze, each mouse had its own directory with subdirectories for each day of experiments. The rewards were marked only once per reward location. The point of reward location and rectangular start box was also marked as a rectangle which was used to mark the start of the exploration and search for the reward. These locations were marked using makesense.ai, where reward locations were marked as points and the start box as a rectangle. The start box dimensions were used to convert pixels to meters.

From the animal's trajectory, the distance and time to reward location in the cheeseboard maze were calculated using a python code custom written by Can Tartanoglu from the Viana da Silva lab. Distance and time to reward location started counting after the mouse left the start box (10 x 10 cm)

and ended when the mouse's nose was detected inside the reward area (a circular area 2 cm in diameter centered on the well containing the reward). A motion subpackage (features.motion.Motion) computed the mouse's track according to maze coordinates. The coordinates were smoothened with the use of a SARIMAX model:

https://www.statsmodels.org/dev/generated/statsmodels.tsa.statespace.sarimax.SARIMAX.html

If time to reward location was more than the maximum duration of a trial (210 s), the value was changed to 210 s.

For five trials in the cheeseboard maze, the code did not give a value for displacement and time to reward location. In two of these, time was manually measured by watching the video with a stopwatch, and distance was manually measured by drawing the animal's trajectory from the video and calculating distance by converting number of pixels to cm using the start box dimensions in FIJI (Schindelin et al., 2012). The manual tracking of distance was performed by Dr. Camin Dean. In the remaining three trials, mice were guided to the reward using a beaker, which made the detection of the mouse challenging. For these trials, maximum trial duration (210 s) was used as time to reward location. For distance to reward location, Dr. Camin Dean measured distance traveled from the start of the video (which shows the mouse still in my hand before being put on the maze and hence overestimates total displacement) until the mouse left the start-box using FIJI, and then this value was subtracted from the total displacement to determine the actual displacement.

2.5.1.2.4 Analysis

The time and distance to reward location in each trial were extracted from tracking data. GraphPad Prism 9 (GraphPad Software, USA) was used for statistical analysis. Outliers on days 6, 7, 13, and 14 (days 13 and 14 correspond to days 6 and 7 of the new reward location) were identified using the ROUT method with Q = 1%. All trials from each day were analyzed separately for each genotype (24 WT and 32 TRPV1 KO trials from 6 and 8 mice, respectively, 4 trials per mouse). Outlier trials were removed and the remaining trials were averaged per mouse. Statistics and graphs show results with and without outliers. Learning curves and performance level per genotype were analyzed using simple linear regression analysis. Mouse average daily performance was used to calculate a mean daily performance per genotype. The line of best fit for each genotype was determined using the mean daily performance per genotype, with R^2 indicating goodness of fit, a slope significantly different from zero denoting learning, and differences in slope and elevation between the two lines suggesting differences between genotypes. Original and new reward locations were analyzed separately. For distance to original reward location, averages per mouse for days 1 and 5 were also analyzed with a one-tailed paired t-test.

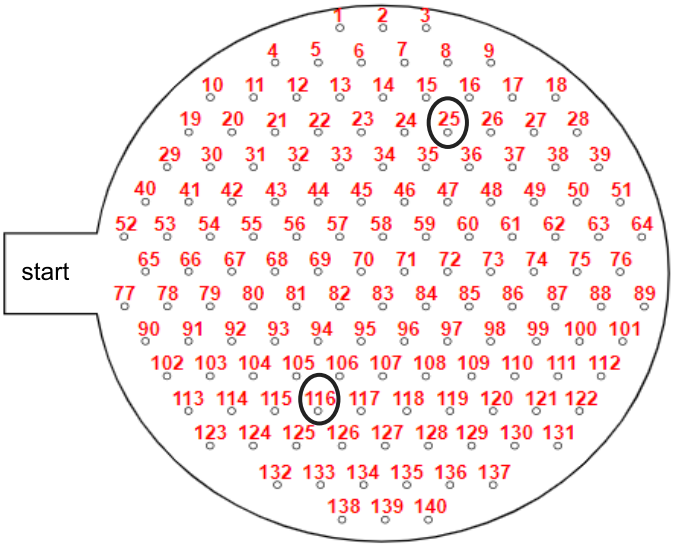

Figure 5: Representation of the cheeseboard maze. The maze was 80 cm in diameter. The start location (10 cm x 10 cm) on the left and the two reward locations used for reference memory and reverse learning (in circles) are marked. In half of the animals, well 25 was used for reference and well 116 for reverse learning, while in the other half of the animals the sequence of reward locations was reversed. Figure was provided by Rina Patel from Silvia Viana da Silva‘s lab and subsequently adapted.

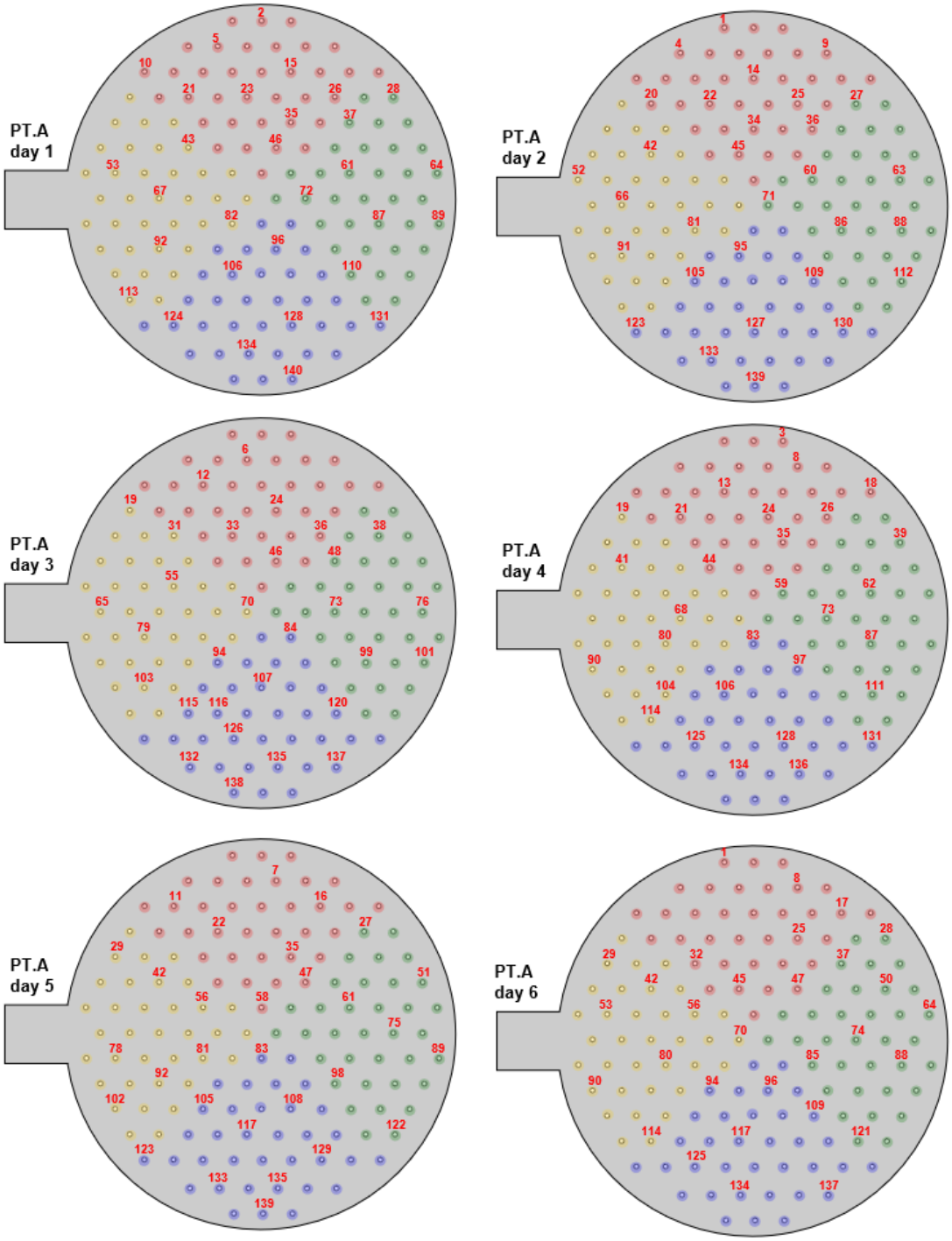

Figure 6: Reward locations used for the training phase on the cheeseboard maze. The wells containing a reward (displayed here with their corresponding numbers) were different for each day. The training phase ended when mice consumed at least 21 out of 30 rewards for two days in a row, which took mice 3-6 days. Figure was provided by Rina Patel from Silvia Viana da Silva's lab.

2.5.2 Open field

This is a widely known behavioral test for anxiety based on the animal's exploratory behavior (Hall & Ballachey, 1932; Hall, 1934; Seibenhener & Wooten, 2015). The open field consisted of a plastic, 75.5 cm x 75.5 cm square arena, with gray floor and black 40 cm high walls. Three cues (a yellow star, a blue circle, and a green rectangle) were placed on three different walls surrounding the arena as proximal visual cues. The arena was standing 71 cm above the floor in the recording room at the Neurowissenschaftliches Forschungszentrum (NWFZ) at the Campus Charité Mitte in Berlin. The open field test was done one day after the last day of reversal learning in the cheeseboard maze, when the animals still had restricted access to food. The open field test took place during the light phase, but only dim light was used while mice were inside. During the open field test, each mouse was placed in the open field near the wall without a cue and left to explore for 15 minutes. A camera (15 fps, acA1300-75gc, operated using pylon Viewer, Basler AG) above the arena was again used to record the animal's location. Tracking was performed as described above with one video recording per mouse. The length of the diagonal of the open field was marked using makesense.ai to convert pixels to meters and to define periphery (the area 15 cm from the walls). Location of the mouse to the center was tolerance modeled, such that the mouse must spend at least 0.5 seconds within the center to be considered center-located. Location in the periphery is then tolerance modeled using the same criteria (at least 0.5 seconds within the periphery to be considered periphery-located). The time in the center and periphery of the open field was calculated from the animal's trajectory using a python code custom written by Can Tartanoglu from the Viana da Silva lab. The percentage of total time spent in the middle of the maze compared to the periphery was used to determine anxiety levels in TRPV1 KO and WT mice. The number of entries into the center and the total displacement were also quantified. A Mann-Whitney U-test was used to compare differences in time spent in the center, entries in the center, and total distance moved between genotypes.

2.6 In vivo electrophysiology

2.6.1 Microdrives

The in vivo recording devices (microdrives) used in this study were similar to those developed and validated by Anikeeva and colleagues (2011; Figure 7). Platinum/iridium (90%/10%) wire (California Fine Wire Company) was used to make the tetrodes by coiling and heating the wire at 140 ^{o}C for 1 minute at the top and 1 minute at the bottom of the cable. Each drive was loaded with four tetrodes (with 4 channels each). The base of the drive was made using a 3D-printed housing, a vented screw, and a thumbnut that allowed the tetrodes to be lowered. Through the screw, two metal cannulas were placed on top of each other and a single plastic cannula was placed inside the metal ones to protect the tetrodes in the center. The EID board, where the tetrodes connected and signal transmission occurred, was placed on top of a 3D-printed stability board. The tetrodes were glued on an optic fiber that provided support for the tetrodes and the drive was covered with rubber cement and epoxy glue to protect the sensitive parts. The tetrode tips were plated with platinum to reduce impedance to 150-250 kΩ at 1 kHz. Support for building the microdrives used in this study was provided by Dr. Silvia Viana da Silva, Rina Patel, and Shimon Jude Swer.

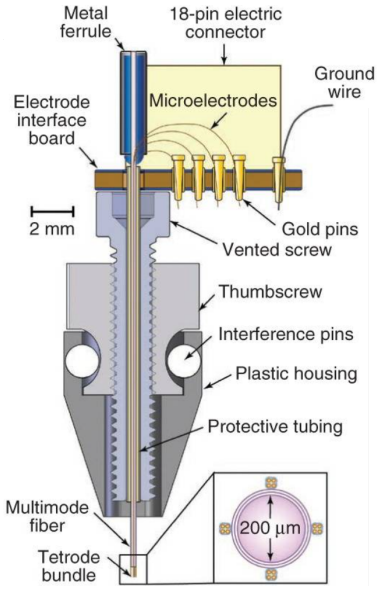

Figure 7: Sketch of the microdrives. Vertical cross section of the microdrives used in this study. Figure by Anikeeva et al., 2011.

2.6.2 Microdrive implantation surgery

Mice were anesthetized with 5% isoflurane (Isofluran CP, CP-Pharma cat. #1214) at 0.4 L/min O_2 in a plexiglass chamber and then placed on a stereotactic frame. There, anesthesia was maintained by delivering ~ 2% isoflurane at 0.4 L/min O_2 through a mask, while analgesia was applied by injecting carprofen subcutaneously (5 mg/kg, Carprosol, CP-Pharma cat. #114). A lubricating ophthalmic gel was used to prevent the mice's eyes from drying, and a heating pad was placed underneath the mice to keep them warm throughout the procedure. Subcutaneous saline injections were given during surgery every ~ 1 h to keep the mice hydrated. After shaving and disinfection of the skin on top of the skull with iodine and ethanol, a ~ 3 mm incision was made, exposing the skull. Bregma and lambda were identified and correct positioning of the head on the frame was confirmed by checking that the difference in the coordinates of bregma and lambda in the z-axis and x-axis was less than 0.2 mm. Four stability screws were implanted on the skull. The ground wire was attached to a fifth screw placed in the left hemisphere, making contact with the cortex. Vetbond was used to glue the screws in place. The craniotomy was on the right hemisphere and the coordinates for targeting the CA1 pyramidal layer were -1.8 mm anteroposterior (AP) and +1.7 mm mediolateral (ML) from Bregma. The drive was then lowered 0.2-0.5 mm from Bregma. The craniotomy was closed with silicone gel to protect the tetrodes and the exposed brain from the dental cement that was then used to cover everything and stabilize the implant. Carprofen and lidocaine (0.05 mL of 1% lidocaine, Lidocain HCl, PZN 03676850, B.Braun) were injected subcutaneously as painkillers during surgery, while buprenorphine (0.1 mg/kg injected subcutaneously, Temgesic, Indivior) and metamizol (1.25 mg/mL in drinking water, Novaminsulfon, PZN 03530394, Ratiopharm) were used for post-operative pain relief. Following surgery, the mice were placed back in their home cage, which was left over a heating pad until they woke from the anesthesia. They were then left to recover for 5 days, during which daily wellness checks were performed to ensure proper recovery.

2.6.3 In vivo SWR recordings

2.6.3.1 Behavioral protocol and data acquisition

The tetrodes were lowered slowly (no more than ~ 0.112 mm in 4 hours) into the hippocampus, to avoid damaging the tissue, over the course of 5-10 days after surgery. To examine local field potential (LFP) and single-unit activity, the microdrive was plugged into a 16-channel, head-mounted preamplifier linked to a digital Neuralynx data acquisition system (Digital Lynx 4SX, Neuralynx, USA). From each tetrode, continuous LFP or spikes were recorded by first amplifying (5,000-20,000×) and then band-pass filtering (1-1000 Hz for LFP or 0.6-6 kHz for spikes). Sampling frequency was 32 kHz. Spike waveforms above 30-45 µV were time-stamped and digitized at 32 kHz for 1 ms.

Recordings started once SWRs and clustered unit activity were present in at least one tetrode, indicating that the tetrode was in the CA1 layer of the hippocampus. On day 1, LFP and cellular spiking activity were recorded during a 1 hour rest (r1), followed by a 20 minute exploration of novel open field 1 (of1), then a 20 minute exploration of novel open field 2 (of2), a second 20 minute exploration of open field 1 (called for simplicity of3), and finally a second 1 hour rest (r2). The mice were then given 40 more minutes to explore of2 divided in 2 sessions on day 1, and 20 more minutes to explore of1. These weren't recorded, but allowed the animal to become familiarized with the two environments. For the same reason, they were given 20 more minutes in each field on day 2 before continuing with recordings. After this, both fields were considered familiar. The tetrodes weren't lowered between day 1 and day 2 to allow recording of the same cells in both novel (day 1) and familiar (day 2) conditions. On day 2, the same protocol was used for recordings, but rest sessions were reduced to 20 minutes each. Following each successful recording, tetrodes were lowered 1/16 of a turn (~ 0.028 mm). When new cells were found, they were recorded again during r1, of1, of2, of3, and r2 for 20 minutes each. The experimental protocol for recordings can be seen on Figure 8. Mice were recorded following this protocol for 3-10 days, until either the tetrodes could not be lowered more because the maximum number of turns was achieved, or it was determined that all tetrodes had passed the CA1 pyramidal layer based on the presence of positive polarity SWs, large theta, and absence of cell clusters. During rest sessions, food was removed from the home cage, but animals still had ad libitum access to water. Between open field sessions, animals were put back in their home cages for 5-10 minutes, so they weren't deprived of water access for more than 20 minutes each time. Sugar pellets and cereal were spread in the open fields to motivate mice to explore the environment, but no food restriction was used at this stage. The recordings were done in dim light conditions and the animal's position was recorded by a camera (at 30 fps, acA1300-75gc, Basler AG) mounted on the ceiling above the platform, which tracked the location of the mouse using a red and a green LED located on either side of the head-mounted preamplifier.

Open field 1 was a 50 cm x 50 cm x 50 cm square black box with a single cue on one wall (white cross) and was cleaned with soap before each exploration. Open field 2 was a 50 cm x 50 cm x 50 cm square box with gray walls and a striped gray and black floor. A single visual cue (concentric green ovals with an empty square in the middle) was placed on one wall and it was cleaned with ethanol before each exploration. Lemon juice was also wiped across the floor and walls of open field 2 to give it a distinct smell.

A

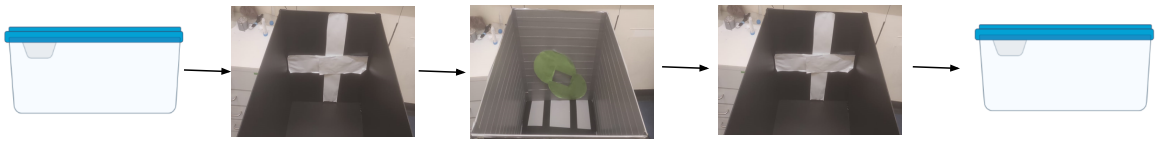

Rest session 1 in home cage | Open field 1 | Open field 2 | Open field 3 (2nd exploration of of1) | Rest session 2 in home cage

B

Day	Protocol
1	Novelty recording: r1 (1 h) -> of1 (20 mins) -> of2 (20 mins) -> of3 (20 mins) -> r2 (1 h) To get familiarized, no recording: of2 (20 mins) -> of1 (20 mins) -> of2 (20 mins)
2	To get familiarized, no recording: of1 (20 mins) -> of2 (20 mins) Familiar environment recording: r1 (20 mins) -> of1 (20 mins) -> of2 (20 mins) -> of3 (20 mins) -> r2 (20 mins)
3-10	Familiar environment recording: r1 (20 mins) -> of1 (20 mins) -> of2 (20 mins) -> of3 (20 mins) -> r2 (20 mins)

Figure 8: Experimental protocol for in vivo electrophysiology. **(A)** Each recording session consisted of a first rest session in the home cage, followed by exploration of open field 1 (of1), exploration of of2 (of2), re-exploration of of1 (of3), and a second rest session in the home cage. **(B)** Recording sessions and familiarization with the open fields across days. Open fields were novel during day 1 recordings and rest sessions lasted for one hour. Mice were allowed to explore the open fields in additional sessions, which were not recorded, in order to get completely familiarized with both open fields before proceedings with day 2 recording. Thus, open fields were considered familiar for day 2 and all following recordings (for which rest sessions only lasted 20 minutes).

2.6.3.2 Data analysis

From the in vivo recordings, SWRs, theta, and delta oscillations were analyzed. In addition, the day with the highest number of cluster units that could be seen during recording for each animal (except the 1st day, during which the open fields were novel) was selected for cluster cutting and cell analysis. All analysis was performed using custom written MATLAB (The Mathworks, Inc.) code provided by Silvia Viana da Silva's lab. For LFP analysis, the tetrode with the best signal (largest SWRs) was chosen for analysis for each recording session, unless the tetrode location (determined via histological processing) was not optimal. In the latter case, the signal was examined and the tetrode best located in the CA1 pyramidal layer was chosen, assuming that this is the tetrode showing the highest change in theta amplitude and number of cells across days (Figure 10). LFPs were analyzed both per recording session (one recording session consisting of the five stages: r1, of1, of2, of3, r2) and per animal (each of the five stages - r1, of1, of2, of3, r2 - averaged per animal across

recording days). The first day of recording for each animal (novelty day) was analyzed separately from the rest. For cell spike analysis, all tetrodes of the selected familiar recording day were used.

2.6.3.3 Analysis of SWRs

Only SWRs that occurred during periods of immobility were analyzed (defined as periods during r1 and r2 when the velocity of the mouse was less than 2 cm/s). Ripples were detected using a method adapted from Blanco et al., 2011, which took the raw LFP and bandpass filtered the data between 150-200 Hz using a filter numerator and zero-phase forward and reverse digital filtering (*FILTFILT* function). The running root mean square (RMS) of the entire LFP in 3 ms bins was created and candidate regions that were more than 3.5 standard deviations larger than the RMS mean were selected. The start and end of a ripple event were taken as the times where RMS passed and dropped below this threshold, and ripple duration was calculated by subtracting the two. Events were included if they were at least 6 ms and less than 500 ms in length. If events were closer than 10 ms apart, they were combined. Events with less than 8 peaks above 3 standard deviations from the mean rectified bandpassed channel were rejected. Ripple rate was calculated by dividing the number of ripple events by the time of immobility (mouse velocity < 2 cm/s). Ripple magnitude was calculated after rectifying the 150-200 Hz bandpassed LFP channel and normalizing the values by dividing with the standard deviation of the channel. The maximum peak from each ripple event was then selected and an average was taken for each session. For ripple peak frequency and power, the raw LFP was normalized using the *normalize* MATLAB function that uses the 'zscore' method (centers the data to have mean equal to zero and scales it to have standard deviation equal to one). Then the normalized LFP was bandpass filtered between 150-200 Hz using the *fftbandpass* function by Jensen (2000), which uses an acausal Fast Fourier Transform (FFT) algorithm (i.e., no phase shift) and constructs the filter function from a hamming window. Snippets were then taken, each starting 120 ms before the start of the ripple event and ending 120 ms after the end of the ripple event. The power spectral density (PSD) estimate for each snippet was calculated via Welch's averaged modified periodogram method using the *PWELCH* MATLAB function with window set at 50 ms and window overlap set at 25 ms. Peak power was taken as the maximum of the resulting PSD estimate and peak frequency as the frequency with the maximum power, then means were calculated for each rest session.

2.6.3.4 Analysis of theta and delta oscillations

For each session, the LFP from the selected tetrode was downsampled at 16 Hz. Segments where the velocity of the mouse was more than 2 cm/s were used for analysis in open fields, while segments where the velocity was less than 2 cm/s were used for rest sessions. The LFP signal was downsampled again at 1 Hz and the wavelet transformation for each sweep took place using the *wavelet* function by Torrence and Compo (1998) with parameters set as follows: amount of time between each Y value (dt) = 1/sampling frequency after downsampling, zero padding on, spacing between discrete scales (dj) = log2(fpassHigh/fpassLow)/round(log2(fpassHigh/fpassLow))/freqRes, smallest scale of the wavelet = 1/fpassHigh, number of scales minus one =

round(log2(fpassHigh/fpassLow)/df), and mother wavelet set to “Morlet”, with fpassHigh (high frequency threshold for bandpass filter) = 200 Hz, fpassLow (low frequency threshold for bandpass filter) = 0.5 Hz and freqRes (resolution in the frequency axis) = 30. The absolute value of the resulting waveform was then also downsampled at 1 Hz and smoothed with a smoothing window = 20 ms. Power was calculated by taking the square of the absolute value of the smoothed waveform and then by taking the mean of the values. For analysis of peak frequency and power, defined frequency bands were plotted against their respective powers as calculated above, with the peak of the plot taken as peak power and the x-value of the peak taken as peak frequency. If no clear peak was detected on the plot, for example due to noise or because the mouse did not explore well in the case of theta oscillations, the value for the session was missing. The theta frequency band was defined as being 4-12 Hz, while for delta it was defined as 0.5-4 Hz.

2.6.3.5 Statistical analysis of LFP parameters

Results from each recording session (one session consisting of the r1, of1, of2, of3, and r2 phases), and results averaged across all recording days per animal were exported from MATLAB version 2020b and imported into GraphPad Prism 9 (GraphPad Software), which was used for statistical analysis and making graphs. Only rest sessions were analyzed for SWRs, while for theta and delta waves the two rest sessions were analyzed separately from the three open field sessions. Variables were analyzed using a repeated measures ANOVA (RMANOVA) test with rest session (r1, r2) or open field session (of1, of2, of3) as within subjects factor and genotype (WT, KO) as between subjects factor. If there were missing values in the dataset, a mixed effects model was used instead. A Šídák's post-hoc test with multiple comparisons correction was then performed to identify specific differences. Main statistics, including post-hoc tests, were based on recording sessions, but the results of the RMANOVAs using animals as experimental units are also reported in respective figure legends. If the sphericity assumption of the RMANOVA was violated, the Greenhouse-Geissner correction was applied.

2.6.3.6 Analysis of putative pyramidal cells, place cells, and interneurons:

2.6.3.6.1 Spike sorting and cell classification

The data from each recording were split into the five phases of our protocol (rest 1 (r1), open field 1 (of1), open field 2 (of2), second exploration of open field 1 (of3), and rest 2 (r2)) using the EventSessionSplitter software (2008, Neuralynx Inc.). The NlxVideoFix software version 1.3 (Skjerpeng, 2007) was used to cut out reflections of the LEDs on the walls of the open fields. Clusters were selected manually using the MClust software (MATLAB version 2009b) by looking at 2D projections of waveform amplitude, energy, and peak-to-valley ratio. The spike waveform, auto-correlogram, and peak plot were checked to reject clusters that might represent noise. Single units with an average firing rate above 6 Hz in all phases (r1, of1, of2, of3, r2) were classified as putative interneurons, while the remaining cells were considered putative pyramidal cells. Place cells were defined as putative pyramidal cells with at least one place field defined as described below.

2.6.3.6.2 Spatial properties of putative pyramidal cells, place cells, and interneurons

Analysis was performed on MATLAB version 2020b. The scripts assigned each detected cell spike to the x-y location of the open field in which they occurred, and a rate map was created for of1, of2, and of3 using 3 cm spatial bins to calculate firing rate. A boxcar averaging procedure followed, during which each pixel was replaced by the average of itself and its neighbors, and the resulting firing rate map matrix was smoothed. The maximum firing rate of a spatial bin in any of the open fields was taken as the peak firing rate of the cell. To define a place field, the peak firing rate of a cell should be at least 3 Hz in a spatial bin, which should be surrounded by at least seven bins in which the firing rate was more than 30% of the peak firing rate. If place fields were less than 2 bins apart, they were merged. A Pearson correlation analysis was used to calculate spatial correlations between the rate maps of the three open field sessions, with a high correlation between of1 and of3 (2nd exploration of of1) suggesting high place field stability and a high correlation between of1 and of2 suggesting low remapping of place fields. The information index was calculated as described by Skaggs and colleagues (1992) and describes how much information about the location of a mouse is conveyed by the firing rate of a cell.

2.6.3.6.3 Statistical analysis

Results for each cell, as well as averages of each cell type per animal, were exported from MATLAB and imported into GraphPad Prism 9 (GraphPad Software) which was used for statistical analysis and for making graphs. A Mann-Whitney U-test was used to compare WT and TRPV1 KO cells and animals, while a chi-square test was used in addition to compare proportions of pyramidal cells that are or are not place cells in the two genotypes.

2.6.4 Histological identification of tetrode location

2.6.4.1 Perfusion

Mice were anesthetized in a plexiglass chamber with 4% isoflurane in O_2 at a rate of 0.4 L/min and then given a lethal injection of Ketamine/Xylasine (160 mg/Kg Ketamine, Ketamin, CP-Pharma cat. #1202, 20 mg/Kg Xylasine, Xyvalet, CP-Pharma cat. #1205) intraperitoneally. Once the breathing rate was sufficiently slow and toe-pinch reflex was absent, mice were first perfused with PBS (10 mM Na_2HPO_4, 137 mM NaCl, 2.7 mM KCl, 1.8 mM KH_2PO_4; pH 7.4) containing 0.3% Heparin (Heparin-Natrium, B. Braun cat. #2147217) and then with 4% Paraformaldehyde in PBS (PFA, Thermo Fisher Scientific cat. #J19943.K2) for 7-8 minutes. The success of the perfusion was assessed by the amount of stiffness of the neck and tail and presence of a pale liver. If the perfusion was not deemed successful, heads were removed and placed in 4% PFA for at least 3 days at 4 °C before proceeding with brain extraction, otherwise they were left in 4% PFA at room temperature for 3-6 hours to improve tissue fixation around the tetrodes. The tetrodes were then slowly moved upwards before carefully extracting the brain from the skull and placing it in 4% PFA for at least 1 day. The brain was then switched to 1x PBS, where it stayed until sectioning.

2.6.4.2 Brain slicing and tissue staining

The brains were mounted on a vibratome (VT1000S, Leica) and 40 µm coronal slices were taken, starting with slices containing lesions caused by the grounding screw and ending with slices containing superficial lesions from posterior stability screws, to ensure all slices with the craniotomy for tetrode insertion were collected. The slices were placed in PBS and subsequently mounted on adhesive microscope slides (SuperFrost Plus, Menzel glasses, Thermo Fisher Scientific cat. #J1800AMNZ), where they were left to dry for 2-6 days.

2.6.4.3 Cresyl-violet staining and imaging

Staining started with a 2 minute rehydration step by placing the slides with the mounted brain slices in distilled H_2O. Dehydration followed by dipping the slides 10 times each in increasing ethanol-concentration solutions (50%, 70%, 80%, 90%, 100%, and 100%). The slides were then placed in Xylene (Applichem, cat #AP211769.2711) solution for at least 2 minutes and then rehydrated by being dipped 10 times each in decreasing ethanol-concentration solutions (100%, 100%, 90%, 80%, 70%, 50%) followed by 1-2 dips in distilled H_2O. Then, the slides were placed in cresyl violet (Sigma-Aldrich, cat. #1.05235.0025, 0.1 g cresyl violet acetate, 100 mL H_2O, 250 µL glacial acetic acid, stirring overnight at room temperature and filtered before use) for 1-2 minutes and the intensity of the staining was checked roughly every 30 s. If the staining was excessive, the slides were quickly dipped once in acetic acid-ethanol (1:2) solution. A final dehydration step as described above followed, before placing the slides for at least two more minutes in Xylene. The slides were then either directly cover-slipped with mounting medium (Invitrogen™Fluoromount-G™ Mounting Medium, cat. #00495802, Thermo Fisher Scientific) and left to dry before imaging, or left to dry overnight, imaged, and then cover-slipped for long-term storage. Imaging was done using a Thorlabs Cerna Microscope for epifluorescence and bright-field with XY platform microscope, using a 4x magnification lens (Thorlabs Inc.) and manual identification of the lesions caused by the tetrodes followed to confirm recordings were made from the CA1 pyramidal layer.

Figure 9 shows representative examples of recording locations from two WT and two KO mice. One of the recorded WT mice (WT-461) had tetrodes located in CA2 and CA3 in addition to CA1 (Figure 10). The tetrode with the biggest change in number of cells and theta amplitude across recording days was inferred to be the track in Figure 10B, which is the one best located in CA1, and was therefore selected for LFP analysis for this mouse. The last three recording days for WT-461 were also excluded from analysis to avoid recordings from CA3; and for the same reason, the first familiar day for this mouse was selected for cell analysis, even though cells from all tetrodes were included here. Two TRPV1 KO mice were excluded from analysis due to having large hippocampal lesions, which might have been caused by gliosis, large craniotomy, or movement of one of the cannulas inside the hippocampus (Figure 11). The CA1 area was destroyed in these mice, so we could not confirm recordings there.

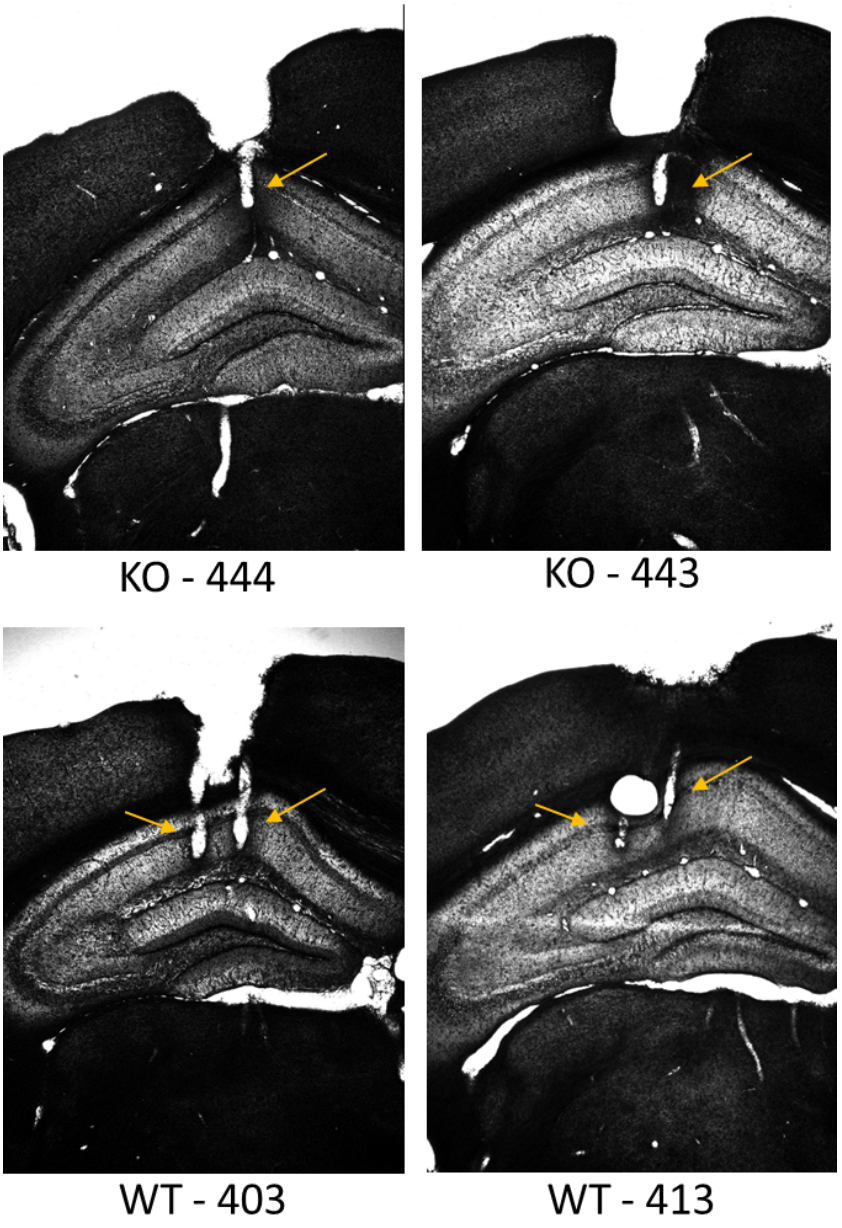

Figure 9: Representative examples of tetrode tracks. Tetrode locations (yellow arrows) identified by manual histological examination are shown for two TRPV1 KO (top) and two WT (bottom) mice.

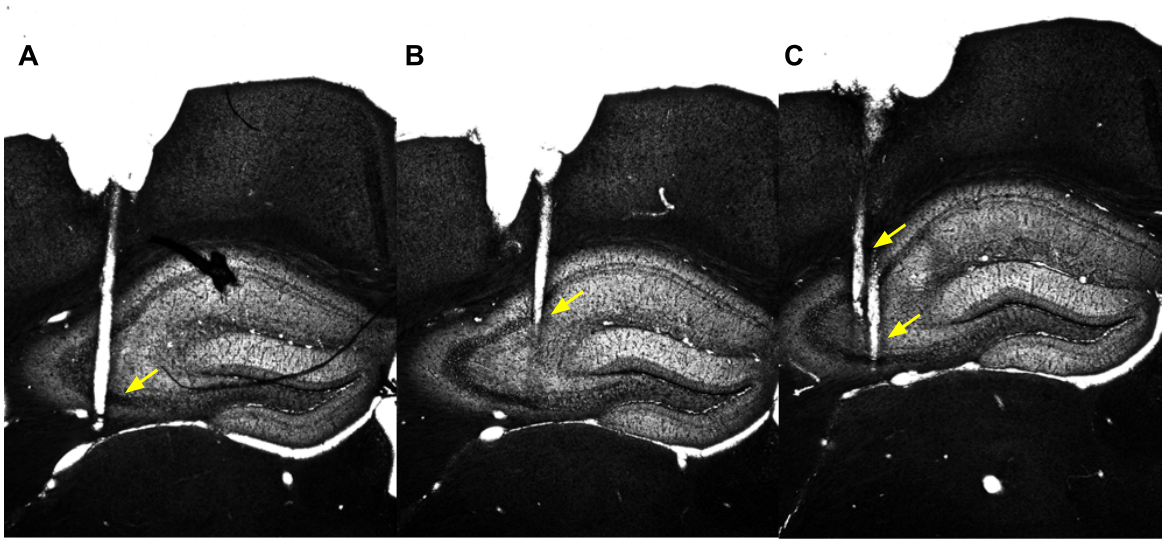

Figure 10: Tetrode location for WT-461 in CA1, CA2, and CA3. (A) Tetrode passed near CA2 and then reached CA3 as it was lowered into the hippocampus. **(B)** Tetrode in the CA1 pyramidal layer. **(C)** Two tetrodes crossed the CA1/CA2 pyramidal layer when they first reached the hippocampus, and at least one reached CA3 later. Yellow arrows indicate tetrode tracks. The tetrode that had the biggest change in number of cells and theta amplitude across recording days was inferred to be the one in **(B)**; and as the one best located in CA1 was selected for LFP analysis for all days. The last three recording days of this mouse were excluded to avoid including recordings from CA3. Because we assumed that during day 2 (the first day of the familiar condition) all tetrodes were located in CA1/2 and not CA3, it was selected for cell analysis and cells from all tetrodes were used.

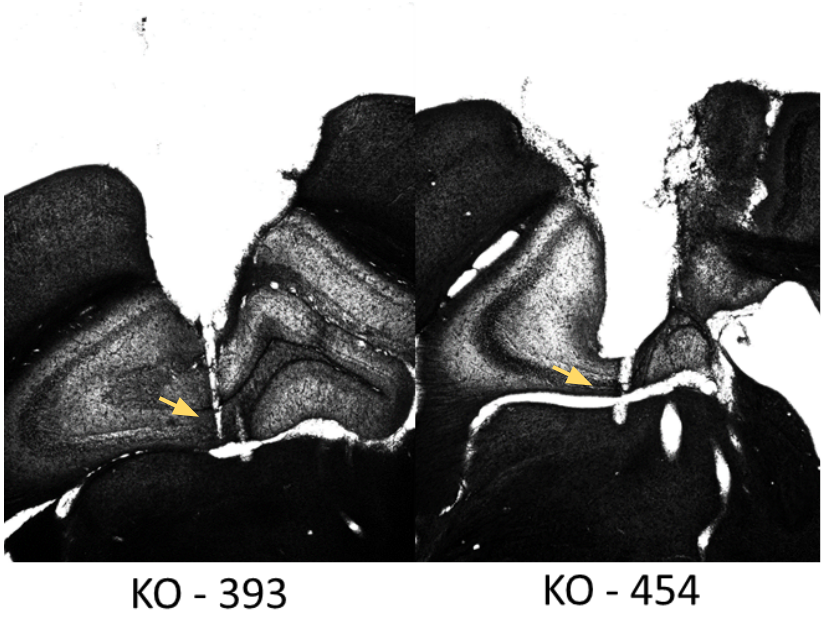

Figure 11: Representative pictures of tetrode location from the two TRPV1 KO mice that were excluded from analysis. Large hippocampal lesions were seen, caused by gliosis, large craniotomy, or movement of one of the cannulas inside the hippocampus. The CA1 area was destroyed, and hence we could not confirm recordings were taken from here. Yellow arrows indicate tetrode tracks.

3. Results:

3.1 The TRPV1 channel and hippocampal oscillations

3.1.1 Effect of temperature and TRPV1 KO on SWRs: sleep simulation

The TRPV1 channel is activated by physiological ranges of heat in the presence of lipids and agonists found in the brain (Cao et al., 2013a). To test if the TRPV1 channel might sense heat, and thereby modify SWRs in the hippocampus (potentially by its presence in OLM neurons), we measured SWRs in a "sleep simulation" experiment. SWRs were recorded at a baseline 31 ^{o}C. Temperature was then increased to 36 ^{o}C (to mimic brain temperature that occurs in sleep), then 38 ^{o}C (waking brain temperature), followed by a second cycle from 36 ^{o}C to 38 ^{o}C. Temperature was then increased to an extreme of 40 ^{o}C, simulating fever, before being returned to 31 ^{o}C to see recovery. Two time points were analyzed, one soon after each temperature step was reached, and one after at least 18 minutes at that temperature had passed. Analysis of SW parameters showed no difference between TRPV1 KO and WT slices in terms of SW amplitude (Figure 12), duration (Figure 13), or rate of occurrence (Figure 14) at start or end of temperature steps. However, there was a significant interaction of genotype and temperature for the probability of SW cluster occurrence at the start of each temperature step and a tendency at the end ($p_{genotype*temperature}$ = 0.041, 0.060 at start and end, respectively; Figure 15). There was no significant difference in cluster occurrence at specific temperatures, but the biggest tendency was a higher occurrence of SW clusters in KO slices at 31 ^{o}C baseline ($p_{31\_baseline}$ = 0.011, 0.0097 at start and end; Figure 15). All parameters were significantly affected by temperature ($p_{temperature}$ for SW amplitude = 0.00036, < 0.0001 at start and end; SW duration = 0.018, 0.049 at start and end; number of SWs per minute < 0.0001 at both time points; probability of cluster occurrence = 0.014, 0.023 at start and end). Figure 16 shows representative SWR traces from a WT and a TRPV1 KO slice at 31 ^{o}C baseline, demonstrating the increased presence of clusters in the TRPV1 KOs.

Ripple amplitude was similar in WT and TRPV1 KO slices (Figure 17), as was peak ripple frequency (Figure 18). Ripple duration significantly increased in TRPV1 KO slices at the beginning of the first temperature step to 36 ^{o}C as shown by the post-hoc test ($p_{36\_1st\_start}$ = 0.0017), even though only a tendency was seen on the interaction of genotype and temperature effects from the main RMANOVA test ($p_{genotype*temperature}$ = 0.07). The same tendency was seen at the end of the 36 ^{o}C temperature step ($p_{36\_1st\_end}$ = 0.011) and other temperatures ($p_{38\_1st\_start}$ = 0.021; Figure 19). Similar to ripple duration, the post-hoc test identified a significant increase in the number of ripple peaks per ripple event in TRPV1 KOs at 36 ^{o}C 1st at the beginning of temperature steps ($p_{36\_1st\_start}$ = 0.0015), with a similar tendency seen at the end ($p_{36\_1st\_end}$ = 0.016) and at other temperatures ($p_{38\_1st\_start}$ = 0.018), even though the main RMANOVA test did not indicate any significant differences (Figure 20). There was a significant effect of genotype for maximum ripple power at the beginning of temperature steps, but not at the end ($p_{genotype}$ = 0.030, 0.22 at start and end, respectively; Figure 21). This is probably because KO slices tended to have higher ripple power in general, but there was no difference between WT and KO slices at specific temperatures. TRPV1 KO mice had higher ripple incidence at both the start and end of temperature steps ($p_{genotype}$ = 0.028, 0.038 at start and end, respectively;

Figure 22). The Bonferroni post-hoc test shows a significant increase in number of ripple events per minute only at the end of 36 °C 1st step ($p_{36\_1st\_end}$ = 0.0062), but the same trend was seen at the start of 36 °C 1st step ($p_{36\_1st\_start}$ = 0.039) and other temperatures ($p_{38\_1st\_end}$ = 0.037). All ripple parameters were significantly affected by temperature or showed a tendency for a temperature effect at both time points (ripple amplitude, duration, frequency, ripple peaks per ripple event, number of ripple events per minute, $p_{temperature}$ < 0.0001 at start and end of temperature steps; ripple power $p_{temperature}$ = 0.053 at start, < 0.0001 at end). Figure 23 shows ripple events from TRPV1 KO and WT slices from the initial minutes at 36 °C 1st, with increased duration and number of ripple peaks per event in the TRPV1 KOs, while Figure 24 shows a 10 s ripple trace during the last minutes at 36 °C 1st to indicate the increased incidence of ripple events in the TRPV1 KOs.

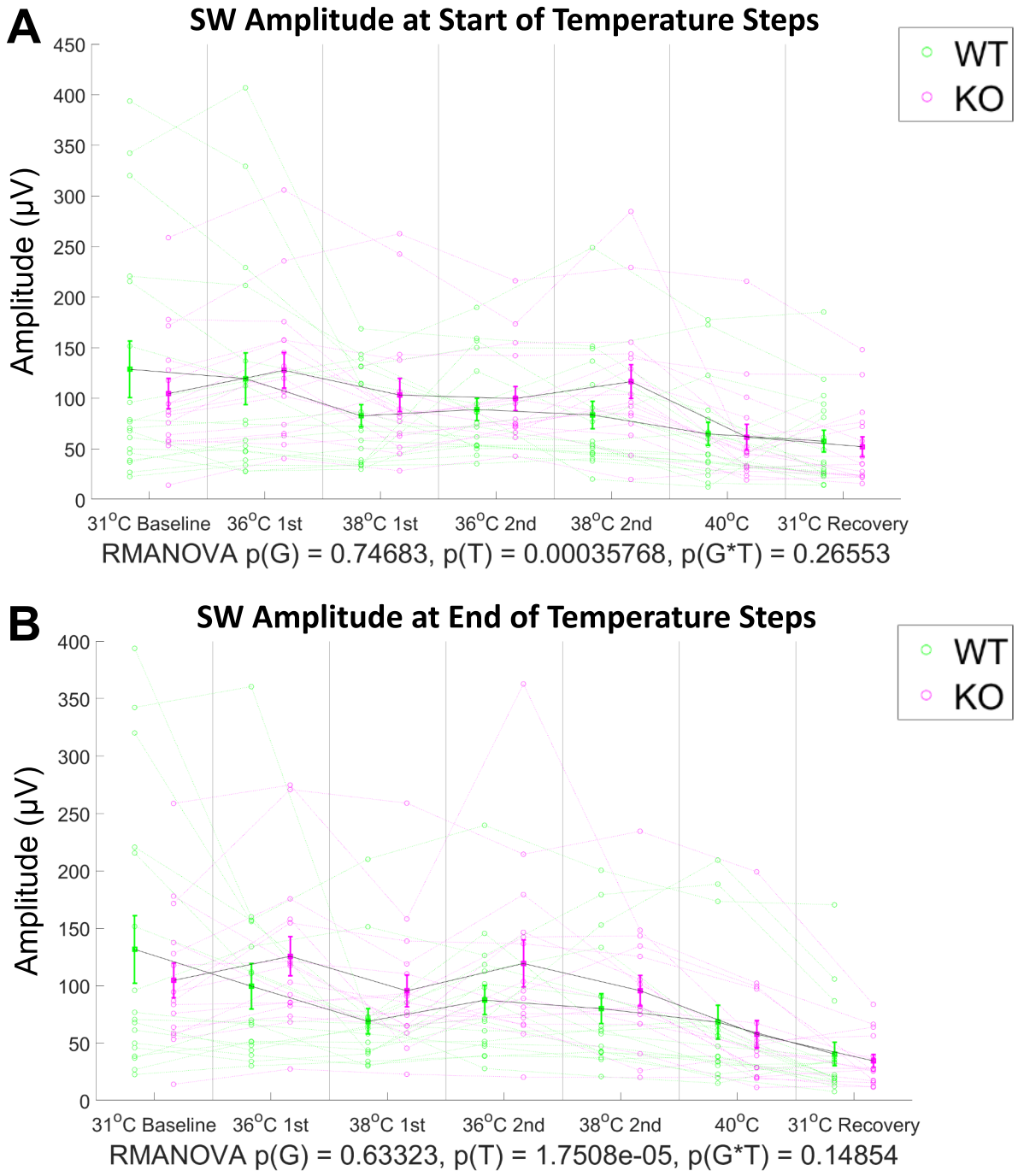

Figure 12: SW amplitude was similar in WT and TRPV1 KO slices. There was no significant effect of genotype on SW amplitude at any temperature. Results are shown for both **(A)** the initial minutes that each temperature was reached and **(B)** the last minutes at each temperature. At both time points, temperature had a significant effect on both genotypes, as SW amplitude seemed to decrease across the experiment. Graphs show mean and SEM with individual values. N_{start} = 18 WT (green), 16 KO (magenta) slices, N_{end} = 17 WT, 16 KO slices from 7 WT and 8 KO mice. The results of the RMANOVAs are shown at the bottom: p(G) = main effect of genotype, p(T) = main effect of temperature, p(G*T) = genotype * temperature interaction effect.

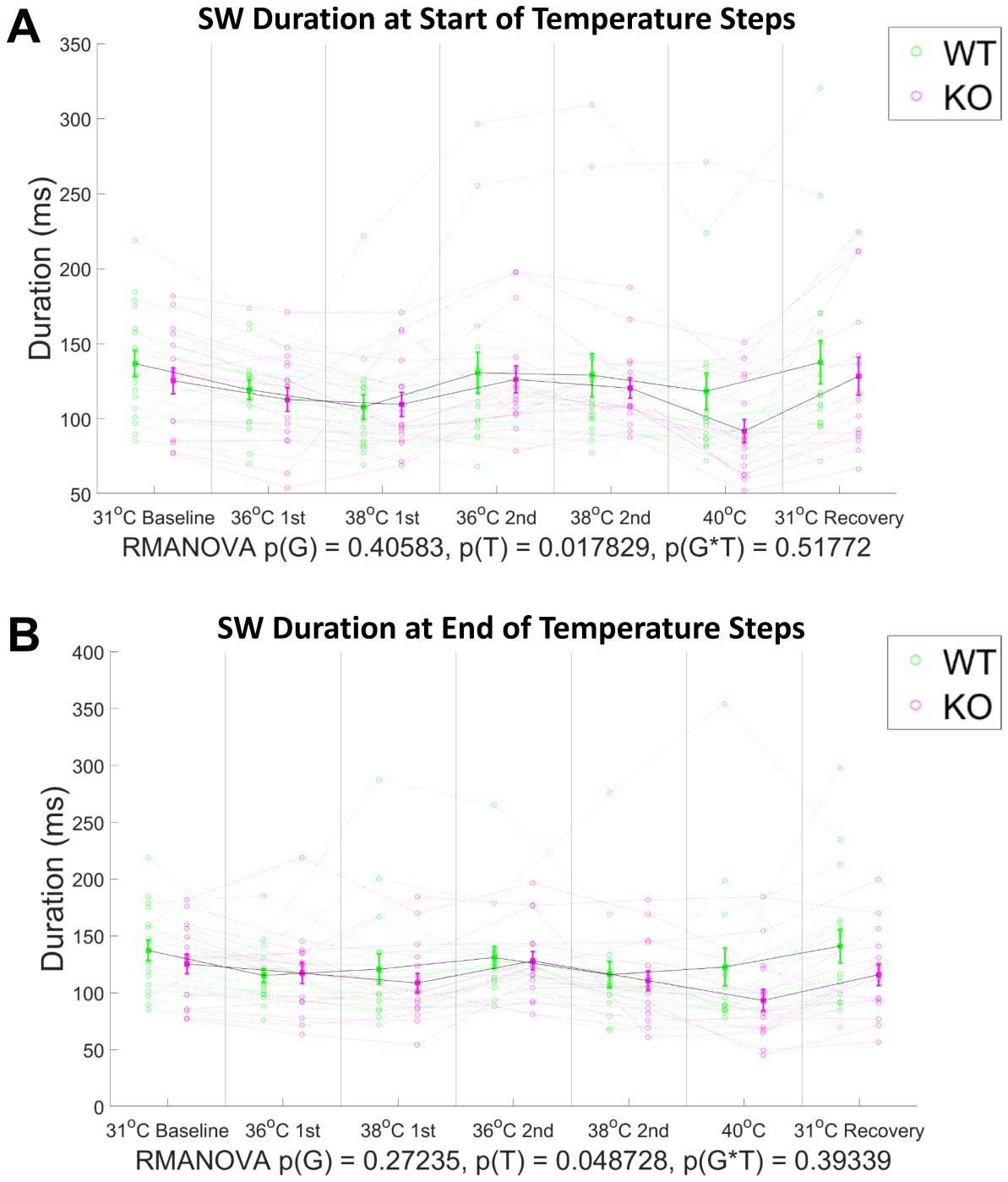

Figure 13: SW duration was similar in WT and TRPV1 KO slices. There was no significant effect of genotype on SW duration at any temperature. Results are shown for both **(A)** the initial minutes after each temperature was reached and **(B)** the last minutes at each temperature. At both time points, temperature had a significant effect independent of genotype. Graphs show mean and SEM with individual values. N_{start} = 18 WT (green), 16 KO (magenta) slices, N_{end} = 17 WT, 16 KO slices from 7 WT and 8 KO mice. The results of the RMANOVAs are shown at the bottom: p(G) = main effect of genotype, p(T) = main effect of temperature, p(G*T) = genotype * temperature interaction effect.

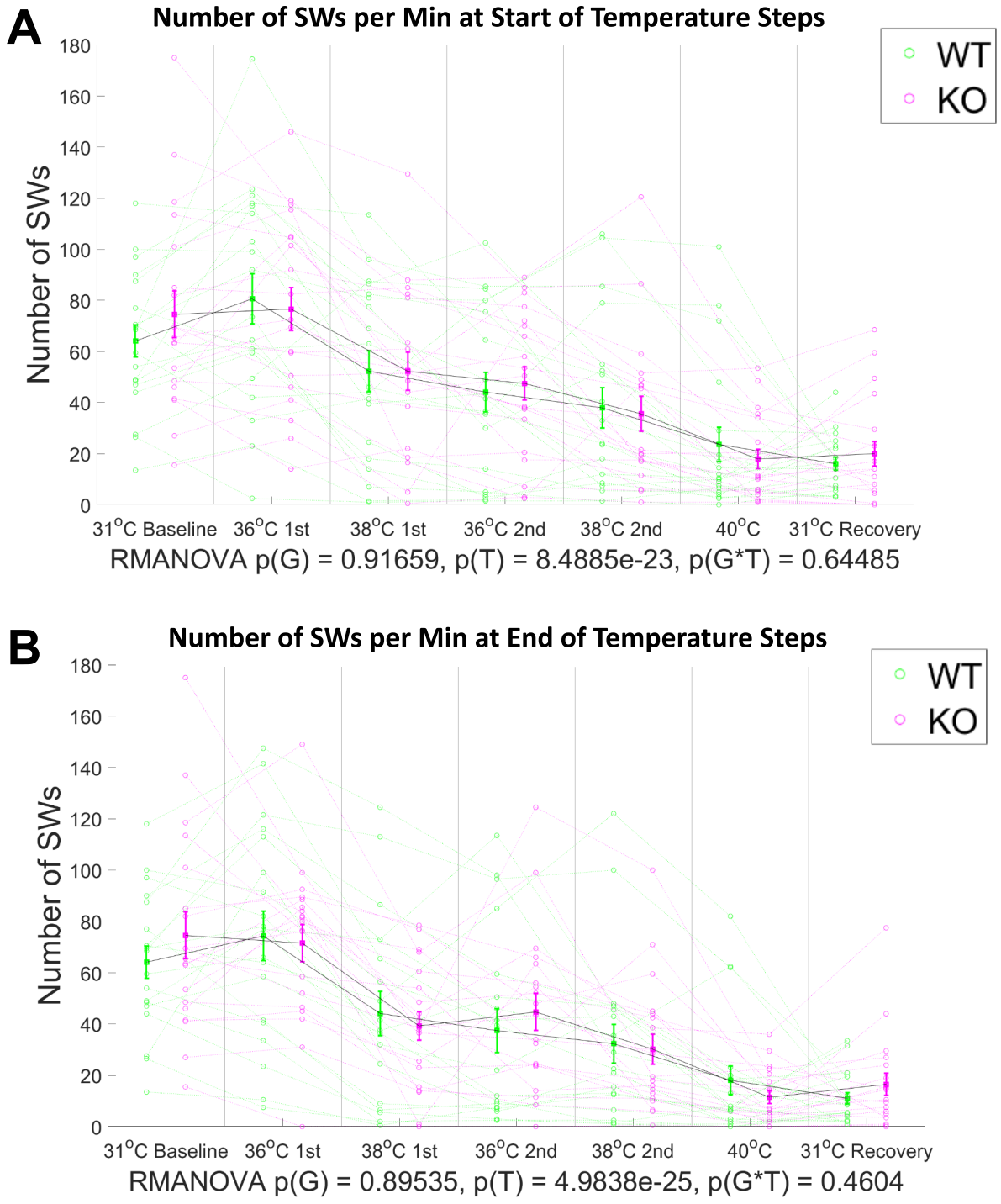

Figure 14: The number of SWs per minute was similar in WT and TRPV1 KO slices. There was no significant effect of genotype on SW rate of occurrence at any temperature. Results are shown for both **(A)** the initial minutes after each temperature was reached and **(B)** the last minutes at each temperature. At both time points, temperature had a significant effect independent of genotype as rate decreased across the experiment. Graphs show mean and SEM with individual values. N = 19 WT (green) and 19 KO (magenta) slices from 7 WT and 8 KO mice. The results of the RMANOVAs are shown at the bottom: p(G) = main effect of genotype, p(T) = main effect of temperature, p(G*T) = genotype * temperature interaction effect.

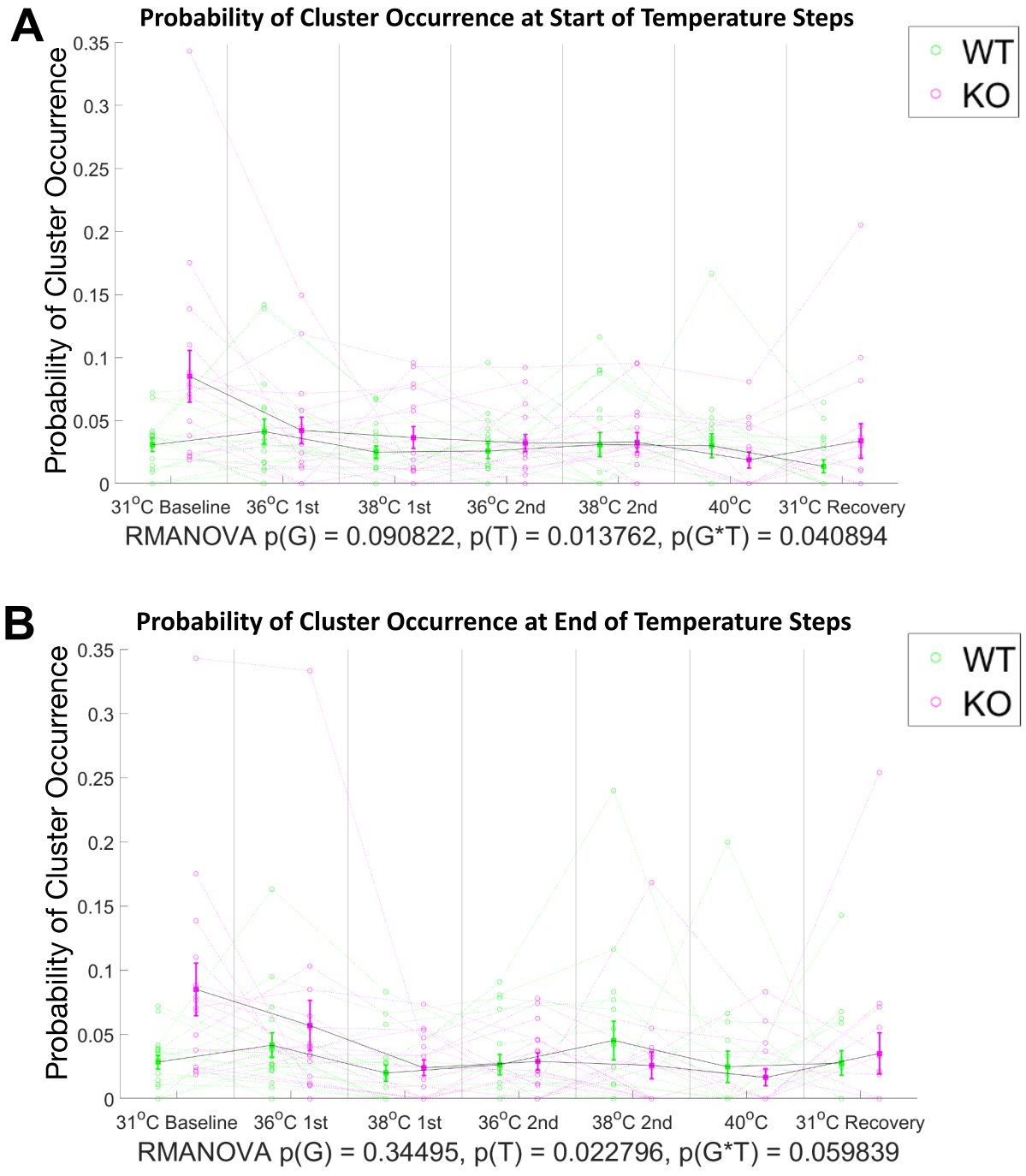

Figure 15: The probability of SW cluster occurrence tended to be higher in the TRPV1 KOs at specific temperatures. Results are shown for **(A)** the initial minutes after each temperature was reached and **(B)** the last minutes at each temperature. Initially, there was a tendency for an effect of genotype, which was not there at the end of temperature steps. The interaction of genotype and temperature was significant at the start, with a similar tendency at the end of temperature steps. This is because at some temperatures the probability of SW occurrence was higher in KO slices, but not in others. The effect seemed to be mainly at 31 °C baseline, but the result of the Bonferroni post-hoc test was not significant at any specific temperature (but $p_{31\_baseline}$ is 0.0107 at start and 0.0097 at end of temperature steps, with $alpha_{Bonferroni}$ = 0.05/7 = 0.00714). Graphs show mean and SEM with individual values. N_{start} = 18 WT (green), 16 KO (magenta) slices, N_{end} = 17 WT, 16 KO slices

from 7 WT and 8 KO mice. The results of the RMANOVAs are shown at the bottom: p(G) = main effect of genotype, p(T) = main effect of temperature, p(G*T) = genotype * temperature interaction effect.

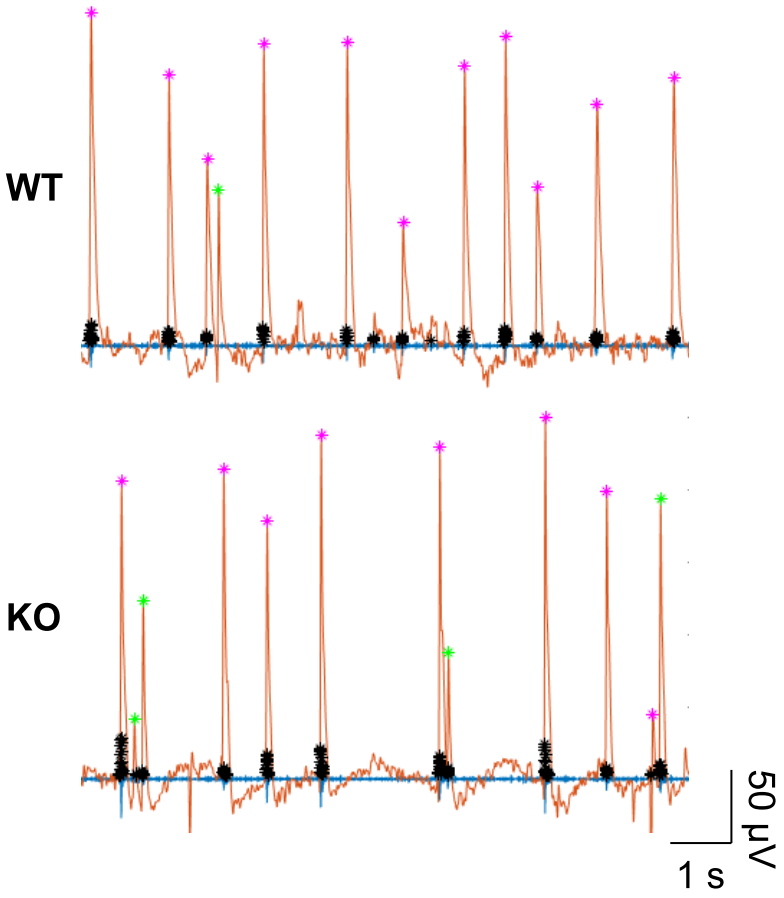

Figure 16: Representative SWR traces from a WT and a TRPV1 KO slice at 31 °C baseline. Both blue and orange traces were high-pass filtered at 0.5 Hz. Orange trace was then low-pass filtered at 40 Hz showing SWs, while the blue trace was bandpass filtered at 140-250 Hz, isolating ripples. Asterisks indicate SWs (pink = primary, green = secondary SWs of a cluster) and ripple (black) peaks detected by the code. A 10-second snippet is shown from each genotype. Notice the increased incidence of secondary SWs, and hence SW clusters, in the KO slice (probability of cluster for this slice = 0.079) compared to the WT slice (probability of cluster for this slice = 0.03).

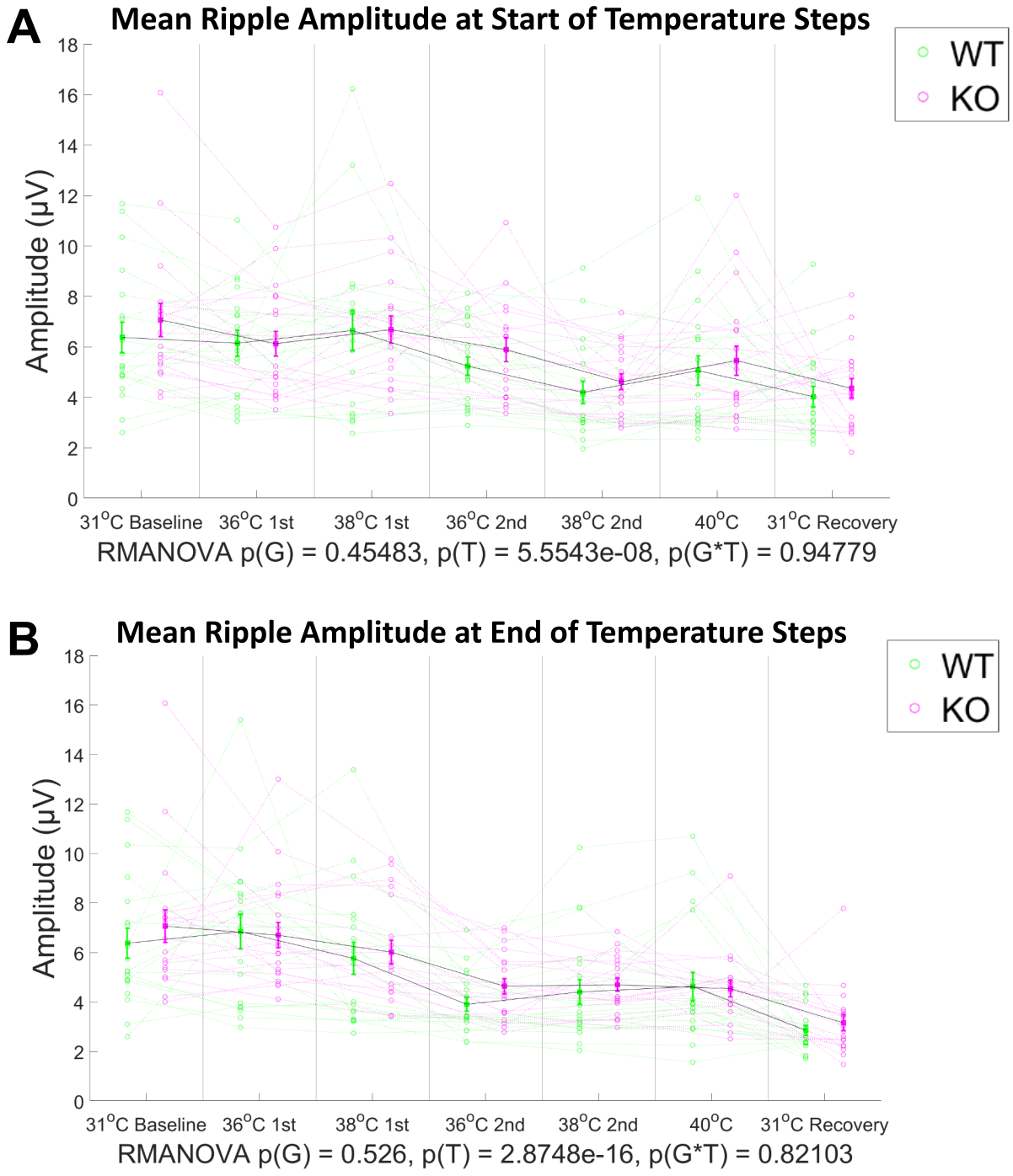

Figure 17: Mean ripple amplitude was similar in WT and TRPV1 KO slices. There was no significant effect of genotype on ripple amplitude at any temperature. Results are shown for both **(A)** the initial minutes after each temperature was reached and **(B)** the last minutes at each temperature. At both time points, temperature had a significant effect independent of genotype, as ripple amplitude decreased across the experiment. Graphs show mean and SEM with individual values. N = 19 WT (green) and 19 KO (magenta) slices from 7 WT and 8 KO mice. The results of the RMANOVAs are shown at the bottom: p(G) = main effect of genotype, p(T) = main effect of temperature, p(G*T) = genotype * temperature interaction effect.

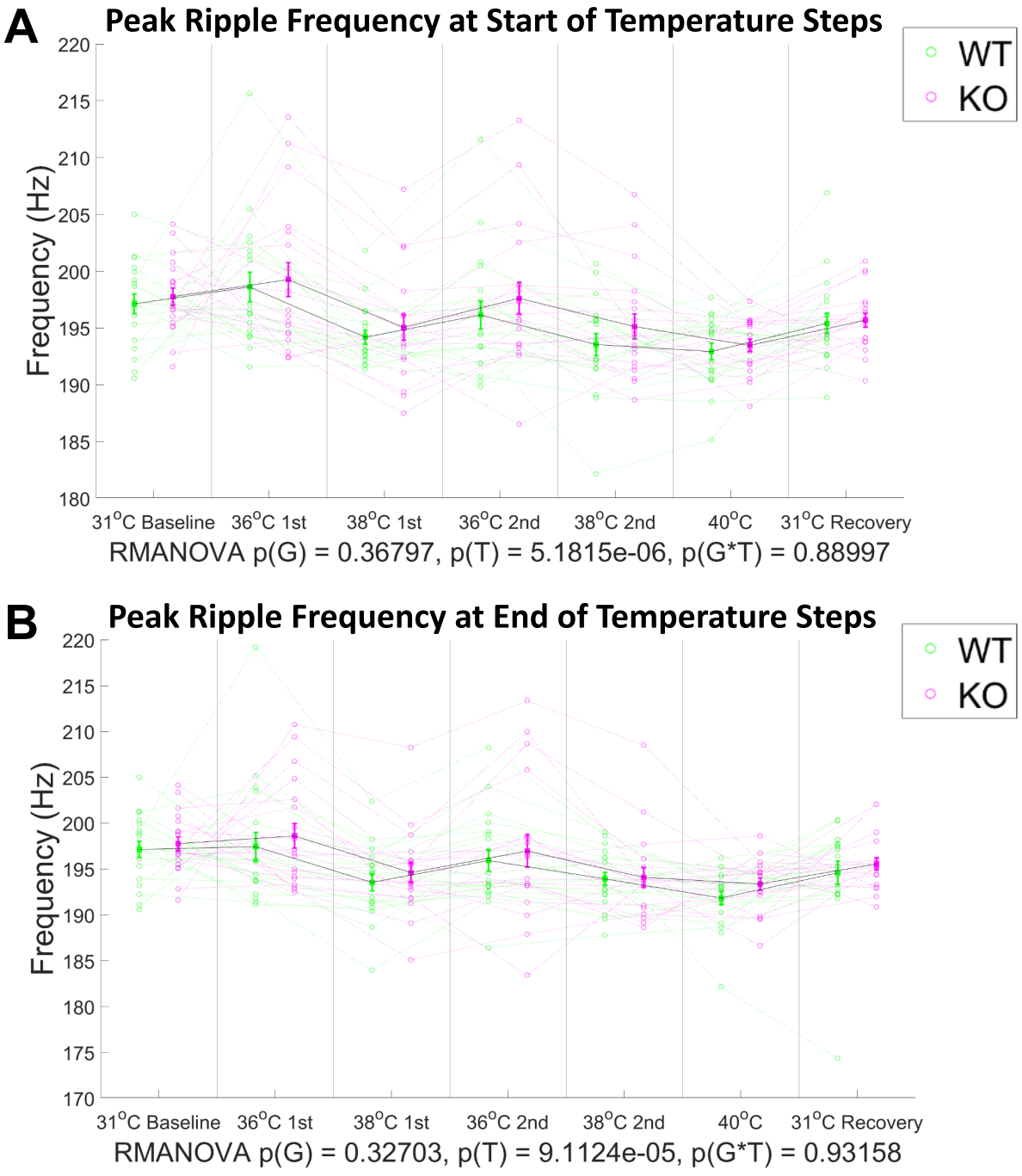

Figure 18: Peak ripple frequency was similar in WT and TRPV1 KO slices. There was no significant effect of genotype on peak ripple frequency at any temperature. Results are shown for both **(A)** the initial minutes after each temperature was reached and **(B)** the last minutes at each temperature. At both time points, temperature had a significant effect independent of genotype. Graphs show mean and SEM with individual values. N = 19 WT (green) and 19 KO (magenta) slices from 7 WT and 8 KO mice. The results of the RMANOVAs are shown at the bottom: p(G) = main effect of genotype, p(T) = main effect of temperature, p(G*T) = genotype * temperature interaction effect.

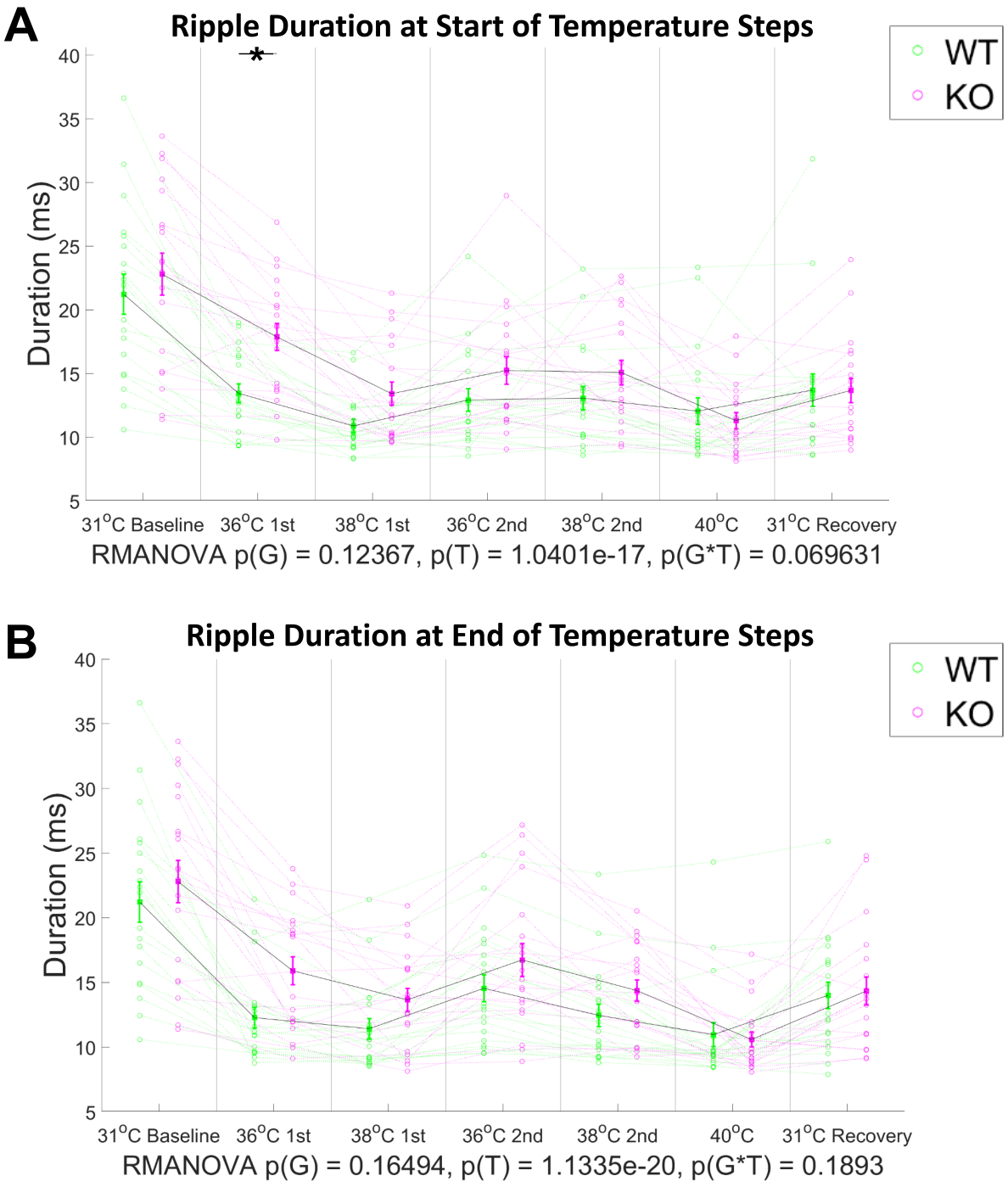

Figure 19: TRPV1 KO slices had longer ripples at specific temperatures. Results are shown for both **(A)** the initial minutes after each temperature was reached and **(B)** the last minutes at each temperature. At the initial minutes at each temperature step, there was a tendency for an interaction effect between genotype and temperature and the comparison between genotypes at 36 °C 1st was significant after Bonferroni correction ($p_{36\_1st\_start}$ = 0.0017). The same tendency was seen at the end of 36 °C 1st ($p_{36\_1st\_end}$ = 0.0108) and other temperatures ($p_{38\_1st\_start}$ = 0.021). At both time points, temperature had a significant effect. Graphs show mean and SEM with individual values. N = 19 WT (green) and 19 KO (magenta) slices from 7 WT and 8 KO mice. The results of the RMANOVAs are

shown at the bottom: p(G) = main effect of genotype, p(T) = main effect of temperature, p(G*T) = genotype * temperature interaction effect, * = p < 0.00714.

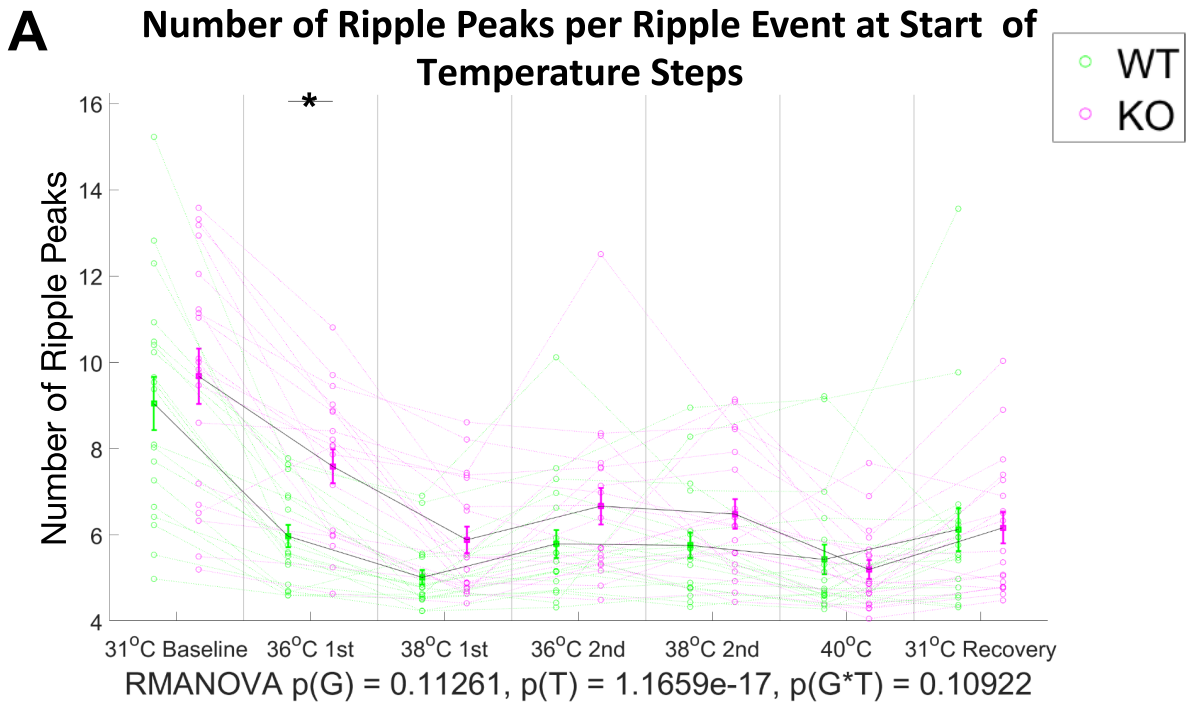

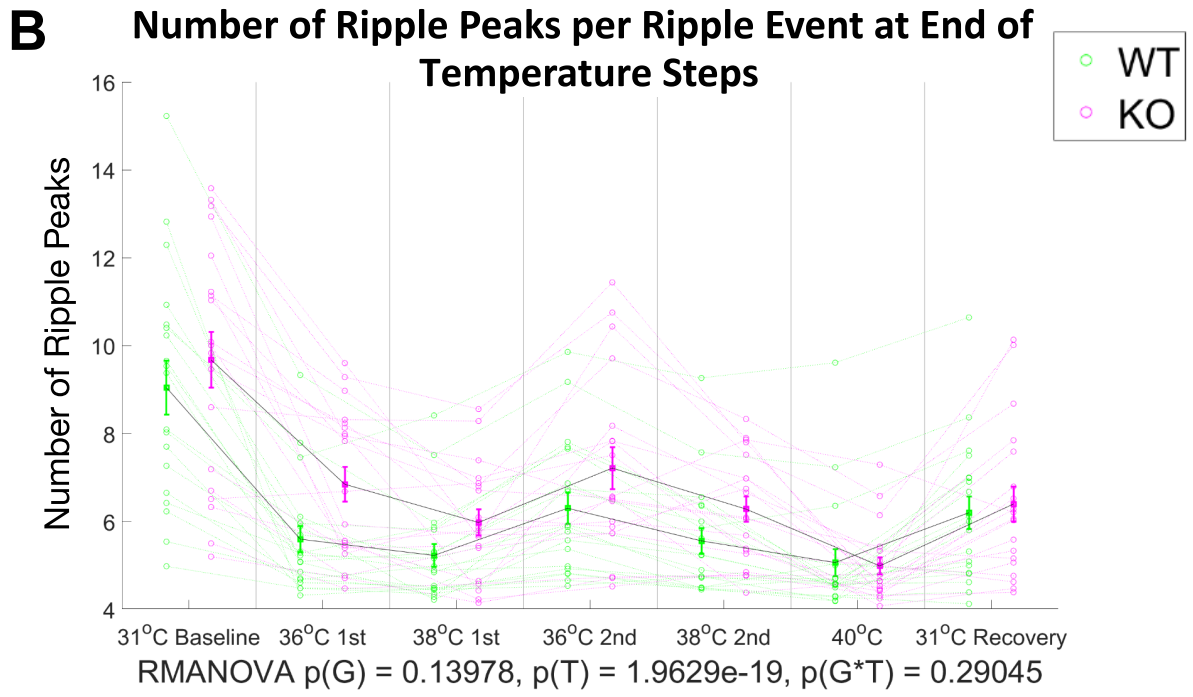

Figure 20: TRPV1 KO slices had more ripple peaks per ripple event at specific temperatures. Results are shown for both **(A)** the initial minutes after each temperature was reached and **(B)** the last minutes at each temperature. At the start of the 36 °C 1st step, the post-hoc test showed significantly more peaks in KO ripples ($p_{36\_1st\_start}$ = 0.0015), but the RMANOVA showed only a significant effect of temperature and not genotype. The same trend was seen at other temperatures (e.g., $p_{38\_1st\_start}$ =

0.018 with $alpha_{Bonferroni}$ = 0.05/7 = 0.00714) and at the second time point ($p_{36\_1st\_end}$ = 0.0164). Graphs show mean and SEM with individual values. N = 19 WT (green) and 19 KO (magenta) slices from 7 WT and 8 KO mice. The results of the RMANOVAs are shown at the bottom: p(G) = main effect of genotype, p(T) = main effect of temperature, p(G*T) = genotype * temperature interaction effect, * = p < 0.00714.

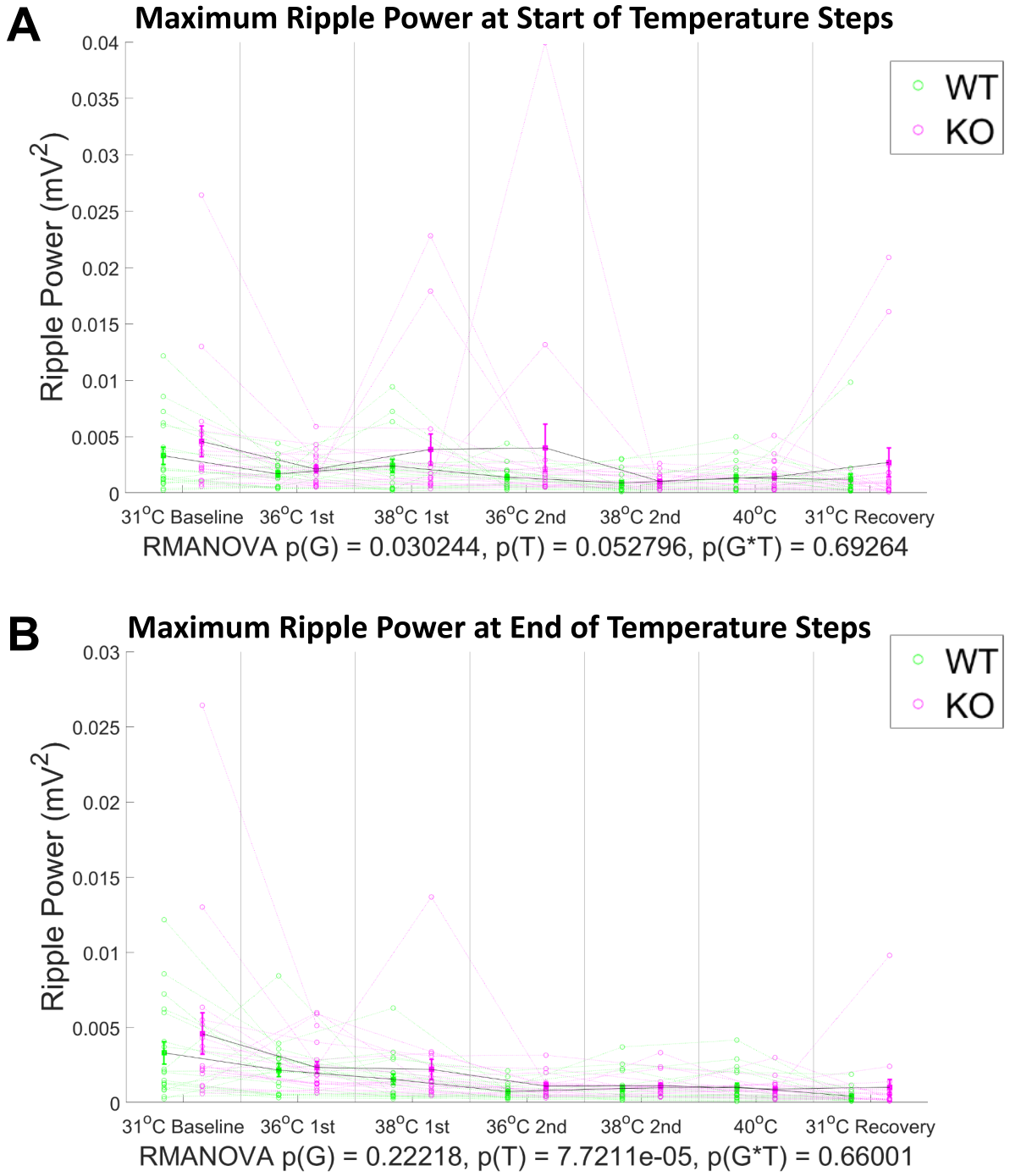

Figure 21: TRPV1 KO slices had higher maximum ripple power during the initial minutes at each temperature. Maximum ripple power is shown for **(A)** the initial minutes after each temperature was reached and **(B)** the last minutes at each temperature. When the initial minutes after each

temperature step was reached were examined, there was a significant effect of genotype due to KOs having higher power throughout the experiment, but after Bonferroni correction no differences were identified at specific temperatures. The effect of temperature on power was only significant at the end time point, but the tendency was also there at the start of temperature steps. In both, ripple power seemed to decrease throughout the experiment. Graphs show mean and SEM with individual values. N = 19 WT (green) and 19 KO (magenta) slices from 7 WT and 8 KO mice. The results of the RMANOVAs are shown at the bottom: p(G) = main effect of genotype, p(T) = main effect of temperature, p(G*T) = genotype * temperature interaction effect.

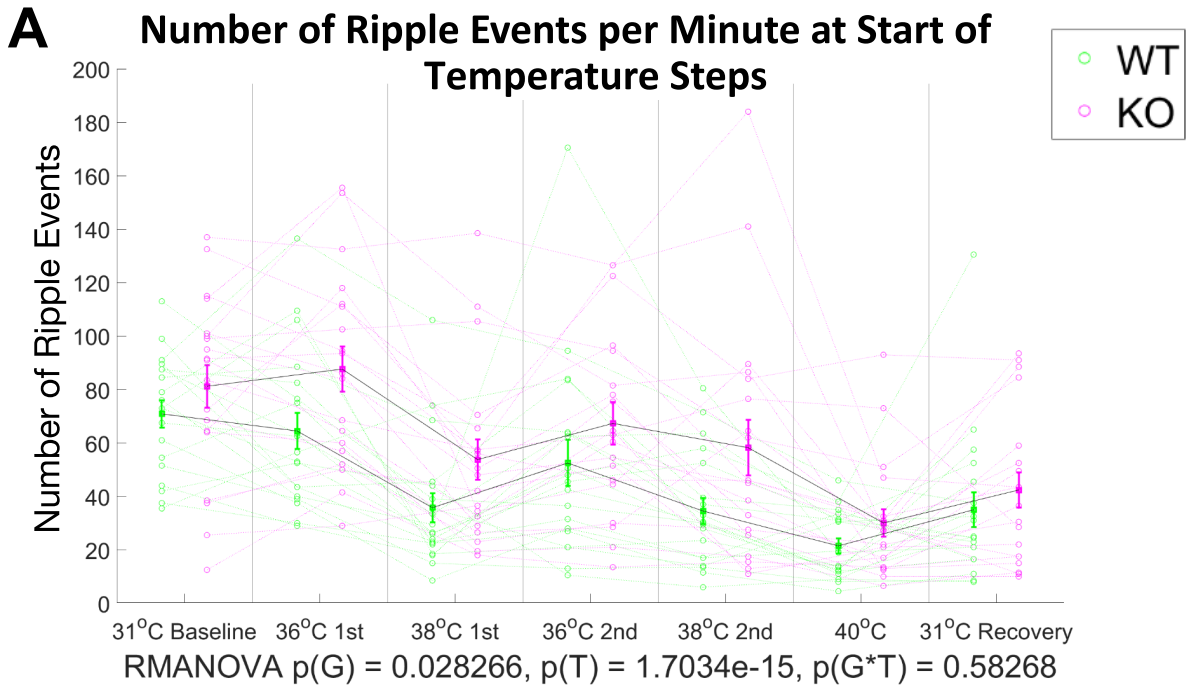

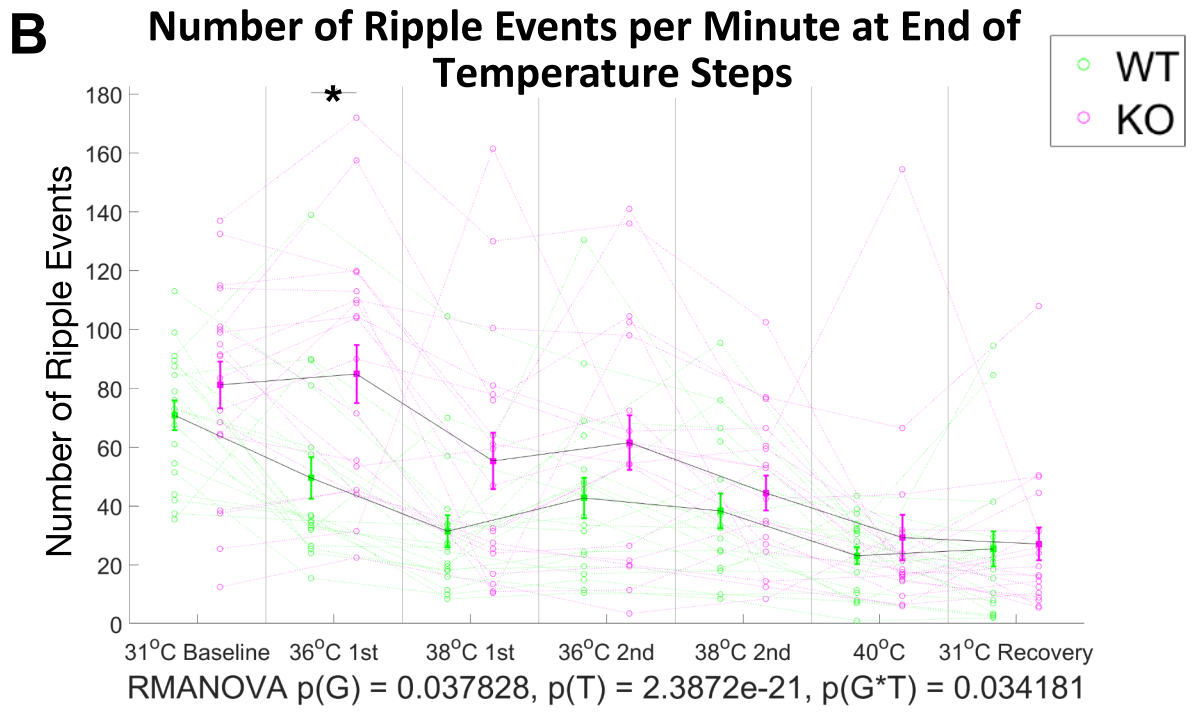

Figure 22: TRPV1 KO slices had more ripple events per minute at most temperatures. Results are shown for both **(A)** the initial minutes after each temperature was reached and **(B)** the last minutes at each temperature. The RMANOVA identified a significant effect of genotype at both time points and a significant genotype*temperature interaction effect at the second time point, denoting that the effect was stronger in some and weaker in other temperatures. The Bonferroni post-hoc test identified a significantly higher ripple occurrence only at 36 °C 1st at the second time point ($p_{36\_1st\_end}$ = 0.0062), but the same trend was seen at the first time point and other temperatures ($p_{36\_1st\_start}$ = 0.039, $p_{38\_1st\_end}$ = 0.037 with $alpha_{Bonferroni}$ = 0.05/7 = 0.00714). The effect of temperature was significant at both time points. Graphs show mean and SEM with individual values. N = 19 WT (green) and 19 KO (magenta) slices from 7 WT and 8 KO mice. The results of the RMANOVAs are shown at the bottom: p(G) = main effect of genotype, p(T) = main effect of temperature, p(G*T) = genotype * temperature interaction effect, * = p < 0.00714.

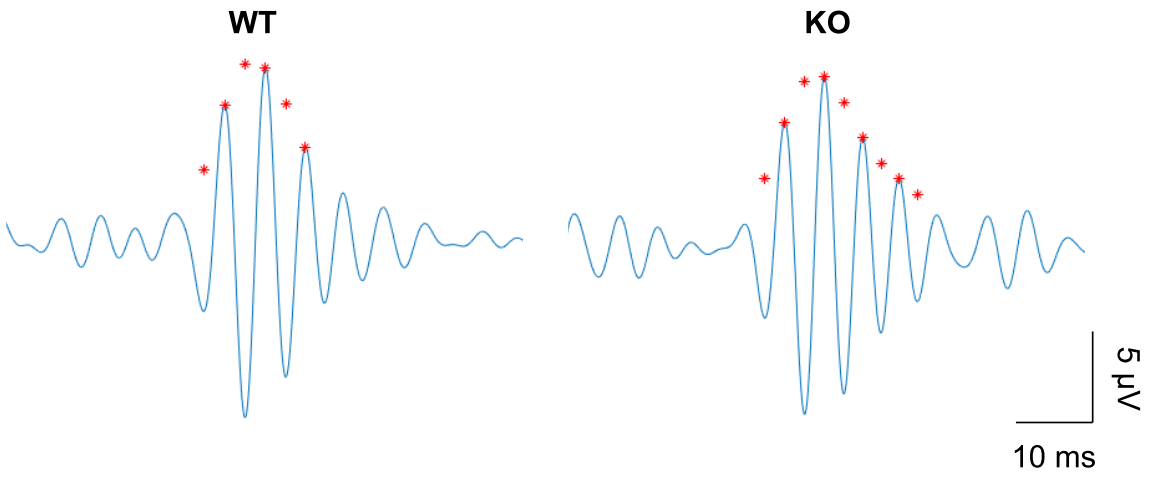

Figure 23: Representative ripple events from TRPV1 KO and WT slices at 36 °C 1st start. The LFP was first high-pass filtered at 0.5 Hz and then bandpass filtered at 140-250 Hz to isolate ripples. A representative ripple event example from each recording is shown. Red asterisks indicate ripple peaks detected by the code. Notice the increased ripple duration and number of ripple peaks per ripple event for KO ripples (mean for this slice: duration = 17 ms, number of ripple peaks per ripple event = 9.4) compared to WT ripple events (mean for this slice: duration = 10 ms, number of ripple peaks per ripple event = 5.6).

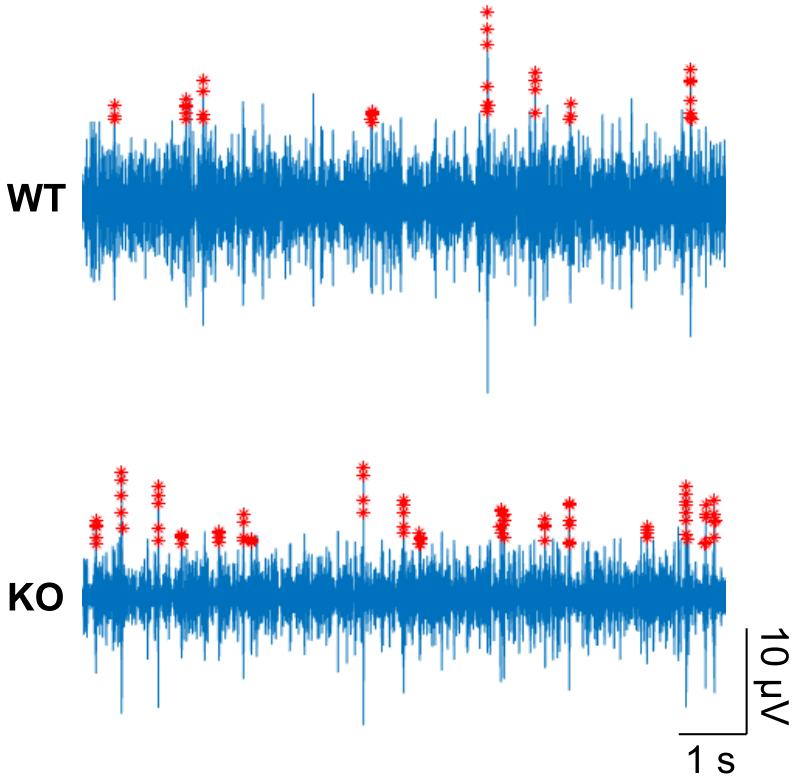

Figure 24: Representative ripple traces from TRPV1 KO and WT slices at 36 °C 1st end. LFP was first high-pass filtered at 0.5 Hz and then bandpass filtered at 140-250 Hz to isolate ripples. Red asterisks indicate ripple peaks detected by the code. A 10-second snippet is shown from each slice after at least 18 minutes at 36 °C for the first time. Notice the increased number of ripple events in the KO recording (mean for this slice = 104 events per minute) compared to the WT one (mean for this slice = 58 events per minute).

3.1.2 Effect of TRPV1 KO on oscillations and single unit recordings in vivo

3.1.2.1 In vivo LFP recordings from TRPV1 KO and WT mice

To compare SWRs in TRPV1 KO and WT mice in vivo, we recorded from tetrodes in dorsal CA1 over 3-10 days. Each recording session consisted of 5 phases: rest 1 (r1) in the home cage, a 20-minute exploration of open field 1 (of1), a 20-minute exploration of open field 2 (of2), a second 20-minute exploration of open field 1 (called for simplicity of3), and finally a second rest (r2) in the home cage. This allows analysis of SWRs in novel (day 1) and familiar (day 2-10) conditions during rest periods before (r1) and after (r2) exploration (tetrodes were not lowered between recording days 1 and 2, hoping to record the same cells across novel and familiar conditions, but were lowered each subsequent day to sample additional populations of cells). It also allows analysis of theta and delta oscillations, properties of pyramidal cells, place cells, and interneurons in single-unit recordings, and remapping (comparing of1 to of2) and stability (comparing of1 to of3) of place fields.

3.1.2.1.1 Effect of TRPV1 KO on SWRs

For SWRs, only rest sessions were analyzed.

3.1.2.1.1.1 SWRs in novel environments

The average ripple waveform for WT and KO mice and individual heatmaps for each mouse in r1 and r2 can be seen in Figure 25. No significant differences between TRPV1 KO and WT animals were seen in the z-score of the maximum ripple peak, a measure of ripple magnitude that represents ripple amplitude normalized to the standard deviation, or in ripple duration, or rate of occurrence (Figure 26A, B, C). Ripple magnitude and duration were similar between rest sessions, while ripple rate was higher in r2 for both WT and KO mice ($p_{rest\_session}$ = 0.0004, $p_{Šídák's\_WT}$ = 0.0140, $p_{Šídák's\_KO}$ = 0.0019). Parameters were measured during periods of immobility (velocity < 2 cm/s) and ripple rate was calculated for the time each mouse spent immobile. As a control, we decided to also test if the percentage of time WT and TRPV1 KO mice spent immobile was similar. WT mice spent significantly more time immobile in r2 compared to r1 ($p_{rest\_session}$ = 0.018, $p_{Šídák's\_WT}$ = 0.034), but no significant differences between genotypes were seen (Figure 26D).

No differences were seen between genotypes in power spectral densities for ripple frequencies (Figure 27A, B). Peak ripple frequency in KO animals was slightly but significantly higher during r2 compared to r1 ($p_{rest\_session}$ = 0.033, $p_{Šídák's\_KO}$ = 0.013; Figure 27C). Peak ripple power was similar between rest sessions, but there was a significant interaction between genotype and rest session ($p_{genotype*rest\_session}$ = 0.0092; Figure 27D) due to KOs having increased ripple power in r2 compared to r1 and WTs having decreased ripple power in r2 compared to r1. However, the differences in each genotype alone were not significant in the post-hoc test.

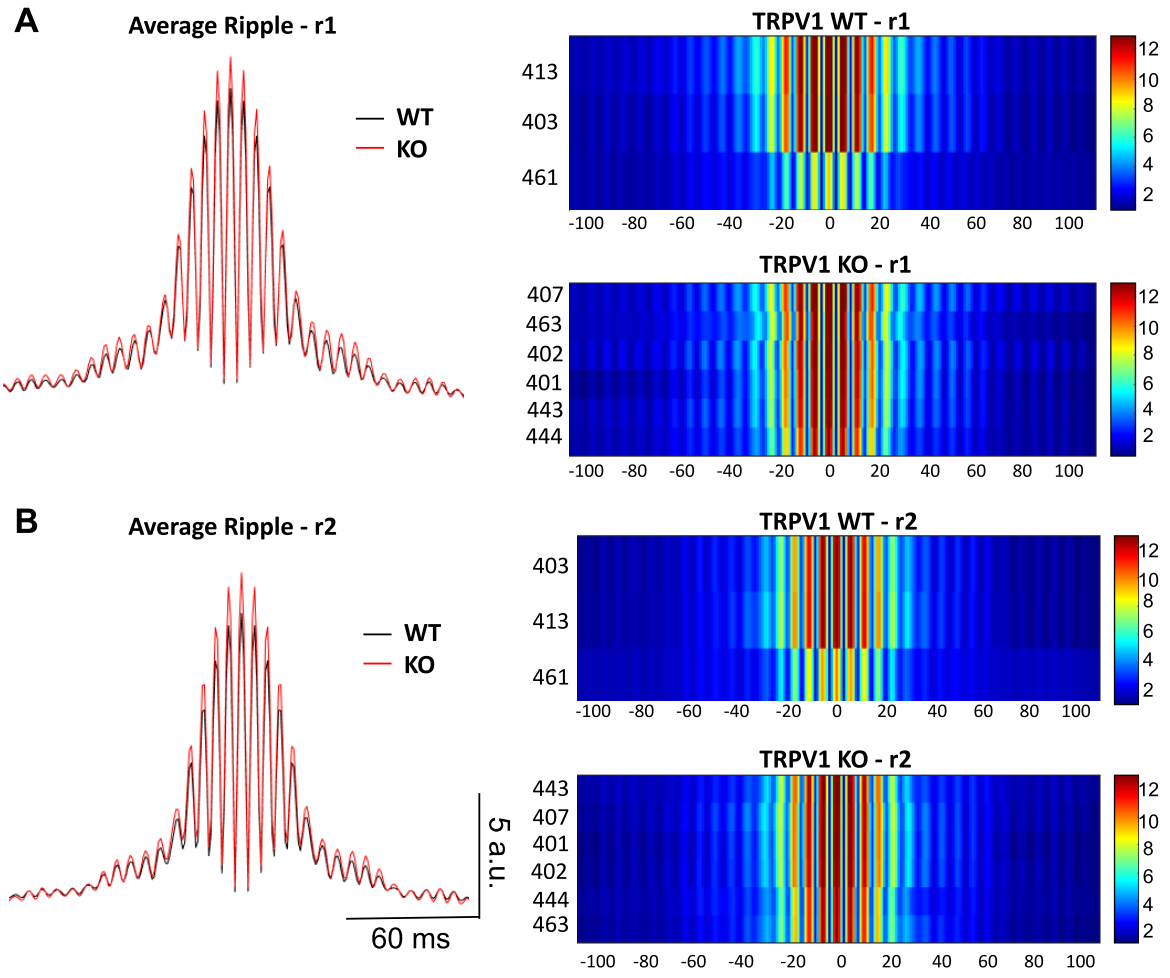

Figure 25: SWRs in novel environments - Ripples in TRPV1 KO and WT mice. Averaged ripple z-score waveform (left) in WT (black) and TRPV1 KO (red) mice and individual ripple heatmaps for three WT (right, top) and six KO (right, bottom) mice recorded during **(A)** r1 and during **(B)** r2. Heatmaps are sorted from highest to lowest ripple magnitude, with mouse number indicated on the y-axis and ms on the x-axis, centered on maximum ripple peak.

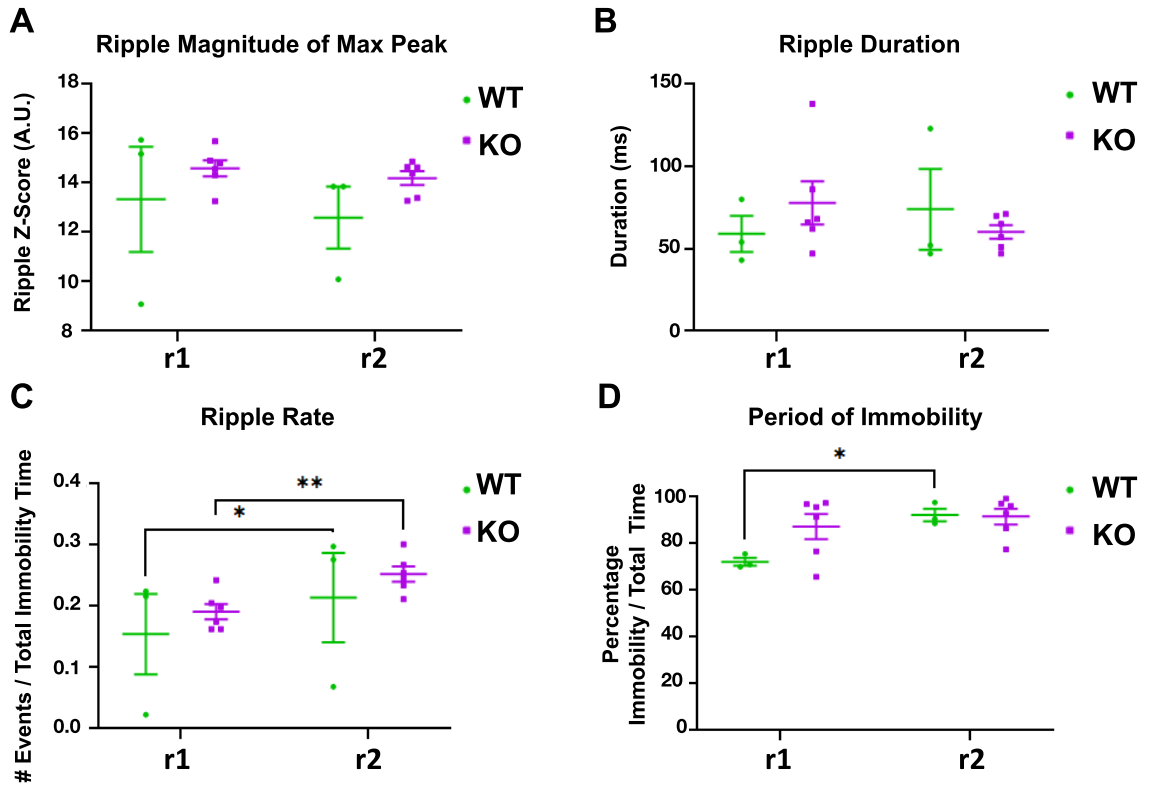

Figure 26: SWRs in novel environments - No significant differences in ripple magnitude, duration, and rate of occurrence between TRPV1 KO and WT mice. (A) The z-score of the maximum ripple peak showed no significant differences between genotypes or rest sessions ($p_{genotype}$ = 0.2621, $p_{rest\_session}$ = 0.1784, $p_{genotype*rest\_session}$ = 0.6605). **(B)** Ripple duration was not different between genotypes or rest sessions ($p_{genotype}$ = 0.8327, $p_{rest\_session}$ = 0.9318, $p_{genotype*rest\_session}$ = 0.3132). **(C)** The rate of ripple occurrence was not significantly different between genotypes, but it increased for both in r2 compared to r1 ($p_{genotype}$ = 0.4602, $p_{rest\_session}$ = 0.0004, $p_{genotype*rest\_session}$ = 0.9344). **(D)** The period of immobility (velocity < 2 cm/s) was not significantly different between genotypes, even though there was a significant increase in r2 compared to r1 for WTs ($p_{genotype}$ = 0.2223, $p_{rest\_session}$ = 0.0181, $p_{genotype*rest\_session}$ = 0.0866). Graphs show mean and SEM, N = 3 WT (green), 6 KO (magenta) mice. The RMANOVA test was used for all parameters. Significant lines indicate the results of the Šídák's post-hoc tests with correction for multiple comparisons, * = $p < 0.05$, ** = $p < 0.01$.

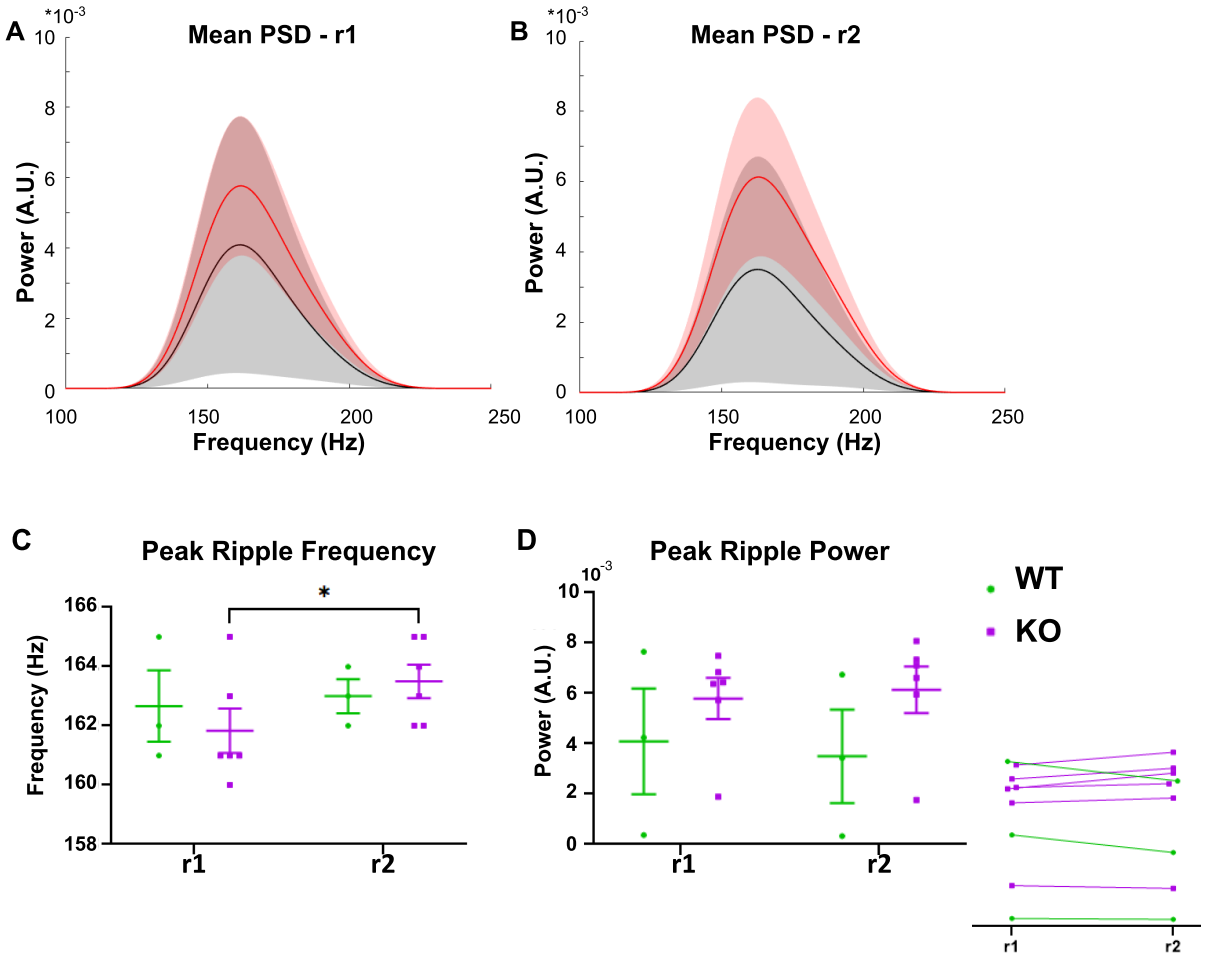

Figure 27: SWRs in novel environments - No significant differences in peak ripple frequency and power between WT and TRPV1 KO mice. Averaged power spectral density and standard deviation for each genotype, with WT in black and TRPV1 KO in red, during **(A)** rest session 1 and **(B)** rest session 2. **(C)** Peak ripple frequency was similar between WT and TRPV1 KO mice. A significant increase in peak ripple frequency is seen in r2 compared to r1, in TRPV1 KO mice ($p_{genotype}$ = 0.8823, $p_{rest\_session}$ = 0.0331, $p_{genotype*rest\_session}$ = 0.1211). **(D)** Peak ripple power was not different between genotypes or rest sessions. A significant interaction between genotype and rest session was seen, as peak ripple power increased for KOs and decreased for WTs in r2 compared to r1, as seen in the insert ($p_{genotype}$ = 0.2700, $p_{rest\_session}$ = 0.3893, $p_{genotype*rest\_session}$ = 0.0092). Graphs show mean and SEM, N = 3 WT (green), 6 KO (magenta) mice. The RMANOVA test was used for all parameters. Significant lines indicate the results of the Šídák's post-hoc tests with correction for multiple comparisons, * = $p < 0.05$.

3.1.2.1.1.2 SWRs in familiar environments

The average z-score waveform (Figure 28) indicates that ripples in TRPV1 KO mice were significantly larger ($p_{genotype}$ = 0.0011; Figure 29A), an effect that was significant in the post-hoc test for both r1 and r2 ($p_{Šídák's\_r1}$ = 0.0005, $p_{Šídák's\_r2}$ = 0.0163). There was also a decrease in ripple magnitude in r2 compared to r1 ($p_{rest\_session}$ = 0.0016; Figure 29A), which the post-hoc test suggested was due to a

decrease in TRPV1 KO ripple magnitude ($p_{Šídák's\_KO}$ = 0.0005). As in the novel environment, no significant differences between TRPV1 KO and WT animals were seen for ripple duration (Figure 29B) or rate, and ripple rate increased in r2 compared to r1, especially in TRPV1 KO mice according to the post-hoc test ($p_{rest\_session}$ = 0.0063, $p_{Šídák's\_KO}$ = 0.013; Figure 29C). There was no difference in the percentage of time WT and TRPV1 KO mice spent immobile, with velocity < 2 cm/s (Figure 29D).

Power spectral densities for WT and TRPV1 KO mice during r1 and r2 indicate that peak ripple frequency was higher in TRPV1 KO mice in r2 ($p_{Šídák's\_r2}$ < 0.0001), but not r1 (unlike in the novel condition, where there was no difference between genotypes). Both WT and TRPV1 KO mice had higher peak ripple frequency in r2 compared to r1 ($p_{genotype}$ = 0.0001, $p_{rest\_session}$ < 0.0001, $p_{genotype*rest\_session}$ < 0.0001, $p_{Šídák's\_WT}$ < 0.0001 , $p_{Šídák's\_KO}$ < 0.0001; Figure 30A, B, C). No difference between genotypes was seen in peak ripple power, which was lower during r2 in both WT and TRPV1 KO mice ($p_{rest\_session}$ < 0.0001, $p_{Šídák's\_WT}$ < 0.0001, $p_{Šídák's\_KO}$ < 0.0001). A significant interaction effect was seen, probably because ripple power in WT mice was higher in r1 but lower in r2 compared to TRPV1 KO mice ($p_{genotype*rest\_session}$ = 0.008; Figure 30D).

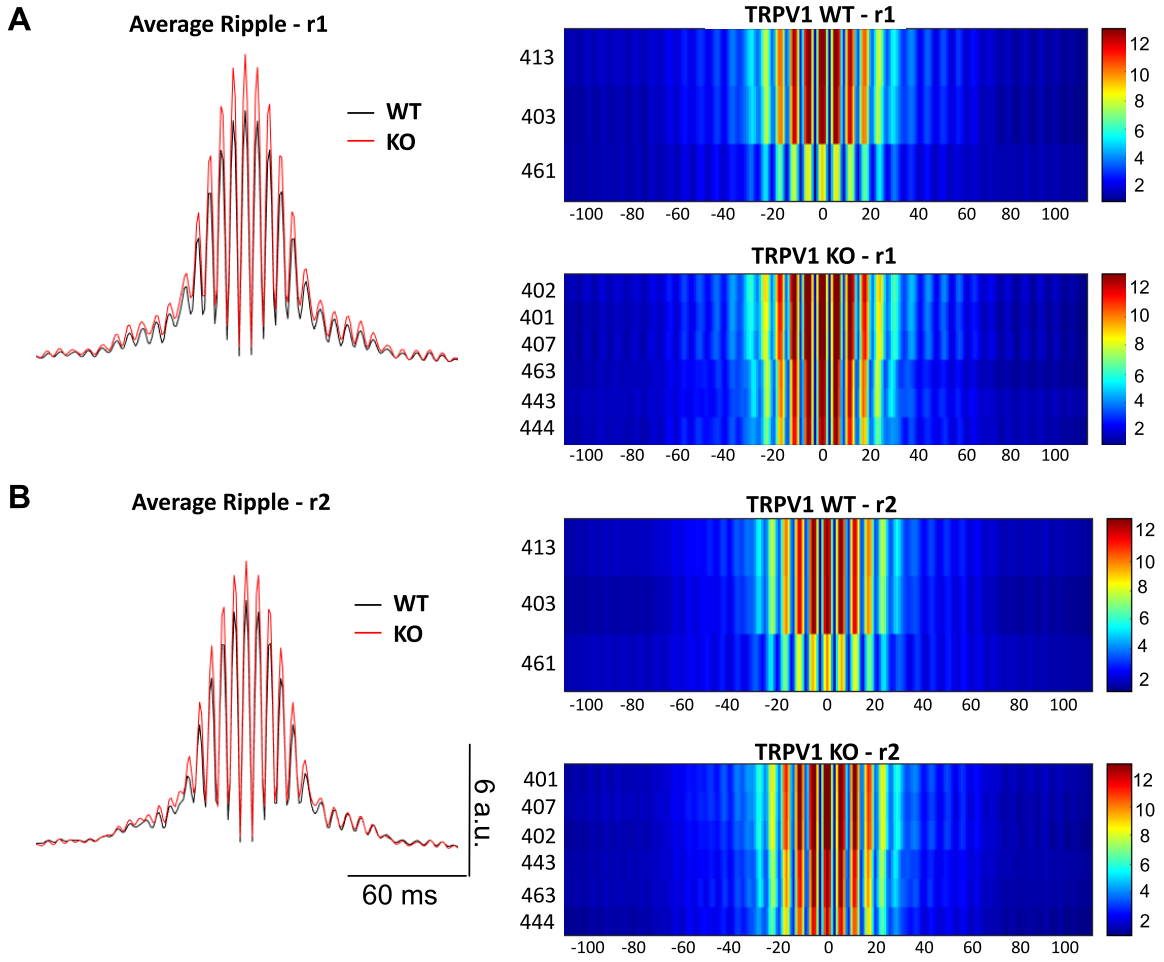

Figure 28: SWRs in familiar environments - Increased ripple magnitude in TRPV1 KO mice. Averaged ripple z-score waveform in WT (black) and TRPV1 KO (red) mice (left), and individual ripple heatmaps

for three WT (top) and six KO (bottom) mice (right) during **(A)** r1 and **(B)** r2. Ripple magnitude was increased in TRPV1 KOs compared to WTs. Heatmaps are sorted from highest to lowest ripple magnitude, with mouse number indicated on the y-axis and ms on the x-axis, centered on maximum ripple peak.

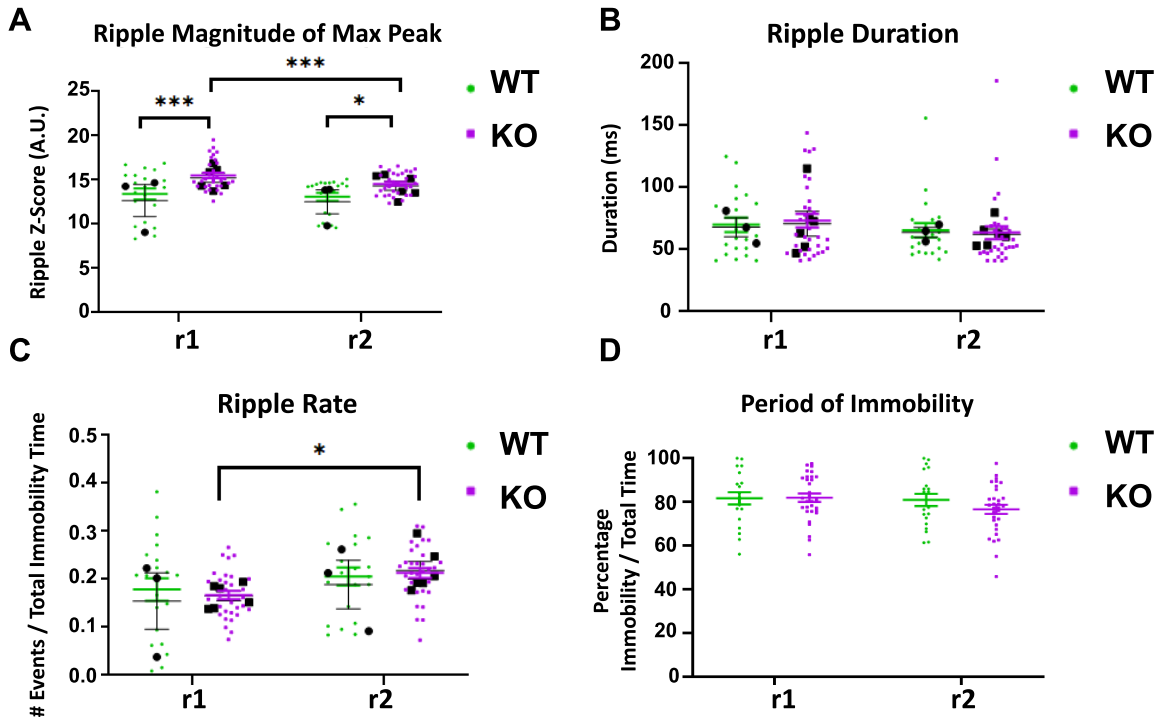

Figure 29: SWRs in familiar environments - Ripple magnitude was significantly higher in TRPV1 KO mice. (A) The z-score of the maximum ripple peak was significantly higher in the TRPV1 KOs ($p_{genotype}$ = 0.0011) and significantly lower in r2 compared to r1 ($p_{rest\_session}$ = 0.0016), with the decrease being significant in the post-hoc test only for the TRPV1 KOs. No significant interaction between genotype and rest session was seen ($p_{genotype*rest\_session}$ = 0.1158). If animals are used as experimental units: $p_{genotype}$ = 0.1307, $p_{rest\_session}$ = 0.0423, $p_{genotype*rest\_session}$ = 0.1105. **(B)** Ripple duration was not different between genotypes or rest sessions ($p_{genotype}$ = 0.8954, $p_{rest\_session}$ = 0.2239, $p_{genotype*rest\_session}$ = 0.6493; If animals are used as experimental units: $p_{genotype}$ = 0.9438, $p_{rest\_session}$ = 0.2808, $p_{genotype*rest\_session}$ = 0.7097). **(C)** The rate of ripple occurrence was not significantly different between genotypes, but increased in r2 compared to r1, with the post-hoc test suggesting the effect was due to an increase in TRPV1 KO ripple rate ($p_{genotype}$ = 0.8900, $p_{rest\_session}$ = 0.0063, $p_{genotype*rest\_session}$ = 0.4713; If animals are used as experimental units: $p_{genotype}$ = 0.6104, $p_{rest\_session}$ = 0.0461, $p_{genotype*rest\_session}$ = 0.6215). **(D)** The period of immobility (velocity < 2 cm/s) was not significantly different between genotypes or rest sessions ($p_{genotype}$ = 0.4399, $p_{rest\_session}$ = 0.1457, $p_{genotype*rest\_session}$ = 0.2696). Graphs show mean and SEM. Main statistics were based on recorded sessions (colored dots and squares with colored lines for mean and SEM, green = 20 WT, magenta = 31 KO sessions), but results are also shown as averaged per animal (black dots N = 3 WT, black squares N = 6 KO mice, with black means and SEM, except for **D** where results are only shown for recording sessions). The reported p values are the

results of the RMANOVAs per recording session or per animal, with significance lines on graphs indicating the results of the Šídák's post-hoc tests per recording session, * = p < 0.05, *** = p < 0.001.

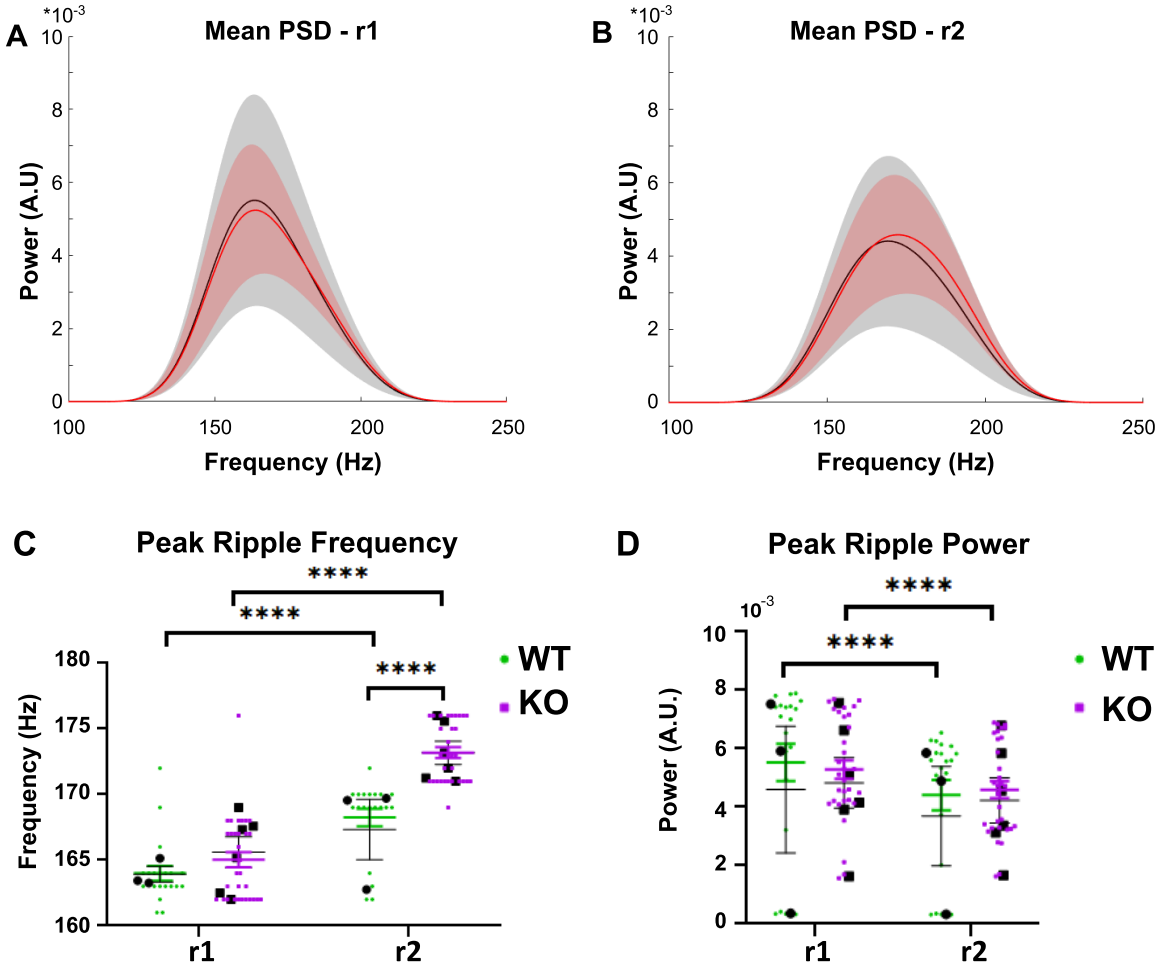

Figure 30: SWRs in familiar environments - Ripple frequency was increased in TRPV1 KO mice during rest session 2. Averaged power spectral density and standard deviation for each genotype in **(A)** rest session 1 and **(B)** rest session 2. **(C)** Peak ripple frequency was significantly higher in TRPV1 KO mice during r2, but not r1. There was a significant increase in r2 compared to r1 in both genotypes ($p_{genotype}$ = 0.0001, $p_{rest\_session}$ < 0.0001, $p_{genotype*rest\_session}$ < 0.0001). If animals are used as experimental units: $p_{genotype}$ = 0.0544, $p_{rest\_session}$ = 0.0007, $p_{genotype*rest\_session}$ = 0.0625. **(D)** Peak ripple power was similar between genotypes and lower in r2 for both genotypes. The significant interaction effect came from WTs having a slightly higher power during r1, but lower power during r2 compare to TRPV1 KOs ($p_{genotype}$ = 0.9616, $p_{rest\_session}$ < 0.0001, $p_{genotype*rest\_session}$ = 0.0080; If animals are used as experimental units: $p_{genotype}$ = 0.8318, $p_{rest\_session}$ = 0.0046, $p_{genotype*rest\_session}$ = 0.4360). Graphs show mean and SEM. Main statistics were based on recorded sessions (colored dots and squares with colored lines for mean and SEM, green = 20 WT, magenta = 31 KO sessions), but results are also shown as averaged per animal (black dots N = 3 WT, black squares N = 6 KO mice, with black means and SEM). The reported p values are the results of the RMANOVAs per recording session or per

animal, with significance lines on graphs indicating the results of the Šídák's post-hoc tests per recording session, **** = $p < 0.0001$.

3.1.2.1.2 Effect of TRPV1 KO on theta oscillations

Theta oscillations in awake mice have been extensively studied for their importance in memory encoding (Herweg et al., 2020); and sleep theta might be involved in memory consolidation, similar to SWRs (Çalışkan & Stork, 2019). Activation of OLM cells, which specifically express TRPV1 in the hippocampus (Hurtado-Zavala et al., 2017) can induce theta waves (Mikulovic et al., 2018). We therefore expected decreased theta power in TRPV1 KO mice.

3.1.2.1.2.1 Theta oscillations in novel environments

Theta frequency and power were analyzed separately for open field and rest sessions. No difference was seen in theta peak frequency between genotypes for any sessions (Figure 31A, B). Theta peak power was also unaffected by genotype, but increased in r2 compared to r1 in both WT and TRPV1 KO mice ($p_{rest\_session}$= 0.0023, $p_{Šídák's\_WT}$ = 0.013, $p_{Šídák's\_KO}$ = 0.020; Figure 31C, D).

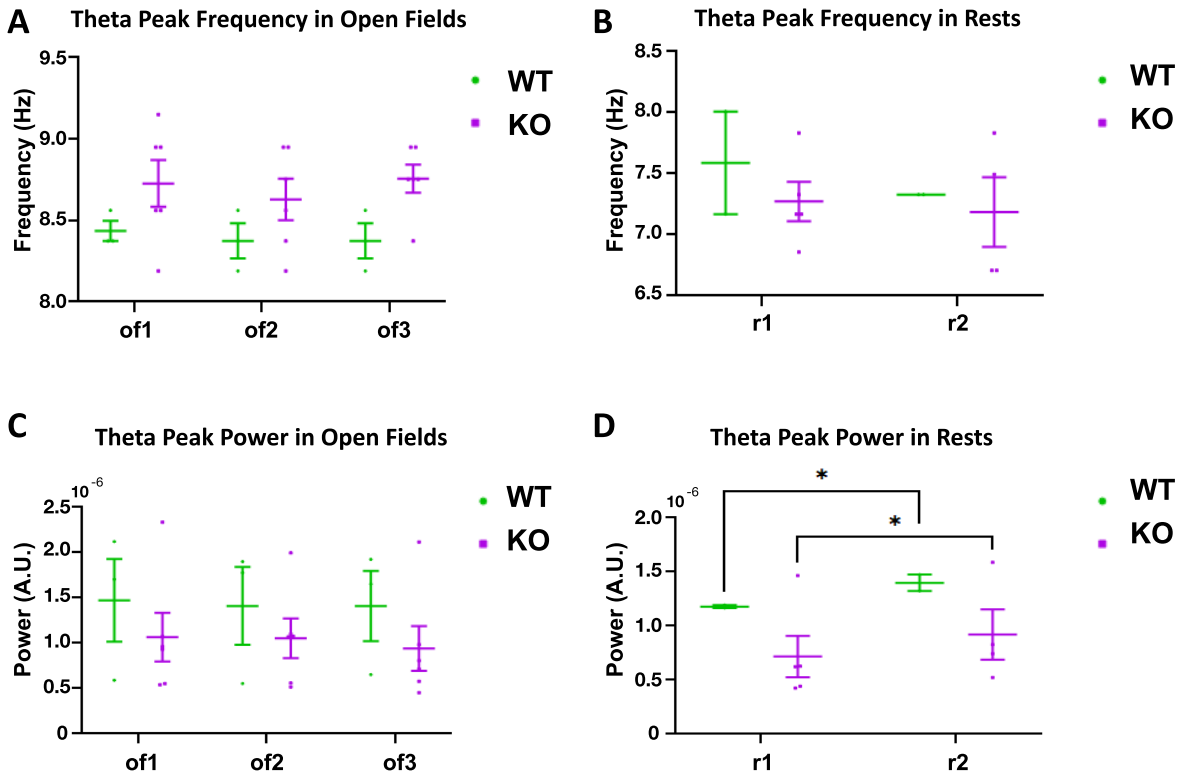

Figure 31: Theta in novel environments - Theta power and frequency were similar between genotypes. (A) In open fields or **(B)** rest sessions, there were no significant differences in theta peak frequency between genotypes or sessions ($p_{genotype}$ = 0.1089, $p_{OF\_session}$ = 0.5351, $p_{genotype*OF\_session}$ =

0.6840 and $p_{genotype}$ = 0.4185, $p_{rest\_session}$ = 0.5411, $p_{genotype*rest\_session}$ = 0.7572, respectively). **(C)** No difference in theta peak power between WT and TRPV1 KO mice was seen during novel exploration of the open fields ($p_{genotype}$ = 0.3921, $p_{OF\_session}$ = 0.2473, $p_{genotype*OF\_session}$ = 0.5828). **(D)** Theta peak power in rest sessions was unaffected by genotype, with both WT and TRPV1 KO showing an increase in theta peak power in r2 compared to r1 ($p_{genotype}$ = 0.1777, $p_{rest\_session}$ = 0.0023, $p_{genotype*rest\_session}$ = 0.1778). Graphs show mean and SEM, N = 3 WT (green) mice in open fields, 2 in rest sessions, N = 6 TRPV1 KO (magenta) mice in open fields, 5 in rest sessions with an extra missing value in r2, RMANOVA for open fields, mixed effects model for rest sessions. The reported p values are the results of the RMANOVAs or mixed effects models. Significance lines indicate the results of the Šídák's post-hoc tests with correction for multiple comparisons, * = $p < 0.05$.

3.1.2.1.2.2 Theta oscillations in familiar environments

TRPV1 KO mice had significantly higher theta frequency in the open fields in familiar environments than WT mice, an effect that was significant for all open field sessions in the post-hoc statistical test ($p_{genotype} < 0.0001$, $p_{Šídák's\_of1} < 0.0001$, $p_{Šídák's\_of2} < 0.0001$, $p_{Šídák's\_of3} = 0.0005$; Figure 32A). There was also a significant decrease in theta frequency in the TRPV1 KOs between of1 and the other two open field explorations ($p_{OF\_session}$ = 0.0028, $p_{Šídák's\_KO\_of1\text{-}2}$ = 0.0023, $p_{Šídák's\_KO\_of1\text{-}3}$ = 0.040). No effect of genotype was seen for theta frequency during rest sessions, but for both WT and TRPV1 KO mice theta frequency was higher in r2 compared to r1 ($p_{rest\_session}$ = 0.0001, $p_{Šídák's\_WT}$ = 0.037, $p_{Šídák's\_KO}$ = 0.0011; Figure 32B). Theta peak power was significantly lower in TRPV1 KO than WT mice during open field exploration ($p_{genotype}$ = 0.013), with a post-hoc test identifying a difference only during of3 ($p_{Šídák's\_of3}$ = 0.040), with a tendency for of1 ($p_{Šídák's\_of1}$ = 0.090) and of2 ($p_{Šídák's\_of2}$ = 0.064; Figure 32C). Open field session also had an effect on theta power ($p_{OF\_Session}$ = 0.015), which came from an increase in theta power in WTs in of1 compared to of3 ($p_{Šídák's\_WT\_of1\text{-}3}$ = 0.023). Theta power in TRPV1 KOs was significantly lower than in WTs also during rest sessions ($p_{genotype}$ = 0.0002, $p_{Šídák's\_r1}$ = 0.0004, $p_{Šídák's\_r2}$ = 0.0002), with power significantly decreasing for WTs and increasing for KOs from r1 to r2 ($p_{rest\_session} < 0.0001$, $p_{Šídák's\_WT}$ = 0.0006, $p_{Šídák's\_KO}$ = 0.0033; Figure 32D). However, if animals are used as experimental units, an opposite trend is seen with an increase in theta power in WT mice from r1 to r2.

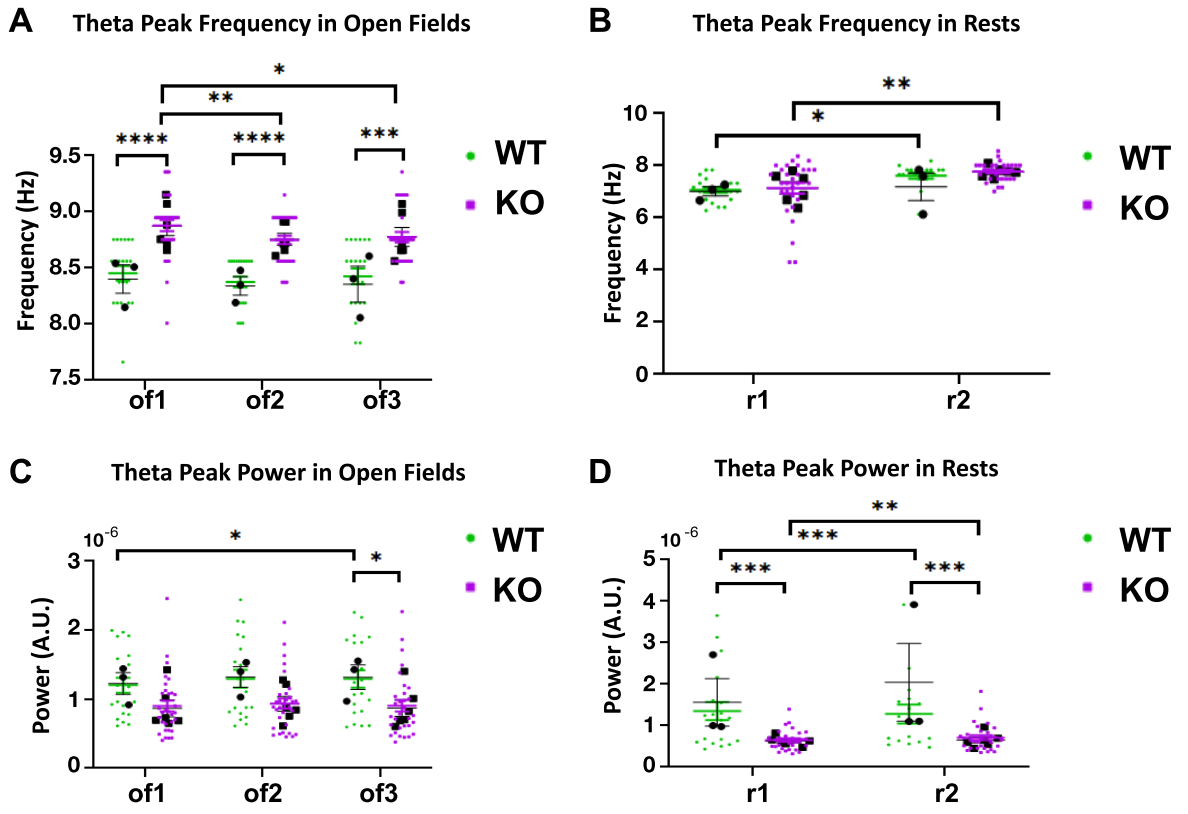

Figure 32: Theta in familiar environments - Theta frequency was higher in TRPV1 KO mice in the open fields, while theta power was lower in TRPV1 KO mice during both open field and rest sessions. (A) In the open fields, theta frequency was significantly higher in TRPV1 KO mice, an effect that was significant during all sessions in the post-hoc test. There was also a significant effect of open field session due to a decrease in TRPV1 KO theta frequency between of1 and of2 and between of1 and of3 ($p_{genotype} < 0.0001$, $p_{OF\_session} = 0.0028$, $p_{genotype*OF\_session} = 0.4301$). If animals are used as experimental units: $p_{genotype} = 0.0125$, $p_{OF\_session} = 0.0631$, $p_{genotype*OF\_session} = 0.6916$. **(B)** Theta frequency was similar between genotypes during rest sessions, with frequency increasing significantly for both genotypes during r2 compared to r1 ($p_{genotype} = 0.4709$, $p_{rest\_session} = 0.0001$, $p_{genotype*rest\_session} = 0.7426$; If animals are used as experimental units: $p_{genotype} = 0.2802$, $p_{rest\_session} = 0.0978$, $p_{genotype*rest\_session} = 0.3306$). **(C)** Theta peak power was significantly lower in TRPV1 KO mice. According to the post-hoc test, the effect was only significant in of3 (but there were similar tendencies in of1 and of2). There was also a significant effect of open field session due to WT theta power being higher in of3 compared to of1 ($p_{genotype} = 0.0126$, $p_{OF\_session} = 0.0152$, $p_{genotype*OF\_session} = 0.1228$). If animals are used as experimental units: $p_{genotype} = 0.0848$, $p_{OF\_session} = 0.1163$, $p_{genotype*OF\_session} = 0.4514$. **(D)** Theta peak power was significantly lower in TRPV1 KO mice during both rest sessions. WT theta power significantly decreased between r1 and r2 (if sessions are used as experimental units, an opposite trend is seen if animals are used), while TRPV1 KO theta power significantly increased from r1 to r2 ($p_{genotype} = 0.0002$, $p_{rest\_session} < 0.0001$, $p_{genotype*rest\_session} = 0.2717$). If animals are used as experimental units: $p_{genotype} = 0.0537$, $p_{rest\_session} = 0.0779$, $p_{genotype*rest\_session} = 0.1061$. Graphs show mean and SEM. Main statistics were based on recorded sessions (colored dots and squares with colored lines for mean and SEM, green = 20 WT, magenta = 31 KO sessions in open fields, RMANOVA, during rest sessions there were 1 WT and 2 KO missing values during r1, 4 WT and 1 KO missing values during r2,

so a mixed effects model was used), but results are also shown as averaged per animal (black dots N = 3 WT, black squares N = 6 KO mice, with black means and SEM, RMANOVA). The reported p values are the results of the RMANOVAs or the mixed effects models per recording session or per animal, with significant lines on graphs indicating the results of the Šídák's post-hoc tests per recording session, * = $p < 0.05$; ** = $p < 0.01$; *** = $p < 0.001$; **** = $p < 0.0001$.

3.1.2.1.3 Effect of TRPV1 KO on delta oscillations

The function of hippocampal delta oscillations is not well understood. SWRs are locked to hippocampal delta (Axmacher et al., 2008b) and changes in delta power have been associated with memory performance (Axmacher et al., 2008a; Wirt et al., 2021). Thus, we analyzed delta waves to have a more comprehensive image of how hippocampal oscillations are altered in TRPV1 KO mice.

3.1.2.1.3.1 Delta oscillations in novel environments

During novel exploration of open fields, no differences were seen in TRPV1 KO mice compared to WT for delta peak frequency (Figure 33A). However, during rest session 1 (but not rest session 2) delta peak frequency was significantly higher in the TRPV1 KOs than in the WTs ($p_{genotype*rest\_session}$ = 0.012, $p_{Šídák's\_r1}$ = 0.0046; Figure 33B). WT delta peak frequency increased significantly from r1 to r2 ($p_{rest\_session}$ = 0.0394, $p_{Šídák's\_WT}$ = 0.016), but TRPV1 KO delta peak frequency remained unchanged and high in both rest sessions. There was no change in delta peak power in open field (Figure 33C) or rest sessions (Figure 33D) in TRPV1 KOs compared to WT. Delta power was increased in r2 compared to r1 ($p_{rest\_session}$ = 0.0097), but the effect was not significant for a specific genotype in the post-hoc test.

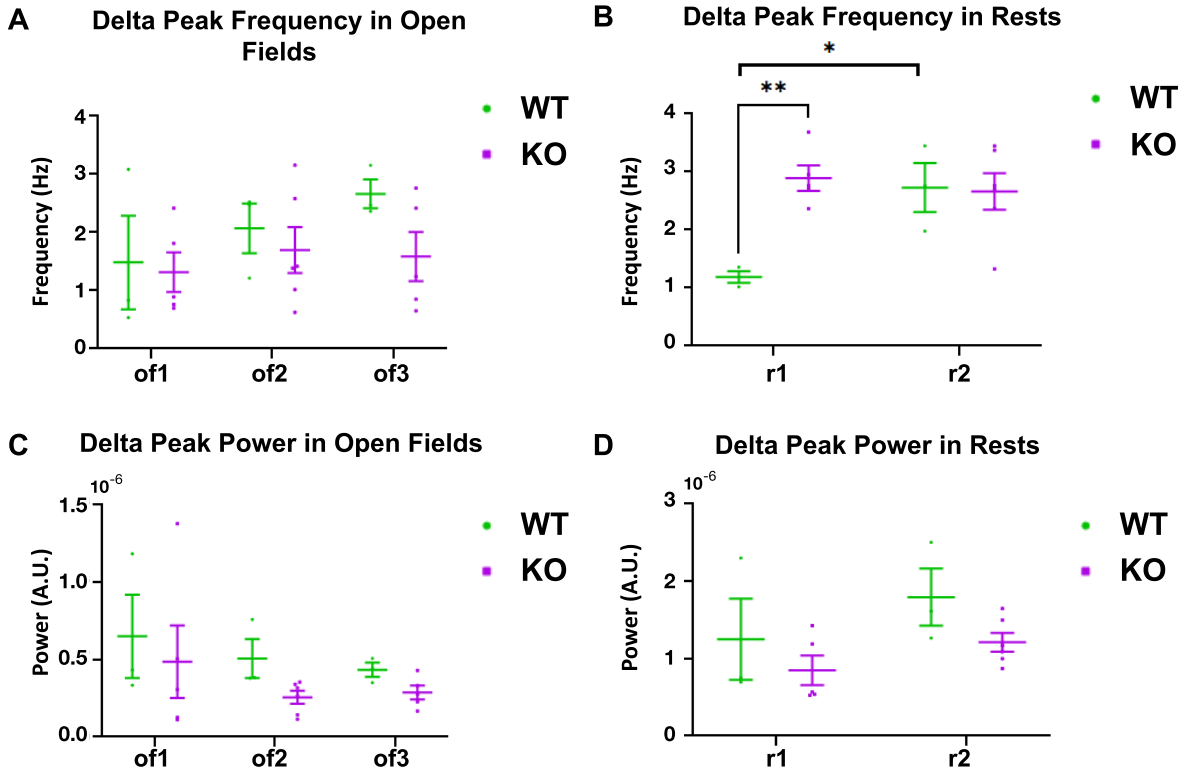

Figure 33: Delta in novel environments - Delta peak frequency was higher in TRPV1 KOs than WTs during rest session 1. (A) In the open fields, there were no significant differences in delta peak frequency between genotypes or sessions ($p_{genotype}$ = 0.3154, $p_{OF\_session}$ = 0.1482, $p_{genotype*OF\_session}$ = 0.5452). **(B)** During r1, TRPV1 KO delta peak frequency was higher compared to WT, with no difference seen in r2. WT delta peak frequency increased significantly from r1 to r2 ($p_{genotype}$ = 0.0622, $p_{rest\_session}$ = 0.0394, $p_{genotype*rest\_session}$ = 0.0116). **(C)** No difference was seen in delta peak power during novel exploration of the open fields ($p_{genotype}$ = 0.2814, $p_{OF\_session}$ = 0.3058, $p_{genotype*OF\_session}$ = 0.8797). **(D)** Delta peak power in rest sessions was also unaffected by genotype. There was a significant increase in delta peak power in r2 compared to r1 in both genotypes, but the change was not significant for any specific genotype in the post-hoc test ($p_{genotype}$ = 0.1824, $p_{rest\_session}$ = 0.0097, $p_{genotype*rest\_session}$ = 0.6347). Graphs show mean and SEM, N = 3 WT (green), 6 KO (magenta, 1 missing value during r1, of1, and of3, mixed effects model) mice. The reported p values are the results of the mixed effects models, with significance lines indicating the results of the Šídák's post-hoc tests with correction for multiple comparisons, * = $p < 0.05$; ** = $p < 0.01$.

3.1.2.1.3.2 Delta oscillations in familiar environments

In familiar environments, delta frequency was significantly lower in TRPV1 KO mice during exploration of of2 ($p_{Šídák's\_of2}$ = 0.0066), but not of1 or of3, hence the interaction of genotype and open field session was also significant ($p_{genotype}$ = 0.024, $p_{genotype*OF\_session}$ = 0.042; Figure 34A). No change in delta peak frequency was seen during rest sessions (Figure 34B). There was no change in delta peak power across genotypes for open fields (Figure 34C). However, TRPV1 KO mice had

significantly decreased delta peak power compared to WTs in both r1 and r2 ($p_{genotype}$ = 0.0008, $p_{Šídák's\_r1}$ = 0.0041, $p_{Šídák's\_r2}$ = 0.0008; Figure 34D).

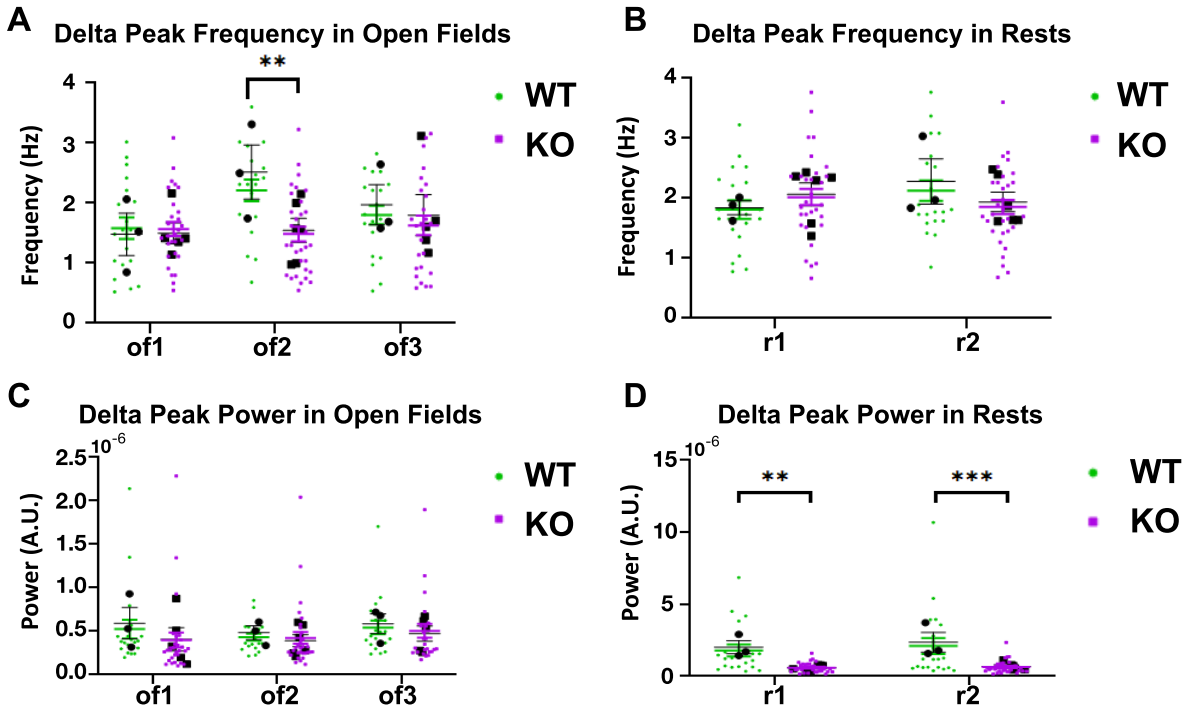

Figure 34: Delta in familiar environments - Delta peak frequency was lower in TRPV1 KOs during open field 2 and delta peak power was lower in TRPV1 KOs during rest sessions. (A) Delta peak frequency was significantly lower in TRPV1 KO mice during exploration of of2, but not of1 or of3 ($p_{genotype}$ = 0.0242, $p_{OF\_session}$ = 0.1867, $p_{genotype*OF\_session}$ = 0.0423). If animals are used as experimental units: $p_{genotype}$ = 0.2383, $p_{OF\_session}$ = 0.2205, $p_{genotype*OF\_session}$ = 0.1977. **(B)** No differences were seen in delta peak frequency during rest sessions ($p_{genotype}$ = 0.8207, $p_{rest\_session}$ = 0.5294, $p_{genotype*rest\_session}$ = 0.0502; If animals are used as experimental units: $p_{genotype}$ = 0.8353, $p_{rest\_session}$ = 0.3575, $p_{genotype*rest\_session}$ = 0.1176). **(C)** Delta peak power was similar across genotypes and open field sessions ($p_{genotype}$ = 0.3635, $p_{OF\_session}$ = 0.5384, $p_{genotype*OF\_session}$ = 0.7903; If animals are used as experimental units: $p_{genotype}$ = 0.3077, $p_{OF\_session}$ = 0.5739, $p_{genotype*OF\_session}$ = 0.7354). **(D)** During rest sessions, delta peak power was significantly lower in TRPV1 KO mice compared to WTs ($p_{genotype}$ = 0.0008, $p_{rest\_session}$ = 0.1997, $p_{genotype*rest\_session}$ = 0.4149). If animals are used as experimental units: $p_{genotype}$ = 0.0049, $p_{rest\_session}$ = 0.1255, $p_{genotype*rest\_session}$ = 0.3591. Graphs show mean and SEM. Main statistics were based on recorded sessions (colored dots and squares with colored lines for mean and SEM, green = 20 WT, magenta = 31 KO sessions, missing values: in r1 = 1 WT, 1 KO; in of1 = 1 WT, 3 KO; in of2 = 2 WT; in of3 = 1 WT, 6 KO, so a mixed effects model was used in all parameters analyzed), but results are also shown as averaged per animal (black dots N = 3 WT, black squares N = 6 KO mice, 1 KO missing value in of1 and of3, so mixed effects models for open field sessions and RMANOVA for rest sessions, with black means and SEM). The reported p values are the results of the mixed effects models per recording session or per animal, with significance lines on graphs indicating the results of the Šídák's post-hoc tests per recording session, ** = $p < 0.01$; *** = $p < 0.001$.

3.1.2.1.4 Velocity check

Theta and delta frequency and power have been reported to be modulated by velocity (Kennedy et al., 2022; Schultheiss et al., 2020). To confirm that the effects seen above were due to differences between genotypes, we compared the average velocity of each mouse in each recording session. For open fields, LFP analysis was performed in instances where the mouse was active, running at a velocity of more than 2 cm/s. Hence, the average velocity for those instances was analyzed. During novel exploration, no significant differences were seen in velocity between genotypes (Figure 35A). There was an increase in velocity of WT mice between of2 and of3 during familiar recordings ($p_{OF\_session}$ = 0.022, $p_{Šídák's\_WT\_of2\text{-}3}$ = 0.044; Figure 35B), but no significant differences between genotypes were seen. During rest sessions, the LFP was analyzed when the mouse was quiet, defined as having a velocity less than 2 cm/s. Analysis of this time period indicated no differences in velocity during novel exploration rest sessions (Figure 35C). TRPV1 KO mice had a significantly higher velocity during r2 compared to r1 after exploration of familiar open fields ($p_{rest\_session}$ = 0.024, $p_{Šídák's\_KO}$ = 0.043; Figure 35D), but again no significant differences between genotypes were detected.

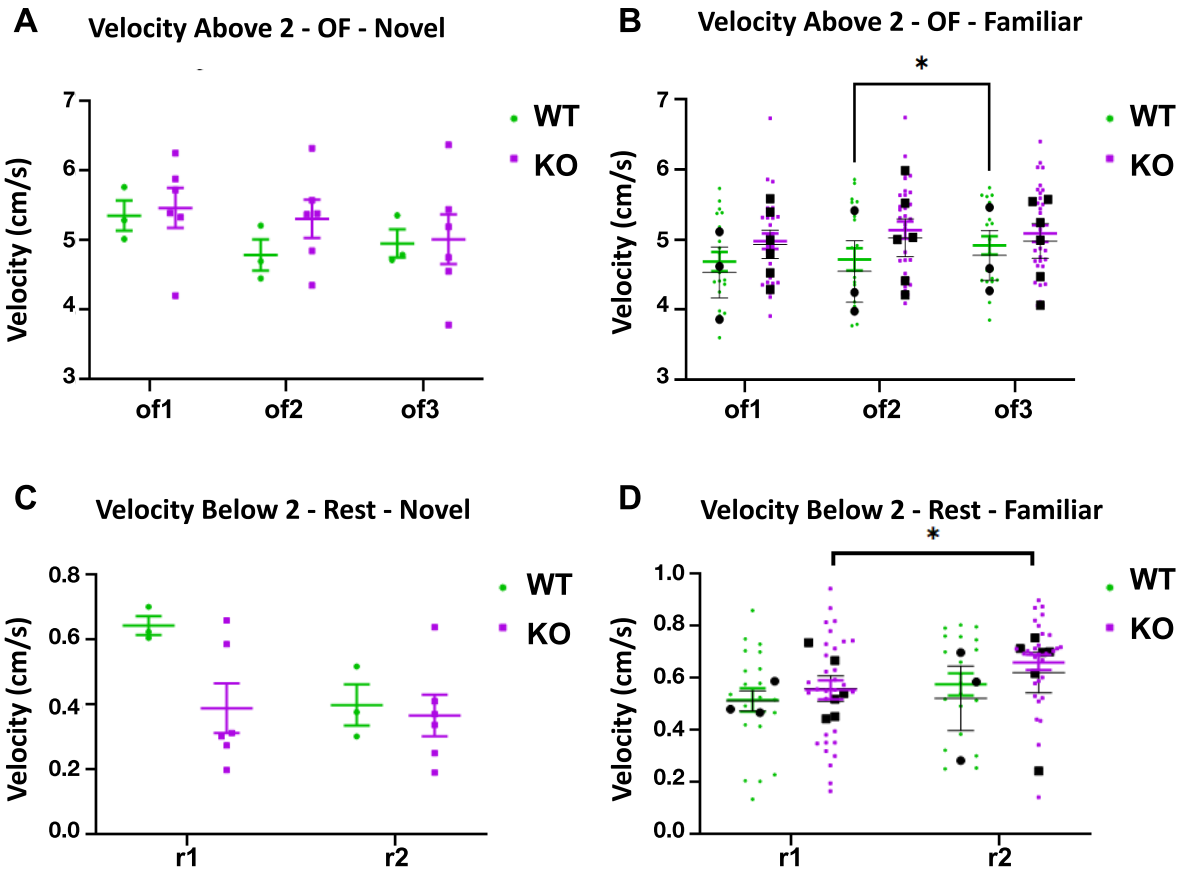

Figure 35: No significant differences in velocity between genotypes. (A) Average velocity above 2 cm/s, which defines the time analyzed for theta and delta effects in the open fields, was not different between genotypes or open field sessions during novel exploration ($p_{genotype}$ = 0.6080, $p_{OF\_session}$ = 0.0732, $p_{genotype*OF\_session}$ = 0.3678). **(B)** Average velocity above 2 cm/s was similar between WT and TRPV1 KO mice in the familiar condition, but a significant increase in velocity is seen for WTs between of2 and of3 ($p_{genotype}$ = 0.0951, $p_{OF\_session}$ = 0.0220, $p_{genotype*OF\_session}$ = 0.1147; If animals are used as

experimental units: $p_{genotype}$ = 0.4215, $p_{OF\_session}$ = 0.2850, $p_{genotype*OF\_session}$ = 0.3160). **(C)** Average velocity below 2 cm/s, which defines the time analyzed for LFP changes in rest sessions, was not significantly different between genotypes or rest sessions in the novel condition ($p_{genotype}$ = 0.1093, $p_{rest\_session}$ = 0.1142, $p_{genotype*rest\_session}$ = 0.1771). **(D)** During recordings in the familiar environment, the average velocity was higher during r2 in the TRPV1 KOs, but no significant differences between genotypes were seen ($p_{genotype}$ = 0.1422, $p_{rest\_session}$ = 0.0239, $p_{genotype*rest\_session}$ = 0.5261; If animals are used as experimental units: $p_{genotype}$ = 0.4131, $p_{rest\_session}$ = 0.6443, $p_{genotype*rest\_session}$ = 0.7393). Graphs show mean and SEM. Main statistics were based on recorded sessions (colored dots and squares with colored lines for mean and SEM, green = 20 WT, magenta = 31 KO sessions), but results are also shown as averaged per animal (black dots N = 3 WT, black squares N = 6 KO mice). The reported p values are the results of the RMANOVAs per recording session or per animal, with significance lines on graphs indicating the results of the Šídák's post-hoc tests per recording session, * = $p < 0.05$.

3.1.2.2 Effect of TRPV1 KO on single-units

Single units from our in vivo electrophysiological recordings were classified as putative pyramidal cells or interneurons based on firing rate, and pyramidal neurons that had at least one place field (see methods) were classified as place cells. The average firing rate was analyzed for all cell types, while place cells were also analyzed for spatial properties.

Figure 36 shows a representative example of a WT and a TRPV1 KO place cell in of1, of2, and second exploration of of1 (of3). Average and peak firing rate for place cells was similar between genotypes (Figure 37A, B). The spatial information carried by TRPV1 KO place cells was significantly lower than WT place cells (p = 0.0024; Figure 37C), but remapping was intact (Figure 37D). TRPV1 KO place fields were less stable between of1 and re-exploration of of1 (of3) (p = 0.0095; Figure 37E) and were significantly larger than WTs (p = 0.025; Figure 37F), indicating less specificity. These results suggest impaired spatial properties in TRPV1 KO mice. The percentage of place cells out of the total number of recorded principal neurons was around 30% in both genotypes (Figure 38A shows quantification from total population of cells while Figure 38B shows quantification per mouse). Lastly, interneurons in KO mice fired significantly less (p = 0.047; Figure 39A), while the average firing rate of pyramidal cells was similar between genotypes (Figure 39B).

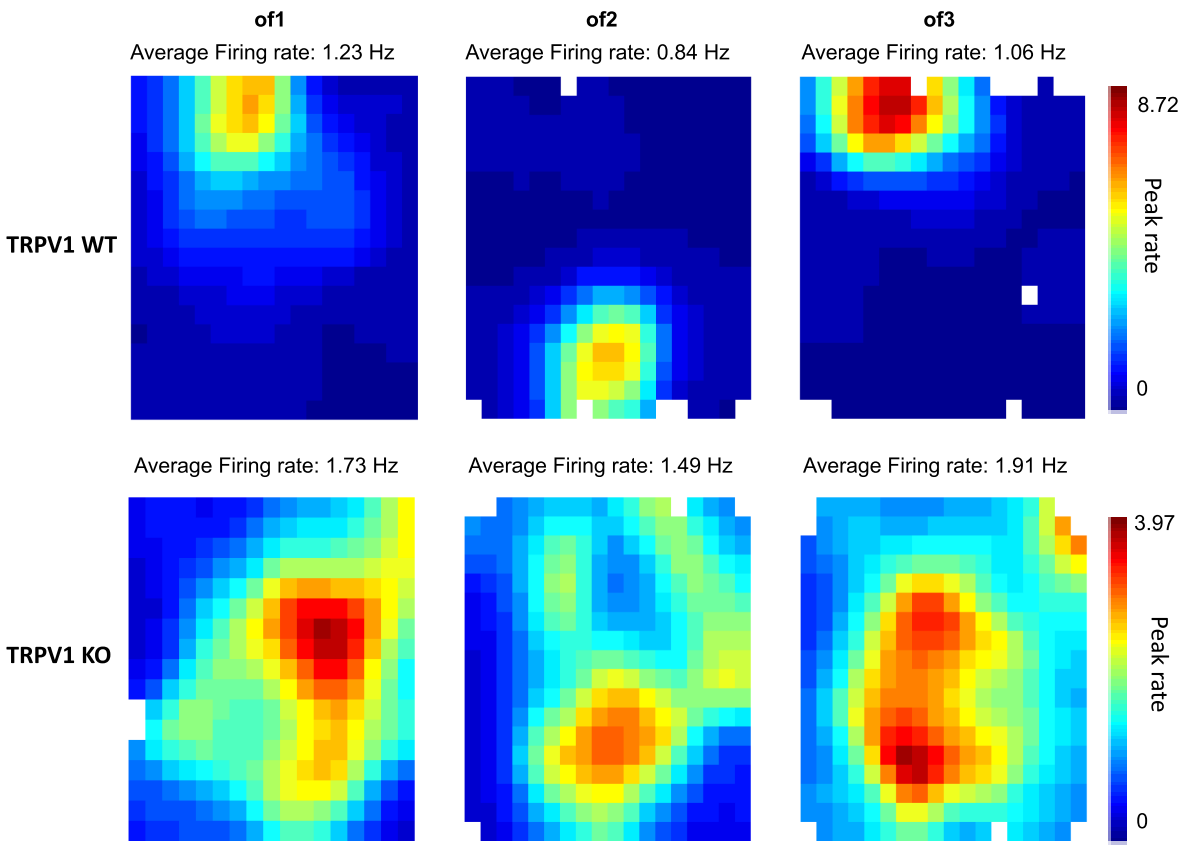

Figure 36: Examples of place maps from CA1 hippocampal cells in WT and TRPV1 KO mice. Heat maps representing the place fields for a single WT (top) or single TRPV1 KO (bottom) place cell in open field 1 (of1), open field 2 (of2), and second exploration of open field 1 (of3). The average firing rate for the two cells in each field is shown above the map. Notice the larger place field size of the TRPV1 KO cell and the higher similarity of place maps in of1 and of3 of the WT cell.

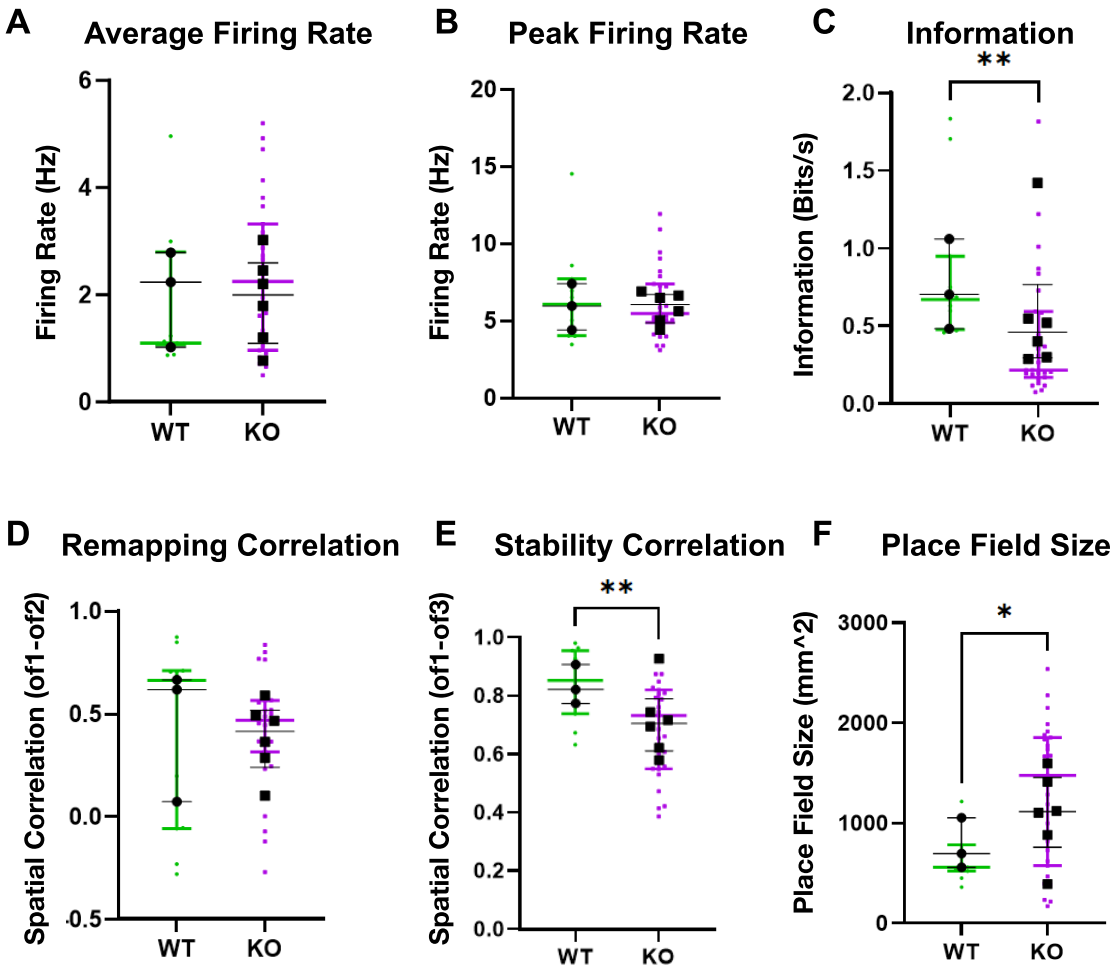

Figure 37: Increased place field size and decreased spatial information and stability correlation in TRPV1 KO place cells. No significant differences were seen in **(A)** place cell average firing rate ($p = 0.3560$; if averaged per animal $p = 0.9048$) and **(B)** peak firing rate ($p > 0.9999$ per cell or per animal). **(C)** Decreased spatial information was carried by TRPV1 KO place cells ($p = 0.0024$; if averaged per animal $p = 0.3810$). **(D)** The remapping correlation was similar between genotypes ($p = 0.7998$; if averaged per animal $p = 0.5476$). **(E)** The stability correlation was significantly lower in TRPV1 KO place cells ($p = 0.0095$; if averaged per animal $p = 0.1667$). **(F)** The place fields were larger in TRPV1 KO mice ($p = 0.0247$; if averaged per animal $p = 0.2619$). Graphs show median and interquartile range (IQR) per cell (N = 11 WT (green dots), N = 27 KO (magenta squares) place cells) and per animal (N = 3 WT (black dots), N = 6 KO (black squares) mice). The main results reported are from the Mann-Whitney U-tests performed on the cell population, followed by the Mann-Whitney U-tests after averaging per animal first, * = $p < 0.05$; ** = $p < 0.01$.

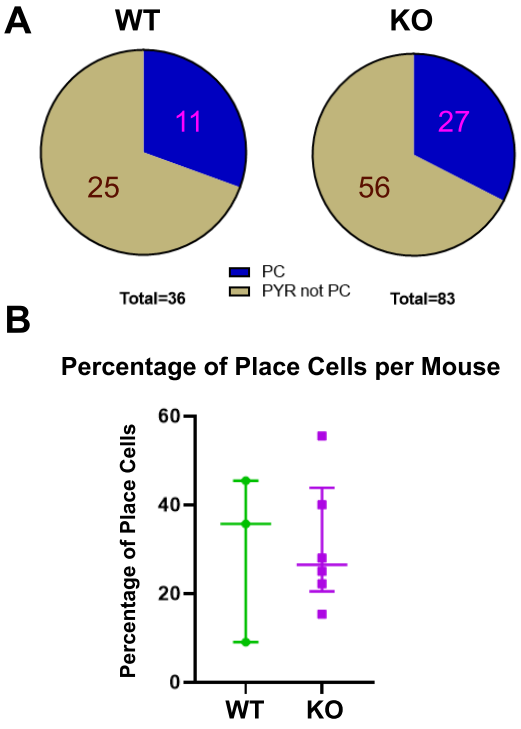

Figure 38: No difference between genotypes in the percentage of place cells. (A) The percentage of pyramidal neurons (PYR) classified as place cells (PC) was similar in WT (30.6%) and TRPV1 KO (32.5%) mice (chi-square test, p = 0.8319). **(B)** The percentage of place cells out of the total number of pyramidal cells per mouse was also quantified, with no differences seen between WT (N = 3, green dots) and TRPV1 KO (N = 6, magenta squares) mice (Mann-Whitney U-test, p > 0.9999). Graph shows median and IQR.

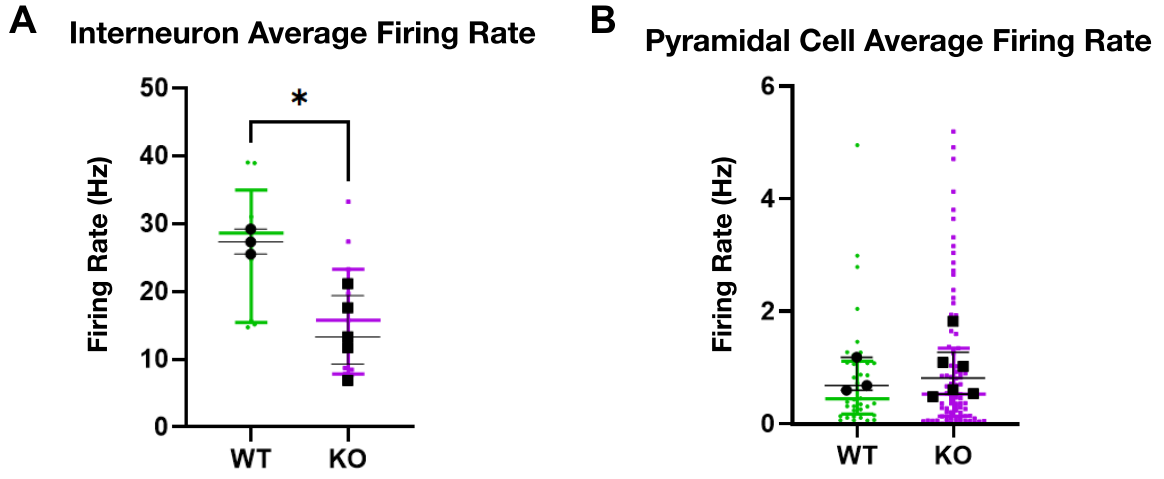

Figure 39: Lower average firing rate in TRPV1 KO interneurons. (A) The average firing rate of interneurons in TRPV1 KO mice was significantly lower than WTs (p = 0.0465; if averaged per animal first p = 0.0357), while **(B)** the average firing rate of pyramidal cells was unaffected (p = 0.8878; if averaged per animal first p = 0.9048). Graphs show median and IQR per cell (Interneurons: N = 9 WT (green dots), N = 11 KO (magenta squares); Pyramidal cells: N = 36 WT (green dots), N = 83 KO (magenta squares)) and per animal (N = 3 WT (black dots), N = 6 KO (black squares) mice, one had no interneurons so N = 5 KO mice for A). The main results reported are from the Mann-Whitney U-tests performed on the cell population, followed by the Mann-Whitney U-tests after averaging per animal first, * = p < 0.05.

3.1.3 Memory performance of TRPV1 KO and WT mice in the cheeseboard maze

TRPV1 KO mice have reduced LTP at CA3-CA1 synapses in vitro (Hurtado-Zavala et al., 2017), which could suggest impaired memory formation and/or consolidation. Above, we also reported alterations in hippocampal LFP and cell activity which are in agreement with dysfunctions in spatial navigation and spatial learning. We therefore used the cheeseboard maze to assess memory, a test where mice have to learn the location of a chocolate milk reward. Mice had 4 trials every day, with less time spent and distance traveled to reward location across days denoting learning. We hypothesized that TRPV1 KO mice would learn the reward location slower than WT mice. After 7 days of learning of the original reward location, the reward location was switched to the opposite quadrant of the maze. This is called reversal learning and is a form of spatial memory extinction and behavioral flexibility. We hypothesized that TRPV1 KO mice would have trouble switching to the new reward location.

There was no difference in distance (Figure 40) or time (Figure 41) to the original reward location between WT and KO mice, as the regression lines had similar slopes and elevations. Before outlier removal, the slope of the regression line for distance to the original reward location was significantly different from zero only for TRPV1 KO mice (p_{WT} = 0.18, p_{KO} = 0.033; Figure 40A). After outlier removal, both WT and TRPV1 KO regression lines had a slope significantly different from zero (p_{WT} = 0.036, p_{KO} = 0.026; Figure 40B). The slope of the regression line for time to original reward location was not significantly different from zero for any genotype before or after outlier removal, but there was a tendency after outlier removal for WT mice learning (with outliers: p_{WT} = 0.59, p_{KO} = 0.49; Figure 41A; without outliers: p_{WT} = 0.067, p_{KO} = 0.21; Figure 41B).

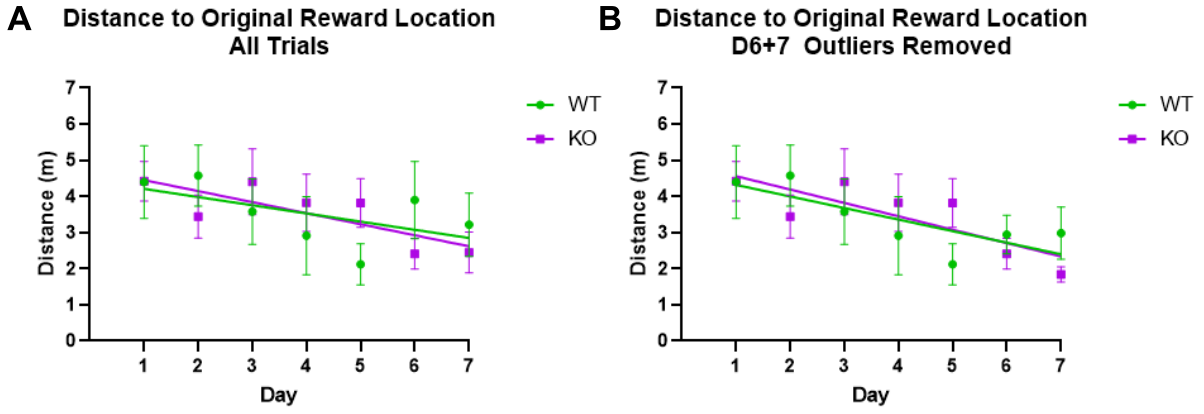

Figure 40: No difference in distance to original reward location between TRPV1 KO and WT mice. **(A)** Distance to original reward location before (R^2 = 0.3237 for WT, 0.6302 for KO) and **(B)** after (R^2 = 0.6167 for WT, 0.6642 for KO) removal of outliers for days 6 (3 WT trials) and 7 (1 WT, 3 KO trials). The slope of the linear regression line for KO mice (N = 8) was significantly different from zero with (p_A = 0.0331) or without (p_B = 0.0255) outliers, indicating successful learning across days. The slope of the WT (N = 6 mice) regression line was significantly different from zero only after removal of outliers (p_A = 0.1825, p_B = 0.0364, but one-tailed paired t-test of WT day 1 versus day 5 p_A = 0.0441). There was no difference in the elevation (p_A = 0.9839, p_B = 0.7772) or slope (p_A = 0.6702, p_B = 0.7631) between the two regression lines, suggesting similar performance of WT and KO mice. Graphs show mean and SEM calculated by first averaging trials (4 per day) per mouse and then averaging mice per

genotype. Outlier analysis (Method ROUT, Q = 1%) was performed separately for WT (24 trials per day) and KO (32 trials per day) trials and separately for trials of days 6 and 7. Regression lines were calculated based on mean daily performance per genotype. Regression line equations: WT_A: Y = -0.2265*X + 4.435, KO_A: Y = -0.3055*X + 4.758; WT_B = : Y = -0.3199*X + 4.638, KO_B = : Y = -0.3705*X + 4.931.

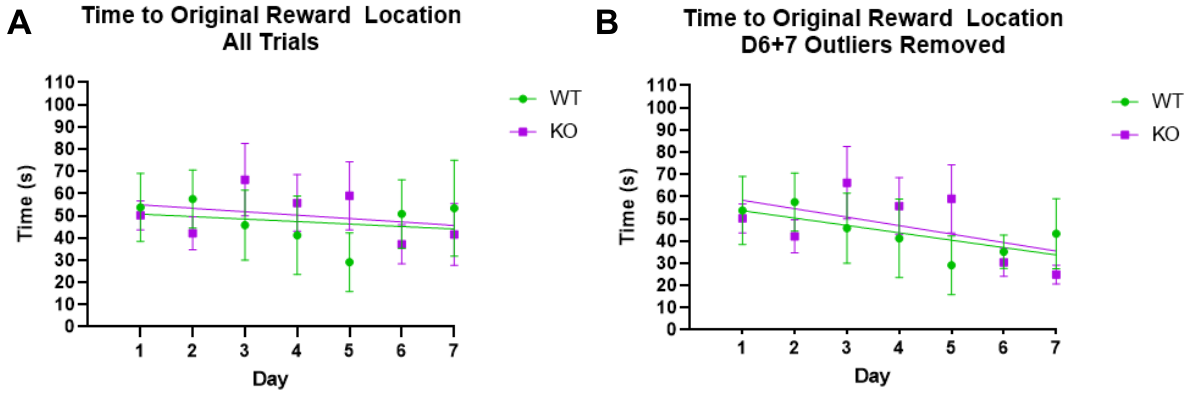

Figure 41: No difference in time to original reward location between TRPV1 KO and WT mice. (A) Time to original reward location before (R^2 = 0.06153 for WT, 0.09924 for KO) and **(B)** after (R^2 = 0.5222 for WT, 0.2930 for KO) removal of outliers for days 6 (3 WT, 2 KO trials) and 7 (2 WT, 3 KO trials). The slope of the linear regression line for WTs (N = 6 mice) and KOs (N = 8) was not significantly different from zero before outlier removal (WT: p_A = 0.5917, KO: p_A = 0.4913). After outlier removal, there was a tendency for WT slope to be different from zero, but not KO (WT: p_B = 0.0666, KO: p_B = 0.2095). This suggests poor learning. There was no difference in the elevation (p_A = 0.6055, p_B = 0.5833) or slope (p_A = 0.8834, p_B = 0.8734) between the two regression lines. Graphs show mean and SEM calculated by first averaging trials (4 per day) per mouse and then averaging mice per genotype group. Outlier analysis (Method ROUT, Q = 1%) was performed separately for WT (24 trials per day) and KO (32 trials per day) trials and separately for trials of days 6 and 7. Regression lines were calculated based on mean daily performance per genotype. Regression line equations: WT_A: Y = -1.117*X + 51.86, KO_A: Y = -1.547*X + 56.47; WT_B = : Y = -3.320*X + 56.98, KO_B = : Y = -3.811*X + 62.19.

On day 8, the reward location was switched to the opposite quadrant of the maze and the 7 days of learning the new reward location started. While the slope was similar between genotypes with or without outliers, the elevations were significantly different, as KO mice traveled a longer distance and took more time to reach the reward across all days ($p < 0.0001$; Figure 42 and 43). The slopes of the regression lines for WT and KO mice with (distance: p_{WT} = 0.049, p_{KO} = 0.0005; time: p_{WT} = 0.029, p_{KO} = 0.0002) and without (distance: p_{WT} = 0.028, p_{KO} = 0.0008; time: p_{WT} = 0.018, p_{KO} = 0.0003) outliers were significantly different from zero, suggesting successful learning of the new reward location by both genotypes.

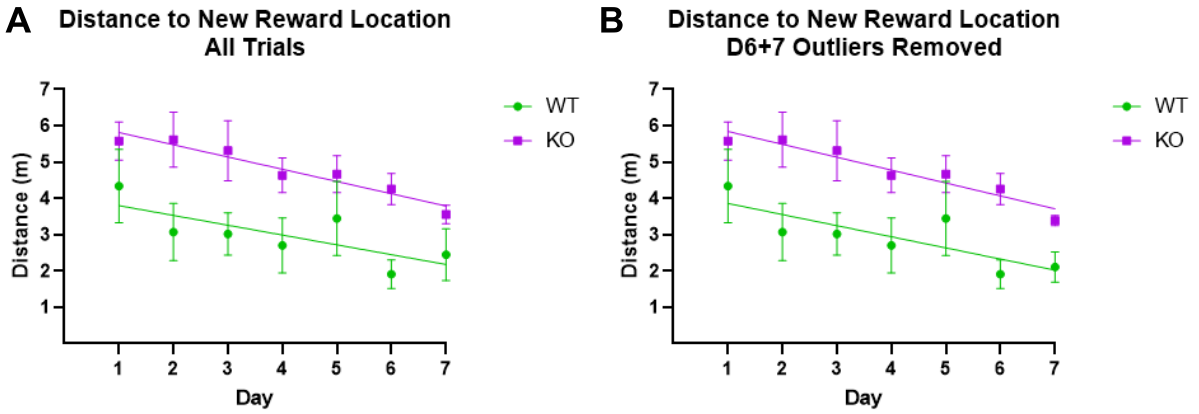

Figure 42: Similar slope but higher elevation of TRPV1 KO regression line for distance to new reward location, compared to WT. (A) Distance to new reward location before (R^2 = 0.5718 for WT, 0.9291 for KO) and **(B)** after (R^2 = 0.6506 for WT, 0.9130 for KO) removal of outliers for days 6 (0 trials) and 7 (2 WT, 1 KO trials). The slope of the linear regression line was significantly different from zero for both WT and KO mice with (WT: p_A = 0.0492, KO: p_A = 0.0005) or without (WT: p_B = 0.0284, KO: p_B = 0.0008) day 6 and 7 outliers. There was no difference in the slope (p_A = 0.5638, p_B = 0.6709) between the two regression lines, but the elevation was significantly higher for KO animals (p_A and p_B < 0.0001). Graphs show mean and SEM calculated by first averaging trials (4 per day) per mouse and then averaging mice per genotype group. Outlier analysis (Method ROUT, Q = 1%) was performed separately for WT (24 trials per day) and KO (32 trials per day) trials and separately for trials of days 6 and 7. Regression lines were calculated based on mean daily performance per genotype. Regression line equations: WT_A: Y = -0.2703*X + 4.071, KO_A: Y = -0.3375*X + 6.152; WT_B = : Y = -0.3066*X + 4.168, KO_B = : Y = -0.3555*X + 6.200.

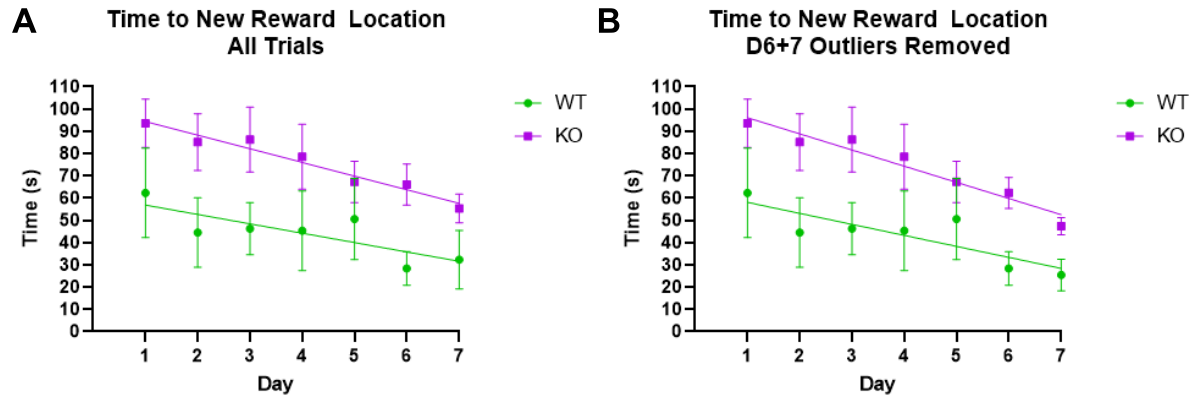

Figure 43: Similar slope but higher elevation of TRPV1 KO regression line for time to new reward location, compared to WT. (A) Time to new reward location before (R^2 = 0.6500 for WT, 0.9532 for KO) and **(B)** after (R^2 = 0.7077 for WT, 0.9406 for KO) removal of outliers for days 6 (1 KO trial) and 7 (2 WT, 2 KO trials). The slope of the linear regression line was significantly different from zero for both WT and KO mice with (WT: p_A = 0.0285, KO: p_A = 0.0002) or without (WT: p_B = 0.0177, KO: p_B = 0.0003) day 6 and 7 outliers. There was no difference in the slope (p_A = 0.2297, p_B = 0.1883) between the two regression lines, but the elevation was significantly higher for KO animals (p_A and p_B <

0.0001). Graphs show mean and SEM calculated by first averaging trials (4 per day) per mouse and then averaging mice per genotype group. Outlier analysis (Method ROUT, Q = 1%) was performed separately for WT (24 trials per day) and KO (32 trials per day) trials and separately for trials of days 6 and 7. Regression lines were calculated based on mean daily performance per genotype. Regression line equations: WT_A: Y = -4.210*X + 61.06, KO_A: Y = -6.141*X + 100.6; WT_B = : Y = -4.947*X + 63.02, KO_B = : Y = -7.262*X + 103.4.

3.1.4 Anxiety levels of TRPV1 KO and WT mice assessed in the open field

A role for the TRPV1 channel in emotional regulation, anxiety, and stress has been suggested by others. While some report an anxiolytic effect of TRPV1 activation (Li et al., 2008), the general consensus is that it is inactivation of the channel that reduces anxiety (Marsch et al., 2007; Hakimizadeh et al., 2012; Santos et al., 2008; You et al., 2012). As anxiety and stress are well documented to impact cognitive processes and memory performance (Sandi, 2013; Lukasik et al., 2019; Maloney et al., 2014), we decided to use the open field test to assess baseline anxiety levels in our mice, expecting to find decreased anxiety in the TRPV1 KOs. Mice were left to explore a new open field for 15 minutes and the percentage of time they spent in the center of the open field, as well as the number of entries into the center, were compared between genotypes. No significant differences were found in either parameter analyzed (Figure 44A, B), indicating similar levels of anxiety in TRPV1 KO and WT mice. There were no deficits in locomotion, as total displacement was similar between genotypes (Figure 44C). The presence of cues in the open field could have confounded the results, since cues were placed on three of the four walls surrounding the open field and mice sometimes explored the cues. This has not been quantified yet, but visual inspection of tracking suggested no difference between exploration of the wall without a cue compared to the other three walls (Figure 45).

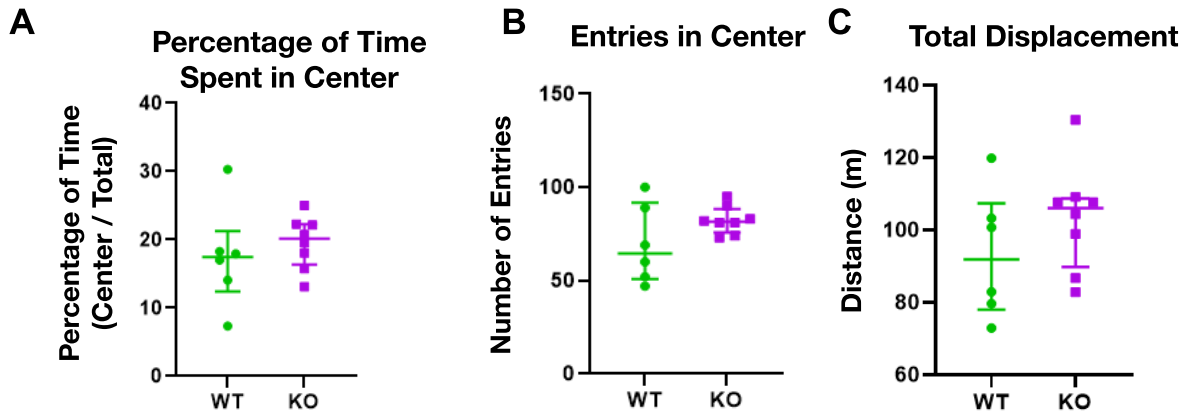

Figure 44: No difference in baseline anxiety levels between TRPV1 KO and WT mice. (A) The percentage of time mice spent in the center of the open field, as well as **(B)** the number of entries in the center of the open field were not significantly different between genotypes (p = 0.3450 and p = 0.2165, respectively, Mann-Whitney U-test, N = 6 WT, 8 KO mice), suggesting similar anxiety levels

between groups. **(C)** Total displacement was similar for WT and KO mice (Mann-Whitney U-test, p = 0.2284) indicating no differences in locomotion. Graphs show median and IQR.

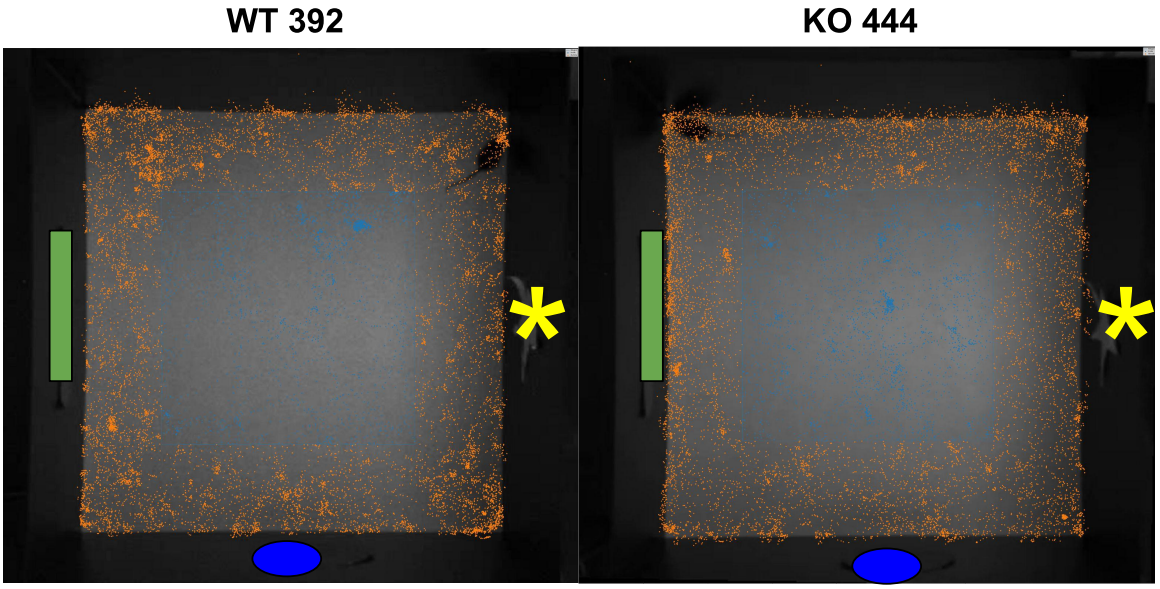

Figure 45: Representative examples of mouse tracking in the open field test. Notice that the mice spent similar time near the wall without a cue compared to the other walls. Shapes represent visual cues: green rectangle, blue circle, and yellow star. Orange dots represent the mouse being detected in the periphery, while blue ones detect the mouse in the center of the maze. These pictures were provided by Dejana Mitrovic and Can Tartanoglu from the Viana da Silva lab, and subsequently adapted.

3.1.5 In vitro induction of febrile seizures

Since the TRPV1 channel can sense heat, and heat causes febrile seizures, we tested if temperature induces aberrant SWRs and epileptiform activity in TRPV1 KO and WT slices from young mice (P18-P25). Slices were recorded in pairs for 10 minutes at 31 °C and then at 38.2 °C, a high temperature mimicking fever. If groups or bursts containing epileptiform discharges (EDs) or continuous EDs were seen (Figure 3), the slice was counted as having epileptiform activity (EA). The percentage of slices per mouse with EA at 31 °C and at 38.2 °C was quantified, and a significant effect of both genotype and temperature was found ($p_{genotype}$ = 0.0092, $p_{temperature}$ = 0.001; Figure 46A). A post-hoc test indicated that WT mice had higher EA than TRPV1 KO mice at 31 °C (p_{31} = 0.0102). The effect of temperature was due to more KO slices having EA at high temperature compared to 31 °C, but the same tendency is seen in WT slices (p_{WT} = 0.099, p_{KO} = 0.0048).

Slices with EA only at 38.2 °C or slices that had EA in both temperatures but stronger EA at 38.2 °C (see methods for criteria) were counted as slices whose EA increased. The percentage of such slices per mouse was also quantified and compared between WT and TRPV1 KO mice. No difference in the percentage of slices with increased EA was seen between genotypes (Figure 46B). Accordingly, when

all slices were pooled together, the percentage of slices whose EA increased, decreased, or showed no change with temperature was similar between genotypes (Figure 46C). This suggests that TRPV1 KO slices are similarly susceptible to febrile seizure induction as WT slices, but might be more resistant to EA, at least at lower temperatures.

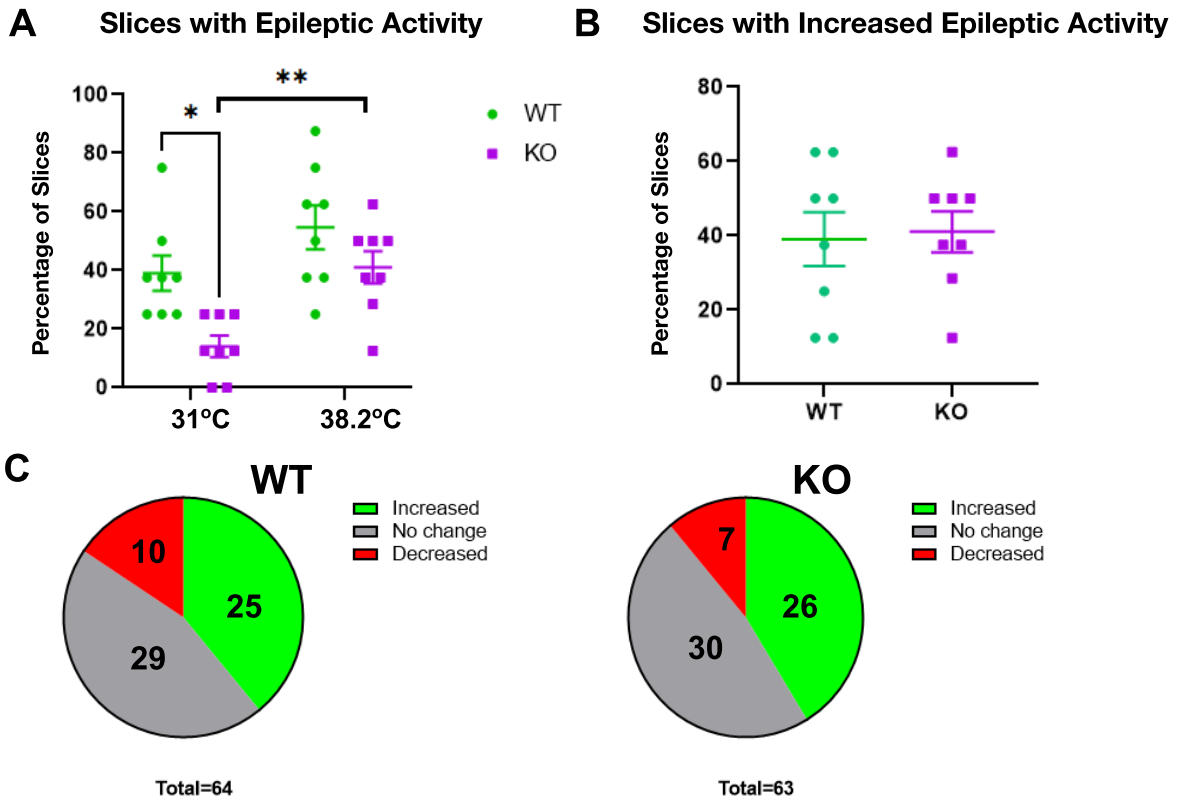

Figure 46: Slices from TRPV1 KO mice had decreased EA at 31 °C, but not at 38.2 °C, compared to WTs. (A) There was a significant effect of both genotype and temperature on the percentage of slices with EA ($p_{genotype}$ = 0.0092, $p_{temperature}$ = 0.001, $p_{genotype*temperature}$ = 0.2898, RMANOVA). The Šidák's post-hoc test identified a significant difference between WT and KO mice at 31 °C, with KO mice showing less EA. The effect of temperature comes from a significantly higher number of KO slices with EA at 38.2 °C compared to 31 °C, with a similar tendency for WT slices. **(B)** The percentage of slices per mouse where EA increased from 31 °C to 38.2 °C was similar between genotypes (Mann-Whitney U-test, p = 0.9497). **(C)** 64 WT and 63 KO slices (from 8 WT and 8 KO mice) were used in this experiment. 39% of WT slices increased their EA at high temperature, 45% had no change in EA levels, and 16% decreased their EA. 41% of KO slices showed an increase in their EA levels, 48% no change, and 11% had less EA at 38.2 °C compared to 31 °C. There were no differences between genotypes (chi-square test, p = 0.7565).

3.2 SWRs and LTP

3.2.1 SWRs recorded before and after LTP induction by high-frequency stimulation

SWRs and synaptic plasticity have long been regarded as associated processes due to their importance in memory formation and consolidation. Mechanistically, Sadowski and colleagues (2016) linked the processes by showing that SWR-associated place cell activity is capable of inducing LTP in vitro, only if replay occurs during SWRs. SWRs have also been related to depotentiation and synaptic downscaling, since SWR facilitation leads to widespread LTD (Bukalo et al., 2013). Previous studies show different effects of HFS on SWRs, but the general consensus is that LTP induction enhances SWRs (Buzsáki, 1984; Papatheodoropoulos, 2010; Behrens et al., 2005), which is what we expected here. However, weak stimulation can also induce SWRs (Jiang et al., 2018; Bazelot et al., 2016; Ellender et al., 2010). In order to control for these effects, we recorded at least 10-minutes of SWRs at baseline before stimulation, after input/output curve to determine stimulation intensity for LTP, after fEPSP baseline of test pulses, and after LTP induction and maintenance. Figure 47 shows the average fEPSP slope as a percentage of baseline fEPSP response, confirming LTP where the response remains increased for at least 1h.

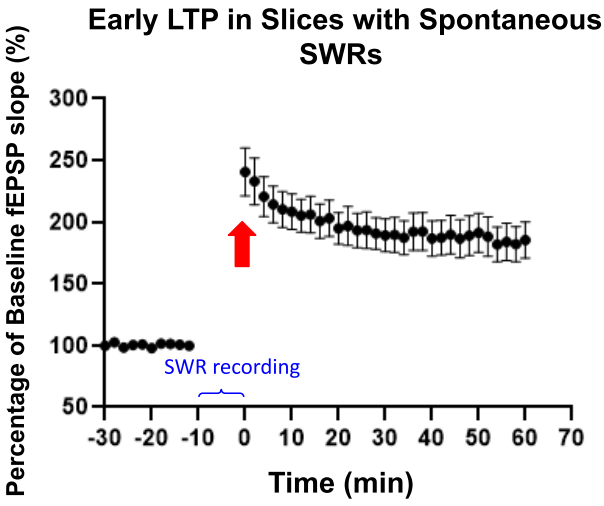

Figure 47: LTP was successfully induced in slices with spontaneous SWRs. The fEPSP slope is depicted as a percentage of baseline fEPSP slope. Trace shows mean and SEM (8 slices from 8 mice). 10 minutes are missing between fEPSP baseline and LTP induction and maintenance, during which SWRs were recorded. Stimulation time at 0 minutes is indicated by a red arrow. This experiment was performed in collaboration with Dmytro Nesterenko in Camin Dean's lab.

A representative example of a 10 s SWR trace in different conditions can be seen in Figure 48, while Figure 49 shows a single SW from the same slice in different conditions. While the RMANOVA suggested a general change in SW amplitude during the experiment ($p = 0.045$; Figure 50A), no significant differences were identified among specific conditions. We saw an increase in SW duration ($p < 0.0001$; Figure 50B) after LTP relative to every other condition ($p_{Baseline\text{-}LTP} = 0.0074$, $p_{I/O\ curve\text{-}LTP} = 0.0097$, $p_{fEPSPbaseline\text{-}LTP} = 0.0025$). However, duration was already significantly increased after fEPSP baseline ($p_{Baseline\text{-}fEPSPbaseline} = 0.0497$), suggesting that previous stimulation also affected SW duration. On the other hand, SW occurrence significantly decreased after LTP compared to baseline ($p_{RMANOVA} = 0.0039$, $p_{Baseline\text{-}LTP} = 0.045$; Figure 50C). The probability of cluster occurrence was unaffected by

stimulation (Figure 50D). Ripples were unchanged during the experiment as no differences were seen between conditions in terms of ripple amplitude, duration, peak frequency, peak power, number of ripple peaks per ripple event, or number of ripple events per minute (Figure 51).

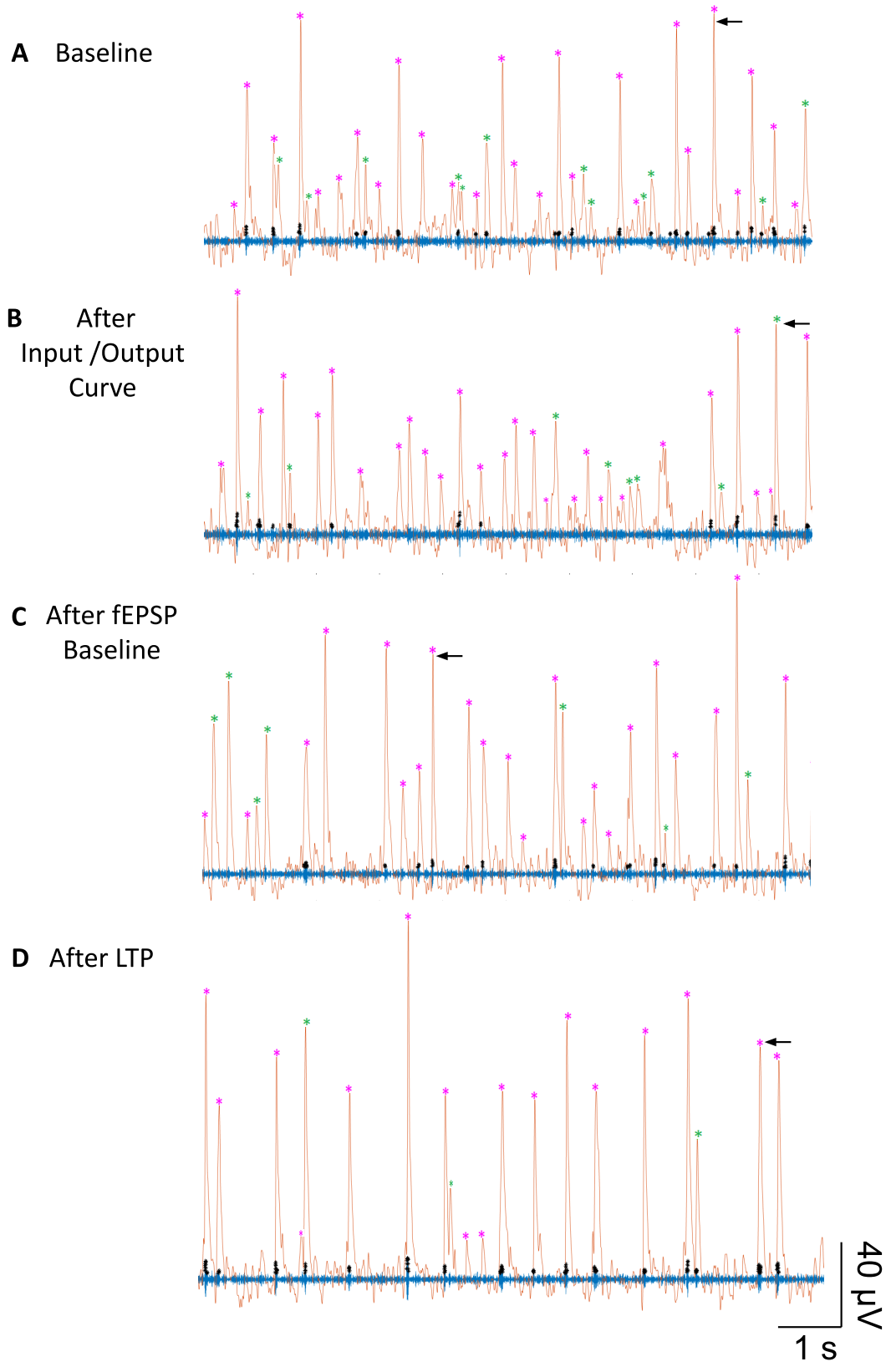

Figure 48: Representative SWR traces from the different conditions of the LTP experiment, showing decreased SW incidence after LTP induction. Both blue and orange traces were high-pass filtered at 0.5 Hz. The orange trace was then low-pass filtered at 40 Hz showing SWs, while the blue trace was bandpassed at 140-250 Hz, isolating ripples. Asterisks indicate SWs (pink = primary, green = secondary SWs of a cluster) and ripple (black) peaks detected by the code. A 10-second snippet is shown from each condition: **(A)** baseline, **(B)** after input/output curve, **(C)** after fEPSP baseline, and **(D)** after LTP. Notice the decreased number of SWs after LTP (mean for this slice = 161 SWs per minute) compared to baseline (mean for this slice = 200 SWs per minute). Black arrows indicate selected SWs shown in Figure 49.

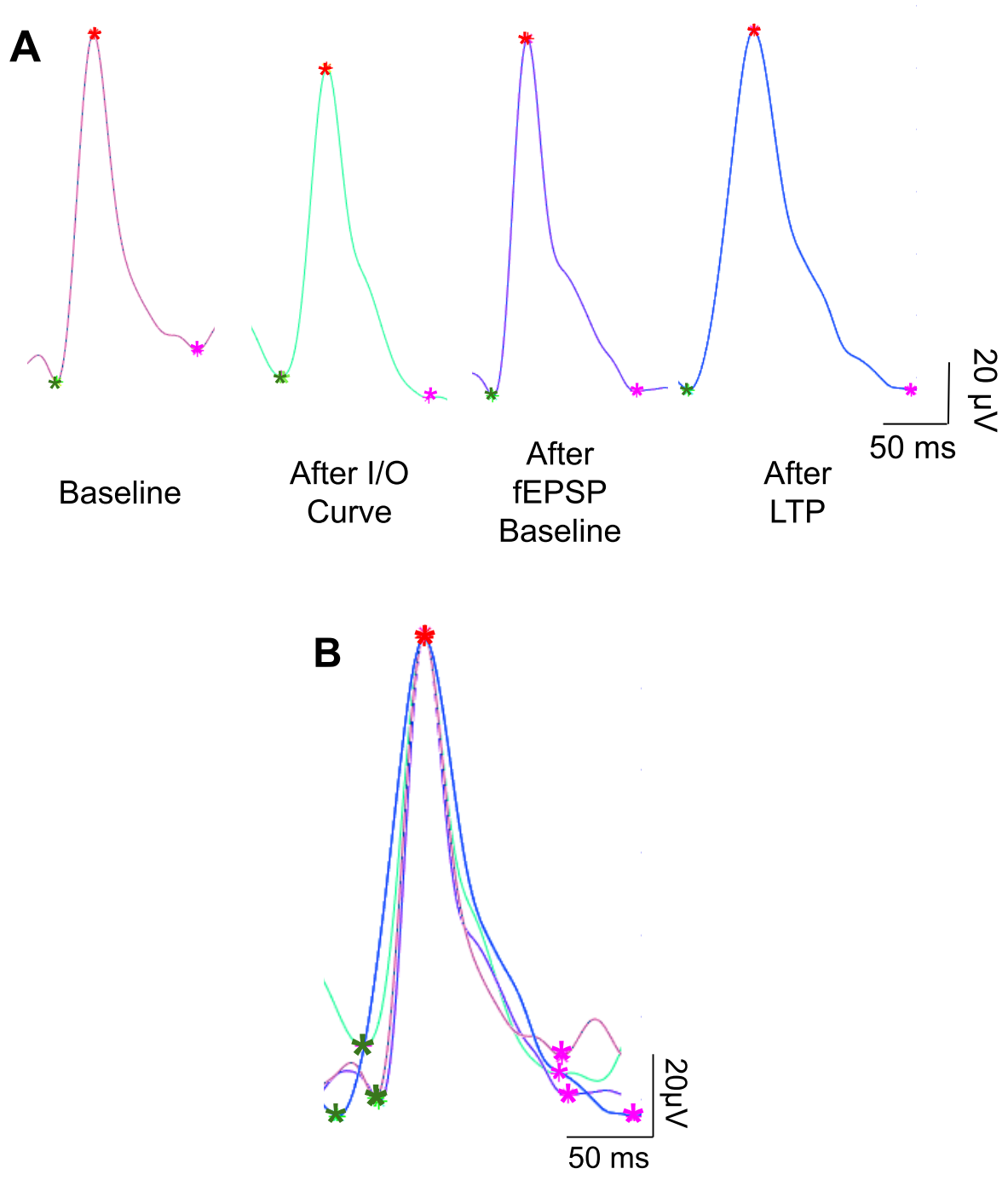

Figure 49: Representative SW events from the different conditions of the LTP experiment, showing increased SW duration after LTP induction. The SWs denoted by black arrows in Figure 48 are shown magnified **(A)** for each condition separately and **(B)** overlaid at SW peak. Note the increased SW duration after LTP (mean for this slice = 132 ms) compared to baseline (mean for this slice = 113 ms), after input/output curve (mean for this slice = 114 ms), and after fEPSP baseline (mean for this slice = 123 ms). Red asterisk denotes SW peak, green asterisk detected SW start, and magenta asterisk detected SW end, with SW duration being the difference in time between start and end points.

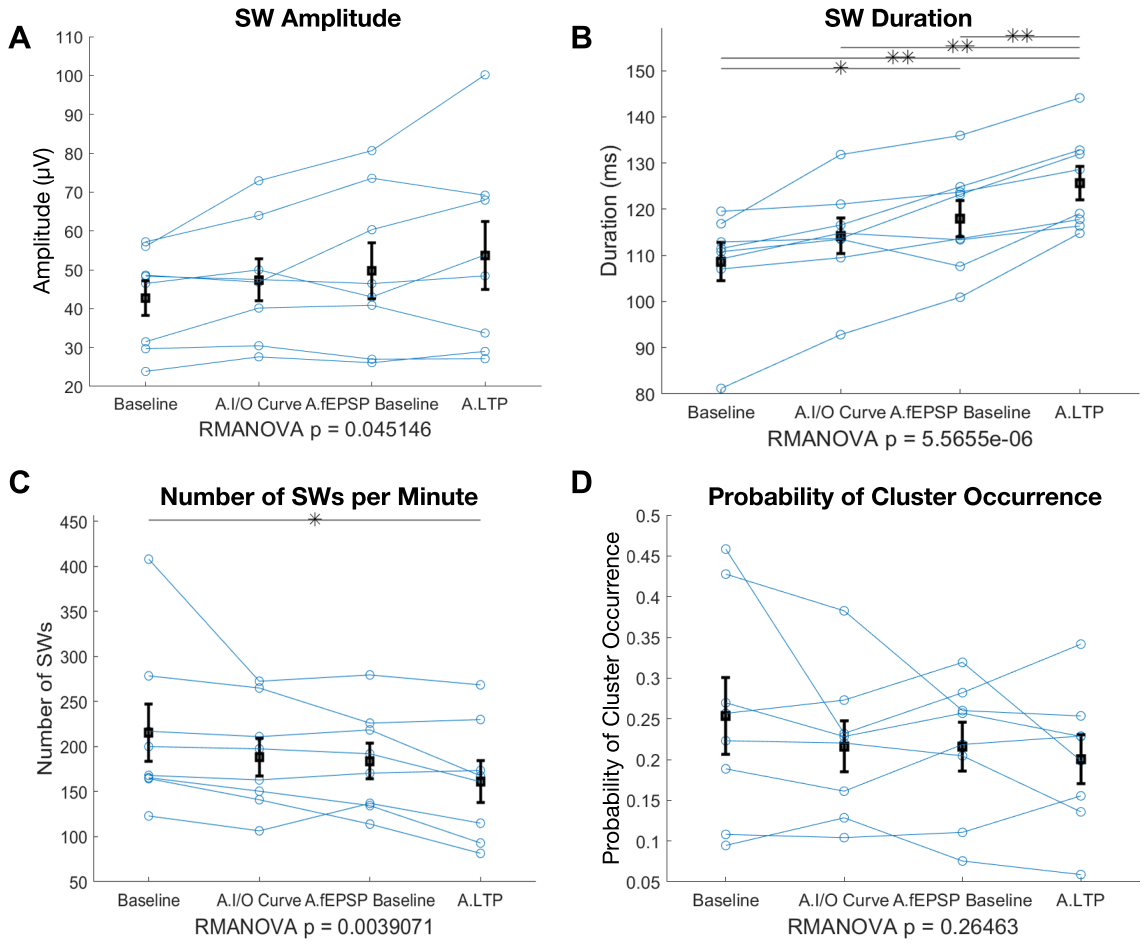

Figure 50: LTP induction increased SW duration, decreased SW incidence, and tended to increase SW amplitude. SWR recordings were taken before any stimulation, after stimulation for input/output curve, after stimulation to determine baseline fEPSP slope, and after LTP induction and confirmation of maintenance of LTP by recording fEPSP slope for 1 hour (4 conditions in each graph). Graphs show mean and SEM, N = 8 slices (from 8 mice). **(A)** Even though an overall increase is observed in the RMANOVA test of SW amplitude (p = 0.045146) no significant differences were seen among specific conditions after the post-hoc test. **(B)** SW duration significantly increased after LTP when compared with any other condition, as well as after stimulation to determine fEPSP baseline compared to before any stimulation. **(C)** The number of SWs per minute significantly decreased after LTP when compared with baseline. **(D)** The probability of SW cluster occurrence did not change with stimulation. The results of the RMANOVAs can be seen at the bottom of each graph, while the

significance lines are based on the results of the Tukey's HSD post-hoc test with multiple comparisons correction (* = $p < 0.05$; ** = $p < 0.01$).

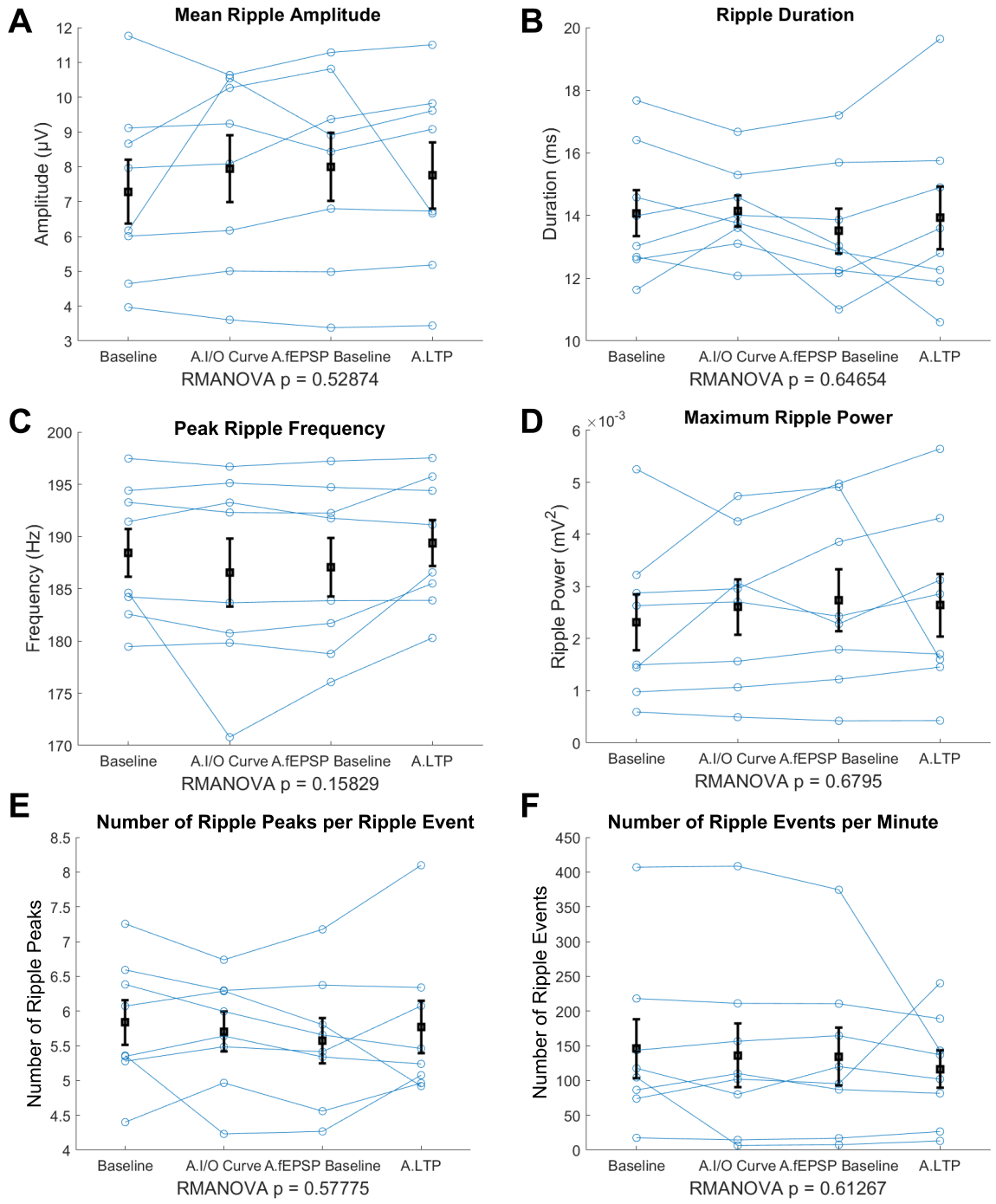

Figure 51: The LTP induction protocol had no effect on ripples. SWR recordings were taken before any stimulation, after stimulation for input/output curve, after stimulation to determine baseline fEPSP slope, and after LTP induction and confirmation of maintenance of LTP by recording fEPSP slope for 1 hour (4 conditions in each graph). Graphs show mean and SEM, N = 8 slices (from 8 mice). The **(A)** ripple amplitude, **(B)** ripple duration, **(C)** peak ripple frequency, **(D)** maximum ripple power,

(E) number of ripple peaks per ripple event, and **(F)** number of ripple events per minute were not affected by any type of stimulation. The results of the RMANOVAs can be seen at the bottom of each graph.

3.2.2 Effect of drugs that affect LTP on SWRs

Several pharmacological agents are known to block or enhance LTP. Anisomycin is a protein synthesis inhibitor. While protein synthesis is not needed for short term plasticity, it is a prerequisite for long-lasting changes. Accordingly, LTP is protein-synthesis dependent and its long-term maintenance is blocked by 20 µM anisomycin (Frey et al., 1988). We hypothesized that anisomycin might have a similar inhibitory effect on SWRs.

3.2.2.1 Effect of blocking protein synthesis, which impairs LTP maintenance, on SWRs

3.2.2.1.1 Incubation with anisomycin

We first tested if SWRs can be generated in the presence of 20 µM anisomycin. SWRs were seen after at least ~ 2.5 hours of incubation in anisomycin (a similar time-course as the appearance of SWRs in control conditions), and no changes were seen in SW amplitude, duration, incidence, or probability of cluster occurrence (Figure 52). No change was seen in ripple amplitude, duration, peak frequency, maximum power, number of ripple peaks per event, or number of ripple events per minute (Figure 53).

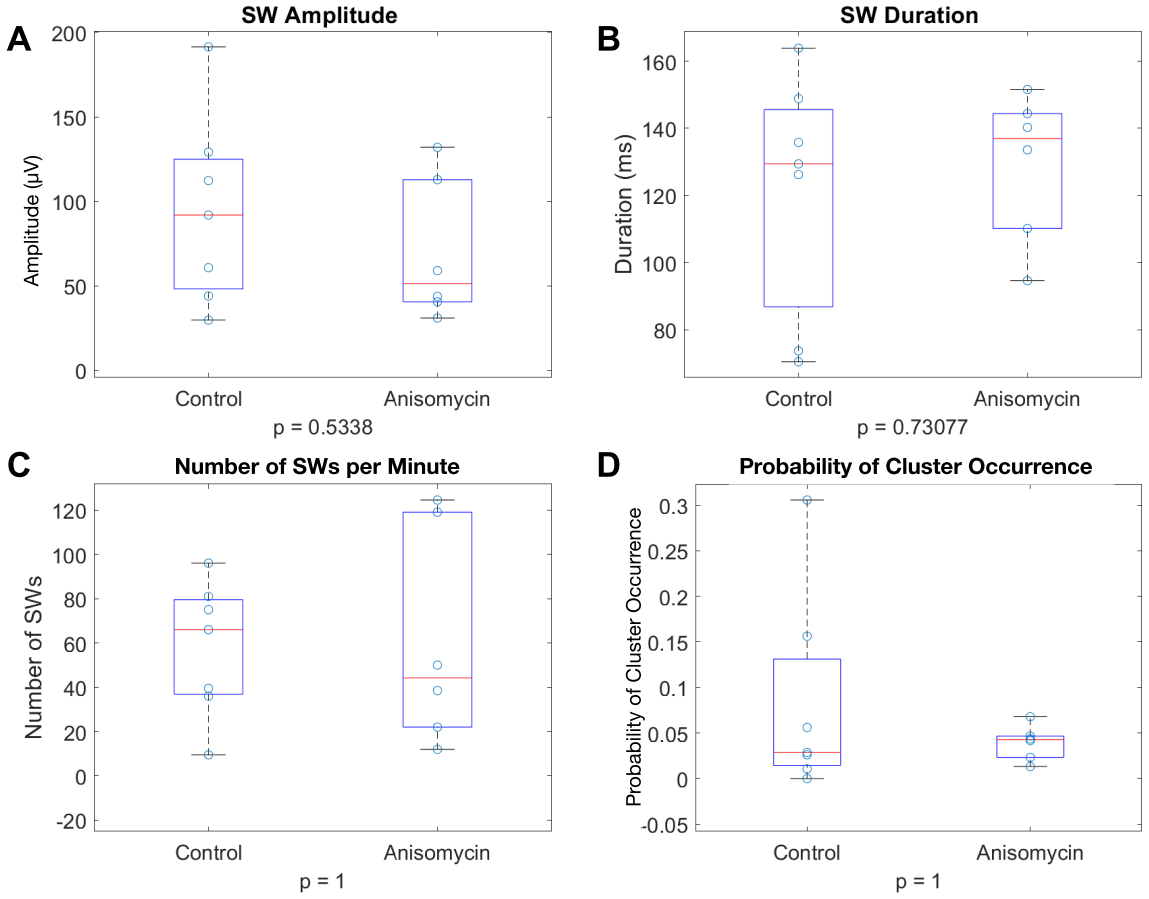

Figure 52: Incubation with 20 µM anisomycin had no effect on SWs. SWR recordings were taken from slices incubated for at least 2.5 h in either drug-free aCSF (control) or aCSF containing 20 µM anisomycin. Graphs show median, IQR, and range, $N_{control}$ = 7 slices, $N_{Anisomycin}$ = 6 slices (from 3 mice, split among conditions). The **(A)** SW amplitude, **(B)** SW duration, **(C)** number of SWs per minute, and **(D)** probability of SW cluster occurrence were not significantly different between the two conditions. The results of the Mann-Whitney U-tests can be seen under each graph.

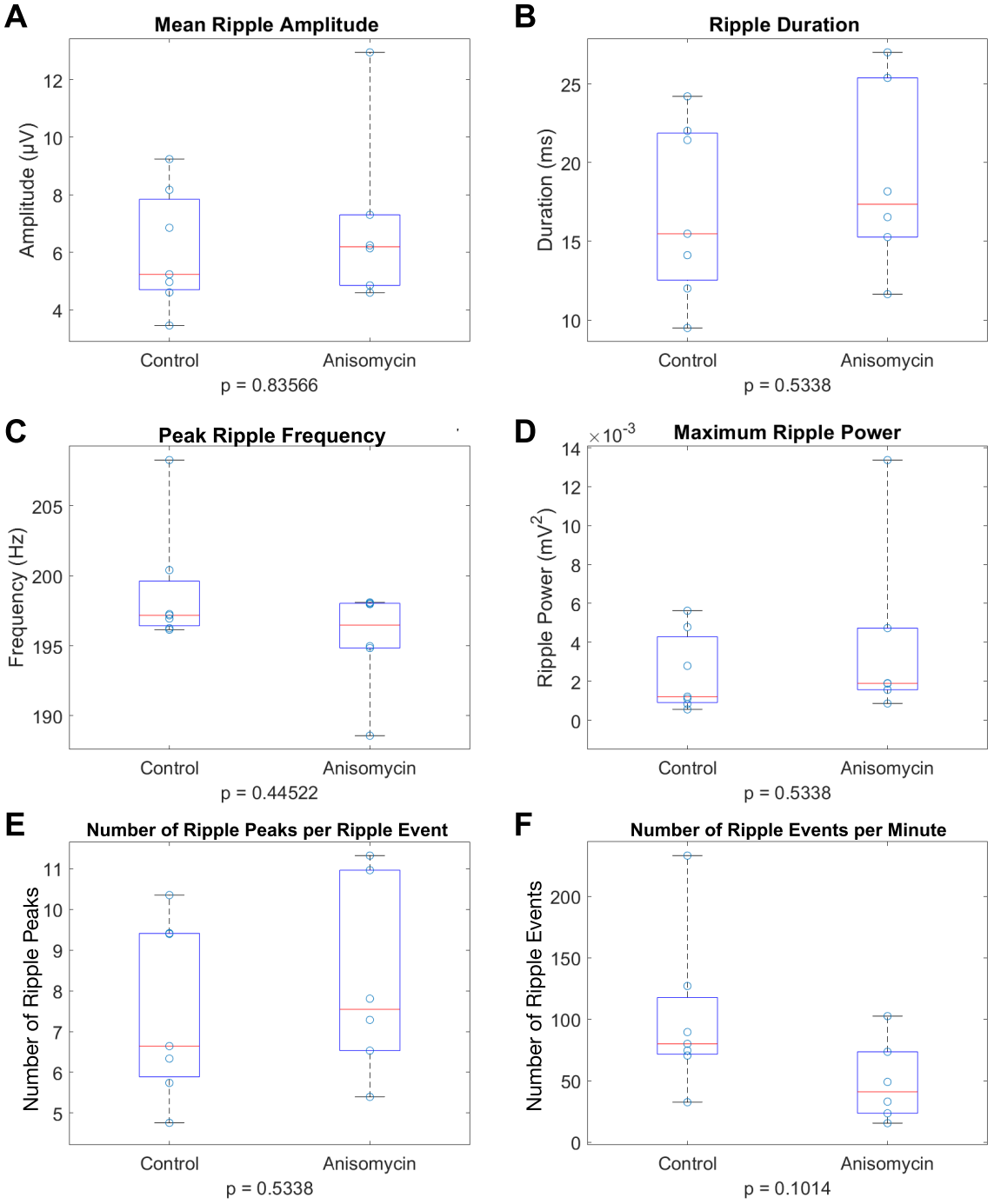

Figure 53: Incubation with 20 µM anisomycin had no effect on ripples. SWR recordings were taken from slices incubated for at least 2.5 h in either drug-free aCSF (control) or aCSF containing 20 µM anisomycin. Graphs show median, IQR, and range, $N_{control}$ = 7 slices, $N_{Anisomycin}$ = 6 slices (from 3 mice, split among conditions). The **(A)** mean ripple amplitude, **(B)** ripple duration, **(C)** peak ripple frequency, **(D)** maximum ripple power, **(E)** number of ripple peaks per ripple event, and **(F)** number of ripple events per minute were not significantly different between the two conditions. The results of the Mann-Whitney U-tests can be seen under each graph.

3.2.2.1.2 Anisomycin application after SWRs were recorded in anisomycin-free aCSF

To see if anisomycin might have a short-term effect on SWRs or if it might affect their maintenance after their generation, we first recorded spontaneously occurring SWRs from naive slices. Then, 20 µM anisomycin was applied for 35 minutes, before washing with drug-free aCSF. 2-minute snippets were taken from the last 20-35 minutes of baseline, the first 3-12 minutes of anisomycin, the last 27-35 minutes of anisomycin, and the last 27-35 minutes of wash.

Anisomycin had no effect on SW amplitude, SW duration, incidence of SWs per minute, or probability of cluster occurrence, as seen in Figure 54. Similarly, no significant change in mean ripple amplitude, ripple duration, peak ripple frequency, maximum power, number of ripple peaks per ripple event, or number of ripple events per minute was observed under any condition (Figure 55).

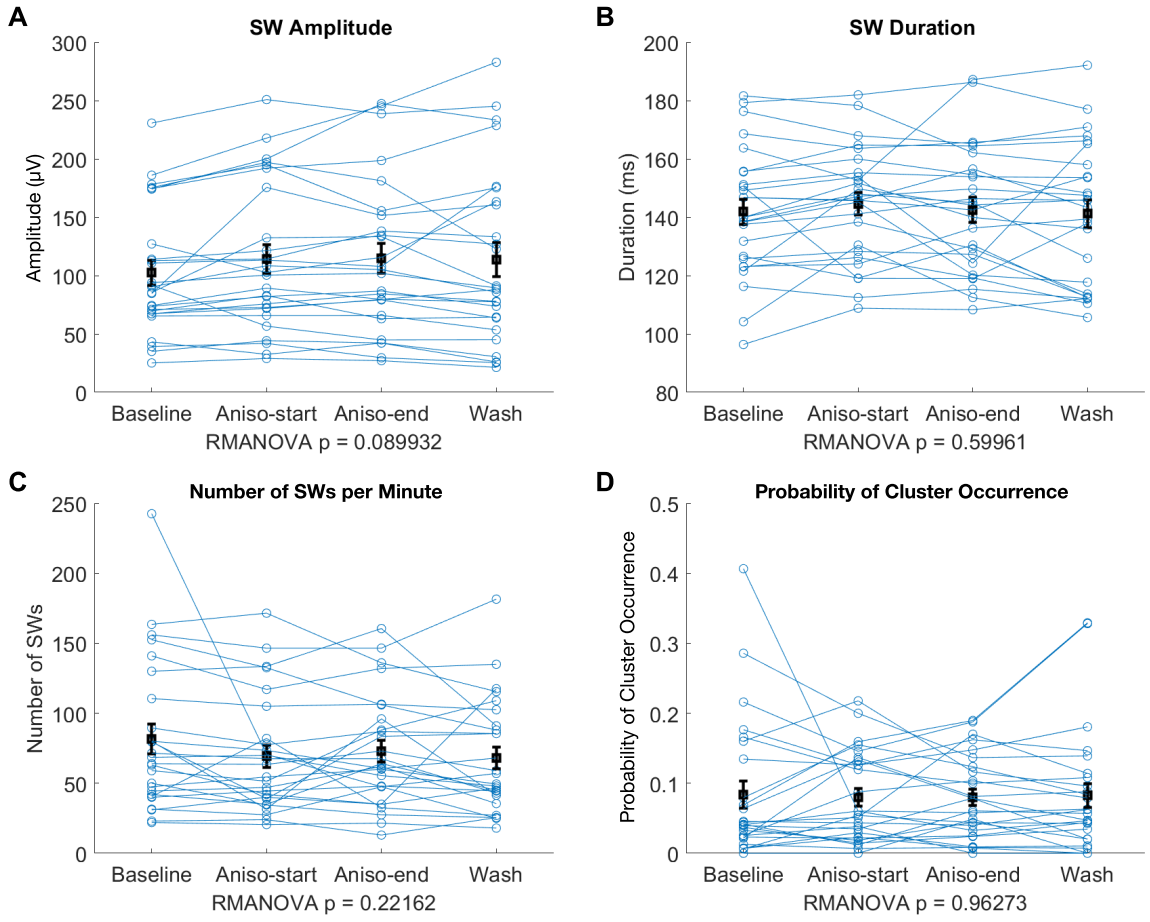

Figure 54: Short-term application of 20 µM anisomycin had no effect on SWs. SWR recordings were taken before anisomycin application, during the first 3-12 minutes of anisomycin application (Aniso-start), after at least 27 minutes of anisomycin application (Aniso-end) and after at least 27 minutes of wash with anisomycin-free aCSF, which correspond to the 4 conditions in each graph. Graphs show mean and SEM, N = 26 slices (from 5 mice). The **(A)** SW amplitude, **(B)** SW duration, **(C)** number of SWs per minute, and **(D)** probability of SW cluster occurrence did not change with anisomycin application. The results of the RMANOVAs can be seen at the bottom of each graph.

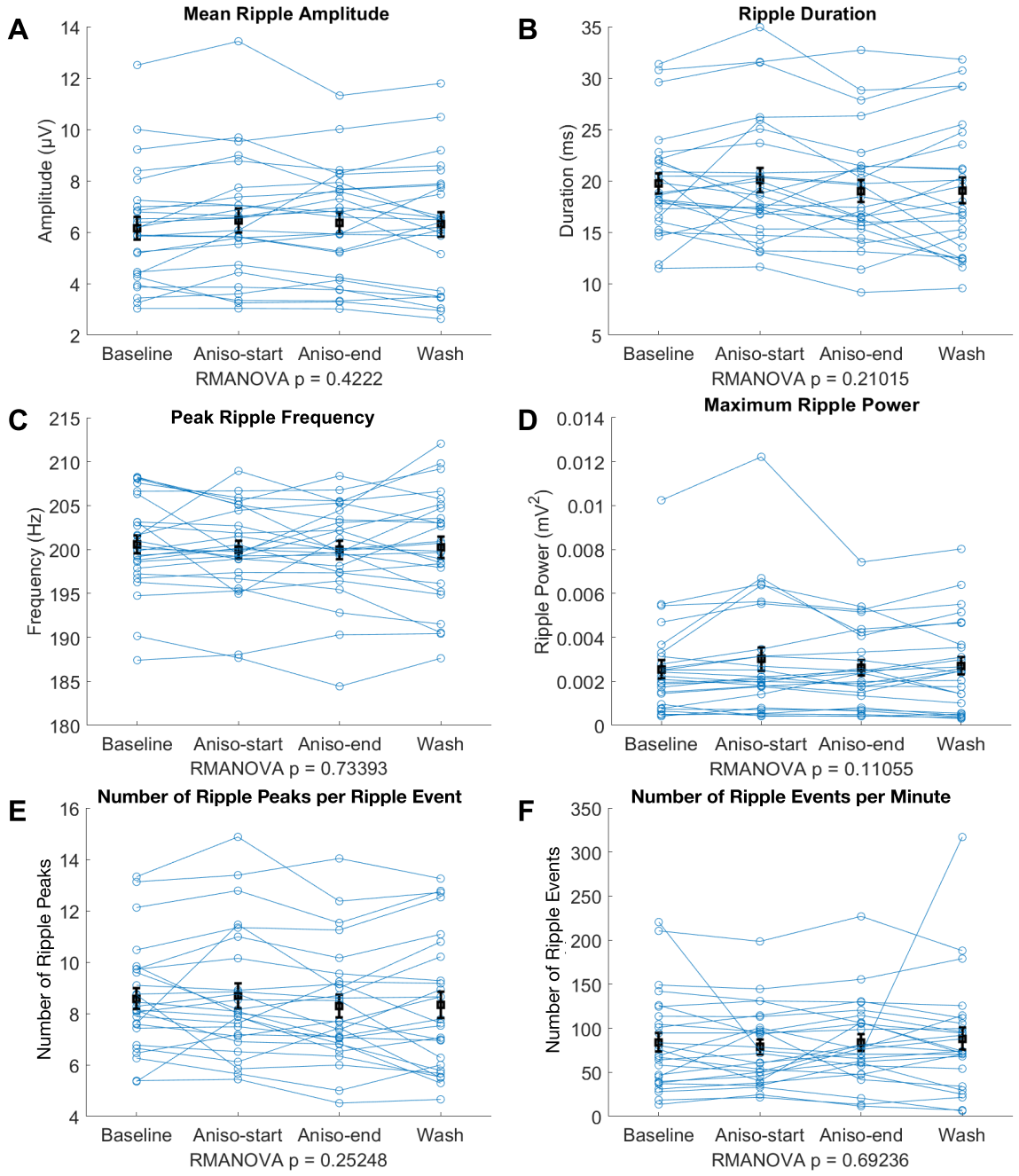

Figure 55: Short-term application of 20 µM anisomycin had no effect on ripples. SWR recordings were taken before anisomycin application, during the first 3-12 minutes of anisomycin application (Aniso-start), after at least 27 minutes of anisomycin application (Aniso-end) and after at least 27 minutes of wash with anisomycin-free aCSF, which correspond to the 4 conditions in each graph. Graphs show mean and SEM, N = 26 slices (from 5 mice). The **(A)** mean ripple amplitude, **(B)** ripple duration, **(C)** peak ripple frequency, **(D)** maximum ripple power, **(E)** number of ripple peaks per ripple event, and **(F)** number of ripple events per minute were not affected by anisomycin. The results of the RMANOVAs can be seen at the bottom of each graph.

3.2.2.2 Effect of HDAC inhibition, which enhances LTP, on SWRs

Suberoylanilide hydroxamic acid (SAHA, also known as Vorinostat and Zolinza) is an FDA-approved drug for the treatment of subcutaneous T-cell lymphoma (Thaler & Mercurio, 2014). It acts by blocking histone deacetylases (HDACs), which play a role in epigenetic regulation by promoting condensed chromatin structure and decreased transcription, as well as other cellular processes through deacetylation of non-histone proteins (Jenuwein & Allis, 2001; Hanson et al., 2013; Spange et al., 2009). SAHA has been shown to enhance excitatory synaptic function, lower the threshold for LTP induction, increase LTP magnitude, and block LTD in vitro (Hanson et al., 2013; Alarcón et al., 2004; Benito et al., 2015), hence having a profound effect on synaptic plasticity. We hypothesized that SAHA application before or after SWR generation would enhance SWRs.

3.2.2.2.1 Incubation with SAHA

We first tested if SWRs can be generated in the presence of 10 µM SAHA in DMSO. SWRs were seen after at least ~ 2.5 hours of incubation in SAHA (similar to control slices), with no changes in SW amplitude, duration, incidence, or probability of cluster occurrence (Figure 56). No change was seen in ripple amplitude, duration, peak ripple frequency, power, or the number of ripple peaks per event (Figure 57A-E), but a significant decrease was found in the number of ripple events per minute ($p = 0.045$; Figure 57F). A representative ripple trace and ripple event are shown on Figure 58 to illustrate the decreased incidence of ripples.

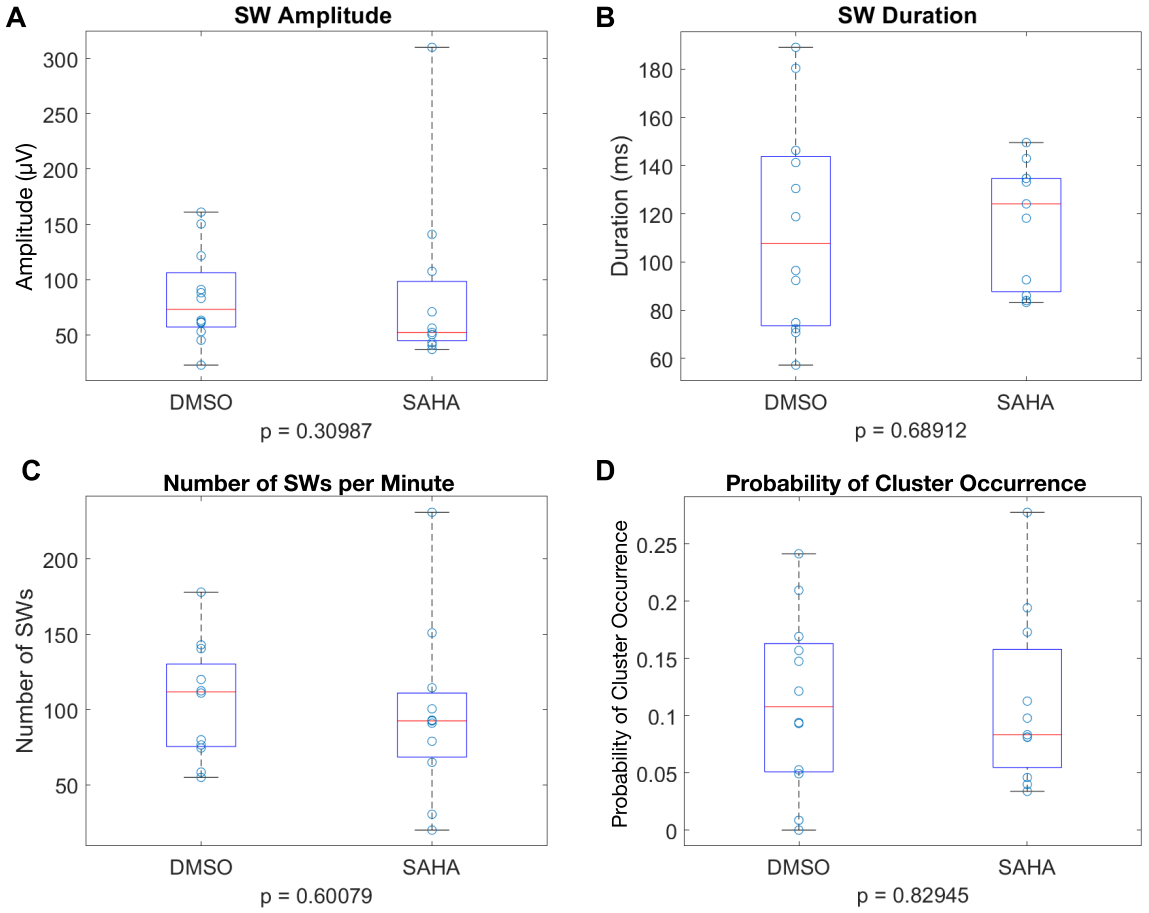

Figure 56: Incubation with 10 µM SAHA had no effect on SWs. SWR recordings were taken from slices incubated for at least 2.5 h in either SAHA-free aCSF (DMSO = control) or aCSF containing 10 µM SAHA. Graphs show median, IQR, and range, N_{DMSO} = 12 slices, N_{SAHA} = 11 slices (from 5 mice, split among conditions). The **(A)** SW amplitude, **(B)** SW duration, **(C)** number of SWs per minute, and **(D)** probability of SW cluster occurrence are not significantly different between the two conditions. The results of the Mann-Whitney U-tests can be seen under each graph.

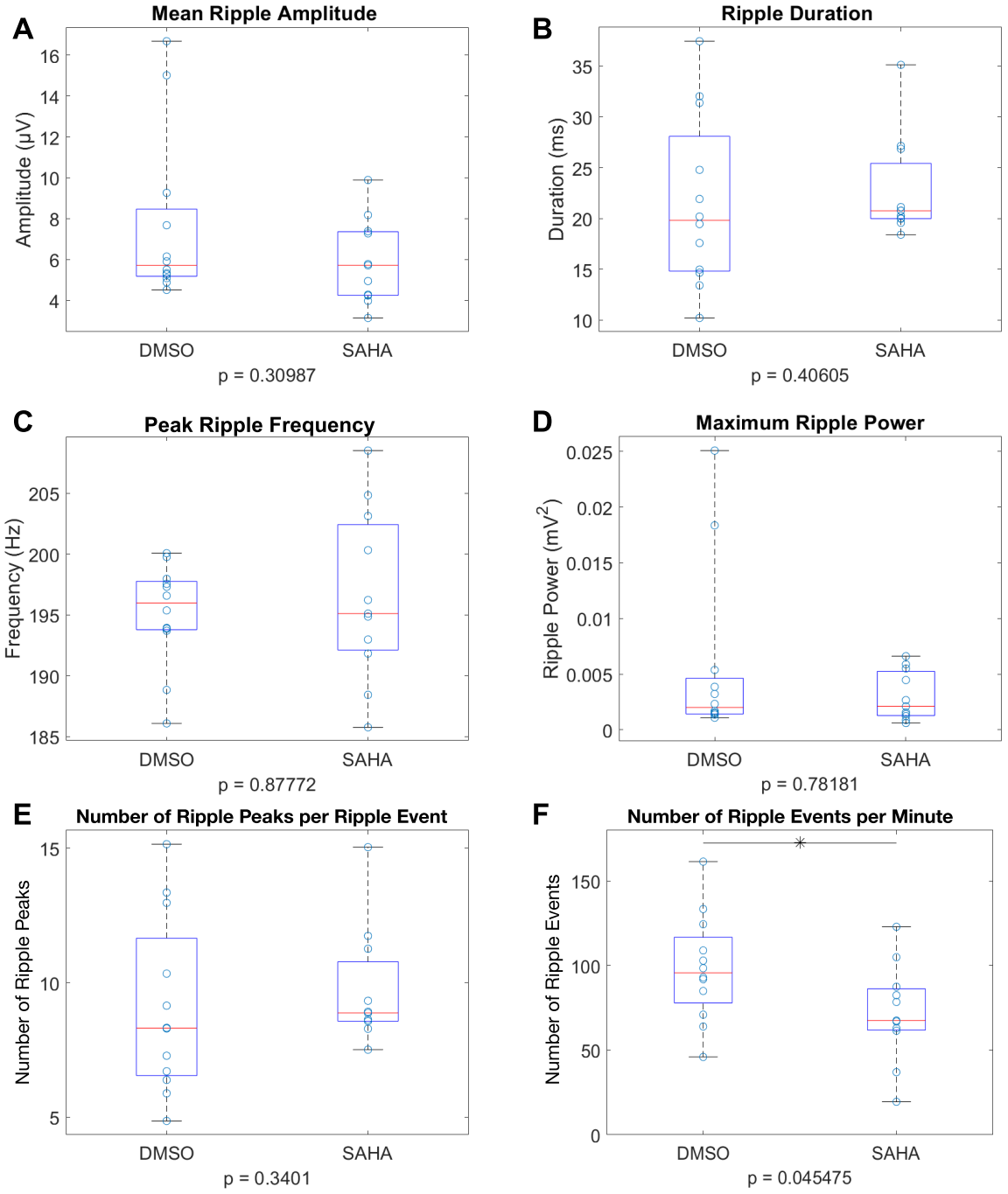

Figure 57: Incubation with 10 µM SAHA decreased ripple occurrence. SWR recordings were taken from slices incubated for at least 2.5 h in either SAHA-free aCSF (DMSO = control) or aCSF containing 10 µM SAHA. Graphs show median, IQR, and range, N_{DMSO} = 12 slices, N_{SAHA} = 11 slices (from 5 mice, split among conditions). The **(A)** mean ripple amplitude, **(B)** ripple duration, **(C)** peak ripple frequency, **(D)** maximum ripple power, and **(E)** number of ripple peaks per ripple event were not significantly different between the two conditions. **(F)** The number of ripple events per minute was significantly decreased after incubation with SAHA. The results of the Mann-Whitney U-tests can be seen under each graph.

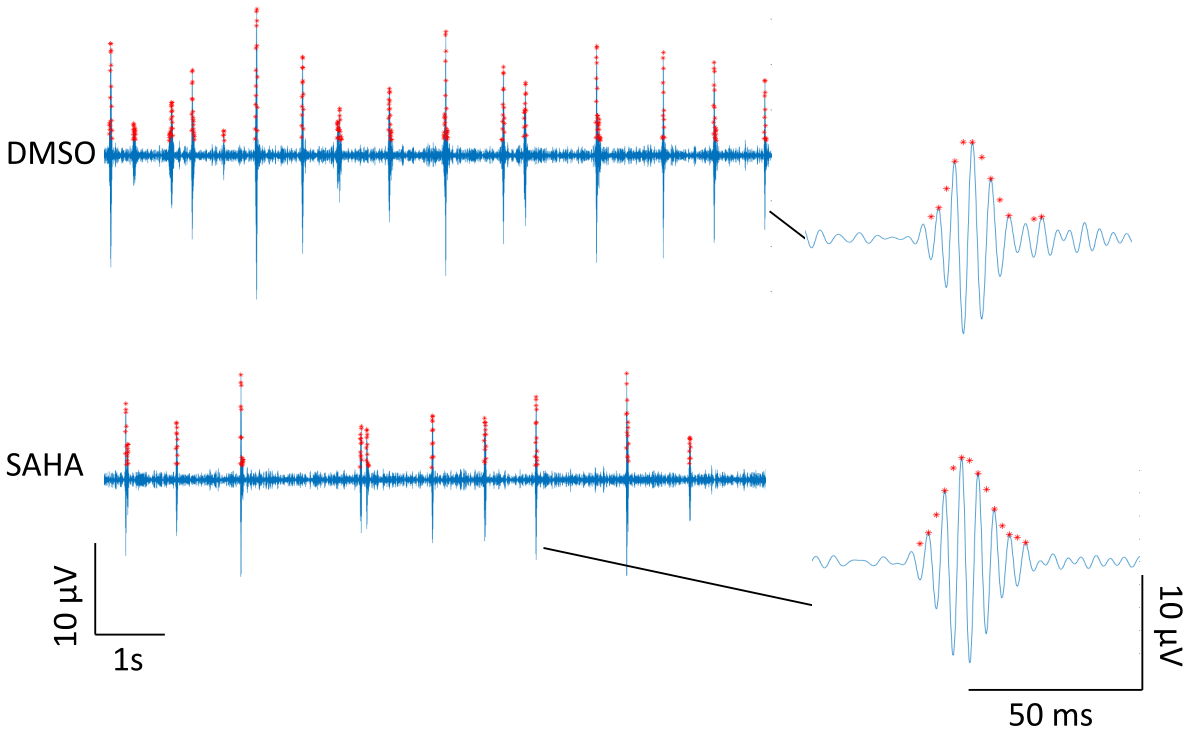

Figure 58: Representative ripple traces from slices incubated with SAHA or DMSO (vehicle) alone, showing decreased ripple occurrence after SAHA incubation. The LFP was first high-pass filtered at 0.5 Hz and then bandpass filtered at 140-250 Hz to isolate ripples. Red asterisks indicate ripple peaks detected by the code. A 10-second snippet is shown from slices incubated in DMSO (top) or SAHA (bottom). Notice the decreased number of ripple events in the presence of SAHA (mean for this slice = 85 events per minute) compared to DMSO (mean for this slice = 67.5 events per minute). A representative ripple event example from each recording is also shown.

3.2.2.2.2 SAHA application after SWRs were recorded in SAHA-free aCSF

To see if SAHA might have a short-term effect on SWRs or if it might affect their maintenance after SWR generation, we first recorded spontaneously occurring SWRs from naive slices. Then, 10 µM SAHA was applied for 35 minutes, before washing with SAHA-free aCSF. 2-minute snippets were taken from the last 20-35 minutes of baseline, the first 3-12 minutes of SAHA, the last 27-35 minutes of SAHA, and the last 27-35 minutes of wash.

SAHA application had no effect on SW amplitude, duration, incidence, or probability of cluster occurrence (Figure 59). Ripples were unaffected in terms of amplitude, frequency, power, or number of ripple events per minute (Figure 60A, C, D, F). The RMANOVA test is significant for ripple duration ($p = 0.038$; Figure 60B) and the number of ripple peaks per ripple event ($p = 0.049$; Figure 60E), but the post-hoc test did not identify any specific differences between conditions. The result of the RMANOVA was therefore attributed to a tendency for both measures to increase slightly throughout the experiment.

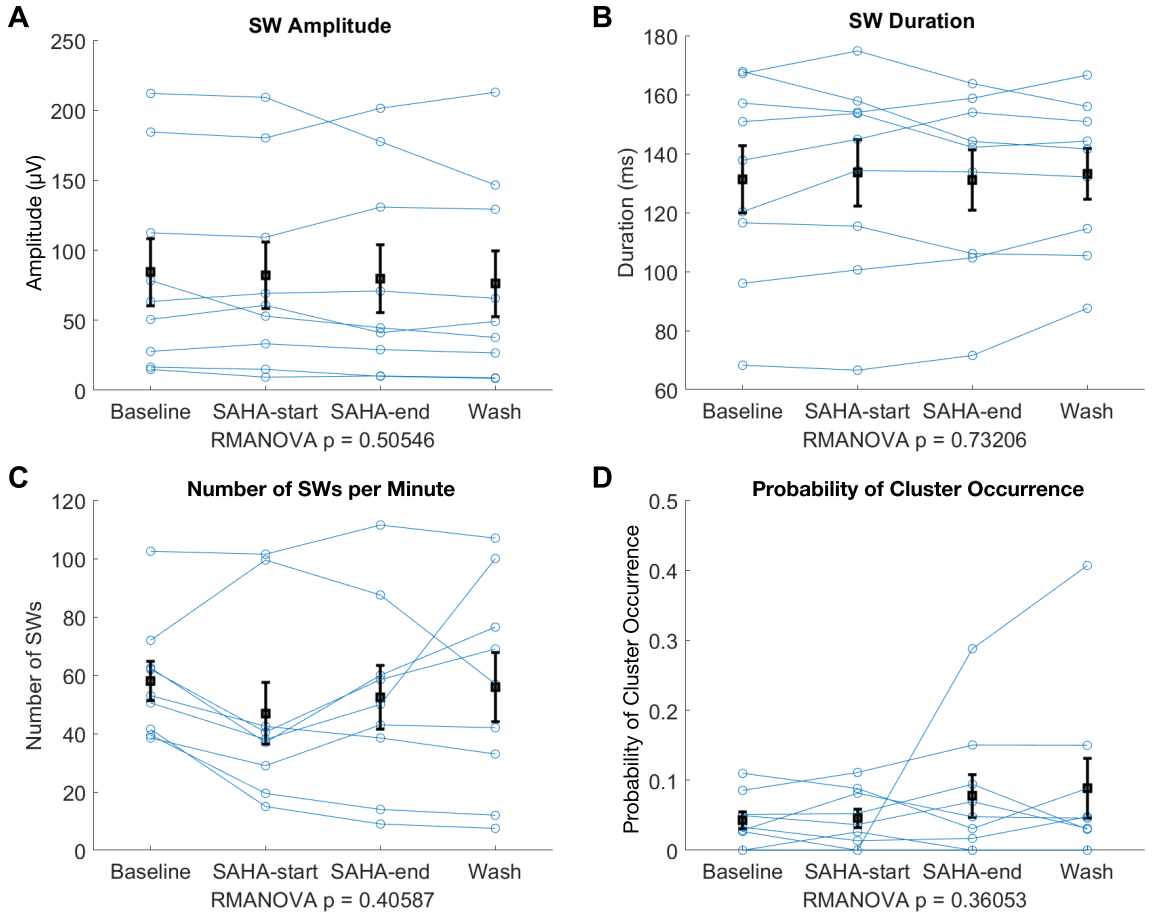

Figure 59: Short-term application of 10 µM SAHA had no effect on SWs. SWR recordings were taken before SAHA application, during the first 3-12 minutes of SAHA application (SAHA-start), after at least 27 minutes of SAHA application (SAHA-end), and after at least 27 minutes of wash with SAHA-free aCSF, which correspond to the 4 conditions in each graph. Graphs show mean and SEM, N = 9 slices (from 2 mice). The **(A)** SW amplitude, **(B)** SW duration, **(C)** number of SWs per minute, and **(D)** probability of SW cluster occurrence did not change with SAHA application. The results of the RMANOVAs can be seen at the bottom of each graph.

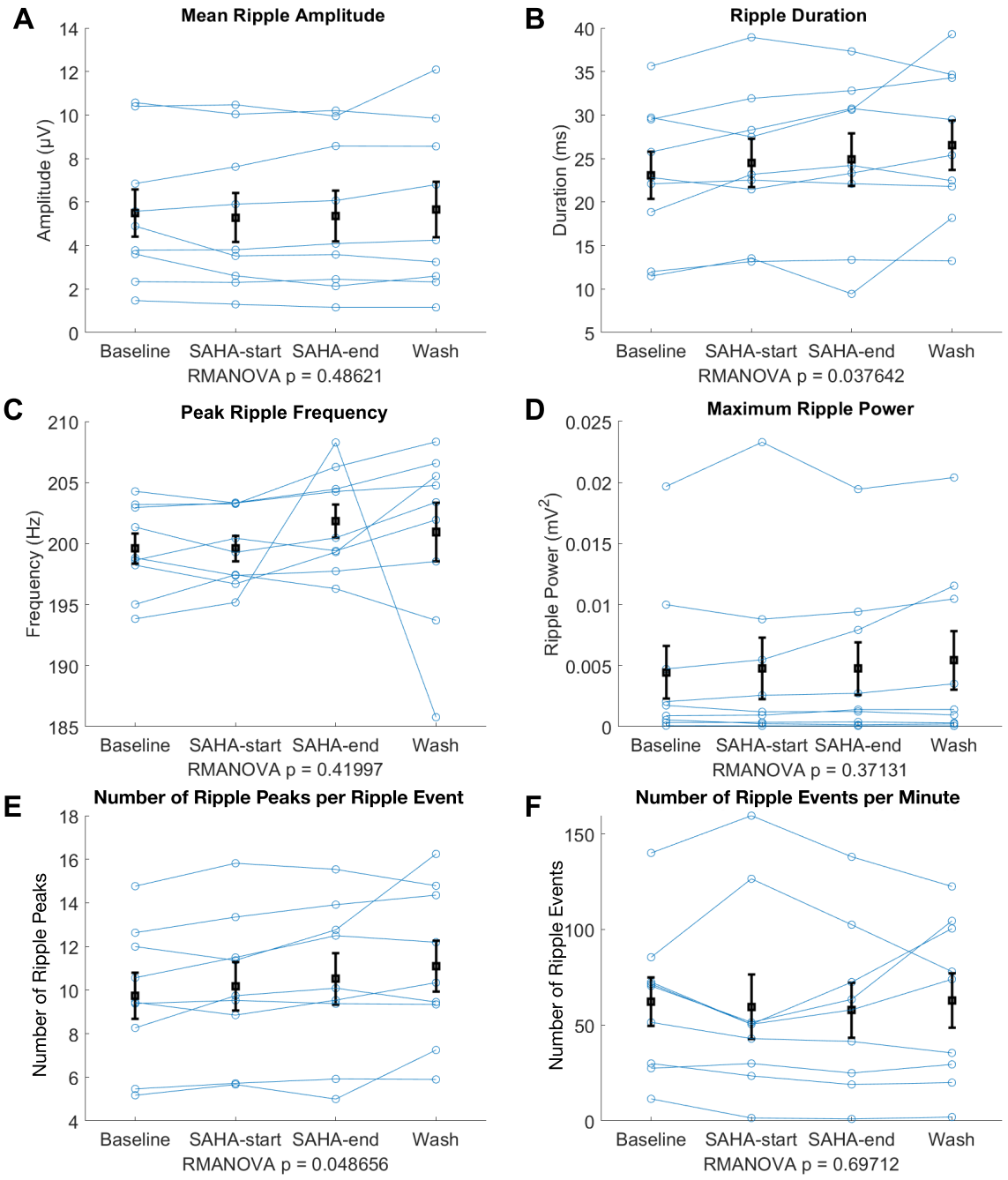

Figure 60: Short-term application of 10 μM SAHA tended to increase ripple duration and number of peaks per event. SWR recordings were taken before SAHA application, during the first 3-12 minutes of SAHA application (SAHA-start), after at least 27 minutes of SAHA application (SAHA-end), and after at least 27 minutes of wash with SAHA-free aCSF, which correspond to the 4 conditions in each graph. Graphs show mean and SEM, N = 9 slices (from 2 mice). **(A)** Mean ripple amplitude was unaffected by SAHA application. **(B)** Ripple duration was increased overall (RMANOVA p = 0.0376), but no significant differences were seen among specific conditions after the post-hoc test. **(C)** Peak ripple frequency and **(D)** maximum ripple power were similar among conditions. **(E)** The number of ripple peaks per ripple event increased overall (RMANOVA p = 0.0487), but no significant differences were seen among specific conditions after the post-hoc test. **(F)** The number of ripple events per

minute was not affected by SAHA application. The results of the RMANOVAs can be seen at the bottom of each graph.

3.2.3 SWRs and Alzheimer's disease - tau experiments

Many SWR alterations are observed in AD models or models of tauopathies. For example, rTg4510 mice have decreased amplitude, power, and rate of SWRs (Witton et al., 2016; Ciupek et al., 2015). Moreover, tau exogenously applied to slices decreased LTP magnitude (Acquarone et al., 2019; Fá et al., 2016). We therefore hypothesized that tau would either prevent SWR generation if slices were pre-incubated with tau before spontaneous SWRs form, or it would reduce SWR amplitude, duration, or occurrence if applied after SWRs appear.

3.2.3.1 ohtau40-H_2O_2 experiments

3.2.3.1.1 Incubation with ohtau40-H_2O_2

We first incubated slices in either drug-free or tau-containing aCSF for at least 2.5 hours. Incubation with tau did not prevent SWR generation, so we recorded SWRs to examine SWR parameters. No differences were seen in SW amplitude, duration, number of SWs per minute, or probability of cluster occurrence, as seen in Figure 61. Ripples were similarly unaffected, as ripple amplitude, duration, frequency, power, number of ripple peaks per ripple event, and number of ripple events per minute were similar in the two groups (Figure 62).

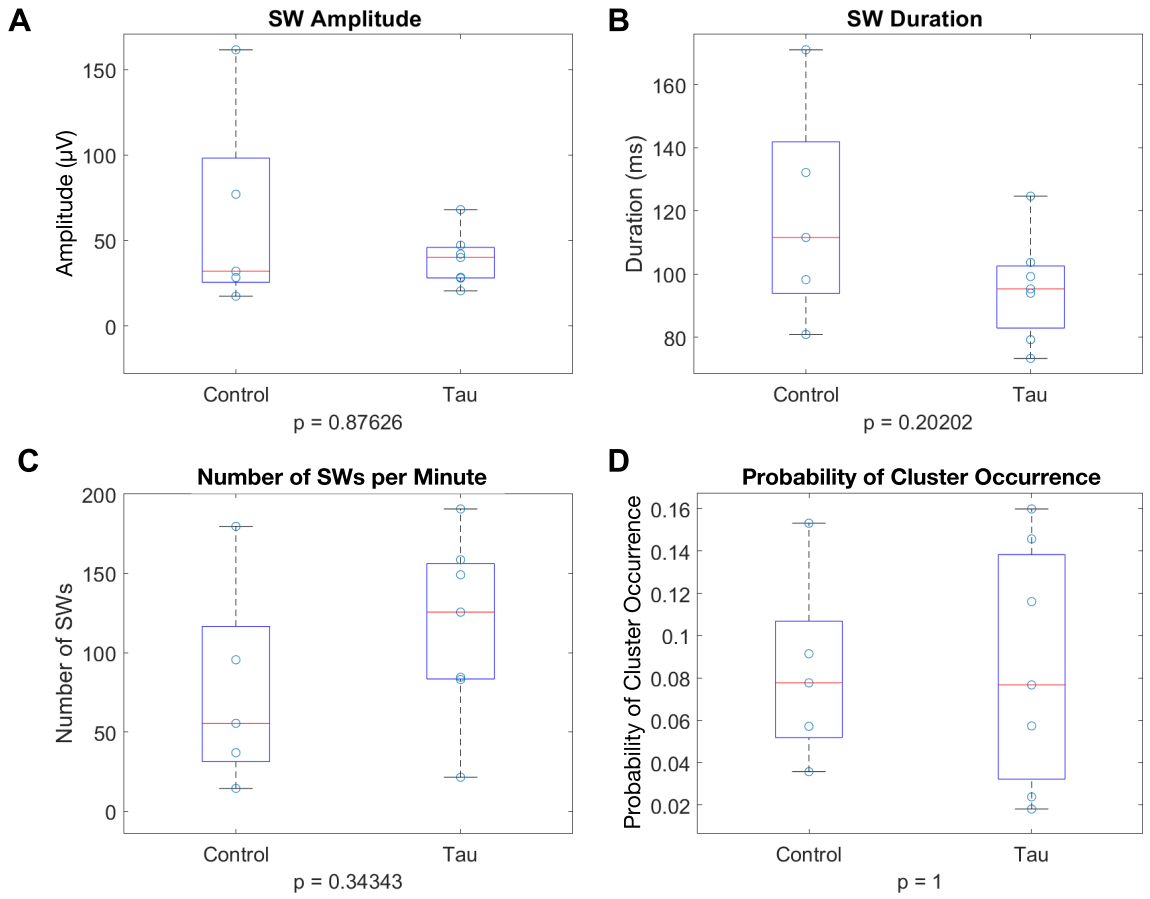

Figure 61: Incubation with 25 nM ohtau40-H_2O_2 had no effect on SWs. SWR recordings were taken from slices incubated for at least 2.5 h in either drug-free aCSF (control) or aCSF containing 25 nM ohtau40-H_2O_2. Graphs show median, IQR, and range, $N_{control}$ = 5 slices, N_{tau} = 7 slices (from 2 mice, split among conditions). The **(A)** SW amplitude, **(B)** SW duration, **(C)** number of SWs per minute, and **(D)** probability of SW cluster occurrence were not significantly different between the two conditions. The results of the Mann-Whitney U-tests can be seen under each graph.

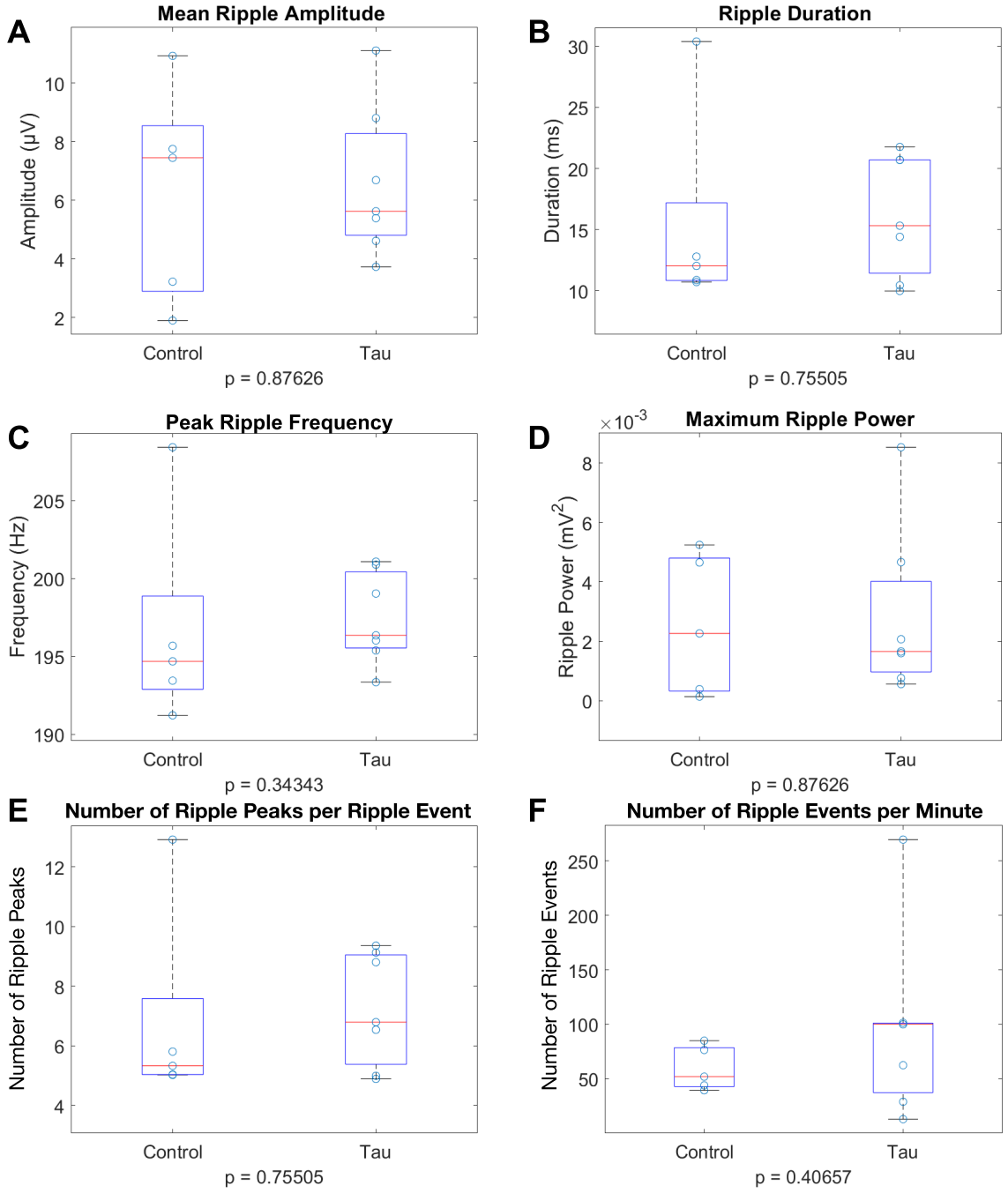

Figure 62: Incubation with 25 nM ohtau40-H_2O_2 had no effect on ripples. SWR recordings were taken from slices incubated for at least 2.5 h in either drug-free aCSF (control) or aCSF containing 25 nM ohtau40-H_2O_2. Graphs show median, IQR, and range, $N_{control}$ = 5 slices, N_{tau} = 7 slices (from 2 mice, split among conditions). The **(A)** mean ripple amplitude, **(B)** ripple duration, **(C)** peak ripple frequency, **(D)** maximum ripple power, **(E)** number of ripple peaks per ripple event, and **(F)** number of ripple events per minute were not significantly different between the two conditions. The results of the Mann-Whitney U-tests can be seen under each graph.

3.2.3.1.2 ohtau40-H_2O_2 application after SWRs were recorded in tau-free aCSF

To test for short-term effects of tau on SWR maintenance, we applied tau after SWRs were recorded in naive slices, and analyzed two time-points, one at the start (first 3-12 minutes) of tau application and one at the end (27-35 minutes). As seen in Figure 63, application of 25 nM ohtau40-H_2O_2 had no effect on SW amplitude, SW duration, number of SWs per minute, or probability of cluster occurrence. In agreement, no significant changes in ripple amplitude, ripple duration, peak ripple frequency, maximum ripple power, or number of ripple peaks per ripple event were observed under any condition (Figure 64A-E). While the RMANOVA suggested a significant change in the number of ripple events per minute ($p = 0.014$, Figure 64F), no significant changes were identified among specific conditions after the post-hoc test. Visual inspection suggests that ripple incidence tended to decrease in the last two conditions of the experiment.

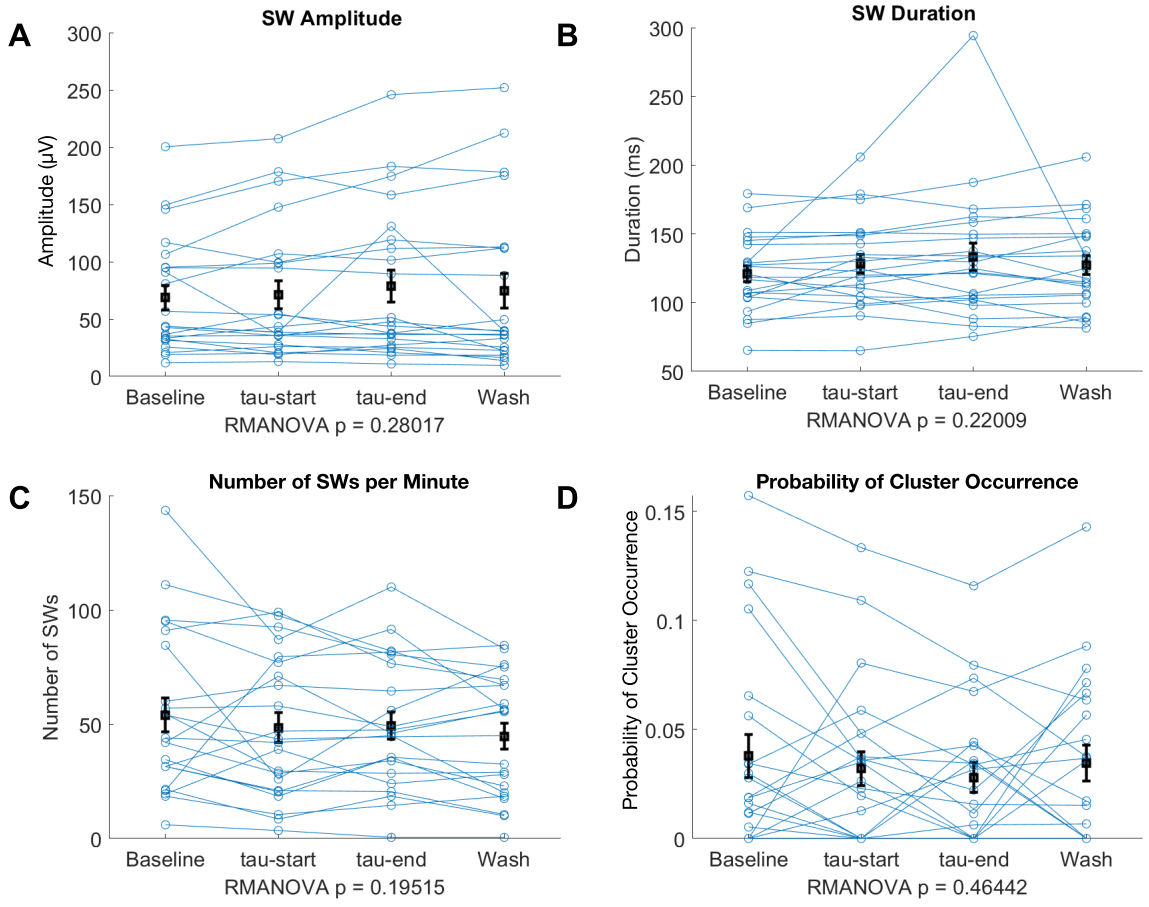

Figure 63: Short-term application of 25 nM ohtau40-H_2O_2 had no effect on SWs. SWR recordings were taken before tau application, during the first 3-12 minutes of tau application (tau-start), after at least 27 minutes of tau application (tau-end), and after at least 27 minutes of wash with tau-free aCSF, which correspond to the 4 conditions in each graph. Graphs show mean and SEM, N = 22 slices (from 6 mice). The **(A)** SW amplitude, **(B)** SW duration, **(C)** number of SWs per minute, and **(D)** probability of SW cluster occurrence did not change with tau application. The results of the RMANOVAs can be seen at the bottom of each graph.

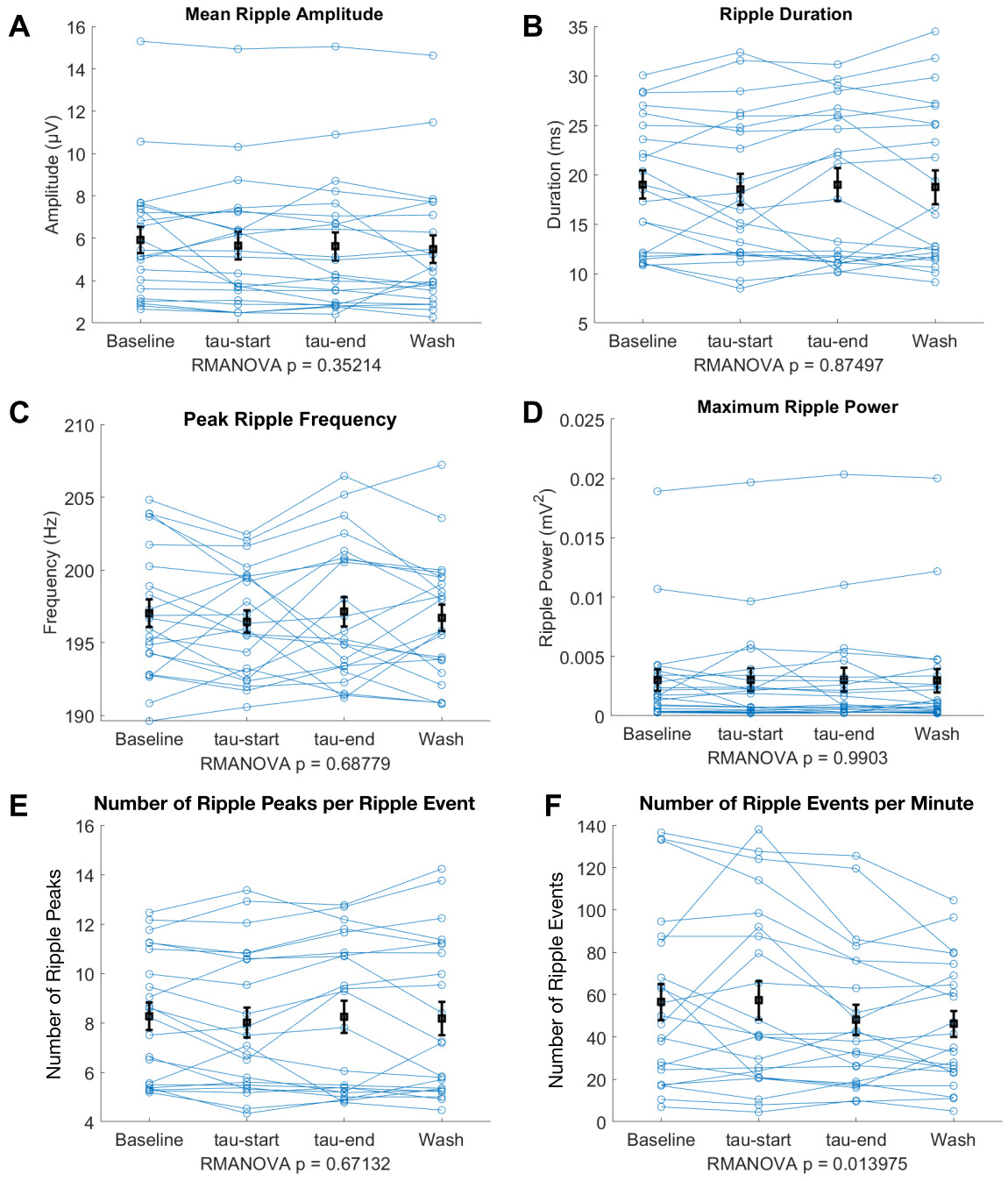

Figure 64: Short-term application of 25 nM ohtau40-H_2O_2 tended to decrease ripple incidence. SWR recordings were taken before tau application, during the first 3-12 minutes of tau application (tau-start), after at least 27 minutes of tau application (tau-end), and after at least 27 minutes of wash with tau-free aCSF, which correspond to the 4 conditions in each graph. Graphs show mean and SEM, N = 22 slices (from 6 mice). The **(A)** mean ripple amplitude, **(B)** ripple duration, **(C)** peak ripple frequency, **(D)** maximum ripple power, and **(E)** number of ripple peaks per ripple event were not affected by tau application. **(F)** The number of ripple events per minute tended to decrease during the experiment (RMANOVA p = 0.014), but no significant differences were seen among specific conditions after the post-hoc test. The results of the RMANOVAs can be seen at the bottom of each graph.

3.2.3.2 ohtau40-heparin application after SWRs were recorded in tau-free aCSF

Above, we used the protocol by Acquarone et al., 2019, to prepare tau. Since we did not see prominent effects with this treatment, we decided to repeat the second type of experiment (application of tau after baseline SWRs have been recorded) using a different method for ohtau40 preparation that leads to greater generation of oligomers and β-sheets (see methods, Figure 4). Slices were prepared and incubated in drug-free aCSF. After at least 2 hours incubation, slices with SWRs were identified and recorded for at least 35 minutes. 25 nM of ohtau40-heparin was applied for 35 minutes, after which slices were washed with drug-free aCSF. 2-minute snippets were taken from the last 20-35 minutes of baseline, the first 3-12 minutes of tau, the last 27-35 minutes of tau, and the last 27-35 minutes of wash.

Tau application in this case caused a significant decrease in SW amplitude after at least 27 minutes of tau application as shown by the post-hoc test ($p_{Baseline\text{-}tauEnd} = 0.029$, $p_{tauStart\text{-}tauEnd} = 0.021$), even though only a tendency is seen in the RMANOVA ($p = 0.063$; Figure 65A). Exposure to ohtau40-heparin had no effect on SW duration (Figure 65B). Furthermore, the number of SWs per minute significantly decreased ($p = 0.00047$; Figure 65C) at the end of tau application compared to baseline and wash ($p_{Baseline\text{-}tauEnd} = 0.00098$, $p_{tauEnd\text{-}Wash} = 0.012$), as well as at the start of tau application compared to baseline ($p_{Baseline\text{-}tauStart} = 0.026$). The probability of cluster occurrence was unaffected by tau (Figure 65D).

Similarly, application of ohtau40-heparin caused a decrease in mean ripple amplitude and power (for both $p < 0.0001$; Figure 66A, D) at the end of tau exposure compared to baseline and at the beginning of tau application. Ripple amplitude and power were also lower during wash compared to baseline (amplitude: $p_{Baseline\text{-}tauEnd} < 0.0001$, $p_{tauStart\text{-}tauEnd} = 0.0078$, $p_{Baseline\text{-}Wash} = 0.00079$; power: $p_{Baseline\text{-}tauEnd} = 0.00105$, $p_{tauStart\text{-}tauEnd} = 0.032$, $p_{Baseline\text{-}Wash} = 0.0012$). Ripple duration and number of ripple peaks per ripple event were unaffected by tau (Figure 66B, E). At the end of tau application, the peak ripple frequency and the number of ripple events per minute were significantly lower compared to baseline ($p_{Baseline\_tauEnd} = 0.033$, Figure 66C; $p_{Baseline\_tauEnd} = 0.0093$, Figure 66F, respectively). Representative SWR traces are seen on Figure 67 to show the change in SW amplitude and SW and ripple incidence, while representative ripple events are shown on Figure 68 to illustrate the decreased amplitude, frequency, and power after tau application.

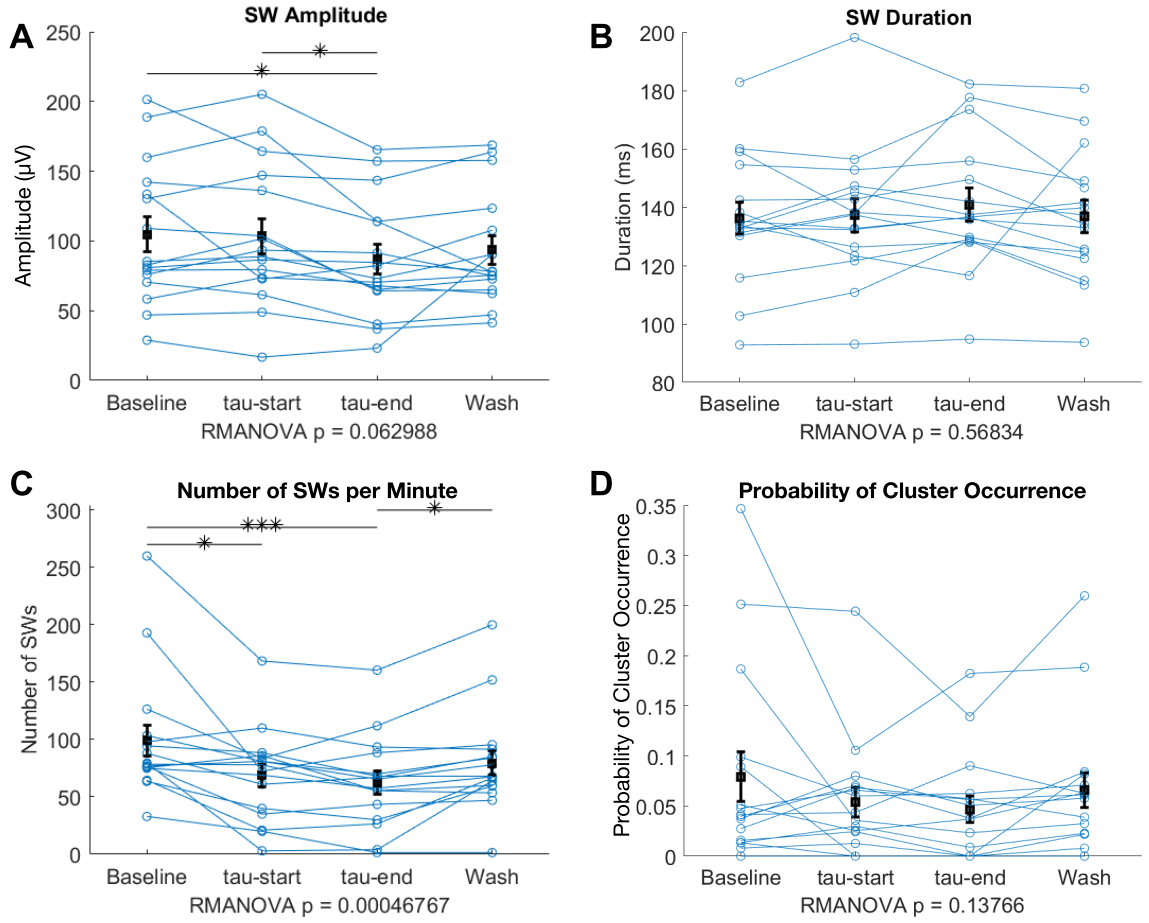

Figure 65: Short-term application of 25 nM ohtau40-heparin decreased SW amplitude and number of SWs per minute. SWR recordings were taken before tau application, during the first 3-12 minutes of tau application (tau-start), after at least 27 minutes of tau application (tau-end), and after at least 27 minutes of wash with tau-free aCSF, which correspond to the 4 conditions in each graph. Graphs show mean and SEM, N = 16 slices (from 8 mice). **(A)** SW amplitude significantly decreased towards the end of tau application compared to baseline and beginning of tau application according to the post-hoc test, but only a tendency was seen in the RMANOVA. **(B)** SW duration was not affected by ohtau40-heparin. **(C)** The number of SWs per minute was significantly lower after at least 27 minutes of tau application compared to baseline and wash conditions, as well as after at least 3 minutes of tau application compared to baseline. **(D)** The probability of SW cluster occurrence was unaffected by ohtau40-heparin. The results of the RMANOVAs can be seen at the bottom of each graph, while the significance lines are based on the results of the Tukey's HSD post-hoc test with multiple comparisons correction (* = $p < 0.05$; *** = $p < 0.001$).

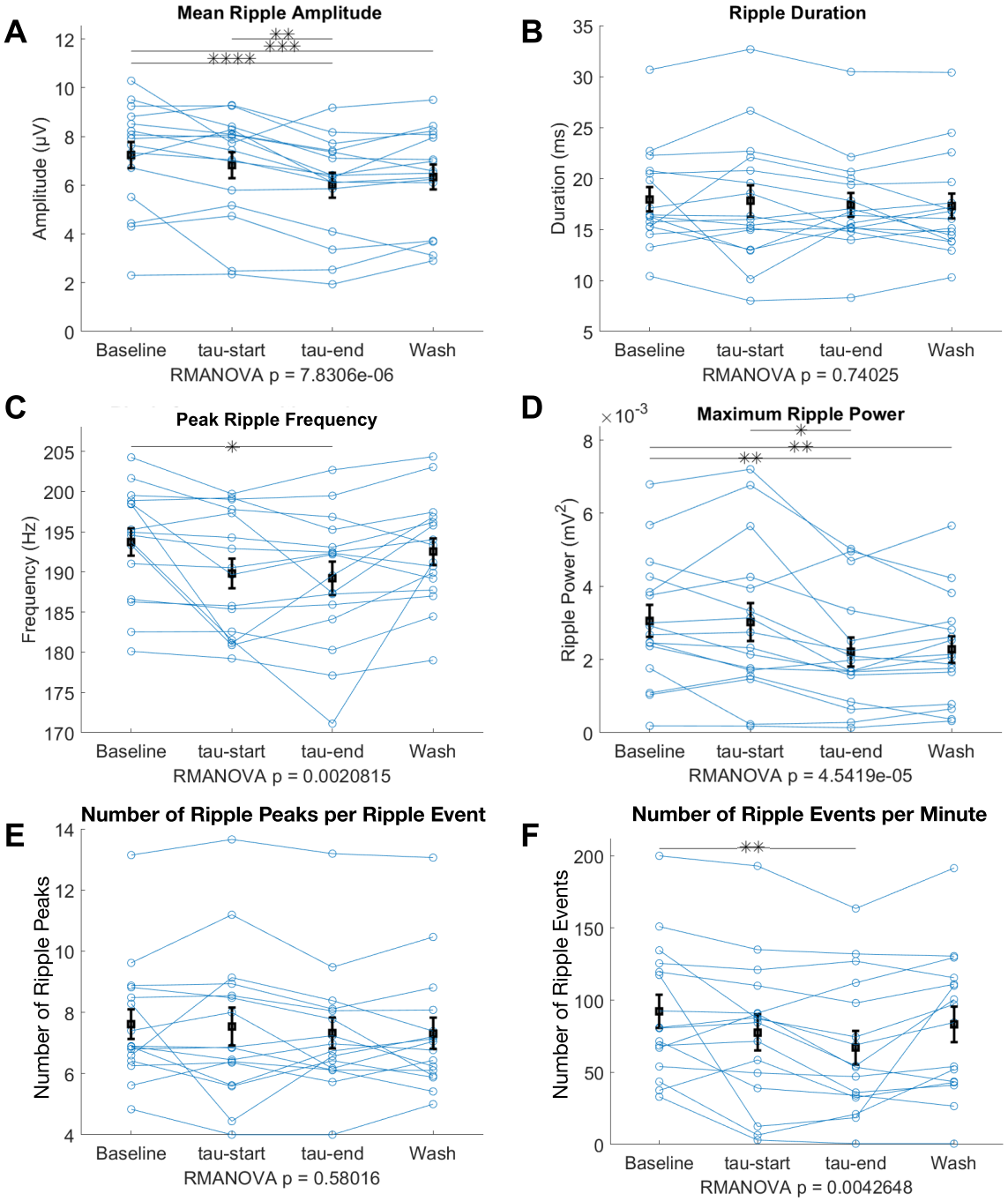

Figure 66: Short-term application of 25 nM ohtau40-heparin decreased ripple amplitude, frequency, power, and number of ripple events per minute. SWR recordings were taken before tau application, during the first 3-12 minutes of tau application (tau-start), after at least 27 minutes of tau application (tau end), and after at least 27 minutes of wash with tau-free aCSF, which correspond to the 4 conditions in each graph. Graphs show mean and SEM, with N = 16 slices (from 8 mice). **(A)** The mean ripple amplitude was significantly lower at the end of tau application compared to baseline or the beginning of tau application, as well as after wash compared to baseline. **(B)** Ripple duration was not affected by ohtau40-heparin application. **(C)** Peak ripple frequency was lower after at least 27 minutes of ohtau40-heparin application compared to baseline. **(D)** Maximum ripple power was significantly lower at the end of tau application compared to baseline or the beginning of tau

application, as well as after wash compared to baseline. **(E)** The number of ripple peaks per ripple event was not affected by ohtau40-heparin. **(F)** The number of ripple events per minute was significantly lower at the end of ohtau40-heparin application compared to baseline. The results of the RMANOVAs can be seen at the bottom of each graph. The significance lines shown on the graphs are based on the results of the Tukey's HSD post-hoc test with multiple comparisons correction (* = p < 0.05; ** = p < 0.01; *** = p < 0.001; **** = p < 0.0001).

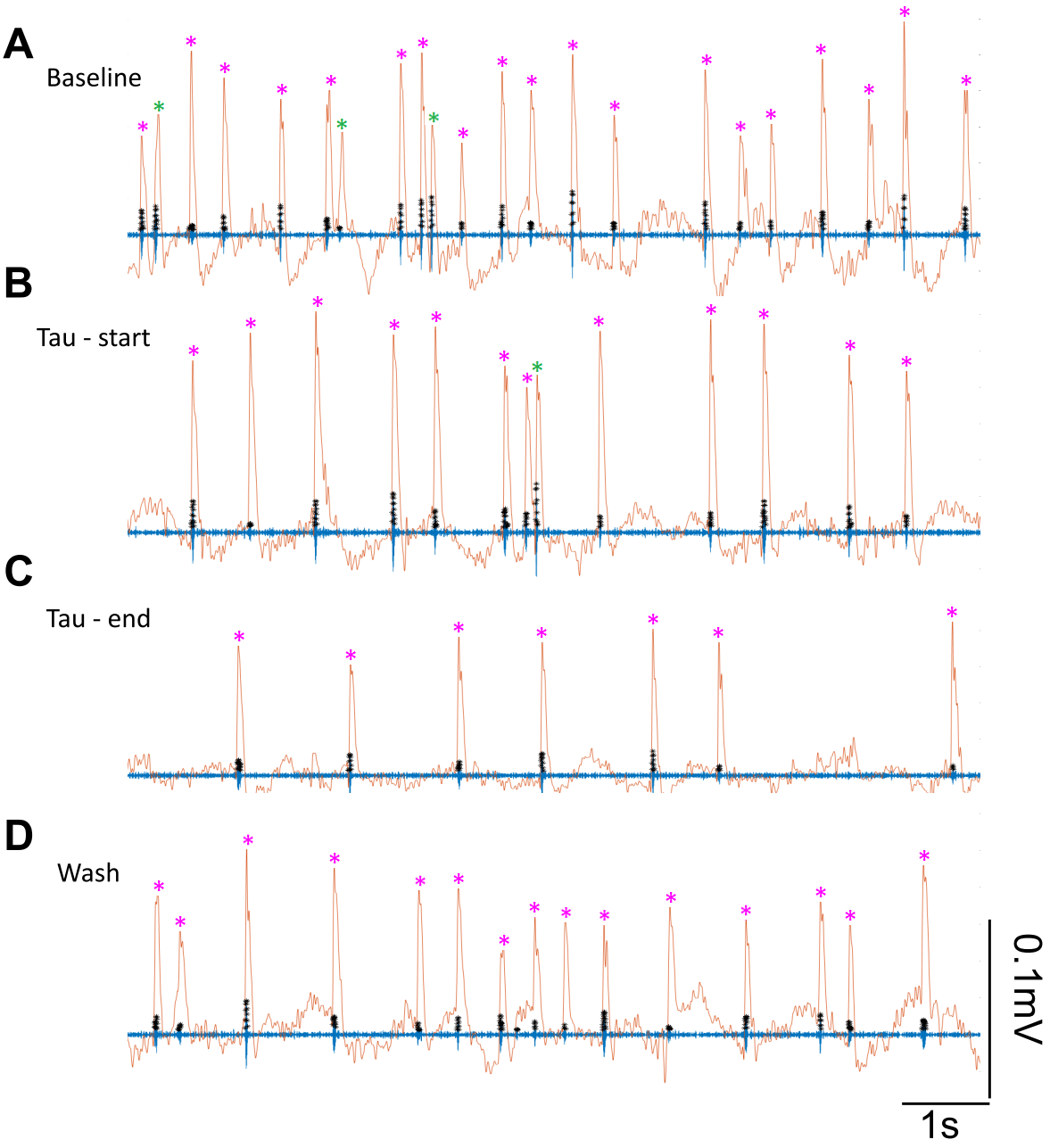

Figure 67: Representative SWR traces from the different conditions of the ohtau40-heparin experiment, showing decreased SW amplitude and decreased SW and ripple incidence after tau application. Both blue and orange traces were high-pass filtered at 0.5 Hz. Orange trace was then

low-pass filtered at 40 Hz showing SWs, while the blue trace was bandpassed at 140-250 Hz, isolating ripples. Asterisks indicate SWs (pink = primary, green = secondary SWs of a cluster) and ripple (black) peaks detected by the code. A 10-second snippet is shown from each condition: **(A)** baseline, **(B)** start of tau application, **(C)** end of tau application, and **(D)** wash. Notice the decreased SW amplitude at the end of tau application (mean for this slice = 65 μV) compared to baseline (mean for this slice = 83 μV) and beginning of tau application (mean for this slice = 102 μV). Also note the decreased number of SWs at the end of tau application (mean for this slice = 70) compared to baseline (mean for this slice = 104) and wash (mean for this slice = 84), as well as between the beginning of tau application (mean for this slice = 81) and baseline. The number of ripples per minute was also decreased at the end of tau application (mean for this slice = 75) compared to baseline (mean for this slice = 135).

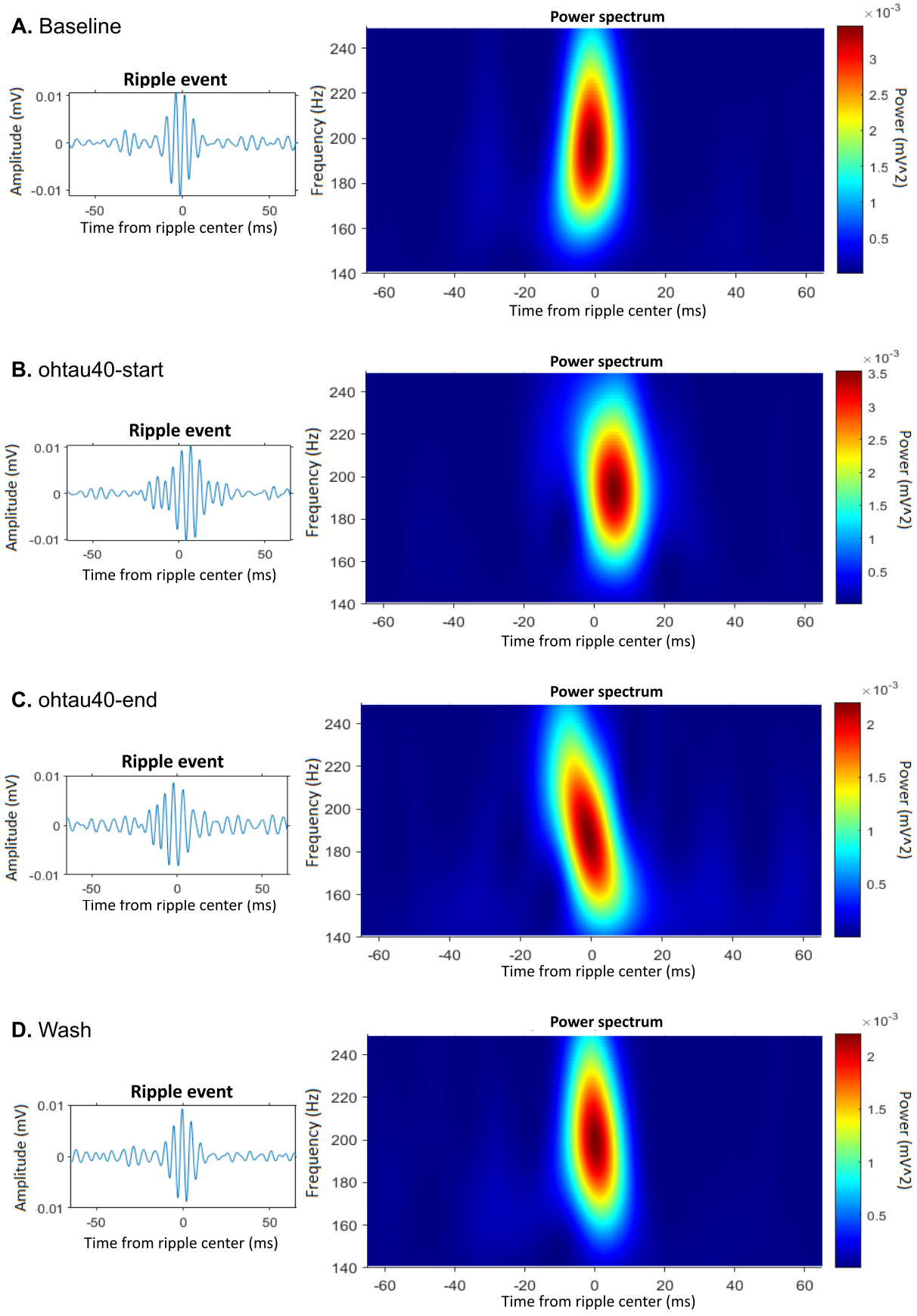

Figure 68: Representative examples of ripple events and power spectra in different conditions of the ohtau40-heparin experiment, showing decreased ripple amplitude, power, and frequency after

tau application. One ripple event from the same slice under each of the four conditions **(A)** baseline, **(B)** start of tau application, **(C)** end of tau application, and **(D)** wash is shown. Notice the lower ripple amplitude and power in the last two conditions (tau-end: 5.5 μV, 2.2 $*10^{-3}mV^2$, wash: 5.9 μV, 2.2 $*10^{-3}$ mV^2) compared to baseline (7.8 μV, $3.5*10^{-3}$ mV^2) and start of tau application (6.6 μV, $3.5*10^{-3}$ mV^2), as well as the lower ripple frequency at the end of tau application (186 Hz) compared to baseline (195 Hz).

4. Discussion

4.1 The TRPV1 channel: hippocampal cell activity, network synchronization, and behavioral performance of TRPV1 KO mice

4.1.1 SWRs in TRPV1 KO mice

4.1.1.1 Enhanced SWRs in TRPV1 KO mice in different temperatures

We studied SWRs in TRPV1 KO mice in vitro and in vivo, expecting to see an impairment similar to that seen for LTP (Hurtado-Zavala et al., 2017). We first recorded from hippocampal slices at various temperatures. The TRPV1 channel is temperature sensitive, so it is possible that the effect of the KO is different or present only at specific temperatures. Because channel inactivation and desensitization have been reported (Sánchez-Moreno et al., 2018; Sanz-Salvador et al., 2012) we decided to analyze two different time points for all temperatures, one at the "beginning" of each temperature step and one at the "end", after at least 18 minutes at that temperature. Most effects were more apparent at the start of each temperature step than at the end, suggesting some channel desensitization, but the same trends were seen in both time points, indicating minimal effects of such desensitization.

31 °C was chosen as baseline, as temperatures between 28-33 °C are often used in these types of experiments (Maier et al., 2009; Papatheodoropoulos, 2010; Liu et al., 2020; Villers & Ris, 2013), and many lines of evidence suggest that slices survive longer at lower temperatures (Karnatovskaia et al., 2014; Buskila et al., 2014). Papatheodoropoulos and coauthors (2007) found that ripple frequency better resembles in vivo values at 32 °C compared to higher temperatures, so some physiological relevance is inferred. The temperature was then raised to 36 °C and then to 38 °C in two cycles. This is the physiological temperature range for sleep (36 °C) and wakefulness (38 °C) in mice and humans. Temperature drops occur during NREM sleep (Harding et al., 2019), which is when SWRs occur. A final increase at 40 °C followed, to examine differences at an extreme point corresponding to a high fever, before returning to 31 °C.

We found no differences between WT and KO mice in terms of SW amplitude, duration, and number of SWs per minute throughout all temperatures. The probability of SW cluster occurrence, however, was increased in the KO slices only at 31 °C baseline. Clusters of SWs are seen both in vivo (Ramadan et al., 2009) and in vitro. Papatheodoropoulos, 2010, hypothesized that primary and secondary SWs in a cluster allow activation of respective cell-assemblies within a temporal window permissive for synaptic plasticity, hence linking the two populations. More clusters would therefore indicate improved memory. Alternatively, more clusters could lead to increased interference with non-associated memories and hence impair memory instead. A relationship between SW cluster probability and synaptic plasticity has been indicated by an increased probability of cluster occurrence after LTP induction (Papatheodoropoulos, 2010). However, TRPV1 KO animals have

increased probability of SW cluster occurrence but impaired LTP (Hurtado-Zavala et al., 2017), demonstrating that the two processes do not always go hand-in-hand.

TRPV1 KO slices had longer ripple events consisting of more peaks than WT slices. Ripple incidence was also higher in the KOs. This effect was the strongest the first time at 36 °C, but similar tendencies were seen across the physiological range temperatures. At the first but not the second time point, genotype also had a significant effect on ripple power, probably because KO slices tended to have higher ripple power in most temperatures. Ripple amplitude and peak frequency, on the other hand, were similar in TRPV1 KO and WT slices. Overall this data indicates enhanced ripples in TRPV1 KO mice.

Fernández-Ruiz et al., 2019, report more long-duration ripples in awake animals during memory-demanding situations and improved memory after optogenetic prolongation of ripples, but not after induction of additional ripples. Increased ripple duration would therefore indicate improved memory performance in TRPV1 KO animals. It has been suggested that negative ripple peaks represent superimposed action potentials of synchronously firing cells, and that positive peaks represent IPSC currents onto pyramidal cell somata (Buzsáki, 2015). Hence, an increased number of peaks per event in the TRPV1 KOs indicates increased neuronal firing during SWRs. Spiking populations are the main contributor to the power of high frequency oscillations (Schomburg et al., 2012). Thus, the increased ripple power in TRPV1 KOs, which correlates with population synchrony in the hippocampus (Buzsáki, 2015), also points to a more synchronized network in TRPV1 KO slices. The spike content of ripples conveys spatial information from explored environments. In Fernández-Ruiz et al. (2019), cells firing during prolonged ripples were spatially selective. In a different scenario, an increased ripple duration such as that seen in the TRPV1 KOs could indicate higher interference between unrelated memories, similar to the effects of increased SW cluster probability, which would lead to worse memory performance. In the future, we should therefore look at the number of cells participating in each ripple and analyze place cell reactivation in more detail (e.g., to see if place cells found during open field sessions are more reactivated during the post- compared to the pre-exploration rest) to better understand the interaction between SWRs and neuronal firing.

Fernández-Ruiz et al., 2019, report no effect of increasing ripple incidence on memory performance, but others suggest this might also act to prolong memory (Oliva et al., 2020). The different conclusions of these two studies could be due to differences in the area stimulated (CA1 or CA2, respectively), species (rats or mice, respectively), type of memory (spatial or social, respectively), or time of optogenetic stimulation (during awake SWRs during task performance or sleep SWRs after social learning, respectively). Nevertheless, increased ripple incidence seen in the TRPV1 KOs suggests improved memory, since decreased ripple incidence is predictive of spatial memory deficits (Jones et al., 2019). In humans, awake ripple rate was increased only during more complex autobiographical memory conditions but not associative memory (Chen et al., 2021); thus, different types of memory might be differently modulated by SWR abundance.

4.1.1.2 Effects of temperature on SWRs and TRPV1 temperature sensitivity

Temperature affected all SWR parameters analyzed. This was expected, as changes in SWRs were reported before at different temperatures (Papatheodoropoulos et al., 2007; Cheah et al., 2021), and temperature has widespread effects, such as changing voltage-gated channel kinetics and intrinsic membrane conductances (Thompson et al., 1985). Nonetheless, the effect of temperature may be contaminated by the effect of time. This experiment was particularly long, sometimes lasting more than 8 hours after slice preparation. While the influence of time on genotype effects is expected to be minimal, as WT and KO recordings had similar durations, each temperature step is taken at a later time point. Hence, experiments where SWRs are recorded for equally long times under similar conditions but held stable at 31 °C should be made, and temperature effects interpreted after taking these into consideration. Indeed, some parameters analyzed in our experiment, such as the number of SWs per minute (Figure 14), seem to decrease relatively linearly as the experiment progresses. While other parameters do not seem to change as linearly with time, they still do not fully recover during the final step at 31 °C. This could either be due to the slice slowly deteriorating or due to irreversible effects of high temperature, which have been reported before (Hodgkin & Katz, 1949; Tancredi et al., 1992). It is also possible that slice deterioration might account for why some effects are statistically significant only the first, but not the second time slices were incubated at 36 °C (e.g., if long duration ripples deteriorate first).

In terms of TRPV1 KO, the main differences in SWRs compared to WT were observed at baseline at 31 °C and the first time at 36 °C, with trends at other temperatures. Initial reports suggested that the TRPV1 channel activates at 42-43 °C (Cesare & McNaughton, 1996), but this temperature threshold is reduced by phospholipids to physiological levels (Prescott & Julius, 2003; Sun & Zakharian, 2015; Cao et al., 2013a), so a role for TRPV1 activation in these temperatures is supported. Other studies show TRPV1 activation even at room temperature under conditions such as low pH (Tominaga et al., 1998). Moreover, the TRPV1 channel is activated by endogenous ligands, the production of which could be affected by temperature. Interestingly, TRPV1 activation itself produces TRPV1 ligands (Manchanda et al., 2021). TRPV1 channel inactivation might also be temperature-dependent and irreversible (Sánchez-Moreno et al., 2018). Nevertheless, because the channel is modulated by multiple inputs, it may act as a coincidence detector of different stimuli, including temperature. Therefore, the effects of TRPV1 KO across a range of temperatures (and possibly at different time-points) is particularly informative.

4.1.1.3 In vivo SWRs are also enhanced in TRPV1 KO mice

In vitro recordings pointed towards enhanced SWRs in TRPV1 KO mice. In vivo, if we focus on recordings performed when the environments were familiar to the animal, SWRs were also stronger in TRPV1 KO animals, as ripple magnitude was increased in TRPV1 KO mice. Ripple magnitude is also increased after, and associated with, successful learning (Eschenko et al., 2008).

TRPV1 KO mice also had a higher peak ripple frequency compared to WT mice during a post-exploration rest session but not a pre-exploration rest session. Both WT and KO mice had faster ripples in the post-exploration rest session compared to the pre-exploration rest session. Similar

changes have been reported before and hypothesized to have a functional effect, e.g., aged mice show a ~ 14 Hz decrease in ripple frequency compared to young mice (Wiegand et al., 2016), and a ~ 7 Hz increase in ripple frequency is seen after learning and correlated with the timing of learning (Ponomarenko et al., 2008). Small changes in peak ripple frequency might lead to impaired coupling between hippocampus and neocortex (Siapas & Wilson, 1998; Cox et al., 2019), interfering with proper consolidation. While a causal relationship between ripple frequency and memory performance has not been shown yet, increased ripple frequency seems to be consistent with enhanced SWRs and memory.

Only TRPV1 KO mice had a significant increase in ripple rate during the post-exploration rest session compared to the pre-exploration rest session. This contradicts literature, as exploration of a familiar environment is usually sufficient to cause an increase in ripple rate in WT animals (Kudrimoti et al., 1999). However, the effect is known to be more pronounced after exploration of a novel environment (Joo & Frank, 2018), with some reporting no change in ripple occurrence after exploration of a familiar environment that does not involve any learning (Eschenko et al., 2008). Accordingly, we see an increase in ripple rate in both WT and TRPV1 KO animals after exploration of the open fields for the first time, when the environments are novel, supporting previous findings that increased ripple rate is present only after a more demanding experience (i.e., learning a new environment).

TRPV1 KO ripple power increased while WT ripple power decreased (although absence of specific differences between TRPV1 KOs and WTs in the post-hoc test suggests a weak effect) following exploration of a novel environment, while both decreased after exploration of familiar environments. Peak ripple frequency was increased only in TRPV1 KO mice after exploration of novel environments, but in both genotypes after exploration of familiar environments; and it was significantly higher in TRPV1 KO mice compared to WTs only after exploration of familiar environments. These observations suggest that TRPV1 may be specifically important for novelty of explorative learning. It is believed that novel experiences are more demanding due to the need for adaptive learning. Exploration of novel environments enhances SWRs (Joo & Frank, 2018) and coordinated hippocampal neural activity (Cheng & Frank 2008), and facilitates LTP induction (Li et al., 2003) and cell assembly reactivation (O'Neill et al., 2008; Cheng & Frank, 2008; Buzsáki, 2015) - where TRPV1 could play a role. However, while statistically not significant, visual inspection suggests that in some cases the same tendencies could be seen under both novel and familiar conditions (e.g., increased ripple magnitude in TRPV1 KO mice), indicating that absence of some of these effects in the novel condition could be due to small sample size (only one novelty session per animal), and the TRPV1 channel may have similar effects in both novel and familiar environments. Further experiments are needed to make strong claims about a differential function of TRPV1 in novel and familiar conditions.

4.1.1.4 Caveats and future directions

In vitro recordings were made from the ventral hippocampus, where SWRs occur spontaneously, while in vivo recordings were taken from dorsal CA1 due to easier accessibility and larger literature on the area in vivo. In terms of spatial memory, the dorsal hippocampus might be more relevant due

to more precise place fields (Jung et al., 1994). Some have suggested that it is not a matter of precision but of scale, such that place fields in the ventral hippocampus may have a larger scale and be more relevant in larger environments (Harland et al., 2017; Keinath et al., 2014), which is not the case in our experimental conditions. In any case, LFP differences between WT and TRPV1 KO mice are interesting in both locations, and further investigation on the effects of TRPV1 KO along the dorsoventral axis of the hippocampus should follow.

In addition, in in vivo recordings we only analyzed SWRs in rest sessions. However, it would be interesting to analyze SWRs from the open field recordings as well, as this could reveal a different effect of TRPV1 KO in awake versus sleep SWRs. Indeed, Roumis & Frank (2015) suggest that sleep SWRs are more important for memory consolidation, while awake SWRs mainly support memory retrieval and planning. Here, we took recording segments where the animal had a speed less than 2 cm/s for analysis of quiet periods. Nevertheless, to make concrete conclusions on sleep versus awake SWRs, additional criteria should be used to better define sleep, such as by measuring the muscle tone in the neck.

4.1.2 TRPV1 KO effects on theta oscillations, delta oscillations, and single units

4.1.2.1 Theta oscillations and the TRPV1 channel

While theta are mostly associated with active exploration and memory encoding, they are also seen during REM sleep. It is believed that theta seen in awake and sleep states differ in terms of frequency, pharmacological sensitivity, generation mechanisms, and function (Kramis et al., 1975; Mikulovic et al., 2018; Montoya & Sainsbury, 1985). We found that theta oscillations were faster in TRPV1 KO mice during familiar open fields but not during rest sessions, suggesting the possibility that TRPV1 is important for waking theta. Even though not statistically significant, the same trend was seen during novel exploration. A moderate decrease (~ 0.8 Hz) in theta frequency has been reported during exploration of a novel but not a familiar environment, which might signal unexpected environmental change (Jeewajee et al., 2008). An increase in theta frequency in TRPV1 KOs might therefore interfere with the salience of a novel environment. Decreased theta frequency seen after cooling of the medial septum (Petersen & Buzsáki, 2020) or chlordiazepoxide injection (Pan & McNaughton, 1997) correlates with learning impairments, with even small decreases (~ 0.35 Hz) being associated with moderate deficits in spatial memory (Pan & McNaughton, 1997). Increased frequency would therefore point towards improved memory in TRPV1 KO animals. Quirk and colleagues (2021), however, used optogenetic stimulation of parvalbumin-positive medial septal area neurons to control the frequency of hippocampal theta oscillations and found no effect in spatial memory at frequencies less than 10 Hz, while at faster frequencies a deficit rather than an improvement was observed. Furthermore, the firing of hippocampal cells was not strongly affected by the stimulation. Hence, we should study how cellular firing is changed in relation to theta oscillations in TRPV1 KO mice in the future, to better understand the relationship between the two.

It has been suggested that REM sleep and associated theta might be involved in memory consolidation (Zielinski et al., 2021) similar to SWRs and NREM sleep; an increase in theta power from rest before exploration to rest after exploration as seen in both WT and TRPV1 KO mice after

exploration of novel environments would support this. However, REM sleep is usually transient in mice and long sleep sessions are required to record it, so it is unlikely that we recorded during REM sleep here and differences are probably more reflecting theta differences between active and inactive states.

Peak theta power was generally lower in TRPV1 KO mice, with a statistically significant effect during re-exploration of the first open field and during rest before and after exploration of familiar environments. Decreased theta power, as seen after brain injury (Fedor et al., 2010) or inhibition of relaxin-3 neurons of the nucleus incertus (Ma et al., 2009), is associated with impaired spatial navigation. Therefore, contrary to the ripple and peak theta frequency results (which might indicate enhanced learning in TRPV1 KOs) decreased theta power in TRPV1 KO mice would be associated with learning impairments. TRPV1 KO mice had higher theta power during rest after exploration compared to rest before exploration in both novel and familiar conditions, while WT mice showed an increase only after novel exploration and a decrease after familiar exploration. While concrete conclusions cannot be made at this stage, it is possible that this reflects impairments with familiarization in TRPV1 KO mice, as they fail to recapitulate the change from an increase to a decrease in theta power seen in WT mice when the environment changes from being novel to familiar. However, an opposite trend was seen in WT mice if animals instead of recording sessions are used as experimental units, so we should treat this result with caution. Peak theta power in WT mice is also lower during the first exploration of the first open field compared to the second exploration in recordings where the environment was familiar, which could reflect increased memory retrieval (Jacobs et al., 2006).

4.1.2.2 Delta oscillations and the TRPV1 channel

The function of delta waves is poorly understood as they are rarely characterized and are associated with widespread cortical silence (Schultheiss et al., 2020), so interpretation of results is challenging. Peak delta frequency was lower in TRPV1 KO mice during familiar exploration of the second open field, but not during exploration of the first open field, re-exploration of the first open field after the second field, or during rest sessions. In the novel condition, TRPV1 KO mice had significantly higher delta frequency only during the rest session before exploration, as WT delta frequency increased to similar levels during the rest session after exploration. These might point towards differences in modulation of delta oscillations in WT and TRPV1 KO mice across novel/familiar and awake/rest delta. Some researchers support that lower frequency (< 1.5 Hz) and higher frequency (> 1.5 Hz) hippocampal delta oscillations might have different functions (Moroni et al., 2008; Ferrara et al., 2012). Considering also that stimulation at ~ 1 Hz leads to synaptic depotentiation, which is important for sharpening specificity of potentiated engrams (Bukalo et al., 2013) and forgetting (Moreno, 2021), differential dysregulation of delta frequencies in TRPV1 KO mice in open field and rest sessions might cause impairments with both memory consolidation and forgetting.

Decreased delta power in TRPV1 KO mice was seen during the rest sessions before and after familiar environment exploration, but not during exploration of open fields. A similar but statistically not significant trend is seen during novelty. An increase in delta power from the rest session before to after novel exploration was also observed, though not significant for specific genotypes. The

decreased delta power during rest sessions might reflect poorer sleep quality (Johnson & Durrant, 2021; Park et al., 2020). On the other hand, mice with memory deficits have increased delta power (Wirt et al., 2021), so a decrease in TRPV1 KO mice might be associated with improved learning. However, since alterations in both theta and delta power were observed, we should analyze the ratio of the two, as it might point towards alterations in their power dynamics, which are also seen in these mice (Wirt et al., 2021). The relationship of SWRs and delta in TRPV1 KO mice should also be further investigated, as the observed phase locking between the two (Axmacher et al., 2008b) might be dysregulated.

4.1.2.3 Velocity as a covariate

Velocity is known to affect theta and delta frequency and power (Kennedy et al., 2022; Schultheiss et al., 2020; Furtunato et al., 2022). Since velocity was not significantly different between genotypes, we considered effects of speed insignificant for conclusions about WT and TRPV1 KO mice. In some cases, however, some influence was still visible. For example, during the rest session before novel environment exploration, non-significant differences in velocity between genotypes inversely mirrored differences in peak delta frequency. Moreover, speed significantly differed between some open field or rest sessions, so interpretation of such effects should take that into consideration. Acceleration has also been reported to modulate theta frequency and power, and, although it seems to do so to a lesser extent than velocity (Kennedy et al., 2022), in the future we should also test if acceleration was similar among WT and TRPV1 KO mice.

4.1.2.4 TRPV1 KO on single-unit activity

Besides changes in local field potentials, single unit activity was also analyzed in vivo in WT and TRPV1 KO mice. Since TRPV1 KOs have impaired LTP, the synaptic correlate of memory, we initially expected impaired remapping of place fields or decreased place field stability in TRPV1 KOs. Decreased theta power - which we found in TRPV1 KOs - is also associated with place field expansion, as both are seen in the hippocampus after muscimol-induced inactivation of the medial entorhinal cortex (Ormond & McNaughton, 2015). On the other hand, it was found that place cell activity during SWRs is crucial for place field stability(Roux et al., 2017), so since KO mice had enhanced ripples we could expect more specific place fields instead.

We separated single units into putative interneurons or pyramidal cells, where ~ 30% of pyramidal cells in both WT and TRPV1 KO mice corresponded to place cells. We found that TRPV1 KO place cells carried significantly lower spatial information, had lower stability correlation between exploration of the same open field, and had larger place fields. These all suggest decreased spatial specificity and stability in TRPV1 KO place cells, which is indicative of spatial memory impairment. For example, Cacucci and colleagues (2008) report lower spatial information content and larger place fields in aged Tg2576 mice, an Alzheimer's disease model.

4.1.2.5 Possible caveats and future directions

We used recording sessions as experimental units, but results were also reported after averaging per animal and trends seemed to follow the same direction as before averaging (except for theta peak power, which decreased during the rest session after exploration of familiar environments compared to the pre-exploration rest if WT recording sessions are used, but an increase is seen if animals are used as experimental units - Figure 32D). Taking recording sessions and cell numbers as experimental units is not uncommon in the field. Moreover, there is evidence supporting that different recording sessions from different locations are independent from each other. For example, ripples were found to exhibit great variation in amplitude and frequency even across simultaneously recorded neighboring locations (Csicsvari et al., 2000). In addition, the presence of three separate theta current generators in the hippocampus has been found (López-Madrona et al., 2020), which could also suggest different effects across different locations. However, it would be better to increase the sample size and perhaps use averages per animal instead of averages of recording sessions to ensure independence of data points. Alternatively, a mixed effects model analysis could be applied with recording sessions as experimental units, but taking the animal from which recordings are made into consideration as a covariate. Increasing the sample size would also help to ensure that results are not biased by outliers.

4.1.3 Behavioral effect of TRPV1 KO

Several lines of evidence suggest that TRPV1 KO mice might have altered memory acquisition or consolidation. Impaired LTP in TRPV1 KO mice, decreased theta power, larger place fields, and decreased place field stability would all point towards impaired spatial memory in TRPV1 KO animals. Ripples, on the other hand, were enhanced in TRPV1 KOs, and theta frequency was also higher in KO animals, both of which are usually indicative of improved consolidation and learning.

Nevertheless, there was no difference in learning a reward location in the cheeseboard maze between WT and TRPV1 KO mice, suggesting intact memory formation and consolidation in TRPV1 KO animals. However, learning per se was weak in both genotypes in this task. The regression lines across learning days for each genotype showed no evidence of learning in terms of time to the original reward. Time to reward location is influenced by the duration an animal may remain immobile (e.g., grooming). Hence, distance traveled to reward location might offer more accurate results. However, when the distance of all trials was analyzed, regression lines only indicated learning in TRPV1 KOs. The average distance traveled decreased from day 1 to day 5 for WT animals, and a paired comparison between days 1 and 5 suggests successful learning, but distance increased on days 6 and 7. This may be because the 1st trial of day 6 was a probe trial, a non-rewarded 3.5-minute exploration of the maze, which could have caused some extinction. Retrospectively, the duration of the probe trial should have been decreased or a reward given at the end of the probe trial to ameliorate such influences. For comparison, most people do a 60 s probe trial in water maze experiments (Morris, 1981; Garthe & Kempermann, 2013). In order to account for this effect, we performed an outlier analysis for WT and TRPV1 KO mice on days 6 and 7, and excluded 4 WT and 3 TRPV1 KO trials. Analysis without outliers shows learning in WT mice.

When the reward location was switched to the opposite quadrant of the maze in a reversal test, regression analysis of both time and distance to reward location showed that WT and KO animals learned the new location. The slopes of the regression lines were not statistically different, suggesting that the rate of learning was similar between genotypes. Removal of outliers for days 6 and 7 revealed similar results.

Interestingly, WT and TRPV1 KO regression lines had significantly different elevations in terms of both time and distance to reward at the new location, showing that TRPV1 KO mice took longer to reach the new reward location across all days. This might suggest that the memory of the original reward location is more persistent in TRPV1 KOs. Unfortunately, we did not have time to analyze data from the probe trials to see if TRPV1 KO mice spent more time near the original reward location, which would support this hypothesis. Importantly, the time and distance traveled to the original reward location after reversal should also be analyzed, to see if TRPV1 KO animals took longer to reach the new reward location because they were looking near the original one. If we see such results, we could hypothesize that TRPV1 mice have a stronger memory of the original reward location and therefore impaired spatial extinction. This is also supported by the lack of extinction effect of the day 6 probe trial in TRPV1 KO mice, which was apparent in WT mice. Marsch and colleagues (2007) found no difference in fear memory extinction between WT and TRPV1 KO mice, but this could be due to different involvement of the hippocampus in fear versus spatial memory tasks. On the other hand, the increased elevation of the KO regression line might be due to decreased motivation or altered stress states, although similar mobility and exploration of the center of the open field in both WTs and TRPV1 KOs argues against this possibility. The cheeseboard maze is a non-aversive natural memory test, and as such is not as “strong” as other tests of memory using aversive stimuli such as the water maze or fear conditioning. Although these tests have the caveats of anxiety and “unnatural” memory confounds, it would be interesting to test WT and TRPV1 KO mice in these tests as well, to see if effects are more robust. Riera and colleagues (2014) used the Barnes Maze and found improved performance in TRPV1 KO mice, while others report impaired memory after fear conditioning (Marsch et al., 2007) or impaired short-term but normal long-term memory in the novel object recognition test and the passive avoidance test (You et al., 2012). Thus, TRPV1 KO effects on memory might be more evident in specific tasks or only present under specific conditions, for example depending on the aversiveness of the task.

It has been previously shown that the TRPV1 channel is involved in emotional regulation, anxiety, and stress, with most studies suggesting an anxiolytic effect of TRPV1 inactivation (Marsch et al., 2007; Hakimizadeh et al., 2012; Santos et al., 2008; You et al., 2012). We could therefore expect increased time and entries in the center of the open field in KO mice. It is widely accepted that anxiety influences memory performance (Sandi, 2013; Lukasik et al., 2019; Maloney et al., 2014), so we wanted to keep the conditions of the open field as similar to the cheeseboard maze as possible in order to be able to directly compare the two. Thus, dim-light was used and food-restriction continued until after the open field test. Under these conditions, we saw no difference in anxiety levels of WT and KO mice, which implies that differences seen in the cheeseboard maze task are not attributed to altered stress states. It has been found that the involvement of the TRPV1 channel in fear memory consolidation depends on how aversive the conditioning stimulus is (Genro et al., 2012). Hence, the absence of differences between genotypes here could be due to the mild conditions of the open field test (dim-light). Alternatively, it could be due to small sample size or

analysis parameters (e.g., definition of center and periphery or analyzing the entire 15-minute exploration versus only the first few minutes), which should be further investigated in the future. Lastly, visual cues were placed in the open field to give the mice a sense of orientation. Even though those were placed high on the walls, mice were observed to jump towards and try to interact with them, which could have increased time spent in the periphery. If this was the case, we would expect to see mice spending more time around the three walls with cues than the wall without. While visual inspection suggests this is not the case (Figure 45) and our percentage of time spent in the center of the open field is similar to those reported in other studies (Holmes et al., 2002; Shoji & Miyakawa, 2019; Matsuo et al., 2010), this is something we should quantify in the future. In any case, since the conditions were the same for WT and KO mice, we believe that the presence of visual cues in the maze does not invalidate conclusions of the open field test.

4.1.4 The TRPV1 channel in febrile seizures

Since the TRPV1 channel is temperature sensitive and febrile seizures might be caused by conversion of SWRs into pathological epileptiform responses due to high temperature, we tested if TRPV1 KO hippocampal slices from young mice might be differentially susceptible to febrile seizures, caused by fever. We studied the effect of temperature elevation in slices, since Tancredi et al., 1992, reported the development of spontaneous epileptiform activity (EA) at 38.2-39.2 ^{o}C in hippocampal slices from Wistar rats aged 2-38 days. Different lines of evidence suggest that TRPV1 inhibition might facilitate (Lee et al., 2011) or protect against (Shirazi et al., 2014) epileptic activity. TRPV1 KO mice had a less severe febrile seizure phenotype (Huang et al., 2015; Kong et al., 2019), so we expected decreased susceptibility to induction of EA by temperature in TRPV1 KO slices.

At the high temperature point of 38.2 ^{o}C, a similar percentage of TRPV1 KO and WT slices expressed EA, and a similar percentage of TRPV1 KO and WT slices (~ 40%) had increased EA (or no change, or a decrease in EA) at 38.2 ^{o}C compared with 31 ^{o}C, indicating no difference in susceptibility, contrary to previous findings (Huang et al., 2015; Kong et al., 2019). The difference could be attributed to TRPV1 expression outside the hippocampus. However, at a baseline temperature of 31 ^{o}C, more WT than TRPV1 KO slices showed EA. This points to a protective effect of TRPV1 inhibition at lower temperatures.

While it is tempting to think that the TRPV1 channel would be active only at the high temperature and not the low one, there is evidence that TRPV1 is also activated at lower temperatures in the presence of endogenous brain lipids and agonists (Cao et al., 2013a; Prescott & Julius, 2003). Evidence of TRPV1 being active at lower temperatures was also apparent in the sleep-wake cycle temperature experiment in adult mice, where effects of TRPV1 KO were more apparent at 31 ^{o}C and 36 ^{o}C than at 38 ^{o}C or 40 ^{o}C. It is therefore possible that the TRPV1 channel is more active at low rather than high temperatures in the hippocampus.

As others (Schuchmann et al., 2006; Tancredi et al., 1992), we observed age-dependent EA in WT slices, which recapitulates the age-dependance of febrile seizures. It is therefore possible that altered temperature sensitivity to febrile seizure induction in TRPV1 KO mice might be more prominent at a different age.

An additional caveat in this experiment is that recordings were made from the surface of the slices, which could be compromised after tissue preparation. We decided that this was preferred to assess EA at multiple sites rather than damaging the slice by multiple puncturing. Nevertheless, increased EA could be indicative of worse preparations.

Our results do not point towards altered susceptibility to febrile seizures in TRPV1 KO mice. However, quantification of elicited epileptic events themselves (e.g., amplitude, frequency, event duration) could reveal differences in the characteristics of EA. Indeed, there was great variability in the type and magnitude of EA we observed, and a question arises as to whether all events are equal. We also observed additional types of events that were not included here, either because we were unsure as to whether they represent real activity, or because they could not be reliably identified in all recordings. Additionally, many slices often had SWRs intermingled with EA; analysis of these SWRs could provide additional insights into the relationship between TRPV1, SWRs, and febrile seizures. Thus, better qualitative and quantitative characterization should follow.

4.1.5 TRPV1 KO effects attributed to decreased activity of OLM interneurons

Given that in the hippocampus the TRPV1 channel is specifically expressed in OLM cells and controls their excitatory innervation (Hurtado-Zavala et al., 2017), we will interpret the results discussed above as a consequence of reduced OLM activation. However, we recognise that further experiments (e.g., activation of OLM cells to rescue effects of TRPV1 KO) are required to confirm this, especially in the case of in vivo results, as effects of the constitutive KO might be due to TRPV1 expression in other brain areas.

A mouse model of temporal lobe epilepsy has increased excitatory input to OLM interneurons which causes an increase in their firing rate (Dugladze et al., 2007). In contrast, the TRPV1 KOs display less epileptiform activity and less excitatory input to OLM neurons. Thus, the decreased firing frequency of interneurons we saw in vivo could simply reflect decreased OLM cell activity. Another possibility is that what we thought reflects decreased interneuron firing rate is due to insufficient criteria to properly differentiate pyramidal cells and interneurons. WT interneurons had a minimum firing rate of ~ 15 Hz, but identified interneurons in TRPV1 KOs had lower firing rates of ~ 6 Hz. Thus, KO interneurons with firing rate ~ 6-15 Hz might actually be misidentified pyramidal cells. In order to check this, we should add additional criteria for putative pyramidal and inhibitory cells based on the shape of the action potential (e.g., peak valley ratio). If these 6-15 Hz cells in TRPV1 KOs are pyramidal cells, their unusually high firing rate (Turi et al., 2019) might reflect disinhibition of CA1 principal cells, which could be due to decreased inhibition by OLM cells at distal pyramidal cell dendrites. Disinhibition is believed to be important for place cell stability (Pedrosa & Clopath, 2020), so it might account for the decreased place cell spatial information and stability correlation, and for the increased place field size we see in single unit recordings in the TRPV1 KO mice.

In vitro, SWR alterations were mostly attributed to the potential disinhibitory effect of OLM activation (or absence thereof) on CA3 inputs to CA1 pyramidal cells. While this is also present in vivo, SWR alterations in behaving mice could reflect not only changes in the isolated hippocampal circuit but also altered processing of extrahippocampal inputs, such as from the entorhinal cortex

(EC). OLM cells are said to gate information processing in the hippocampus by inhibiting inputs from the EC on distal CA1 pyramidal dendrites (Leão et al., 2012). We therefore expected a bigger effect of TRPV1 KO (and hence OLM silencing) in vivo. While not identical, results from both in vivo and in vitro experiments point towards enhanced SWRs in TRPV1 KO mice.

OLM cells fire after the maximum ripple peak (Pangalos et al., 2013), which could point to a role in ripple termination through desynchronization of local circuits. In agreement with this hypothesis, we saw increased ripple duration and incidence in TRPV1 KO slices compared to WTs at physiological temperatures. In vivo, we saw increased ripple magnitude and frequency. Ripple frequency is said to be determined by parvalbumin (PV) interneurons, where stronger excitation of PV interneurons is associated with faster frequencies (Buzsáki, 2015). Moreover, increased spiking is expected to lead to increased ripple amplitude (Schomburg et al., 2012). Since OLM cells inhibit both PV-positive bistratified cells and pyramidal cells, decreased OLM activity in TRPV1 KO mice could lead to both enhanced PV cell activity and increased excitation through pyramidal cell disinhibition, thus resulting in faster and larger ripples. However, others report increased ripple amplitude due to reduced activity of PV cells (Rácz et al., 2009).

Theta power was lower, but theta frequency was higher in TRPV1 KO mice compared to WTs. OLM cells are active during theta (Klausberger et al., 2003), inhibiting EC input on CA1 cells. EC input is important for generation of type 1 theta oscillations, which have higher frequency. Furthermore, OLM cell activation generates the lower frequency type 2 theta (Mikulovic et al., 2018). Hence, higher theta frequency in TRPV1 KO mice is consistent with OLM cell silencing. Lower theta power might also be caused by decreased OLM activity in the TRPV1 KOs, as OLM cells contribute to generation of theta oscillations (Mikulovic et al., 2018; Gloveli et al., 2005).

Current analysis suggests no deficits in spatial memory acquisition or consolidation in TRPV1 KO mice, but a possible role in spatial memory extinction is hypothesized. Intraventricular application of somatostatin, which is expressed in OLM cells (Hurtado-Zavala et al., 2017), was found to delay extinction of active avoidance behavior (Vécsei et al., 1986). Additionally, increased PV-interneuron activity, expected in TRPV1 KOs, led to ripple enhancement and fear memory persistence (Çaliskan et al., 2016), which would support this hypothesis, although further analysis and experiments are needed to substantiate it.

4.2 The relationship between SWRs and LTP

4.2.1 Effect of HFS on spontaneous SWRs

SWRs and LTP are associated, as both are important memory processes. The timing of synaptic input relative to SWRs can determine if LTP will occur (Sadowski et al., 2016) and high frequency stimulation (HFS) that induces LTP can generate SWRs (Behrens et al., 2005). TRPV1 KO mice have impaired LTP (Hurtado-Zavala et al., 2017), yet we saw enhanced SWRs in TRPV1 KO mice, showing that the two processes don't always go together, even though both are positively correlated with memory consolidation. To examine the relationship between LTP and SWRs in more detail, we

induced LTP electrically by HFS or added pharmacological agents known to alter LTP, and examined effects on SWRs.

After LTP, there was a significant increase in SW duration, which is associated with improved memory performance (Fernández-Ruiz et al., 2019; Eschenko et al., 2008; Prince et al., 2021). Weaker stimulation (test pulses prior to HFS) before LTP induction already caused a significant increase in SW duration, but SW duration was further increased by HFS-induced LTP. SW amplitude increased in response to increasing stimulation, but not significantly in the post-hoc test compared to unstimulated baseline SWRs. Increasing the sample size could help clarify such effects. SW incidence, on the other hand, significantly decreased only after LTP. This contradicts Buzsáki (1984), who found increased incidence and amplitude of SWs after in vivo HFS. HFS has also been used to generate SWRs in slices (Behrens et al., 2005). However, the stimulation used by this study is much higher than what we applied to our slices. Furthermore, SWR generation by HFS results in a much lower SW incidence (Behrens et al., 2005: < 16 SWs per minute) than what we saw in our experiments in slices which already have spontaneously generated SWRs. HFS might therefore affect spontaneous SWRs differently, especially considering that electrical stimulation during SWRs can disrupt them and cause a short-term decrease in SWR incidence (Ego-Stengel & Wilson, 2010). This might be particularly relevant in our experiment, as our baseline rate of SWR occurrence was exceptionally high (baseline = 216 SWs per minute). The probability of clusters was also higher (0.25) in this experiment compared to other experiments (e.g., TRPV1 WT at 31 °C baseline: 64 SW/min., 0.03 cluster probability, anisomycin experiment baseline = 82 SW/min, 0.08 cluster probability). This may be due to the use of aCSF with higher potassium concentration (selected because it facilitates LTP and has been used previously in the lab for LTP experiments) that makes slices more excitable. Papatheodoropoulos (2010) used an aCSF similar to ours and also reported a high spontaneous SWR incidence (172 SWs per minute) and probability of SW clusters (0.5). In their slices, HFS comparable to ours increased probability of SW cluster occurrence but decreased incidence of primary SWs, keeping the total SWR rate constant. It therefore seems that the network maintains a homeostasis rather than undergoing uncontrolled potentiation. The same is suggested by in vivo experiments showing increased incidence but decreased duration of SWRs after exploration of a familiar environment (Kudrimoti et al., 1999). This could explain why SW incidence is decreased in our experiments, as SW duration and amplitude increase. A compensatory mechanism between SWR duration and incidence is also suggested by Girardeau and colleagues (2014), who show that disruption of SWRs (resulting in decreased SWR duration) after learning leads to increased SWR occurrence. Another possibility is that increased SW duration is due to merging of SWs, leading to decreased SW number. While the probability of cluster occurrence was similar in our experiment before and after HFS-induced LTP, it might be informative to quantify the number of secondary SWs per cluster, where a decrease would support a possible merging of individual SW events.

Weak stimulation that does not induce LTP is also reported to increase SW incidence, but in this case usually a single SW is generated right after each pulse, leading to only short-term effects (Jiang et al., 2018; Bazelot et al., 2016; Ellender et al., 2010). We expect that such effects of stimulation were not present in our recordings, which took place a short time after and not simultaneously with each stimulation step. Nevertheless, Jiang et al., 2018, comment that when a stimulation fell near a

spontaneous event, the stimulation failed to elicit a SW, in agreement with our hypothesis that SWRs are not generated in our slices due to their high rate of spontaneous SWs.

SWRs have been proposed as the physiological candidate for LTP, as the fast ripple oscillations might mimic tetanic stimulation and neuronal co-activation is important in both processes (Buzsáki, 1989; Buzsáki, 2015). Bicuculline-induced population bursts in CA3, thought to simulate SWRs, induce LTP at CA3-CA1 synapses (Buzsáki et al., 1987), and the timing of synaptic input relative to SWR occurrence can determine whether LTP will occur (Sadowski et al., 2016; King et al., 1999). However, SWR enhancement also leads to widespread depotentiation (Bukalo et al., 2013), and SWR inhibition during sleep prevents spontaneous depotentiation, which can also be seen in slices with SWRs (Norimoto et al., 2018). Hence, SWRs might be more important for global downscaling in order to preserve the signal-to-noise ratio and avoid interference from unrelated information. It would be therefore interesting to see how LTD-inducing LFS might affect SWRs, as well as if TRPV1 KO mice have enhanced spontaneous or LFS-induced depotentiation.

4.2.2 Dependence of SWRs on protein synthesis and histone deacetylases

LTP maintenance is blocked if protein synthesis is inhibited; for example, after anisomycin application (Frey et al., 1988). We therefore expected that anisomycin might block SWR generation or lead to weakening of SWRs. Incubation with anisomycin did not prevent SWR generation, and neither short-term nor long-term drug application changed SWR parameters. Thus, spontaneous SWRs in hippocampal slices are protein synthesis independent. It would be interesting to see, however, if anisomycin application and LTP inhibition would block expression of responses to HFS discussed above.

Suberoylanilide hydroxamic acid (SAHA) is a histone deacetylase (HDAC) inhibitor. SAHA lowers the threshold for LTP induction and increases the magnitude of potentiation. It also blocks LTD and increases the size of miniature-EPSPs, a measure of spontaneous activity (Hanson et al., 2013; Alarcón et al., 2004; Benito et al., 2015). We expected an enhancement of SWRs after SAHA treatment. Instead, incubation with SAHA decreased ripple incidence. Short term application after SWR generation possibly caused a small increase in ripple duration and number of peaks per ripple event. However, conclusive statements cannot be made, as post-hoc analysis did not identify differences among specific conditions and the possible effect on ripple duration and number of peaks was not reversed after washing. An increase in these parameters, however, would agree with SWR enhancement. The decreased ripple occurrence seen after incubation with SAHA could then be due to excitotoxicity induced by long-term application of the drug. In experiments performed by my colleague Hanna Dubrovska in Camin Dean's lab involving SAHA application on hippocampal cultures, short-term application enhanced synapse function, but longer-term (several hour) application caused cell death, in agreement with an excitotoxic effect of long-term treatment with SAHA.

4.2.3 Effect of tau oligomers on SWRs

Oligomeric tau is prevalent in Alzheimer's disease and is thought to promote neurodegeneration, but effects on circuit function are not as well known. We therefore tested the effects of aggregated tau on SWRs in hippocampal slices. Since tau decreases LTP magnitude (Fá et al., 2016), and SWRs have decreased amplitude, power, and incidence in mouse models of tauopathies (Witton et al., 2016; Ciupek et al., 2015), we expected a reduction of SWRs after tau application.

We initially used the protocol by Acquarone et al., 2019, to prepare tau aggregates. Pre-incubation of hippocampal slices with tau did not block the generation of SWRs and did not alter the properties of SWRs. Short-term application of tau also did not affect SWRs except for a significant effect on the number of ripple events per minute, which appeared lower at the end of tau application and during wash, but no differences among specific conditions were identified by post-hoc analysis. We therefore decided to test a different oligomeric preparation that results in larger oligomeric species and the presence of β-sheets (Figure 4). Because of time and drug amount limitations, we only tested the effect of short-term application of this preparation of tau. In this case, application of tau not only significantly decreased ripple incidence, but also significantly reduced ripple amplitude, power, and peak frequency, as well as SW amplitude and rate of occurrence. These results suggest that larger oligomeric species are more detrimental to SWRs than smaller ones, consistent with the hypothesis that the size of tau species affects toxicity levels (Honson & Kuret, 2008). Furthermore, our results are in agreement with others reporting diminished SWRs in tauopathy and AD mouse models, and such changes are often associated with memory impairments.

Most parameters in our experiment showed at least a partial return to baseline after washout of tau, consistent with effects being attributed to tau application rather than slice degradation. Ripple amplitude and power, on the other hand, remained significantly decreased following washout. It is possible that a longer washout is required for complete rescue of effects. Another explanation is that tau oligomers taken up by neurons lead to aggregation of endogenous tau (Jiang et al., 2020), which could cause sustained degeneration of SWRs even in the absence of exogenously applied tau. It is possible then that recorded SWRs would deteriorate further after a longer wash duration, as more endogenous tau aggregates. Furthermore, longer tau application or pre-incubation with the tau preparation that results in larger oligomeric species and β-sheets could result in even more pronounced and irreversible SWR impairments or completely abolish SWRs.

Tau has six major isoforms, which are associated with different (mis)folding and propagation properties (Dujardin et al., 2018) and can lead to heterogeneous clinical presentation (Zhang et al., 2022b). Furthermore, a synergy is proposed between tau and Aβ pathology in AD (Busche & Hyman, 2020). The effect of different tau isoforms or combinations of tau and Aβ on SWRs in hippocampal slices could therefore also be investigated in the future.

5. Conclusion

We found that both in vivo and in vitro SWRs were enhanced in TRPV1 KO mice. Theta oscillations in TRPV1 KO mice had higher frequency and lower power than in WTs, and the power of delta oscillations was also lower in TRPV1 KOs. Spatial tuning of hippocampal place cells was impaired in TRPV1 KO mice, as place fields were larger and less stable between explorations of the same environment. Memory acquisition and consolidation were intact in the cheeseboard maze task, but memory extinction might be compromised in TRPV1 KOs. SWRs transform into epileptiform discharges and pathological ripples during seizures. Because the TRPV1 channel is temperature sensitive, we hypothesized it might be involved in febrile seizure induction. While we did not find alterations in susceptibility to febrile seizure induction in TRPV1 KO slices, our results point toward a protective effect of TRPV1 inhibition in epilepsy at lower temperatures.

We also found that SWRs and LTP are not always positively correlated with each other. We found increased duration but decreased incidence of SWs after LTP induction. SWRs were unaffected by inhibition of protein synthesis, which blocks LTP. Short-term SAHA application, which increases LTP, only minimally enhanced SWRs, while long-term application decreased SWR incidence.

Lastly, we found that small oligomers of tau (a hallmark of AD pathology) had minimal effects, while larger aggregates of tau strongly reduced SWRs, consistent with literature showing SWR impairments in AD mice.

6. References

Acquarone E, Argyrousi EK, van den Berg M, Gulisano W, Fà M, Staniszewski A, Calcagno E, Zuccarello E, D'Adamio L, Deng SX, Puzzo D, Arancio O, Fiorito J. Synaptic and memory dysfunction induced by tau oligomers is rescued by up-regulation of the nitric oxide cascade. Mol Neurodegener. 2019 Jun 27;14(1):26. doi: 10.1186/s13024-019-0326-4. PMID: 31248451; PMCID: PMC6598340.

Acs G, Palkovits M, Blumberg PM. Specific binding of [3H]resiniferatoxin by human and rat preoptic area, locus ceruleus, medial hypothalamus, reticular formation and ventral thalamus membrane preparations. Life Sci. 1996;59(22):1899-908. doi: 10.1016/s0024-3205(96)00537-1. PMID: 8950287.

Adamczyk P, Miszkiel J, McCreary AC, Filip M, Papp M, Przegaliński E. The effects of cannabinoid CB1, CB2 and vanilloid TRPV1 receptor antagonists on cocaine addictive behavior in rats. Brain Res. 2012 Mar 20;1444:45-54. doi: 10.1016/j.brainres.2012.01.030. Epub 2012 Jan 20. PMID: 22325096.

Addis DR, Schacter DL. The hippocampus and imagining the future: where do we stand? Front Hum Neurosci. 2012 Jan 4;5:173. doi: 10.3389/fnhum.2011.00173. PMID: 22291625; PMCID: PMC3251274.

Aggleton JP, Christiansen K. The subiculum: the heart of the extended hippocampal system. Prog Brain Res. 2015;219:65-82. doi: 10.1016/bs.pbr.2015.03.003. Epub 2015 May 14. PMID: 26072234.

Aguiar DC, Terzian AL, Guimarães FS, Moreira FA. Anxiolytic-like effects induced by blockade of transient receptor potential vanilloid type 1 (TRPV1) channels in the medial prefrontal cortex of rats. Psychopharmacology (Berl). 2009 Aug;205(2):217-25. doi: 10.1007/s00213-009-1532-5. Epub 2009 Apr 22. PMID: 19387617.

Ahern GP, Wang X, Miyares RL. Polyamines are potent ligands for the capsaicin receptor TRPV1. J Biol Chem. 2006 Mar 31;281(13):8991-5. doi: 10.1074/jbc.M513429200. Epub 2006 Jan 23. PMID: 16431906.

Alarcón JM, Malleret G, Touzani K, Vronskaya S, Ishii S, Kandel ER, Barco A. Chromatin acetylation, memory, and LTP are impaired in CBP+/- mice: a model for the cognitive deficit in Rubinstein-Taybi syndrome and its amelioration. Neuron. 2004 Jun 24;42(6):947-59. doi: 10.1016/j.neuron.2004.05.021. PMID: 15207239.

Alfoeldi P, Rubicsek G, Cserni G, Obal F. (1990). Brain and core temperatures and peripheral vasomotion during sleep and wakefulness at various ambient temperatures in the rat. Pfluegers Archiv European Journal of Physiology, 417(3), 336–341. doi:10.1007/bf00371001

Al-Hayani A, Wease KN, Ross RA, Pertwee RG, Davies SN. The endogenous cannabinoid anandamide activates vanilloid receptors in the rat hippocampal slice. Neuropharmacology. 2001 Dec;41(8):1000-5. doi: 10.1016/s0028-3908(01)00145-9. PMID: 11747904.

Allen MJ, Sabir S, Sharma S. GABA Receptor. [Updated 2022 Feb 17]. In: StatPearls [Internet]. Treasure Island (FL): StatPearls Publishing; 2022 Jan-. Available from: https://www.ncbi.nlm.nih.gov/books/NBK526124/

Almeida-Filho DG, Lopes-dos-Santos V, Vasconcelos NA, Miranda JG, Tort AB, Ribeiro S. An investigation of Hebbian phase sequences as assembly graphs. Front Neural Circuits. 2014 Apr 8;8:34. doi: 10.3389/fncir.2014.00034. PMID: 24782715; PMCID: PMC3986516.

Altimus C, Harrold J, Jaaro-Peled H, Sawa A, Foster DJ. Disordered ripples are a common feature of genetically distinct mouse models relevant to schizophrenia. Mol Neuropsychiatry. 2015 May;1(1):52-59. doi: 10.1159/000380765. PMID: 26417572; PMCID: PMC4582688.

Anand U, Jones B, Korchev Y, Bloom SR, Pacchetti B, Anand P, Sodergren MH. CBD Effects on TRPV1 Signaling Pathways in Cultured DRG Neurons. J Pain Res. 2020 Sep 11;13:2269-2278. doi: 10.2147/JPR.S258433. PMID: 32982390; PMCID: PMC7494392.

Andersen P, Moser EI. Brain temperature and hippocampal function. Hippocampus. 1995;5(6):491-8. doi: 10.1002/hipo.450050602. PMID: 8646277.

Anikeeva P, Andalman AS, Witten I, Warden M, Goshen I, Grosenick L, Gunaydin LA, Frank LM, Deisseroth K. Optetrode: a multichannel readout for optogenetic control in freely moving mice. Nat Neurosci. 2011 Dec 4;15(1):163-70. doi: 10.1038/nn.2992. PMID: 22138641; PMCID: PMC4164695.

Anstötz M, Lee SK, Maccaferri G. Expression of TRPV1 channels by Cajal-Retzius cells and layer-specific modulation of synaptic transmission by capsaicin in the mouse hippocampus. J Physiol. 2018 Aug;596(16):3739-3758. doi: 10.1113/JP275685. Epub 2018 Jun 24. PMID: 29806907; PMCID: PMC6092290.

Arking DE, Cutler DJ, Brune CW, Teslovich TM, West K, Ikeda M, Rea A, Guy M, Lin S, Cook EH, Chakravarti A. A common genetic variant in the neurexin superfamily member CNTNAP2 increases familial risk of autism. Am J Hum Genet. 2008 Jan;82(1):160-4. doi: 10.1016/j.ajhg.2007.09.015. PMID: 18179894; PMCID: PMC2253968.

Arszovszki A, Borhegyi Z, Klausberger T. Three axonal projection routes of individual pyramidal cells in the ventral CA1 hippocampus. Front Neuroanat. 2014 Jun 25;8:53. doi: 10.3389/fnana.2014.00053. PMID: 25009471; PMCID: PMC4069485.

Atkinson, RC, Shiffrin RM. Human memory: A proposed system and its control processes. In K. Spence (Ed.), The psychology of learning and motivation (Vol. 2). Oxford, England: Academic Press, 1968.

Avoli M. The epileptic hippocampus revisited: back to the future. Epilepsy Curr. 2007 Jul-Aug;7(4):116-8. doi: 10.1111/j.1535-7511.2007.00194.x. PMID: 17694174; PMCID: PMC1941908.

Axmacher N, Elger CE, Fell J. Ripples in the medial temporal lobe are relevant for human memory consolidation. Brain. 2008b Jul;131(Pt 7):1806-17. doi: 10.1093/brain/awn103. Epub 2008b May 24. PMID: 18503077.

Axmacher N, Haupt S, Fernández G, Elger CE, Fell J. The role of sleep in declarative memory consolidation--direct evidence by intracranial EEG. Cereb Cortex. 2008a Mar;18(3):500-7. doi: 10.1093/cercor/bhm084. Epub 2007 Jun 14. PMID: 17573370.

Balleza-Tapia H, Crux S, Andrade-Talavera Y, Dolz-Gaiton P, Papadia D, Chen G, Johansson J, Fisahn A. TrpV1 receptor activation rescues neuronal function and network gamma oscillations from Aβ-induced impairment in mouse hippocampus in vitro. Elife. 2018 Nov 12;7:e37703. doi: 10.7554/eLife.37703. PMID: 30417826; PMCID: PMC6281315.

Bannerman DM, Grubb M, Deacon RM, Yee BK, Feldon J, Rawlins JN. Ventral hippocampal lesions affect anxiety but not spatial learning. Behav Brain Res. 2003 Feb 17;139(1-2):197-213. doi: 10.1016/s0166-4328(02)00268-1. PMID: 12642189.

Bazelot M, Teleńczuk MT, Miles R. Single CA3 pyramidal cells trigger sharp waves in vitro by exciting interneurones. J Physiol. 2016 May 15;594(10):2565-77. doi: 10.1113/JP271644. Epub 2016 Feb 9. PMID: 26728572; PMCID: PMC4865576.

Behrens CJ, van den Boom LP, de Hoz L, Friedman A, Heinemann U. Induction of sharp wave-ripple complexes in vitro and reorganization of hippocampal networks. Nat Neurosci. 2005 Nov;8(11):1560-7. doi: 10.1038/nn1571. Epub 2005 Oct 16. PMID: 16222227.

Bell LA, Bell KA, McQuiston AR. Synaptic muscarinic response types in hippocampal CA1 interneurons depend on different levels of presynaptic activity and different muscarinic receptor subtypes. Neuropharmacology. 2013 Oct;73:160-73. doi: 10.1016/j.neuropharm.2013.05.026. Epub 2013 Jun 5. PMID: 23747570; PMCID: PMC3783005.

Benítez-Angeles M, Morales-Lázaro SL, Juárez-González E, Rosenbaum T. TRPV1: Structure, Endogenous Agonists, and Mechanisms. Int J Mol Sci. 2020 May 12;21(10):3421. doi: 10.3390/ijms21103421. PMID: 32408609; PMCID: PMC7279265.

Benito E, Urbanke H, Ramachandran B, Barth J, Halder R, Awasthi A, Jain G, Capece V, Burkhardt S, Navarro-Sala M, Nagarajan S, Schütz AL, Johnsen SA, Bonn S, Lührmann R, Dean C, Fischer A. HDAC inhibitor-dependent transcriptome and memory reinstatement in cognitive decline models. J Clin Invest. 2015 Sep;125(9):3572-84. doi: 10.1172/JCI79942. Epub 2015 Aug 17. PMID: 26280576; PMCID: PMC4588238.

Benninger F, Freund TF, Hájos N. Control of excitatory synaptic transmission by capsaicin is unaltered in TRPV1 vanilloid receptor knockout mice. Neurochem Int. 2008 Jan;52(1-2):89-94. doi: 10.1016/j.neuint.2007.06.008. Epub 2007 Jun 21. PMID: 17651868; PMCID: PMC2194163.

Bennion D, Jensen T, Walther C, Hamblin J, Wallmann A, Couch J, Blickenstaff J, Castle M, Dean L, Beckstead S, Merrill C, Muir C, St Pierre T, Williams B, Daniel S, Edwards JG. Transient receptor potential vanilloid 1 agonists modulate hippocampal CA1 LTP via the GABAergic system. Neuropharmacology. 2011 Sep;61(4):730-8. doi: 10.1016/j.neuropharm.2011.05.018. Epub 2011 May 27. PMID: 21645527.

Bertram EH, Zhang DX. Thalamic excitation of hippocampal CA1 neurons: a comparison with the effects of CA3 stimulation. Neuroscience. 1999;92(1):15-26. doi: 10.1016/s0306-4522(98)00712-x. PMID: 10392827.

Bezaire MJ, Soltesz I. Quantitative assessment of CA1 local circuits: knowledge base for interneuron-pyramidal cell connectivity. Hippocampus. 2013 Sep;23(9):751-85. doi: 10.1002/hipo.22141. Epub 2013 Jul 10. PMID: 23674373; PMCID: PMC3775914.

Bhaskaran MD, Smith BN. Effects of TRPV1 activation on synaptic excitation in the dentate gyrus of a mouse model of temporal lobe epilepsy. Exp Neurol. 2010 Jun;223(2):529-36. doi: 10.1016/j.expneurol.2010.01.021. Epub 2010 Feb 8. PMID: 20144892; PMCID: PMC2864369.

Bhave G, Hu HJ, Glauner KS, Zhu W, Wang H, Brasier DJ, Oxford GS, Gereau RW 4th. Protein kinase C phosphorylation sensitizes but does not activate the capsaicin receptor transient receptor potential vanilloid 1 (TRPV1). Proc Natl Acad Sci U S A. 2003 Oct 14;100(21):12480-5. doi: 10.1073/pnas.2032100100. Epub 2003 Oct 1. PMID: 14523239; PMCID: PMC218783.k

Bienenstock EL, Cooper LN, Munro PW. Theory for the development of neuron selectivity: orientation specificity and binocular interaction in visual cortex. J Neurosci. 1982 Jan;2(1):32-48. doi: 10.1523/JNEUROSCI.02-01-00032.1982. PMID: 7054394; PMCID: PMC6564292.

Bir SC, Ambekar S, Kukreja S, Nanda A. Julius Caesar Arantius (Giulio Cesare Aranzi, 1530-1589) and the hippocampus of the human brain: history behind the discovery. J Neurosurg. 2015 Apr;122(4):971-5. doi: 10.3171/2014.11.JNS132402. Epub 2015 Jan 9. PMID: 25574573.

Bisaz R, Travaglia A, Alberini CM. The neurobiological bases of memory formation: from physiological conditions to psychopathology. Psychopathology. 2014;47(6):347-56. doi: 10.1159/000363702. Epub 2014 Oct 3. PMID: 25301080; PMCID: PMC4246028.

Blackwood DH, Fordyce A, Walker MT, St Clair DM, Porteous DJ, Muir WJ: Schizophrenia and affective disorders - cosegregation with a translocation at chromosome 1q42 that directly disrupts brain-expressed genes: clinical and P300 findings in a family. Am J Hum Genet 2001;69:428-433.

Blanco JA, Stead M, Krieger A, Stacey W, Maus D, Marsh E, Viventi J, Lee KH, Marsh R, Litt B, Worrell GA. Data mining neocortical high-frequency oscillations in epilepsy and controls. Brain. 2011 Oct;134(Pt 10):2948-59. doi: 10.1093/brain/awr212. Epub 2011 Sep 8. PMID: 21903727; PMCID: PMC3187540.

Bland BH, Colom LV, Konopacki J, Roth SH. Intracellular records of carbachol-induced theta rhythm in hippocampal slices. Brain Res. 1988 May 3;447(2):364-8. doi: 10.1016/0006-8993(88)91141-9. PMID: 3390706.

Blednov YA, Harris RA. Deletion of vanilloid receptor (TRPV1) in mice alters behavioral effects of ethanol. Neuropharmacology. 2009 Mar;56(4):814-20. doi: 10.1016/j.neuropharm.2009.01.007. PMID: 19705551; PMCID: PMC2775500.

Bliss TV, Collingridge GL. Expression of NMDA receptor-dependent LTP in the hippocampus: bridging the divide. Mol Brain. 2013 Jan 22;6:5. doi: 10.1186/1756-6606-6-5. PMID: 23339575; PMCID: PMC3562207.

Bliss TV, Lomo T. Long-lasting potentiation of synaptic transmission in the dentate area of the anaesthetized rabbit following stimulation of the perforant path. J Physiol. 1973 Jul;232(2):331-56. doi: 10.1113/jphysiol.1973.sp010273. PMID: 4727084; PMCID: PMC1350458.

Bloom GS. Amyloid-β and tau: the trigger and bullet in Alzheimer disease pathogenesis. JAMA Neurol. 2014 Apr;71(4):505-8. doi: 10.1001/jamaneurol.2013.5847. PMID: 24493463.

Bragin A, Engel J Jr, Wilson CL, Fried I, Buzsáki G. High-frequency oscillations in human brain. Hippocampus. 1999a;9(2):137-42. doi: 10.1002/(SICI)1098-1063(1999)9:2<137::AID-HIPO5>3.0.CO;2-0. PMID: 10226774.

Bragin A, Engel J Jr, Wilson CL, Fried I, Mathern GW. Hippocampal and entorhinal cortex high-frequency oscillations (100--500 Hz) in human epileptic brain and in kainic acid--treated rats with chronic seizures. Epilepsia. 1999b Feb;40(2):127-37. doi: 10.1111/j.1528-1157.1999.tb02065.x. PMID: 9952257.

Bragin A, Wilson CL, Almajano J, Mody I, Engel J Jr. High-frequency oscillations after status epilepticus: epileptogenesis and seizure genesis. Epilepsia. 2004 Sep;45(9):1017-23. doi: 10.1111/j.0013-9580.2004.17004.x. PMID: 15329064.

Brasted PJ, Bussey TJ, Murray EA, Wise SP. Role of the hippocampal system in associative learning beyond the spatial domain. Brain. 2003 May;126(Pt 5):1202-23. doi: 10.1093/brain/awg103. PMID: 12690059.

Brederson JD, Kym PR, Szallasi A. Targeting TRP channels for pain relief. Eur J Pharmacol. 2013 Sep 15;716(1-3):61-76. doi: 10.1016/j.ejphar.2013.03.003. Epub 2013 Mar 14. PMID: 23500195.

Brito R, Sheth S, Mukherjea D, Rybak LP, Ramkumar V. TRPV1: A Potential Drug Target for Treating Various Diseases. Cells. 2014 May 23;3(2):517-45. doi: 10.3390/cells3020517. PMID: 24861977; PMCID: PMC4092862.

Brown TE, Chirila AM, Schrank BR, Kauer JA. Loss of interneuron LTD and attenuated pyramidal cell LTP in Trpv1 and Trpv3 KO mice. Hippocampus. 2013 Aug;23(8):662-71. doi: 10.1002/hipo.22125. Epub 2013 Jun 3. PMID: 23536486; PMCID: PMC3891370.

Buhl DL, Harris KD, Hormuzdi SG, Monyer H, Buzsáki G. Selective impairment of hippocampal gamma oscillations in connexin-36 knock-out mouse in vivo. J Neurosci. 2003 Feb 1;23(3):1013-8. doi: 10.1523/JNEUROSCI.23-03-01013.2003. PMID: 12574431; PMCID: PMC6741916.

Bukalo O, Campanac E, Hoffman DA, Fields RD. Synaptic plasticity by antidromic firing during hippocampal network oscillations. Proc Natl Acad Sci U S A. 2013 Mar 26;110(13):5175-80. doi: 10.1073/pnas.1210735110. Epub 2013 Mar 11. PMID: 23479613; PMCID: PMC3612622.

Burns A, Iliffe S. Alzheimer's disease. BMJ. 2009 Feb 5;338:b158. doi: 10.1136/bmj.b158. Erratum in: BMJ. 2009 Apr 1. doi: 10.1136/bmj.b1349. PMID: 19196745.

Busche MA, Hyman BT. Synergy between amyloid-β and tau in Alzheimer's disease. Nat Neurosci. 2020 Oct;23(10):1183-1193. doi: 10.1038/s41593-020-0687-6. Epub 2020 Aug 10. PMID: 32778792.

Buskila Y, Breen PP, Tapson J, van Schaik A, Barton M, Morley JW. Extending the viability of acute brain slices. Sci Rep. 2014 Jun 16;4:5309. doi: 10.1038/srep05309. PMID: 24930889; PMCID: PMC4058870.

Buzsáki G, Haas HL, Anderson EG. Long-term potentiation induced by physiologically relevant stimulus patterns. Brain Res. 1987. Dec 1;435(1-2):331-3. doi: 10.1016/0006-8993(87)91618-0. PMID: 3427460.

Buzsáki G, Leung LW, Vanderwolf CH. Cellular bases of hippocampal EEG in the behaving rat. Brain Res. 1983 Oct;287(2):139-71. doi: 10.1016/0165-0173(83)90037-1. PMID: 6357356.

Buzsáki G, Ponomareff GL, Bayardo F, Ruiz R, Gage FH. 1989. Neuronal activity in the subcortically denervated hippocampus: A chronic model for epilepsy. Neuroscience 28:527–538.

Buzsáki G. Hippocampal sharp wave-ripple: A cognitive biomarker for episodic memory and planning. Hippocampus. 2015 Oct;25(10):1073-188. doi: 10.1002/hipo.22488. PMID: 26135716; PMCID: PMC4648295.

Buzsáki G. Hippocampal sharp waves: their origin and significance. Brain Res. 1986 Nov 29;398(2):242-52. doi: 10.1016/0006-8993(86)91483-6. PMID: 3026567.

Buzsáki G. Long-term changes of hippocampal sharp waves following high frequency afferent activation. Brain Res. 1984 May 21;300(1):179-82. doi: 10.1016/0006-8993(84)91356-8. PMID: 6329428.

Buzsáki G. Rythms of the Brain. Oxford University Press. Inc. NY, USA. 2006

Buzsáki G. Theta oscillations in the hippocampus. Neuron. 2002 Jan 31;33(3):325-40. doi: 10.1016/s0896-6273(02)00586-x. PMID: 11832222.

Buzsáki G. Two-stage model of memory trace formation: a role for "noisy" brain states. Neuroscience. 1989;31(3):551-70. doi: 10.1016/0306-4522(89)90423-5. PMID: 2687720.

Cacucci F, Wills TJ, Lever C, Giese KP, O'Keefe J. Experience-dependent increase in CA1 place cell spatial information, but not spatial reproducibility, is dependent on the autophosphorylation of the alpha-isoform of the calcium/calmodulin-dependent protein kinase II. J Neurosci. 2007 Jul 18;27(29):7854-9. doi: 10.1523/JNEUROSCI.1704-07.2007. PMID: 17634379; PMCID: PMC2680063.

Cacucci F, Yi M, Wills TJ, Chapman P, O'Keefe J. Place cell firing correlates with memory deficits and amyloid plaque burden in Tg2576 Alzheimer mouse model. Proc Natl Acad Sci U S A. 2008 Jun 3;105(22):7863-8. doi: 10.1073/pnas.0802908105. Epub 2008 May 27. PMID: 18505838; PMCID: PMC2396558.

Çaliskan G, Müller I, Semtner M, Winkelmann A, Raza AS, Hollnagel JO, Rösler A, Heinemann U, Stork O, Meier JC. Identification of Parvalbumin Interneurons as Cellular Substrate of Fear Memory Persistence. Cereb Cortex. 2016 May;26(5):2325-2340. doi: 10.1093/cercor/bhw001. Epub 2016 Feb 22. PMID: 26908632; PMCID: PMC4830301.

Çalışkan G, Stork O. Hippocampal network oscillations at the interplay between innate anxiety and learned fear. Psychopharmacology (Berl). 2019 Jan;236(1):321-338. doi: 10.1007/s00213-018-5109-z. Epub 2018 Nov 11. PMID: 30417233.

Camina E, Güell F. The Neuroanatomical, Neurophysiological and Psychological Basis of Memory: Current Models and Their Origins. Front Pharmacol. 2017 Jun 30;8:438. doi: 10.3389/fphar.2017.00438. PMID: 28713278; PMCID: PMC5491610.

Campos AC, Guimarães FS. Evidence for a potential role for TRPV1 receptors in the dorsolateral periaqueductal gray in the attenuation of the anxiolytic effects of cannabinoids. Prog Neuropsychopharmacol Biol Psychiatry. 2009 Nov 13;33(8):1517-21. doi: 10.1016/j.pnpbp.2009.08.017. Epub 2009 Sep 6. PMID: 19735690.

Cao E, Cordero-Morales JF, Liu B, Qin F, Julius D. TRPV1 channels are intrinsically heat sensitive and negatively regulated by phosphoinositide lipids. Neuron. 2013a Feb 20;77(4):667-79. doi: 10.1016/j.neuron.2012.12.016. PMID: 23439120; PMCID: PMC3583019.

Cao E, Liao M, Cheng Y, Julius D. TRPV1 structures in distinct conformations reveal activation mechanisms. Nature. 2013b Dec 5;504(7478):113-8. doi: 10.1038/nature12823. PMID: 24305161; PMCID: PMC4023639.

Carnevale V, Rohacs T. TRPV1: A Target for Rational Drug Design. Pharmaceuticals (Basel). 2016 Aug 23;9(3):52. doi: 10.3390/ph9030052. PMID: 27563913; PMCID: PMC5039505.

Carr MF, Jadhav SP, Frank LM. Hippocampal replay in the awake state: a potential substrate for memory consolidation and retrieval. Nat Neurosci. 2011 Feb;14(2):147-53. doi: 10.1038/nn.2732. PMID: 21270783; PMCID: PMC3215304.

Caterina MJ, Leffler A, Malmberg AB, Martin WJ, Trafton J, Petersen-Zeitz KR, Koltzenburg M, Basbaum AI, Julius D. Impaired nociception and pain sensation in mice lacking the capsaicin

receptor. Science. 2000 Apr 14;288(5464):306-13. doi: 10.1126/science.288.5464.306. PMID: 10764638.

Cavanaugh DJ, Chesler AT, Bráz JM, Shah NM, Julius D, Basbaum AI. Restriction of transient receptor potential vanilloid-1 to the peptidergic subset of primary afferent neurons follows its developmental downregulation in nonpeptidergic neurons. J Neurosci. 2011b Jul 13;31(28):10119-27. doi: 10.1523/JNEUROSCI.1299-11.2011. PMID: 21752988; PMCID: PMC3147010.

Cavanaugh DJ, Chesler AT, Jackson AC, Sigal YM, Yamanaka H, Grant R, O'Donnell D, Nicoll RA, Shah NM, Julius D, Basbaum AI. Trpv1 reporter mice reveal highly restricted brain distribution and functional expression in arteriolar smooth muscle cells. J Neurosci. 2011a Mar 30;31(13):5067-77. doi: 10.1523/JNEUROSCI.6451-10.2011. PMID: 21451044; PMCID: PMC3087977.

Cenquizca LA, Swanson LW. Spatial organization of direct hippocampal field CA1 axonal projections to the rest of the cerebral cortex. Brain Res Rev. 2007 Nov;56(1):1-26. doi: 10.1016/j.brainresrev.2007.05.002. Epub 2007 May 10. PMID: 17559940; PMCID: PMC2171036.

Cesare P, McNaughton P. A novel heat-activated current in nociceptive neurons and its sensitization by bradykinin. Proc Natl Acad Sci U S A. 1996 Dec 24;93(26):15435-9. doi: 10.1073/pnas.93.26.15435. PMID: 8986829; PMCID: PMC26422.

Chadwick A, van Rossum MC, Nolan MF. Independent theta phase coding accounts for CA1 population sequences and enables flexible remapping. Elife. 2015 Feb 2;4:e03542. doi: 10.7554/eLife.03542. PMID: 25643396; PMCID: PMC4383210.

Chang CH, Gean PW. The Ventral Hippocampus Controls Stress-Provoked Impulsive Aggression through the Ventromedial Hypothalamus in Post-Weaning Social Isolation Mice. Cell Rep. 2019 Jul 30;28(5):1195-1205.e3. doi: 10.1016/j.celrep.2019.07.005. PMID: 31365864.

Chávez AE, Chiu CQ, Castillo PE. TRPV1 activation by endogenous anandamide triggers postsynaptic long-term depression in dentate gyrus. Nat Neurosci. 2010 Dec;13(12):1511-8. doi: 10.1038/nn.2684. Epub 2010 Nov 14. PMID: 21076423; PMCID: PMC3058928.

Chávez AE, Hernández VM, Rodenas-Ruano A, Chan CS, Castillo PE. Compartment-specific modulation of GABAergic synaptic transmission by TRPV1 channels in the dentate gyrus. J Neurosci. 2014 Dec 10;34(50):16621-9. doi: 10.1523/JNEUROSCI.3635-14.2014. PMID: 25505315; PMCID: PMC4261091.

Cheah CS, Beckman MA, Catterall WA, Oakley JC. Sharp Wave Ripple Frequency and Interictal Epileptic Discharges Increase in Tandem During Thermal Induction of Seizures in a Mouse Model of Genetic Epilepsy. Front Cell Neurosci. 2021 Oct 18;15:751762. doi: 10.3389/fncel.2021.751762. PMID: 34733140; PMCID: PMC8558377.

Cheah CS, Lundstrom BN, Catterall WA, Oakley JC. Impairment of Sharp Wave Ripples in a Murine Model of Dravet Syndrome. J Neurosci. 2019 Nov 13;39(46):9251-9260. doi: 10.1523/JNEUROSCI.0890-19.2019. Epub 2019 Sep 19. PMID: 31537705; PMCID: PMC6855681.

Chen CY, Li W, Qu KP, Chen CR. Piperine exerts anti-seizure effects via the TRPV1 receptor in mice. Eur J Pharmacol. 2013 Aug 15;714(1-3):288-94. doi: 10.1016/j.ejphar.2013.07.041. Epub 2013 Jul 31. PMID: 23911889.

Chen YY, Aponik-Gremillion L, Bartoli E, Yoshor D, Sheth SA, Foster BL. Stability of ripple events during task engagement in human hippocampus. Cell Rep. 2021 Jun 29;35(13):109304. doi: 10.1016/j.celrep.2021.109304. PMID: 34192546; PMCID: PMC8288441.

Cheng S, Frank LM. New experiences enhance coordinated neural activity in the hippocampus. Neuron. 2008 Jan 24;57(2):303-13. doi: 10.1016/j.neuron.2007.11.035. PMID: 18215626; PMCID: PMC2244590.

Cho SJ, Vaca MA, Miranda CJ, N'Gouemo P. Inhibition of transient potential receptor vanilloid type 1 suppresses seizure susceptibility in the genetically epilepsy-prone rat. CNS Neurosci Ther. 2018 Jan;24(1):18-28. doi: 10.1111/cns.12770. Epub 2017 Nov 3. PMID: 29105300; PMCID: PMC5730470.

Choi JH, Sim SE, Kim JI, Choi DI, Oh J, Ye S, Lee J, Kim T, Ko HG, Lim CS, Kaang BK. Interregional synaptic maps among engram cells underlie memory formation. Science. 2018 Apr 27;360(6387):430-435. doi: 10.1126/science.aas9204. PMID: 29700265.

Choi S, Lovinger DM. Decreased probability of neurotransmitter release underlies striatal long-term depression and postnatal development of corticostriatal synapses. Proc Natl Acad Sci U S A. 1997 Mar 18;94(6):2665-70. doi: 10.1073/pnas.94.6.2665. PMID: 9122253; PMCID: PMC20146.

Chuang HH, Prescott ED, Kong H, Shields S, Jordt SE, Basbaum AI, Chao MV, Julius D. Bradykinin and nerve growth factor release the capsaicin receptor from PtdIns(4,5)P2-mediated inhibition. Nature. 2001 Jun 21;411(6840):957-62. doi: 10.1038/35082088. PMID: 11418861.

Citri A, Malenka RC. Synaptic plasticity: multiple forms, functions, and mechanisms. Neuropsychopharmacology. 2008 Jan;33(1):18-41. doi: 10.1038/sj.npp.1301559. Epub 2007 Aug 29. PMID: 17728696.

Ciupek SM, Cheng J, Ali YO, Lu HC, Ji D. Progressive functional impairments of hippocampal neurons in a tauopathy mouse model. J Neurosci. 2015;35(21):8118-8131. doi:10.1523/JNEUROSCI.3130-14.2015

Colgin LL, Kubota D, Jia Y, Rex CS, Lynch G. Long-term potentiation is impaired in rat hippocampal slices that produce spontaneous sharp waves. J Physiol. 2004 Aug 1;558(Pt 3):953-61. doi: 10.1113/jphysiol.2004.068080. Epub 2004 Jun 11. PMID: 15194734; PMCID: PMC1665012.

Colgin LL. Oscillations and hippocampal-prefrontal synchrony. Curr Opin Neurobiol. 2011 Jun;21(3):467-74. doi: 10.1016/j.conb.2011.04.006. Epub 2011 May 14. PMID: 21571522; PMCID: PMC3578407.

Colgin LL. Rhythms of the hippocampal network. Nat Rev Neurosci. 2016 Apr;17(4):239-49. doi: 10.1038/nrn.2016.21. Epub 2016 Mar 10. PMID: 26961163; PMCID: PMC4890574.

Collingridge GL, Kehl SJ, McLennan H. Excitatory amino acids in synaptic transmission in the Schaffer collateral-commissural pathway of the rat hippocampus. J Physiol. 1983 Jan;334:33-46. doi: 10.1113/jphysiol.1983.sp014478. PMID: 6306230; PMCID: PMC1197298.

Collingridge GL, Peineau S, Howland JG, Wang YT. Long-term depression in the CNS. Nat Rev Neurosci. 2010 Jul;11(7):459-73. doi: 10.1038/nrn2867. PMID: 20559335.

Corkin S. What's new with the amnesic patient H.M.? Nat Rev Neurosci. 2002 Feb;3(2):153-60. doi: 10.1038/nrn726. PMID: 11836523.

Costa B, Giagnoni G, Franke C, Trovato AE, Colleoni M. Vanilloid TRPV1 receptor mediates the antihyperalgesic effect of the nonpsychoactive cannabinoid, cannabidiol, in a rat model of acute inflammation. Br J Pharmacol. 2004 Sep;143(2):247-50. doi: 10.1038/sj.bjp.0705920. Epub 2004 Aug 16. PMID: 15313881; PMCID: PMC1575333.

Coupé P, Manjón JV, Lanuza E, Catheline G. Lifespan Changes of the Human Brain In Alzheimer's Disease. Sci Rep. 2019 Mar 8;9(1):3998. doi: 10.1038/s41598-019-39809-8. PMID: 30850617; PMCID: PMC6408544.

Cox R, Rüber T, Staresina BP, Fell J. Heterogeneous profiles of coupled sleep oscillations in human hippocampus. Neuroimage. 2019 Nov 15;202:116178. doi: 10.1016/j.neuroimage.2019.116178. Epub 2019 Sep 7. PMID: 31505272; PMCID: PMC6853182.

Cristino L, de Petrocellis L, Pryce G, Baker D, Guglielmotti V, Di Marzo V. Immunohistochemical localization of cannabinoid type 1 and vanilloid transient receptor potential vanilloid type 1 receptors in the mouse brain. Neuroscience. 2006;139(4):1405-15. doi: 10.1016/j.neuroscience.2006.02.074. Epub 2006 Apr 17. PMID: 16603318.

Csernai M, Borbély S, Kocsis K, Burka D, Fekete Z, Balogh V, Káli S, Emri Z, Barthó P. Dynamics of sleep oscillations is coupled to brain temperature on multiple scales. J Physiol. 2019 Aug;597(15):4069-4086. doi: 10.1113/JP277664. Epub 2019 Jun 13. PMID: 31197831.

Csicsvari J, Hirase H, Czurkó A, Mamiya A, Buzsáki G. Fast network oscillations in the hippocampal CA1 region of the behaving rat. J Neurosci. 1999 Aug 15;19(16):RC20. doi: 10.1523/JNEUROSCI.19-16-j0001.1999. PMID: 10436076; PMCID: PMC6782850.

Csicsvari J, Hirase H, Mamiya A, Buzsáki G. Ensemble patterns of hippocampal CA3-CA1 neurons during sharp wave-associated population events. Neuron. 2000 Nov;28(2):585-94. doi: 10.1016/s0896-6273(00)00135-5. PMID: 11144366.

Csicsvari J, Jamieson B, Wise KD, Buzsáki G. Mechanisms of gamma oscillations in the hippocampus of the behaving rat. Neuron. 2003 Jan 23;37(2):311-22. doi: 10.1016/s0896-6273(02)01169-8. PMID: 12546825.

Cui Y, Perez S, Venance L. Endocannabinoid-LTP Mediated by CB1 and TRPV1 Receptors Encodes for Limited Occurrences of Coincident Activity in Neocortex. Front Cell Neurosci. 2018 Jul 5;12:182. doi: 10.3389/fncel.2018.00182. PMID: 30026689; PMCID: PMC6041431.

Davies P, Maloney AJ. Selective loss of central cholinergic neurons in Alzheimer's disease. Lancet. 1976 Dec 25;2(8000):1403. doi: 10.1016/s0140-6736(76)91936-x. PMID: 63862.

Davis LG, Dibner MD, Battey JF. Agarose Gel Electrophoresis. In: Basic Methods in Molecular Biology, edited by: Davis LG, Dibner MD, Battey JF. Elsevier Inc. 1986; 58–61. doi:10.1016/b978-0-444-01082-7.50022-9

Davis RL, Zhong Y. The Biology of Forgetting-A Perspective. Neuron. 2017 Aug 2;95(3):490-503. doi: 10.1016/j.neuron.2017.05.039. PMID: 28772119; PMCID: PMC5657245.

de Oliveira Alvares L, Pasqualini Genro B, Diehl F, Molina VA, Quillfeldt JA. Opposite action of hippocampal CB1 receptors in memory reconsolidation and extinction. Neuroscience. 2008 Jul 17;154(4):1648-55. doi: 10.1016/j.neuroscience.2008.05.005. Epub 2008 May 10. PMID: 18554811.

De Petrocellis L, Harrison S, Bisogno T, Tognetto M, Brandi I, Smith GD, Creminon C, Davis JB, Geppetti P, Di Marzo V. The vanilloid receptor (VR1)-mediated effects of anandamide are potently enhanced by the cAMP-dependent protein kinase. J Neurochem. 2001 Jun;77(6):1660-3. doi: 10.1046/j.1471-4159.2001.00406.x. PMID: 11413249.

DeBow S, Colbourne F. Brain temperature measurement and regulation in awake and freely moving rodents. Methods. 2003 Jun;30(2):167-71. doi: 10.1016/s1046-2023(03)00080-x. PMID: 12725783.

Dessaint J, Yu W, Krause JE, Yue L. Yohimbine inhibits firing activities of rat dorsal root ganglion neurons by blocking Na+ channels and vanilloid VR1 receptors. Eur J Pharmacol. 2004 Feb 6;485(1-3):11-20. doi: 10.1016/j.ejphar.2003.11.039. PMID: 14757119.

Diba K, Buzsáki G. Forward and reverse hippocampal place-cell sequences during ripples. Nat Neurosci. 2007 Oct;10(10):1241-2. doi: 10.1038/nn1961. Epub 2007 Sep 2. PMID: 17828259; PMCID: PMC2039924.

Dong Z, Han H, Li H, Bai Y, Wang W, Tu M, Peng Y, Zhou L, He W, Wu X, Tan T, Liu M, Wu X, Zhou W, Jin W, Zhang S, Sacktor TC, Li T, Song W, Wang YT. Long-term potentiation decay and memory loss are mediated by AMPAR endocytosis. J Clin Invest. 2015 Jan;125(1):234-47. doi: 10.1172/JCI77888. Epub 2014 Dec 1. PMID: 25437879; PMCID: PMC4382266.

Draguhn A, Traub RD, Schmitz D, Jefferys JG. Electrical coupling underlies high-frequency oscillations in the hippocampus in vitro. Nature. 1998 Jul 9;394(6689):189-92. doi: 10.1038/28184. PMID: 9671303.

Drebot II, Storozhuk MV, Kostyuk PG. An unexpected effect of capsaicin on spontaneous GABA-ergic IPSCS in hippocampal cell cultures. Neurophysiology. 2006; 38, 308–311, https://doi.org/10.1007/s11062-006-0063-5

Du Y, Fu M, Huang Z, Tian X, Li J, Pang Y, Song W, Tian Wang Y, Dong Z. TRPV1 activation alleviates cognitive and synaptic plasticity impairments through inhibiting AMPAR endocytosis in APP23/PS45 mouse model of Alzheimer's disease. Aging Cell. 2020 Mar;19(3):e13113. doi: 10.1111/acel.13113. Epub 2020 Feb 14. PMID: 32061032; PMCID: PMC7059138.

Dugladze T, Vida I, Tort AB, Gross A, Otahal J, Heinemann U, Kopell NJ, Gloveli T. Impaired hippocampal rhythmogenesis in a mouse model of mesial temporal lobe epilepsy. Proc Natl Acad Sci U S A. 2007 Oct 30;104(44):17530-5. doi: 10.1073/pnas.0708301104. Epub 2007 Oct 22. PMID: 17954918; PMCID: PMC2077290.

Dujardin S, Bégard S, Caillierez R, Lachaud C, Carrier S, Lieger S, Gonzalez JA, Deramecourt V, Déglon N, Maurage CA, Frosch MP, Hyman BT, Colin M, Buée L. Different tau species lead to heterogeneous tau pathology propagation and misfolding. Acta Neuropathol Commun. 2018 Nov 29;6(1):132. doi: 10.1186/s40478-018-0637-7. PMID: 30497516; PMCID: PMC6263555.

Durand CM, Betancur C, Boeckers TM, Bockmann J, Chaste P, Fauchereau F, Nygren G, Rastam M, Gillberg IC, Anckarsäter H, Sponheim E, Goubran-Botros H, Delorme R, Chabane N, Mouren-Simeoni MC, de Mas P, Bieth E, Rogé B, Héron D, Burglen L, Gillberg C, Leboyer M, Bourgeron T. Mutations in the gene encoding the synaptic scaffolding protein SHANK3 are associated with autism spectrum disorders. Nat Genet. 2007 Jan;39(1):25-7. doi: 10.1038/ng1933. Epub 2006 Dec 17. PMID: 17173049; PMCID: PMC2082049.

Dvorak-Carbone H, Schuman EM. Long-term depression of temporoammonic-CA1 hippocampal synaptic transmission. J Neurophysiol. 1999 Mar;81(3):1036-44. doi: 10.1152/jn.1999.81.3.1036. PMID: 10085331.

Ecker A, Bagi B, Vértes E, Steinbach-Németh O, Karlócai MR, Papp OI, Miklós I, Hájos N, Freund TF, Gulyás AI, Káli S. Hippocampal sharp wave-ripples and the associated sequence replay emerge from structured synaptic interactions in a network model of area CA3. Elife. 2022 Jan 18;11:e71850. doi: 10.7554/eLife.71850. PMID: 35040779; PMCID: PMC8865846.

Edwards JG. TRPV1 in the central nervous system: synaptic plasticity, function, and pharmacological implications. Prog Drug Res. 2014;68:77-104. doi: 10.1007/978-3-0348-0828-6_3. PMID: 24941665.

Egan P. fwhm. 2022. (https://www.mathworks.com/matlabcentral/fileexchange/10590-fwhm), MATLAB Central File Exchange. Retrieved December 27, 2022.

Ego-Stengel V, Wilson MA. Disruption of ripple-associated hippocampal activity during rest impairs spatial learning in the rat. Hippocampus. 2010 Jan;20(1):1-10. doi: 10.1002/hipo.20707. PMID: 19816984; PMCID: PMC2801761.

Ellender TJ, Nissen W, Colgin LL, Mann EO, Paulsen O. Priming of hippocampal population bursts by individual perisomatic-targeting interneurons. J Neurosci. 2010 Apr 28;30(17):5979-91. doi: 10.1523/JNEUROSCI.3962-09.2010. PMID: 20427657; PMCID: PMC3763476.

Ellingson JM, Silbaugh BC, Brasser SM. Reduced oral ethanol avoidance in mice lacking transient receptor potential channel vanilloid receptor 1. Behav Genet. 2009 Jan;39(1):62-72. doi: 10.1007/s10519-008-9232-1. Epub 2008 Oct 7. PMID: 18839303; PMCID: PMC3155820.

Eschenko O, Ramadan W, Mölle M, Born J, Sara SJ. Sustained increase in hippocampal sharp wave ripple activity during slow-wave sleep after learning. Learn Mem. 2008 Apr 2;15(4):222-8. doi: 10.1101/lm.726008. PMID: 18385477; PMCID: PMC2327264.

Fá M, Puzzo D, Piacentini R, Staniszewski A, Zhang H, Baltrons MA, Li Puma DD, Chatterjee I, Li J, Saeed F, Berman HL, Ripoli C, Gulisano W, Gonzalez J, Tian H, Costa JA, Lopez P, Davidowitz E, Yu WH, Haroutunian V, Brown LM, Palmeri A, Sigurdsson EM, Duff KE, Teich AF, Honig LS, Sierks M, Moe JG, D'Adamio L, Grassi C, Kanaan NM, Fraser PE, Arancio O. Extracellular Tau Oligomers Produce An Immediate Impairment of LTP and Memory. Sci Rep. 2016 Jan 20;6:19393. doi: 10.1038/srep19393. PMID: 26786552; PMCID: PMC4726138.

Fanselow MS, Dong HW. Are the dorsal and ventral hippocampus functionally distinct structures? Neuron. 2010 Jan 14;65(1):7-19. doi: 10.1016/j.neuron.2009.11.031. PMID: 20152109; PMCID: PMC2822727.

Fatahi Z, Reisi Z, Rainer G, Haghparast A, Khani A. Cannabinoids induce apathetic and impulsive patterns of choice through CB1 receptors and TRPV1 channels. Neuropharmacology. 2018 May 1;133:75-84. doi: 10.1016/j.neuropharm.2018.01.021. PMID: 29355640.

Fedor M, Berman RF, Muizelaar JP, Lyeth BG. Hippocampal θ dysfunction after lateral fluid percussion injury. J Neurotrauma. 2010 Sep;27(9):1605-15. doi: 10.1089/neu.2010.1370. PMID: 20597686; PMCID: PMC2966852.

Felix-Ortiz AC, Beyeler A, Seo C, Leppla CA, Wildes CP, Tye KM. BLA to vHPC inputs modulate anxiety-related behaviors. Neuron. 2013 Aug 21;79(4):658-64. doi: 10.1016/j.neuron.2013.06.016. PMID: 23972595; PMCID: PMC4205569.

Fernández-Ruiz A, Oliva A, Fermino de Oliveira E, Rocha-Almeida F, Tingley D, Buzsáki G. Long-duration hippocampal sharp wave ripples improve memory. Science. 2019 Jun 14;364(6445):1082-1086. doi: 10.1126/science.aax0758. PMID: 31197012; PMCID: PMC6693581.

Ferraguti F, Shigemoto R. Metabotropic glutamate receptors. Cell Tissue Res. 2006 Nov;326(2):483-504. doi: 10.1007/s00441-006-0266-5. Epub 2006 Jul 18. PMID: 16847639.

Ferrara M, Moroni F, De Gennaro L, Nobili L. Hippocampal sleep features: relations to human memory function. Front Neurol. 2012 Apr 17;3:57. doi: 10.3389/fneur.2012.00057. PMID: 22529835; PMCID: PMC3327976.

Finnerty GT, Jefferys JG. Functional connectivity from CA3 to the ipsilateral and contralateral CA1 in the rat dorsal hippocampus. Neuroscience. 1993 Sep;56(1):101-8. doi: 10.1016/0306-4522(93)90566-x. PMID: 8232909.

Fischer V, Both M, Draguhn A, Egorov AV. Choline-mediated modulation of hippocampal sharp wave-ripple complexes in vitro. J Neurochem. 2014 Jun;129(5):792-805. doi: 10.1111/jnc.12693. Epub 2014 Mar 19. PMID: 24673342.

Fortin NJ, Wright SP, Eichenbaum H. Recollection-like memory retrieval in rats is dependent on the hippocampus. Nature. 2004 Sep 9;431(7005):188-91. doi: 10.1038/nature02853. PMID: 15356631; PMCID: PMC4053162.

Foster DJ, Wilson MA. Hippocampal theta sequences. Hippocampus. 2007;17(11):1093-9. doi: 10.1002/hipo.20345. PMID: 17663452.

Foster DJ, Wilson MA. Reverse replay of behavioural sequences in hippocampal place cells during the awake state. Nature. 2006 Mar 30;440(7084):680-3. doi: 10.1038/nature04587. Epub 2006 Feb 12. PMID: 16474382.

Frankland PW, Cestari V, Filipkowski RK, McDonald RJ, Silva AJ. The dorsal hippocampus is essential for context discrimination but not for contextual conditioning. Behav Neurosci. 1998 Aug;112(4):863-74. doi: 10.1037//0735-7044.112.4.863. PMID: 9733192.

Frankland PW, Josselyn SA, Köhler S. The neurobiological foundation of memory retrieval. Nat Neurosci. 2019 Oct;22(10):1576-1585. doi: 10.1038/s41593-019-0493-1. Epub 2019 Sep 24. PMID: 31551594; PMCID: PMC6903648.

Freund TF, Buzsáki G. Interneurons of the hippocampus. Hippocampus. 1996;6(4):347-470. doi: 10.1002/(SICI)1098-1063(1996)6:4<347::AID-HIPO1>3.0.CO;2-I. PMID: 8915675.

Frey U, Krug M, Reymann KG, Matthies H. Anisomycin, an inhibitor of protein synthesis, blocks late phases of LTP phenomena in the hippocampal CA1 region in vitro. Brain Res. 1988 Jun 14;452(1-2):57-65. doi: 10.1016/0006-8993(88)90008-x. PMID: 3401749.

Fujii S, Saito K, Miyakawa H, Ito K, Kato H. Reversal of long-term potentiation (depotentiation) induced by tetanus stimulation of the input to CA1 neurons of guinea pig hippocampal slices. Brain Res. 1991 Jul 26;555(1):112-22. doi: 10.1016/0006-8993(91)90867-u. PMID: 1681992.

Furtunato AMB, Pedrosa R, Lobão-Soares B, Tort ABL, Belchior H. Hippocampal delta oscillations entrain neuronal activity, modulate gamma amplitude and convey information about running speed on a treadmill, bioRxiv 2022.01.24.477542; doi: https://doi.org/10.1101/2022.01.24.477542

Gan J, Weng SM, Pernía-Andrade AJ, Csicsvari J, Jonas P. Phase-Locked Inhibition, but Not Excitation, Underlies Hippocampal Ripple Oscillations in Awake Mice In Vivo. Neuron. 2017 Jan 18;93(2):308-314. doi: 10.1016/j.neuron.2016.12.018. Epub 2016 Dec 29. PMID: 28041883; PMCID: PMC5263253.

Garthe A, Kempermann G. An old test for new neurons: refining the Morris water maze to study the functional relevance of adult hippocampal neurogenesis. Front Neurosci. 2013 May 3;7:63. doi: 10.3389/fnins.2013.00063. PMID: 23653589; PMCID: PMC3642504.

Genro BP, de Oliveira Alvares L, Quillfeldt JA. Role of TRPV1 in consolidation of fear memories depends on the averseness of the conditioning procedure. Neurobiol Learn Mem. 2012 May;97(4):355-60. doi: 10.1016/j.nlm.2012.01.002. Epub 2012 Jan 17. PMID: 22270459.

Gerrard JL, Burke SN, McNaughton BL, Barnes CA. Sequence reactivation in the hippocampus is impaired in aged rats. J Neurosci. 2008 Jul 30;28(31):7883-90. doi: 10.1523/JNEUROSCI.1265-08.2008. PMID: 18667620; PMCID: PMC2703197.

Gibson HE, Edwards JG, Page RS, Van Hook MJ, Kauer JA. TRPV1 channels mediate long-term depression at synapses on hippocampal interneurons. Neuron. 2008 Mar 13;57(5):746-59. doi: 10.1016/j.neuron.2007.12.027. PMID: 18341994; PMCID: PMC2698707.

Gillespie AK, Jones EA, Lin YH, Karlsson MP, Kay K, Yoon SY, Tong LM, Nova P, Carr JS, Frank LM, Huang Y. Apolipoprotein E4 Causes Age-Dependent Disruption of Slow Gamma Oscillations during Hippocampal Sharp Wave Ripples. Neuron. 2016 May 18;90(4):740-51. doi: 10.1016/j.neuron.2016.04.009. Epub 2016 May 5. PMID: 27161522; PMCID: PMC5097044.

Girardeau G, Benchenane K, Wiener SI, Buzsáki G, Zugaro MB. Selective suppression of hippocampal ripples impairs spatial memory. Nat Neurosci. 2009 Oct;12(10):1222-3. doi: 10.1038/nn.2384. Epub 2009 Sep 13. PMID: 19749750.

Girardeau G, Cei A, Zugaro M. Learning-induced plasticity regulates hippocampal sharp wave-ripple drive. J Neurosci. 2014 Apr 9;34(15):5176-83. doi: 10.1523/JNEUROSCI.4288-13.2014. PMID: 24719097; PMCID: PMC6609006.

Girardeau G, Inema I, Buzsáki G. Reactivations of emotional memory in the hippocampus-amygdala system during sleep. Nat Neurosci. 2017 Nov;20(11):1634-1642. doi: 10.1038/nn.4637. Epub 2017 Sep 11. PMID: 28892057.

Gloveli T, Dugladze T, Rotstein HG, Traub RD, Monyer H, Heinemann U, Whittington MA, Kopell NJ. Orthogonal arrangement of rhythm-generating microcircuits in the hippocampus. Proc Natl Acad Sci U S A. 2005 Sep 13;102(37):13295-300. doi: 10.1073/pnas.0506259102. Epub 2005 Sep 2. PMID: 16141320; PMCID: PMC1201613.

Granger AJ, Nicoll RA. LTD expression is independent of glutamate receptor subtype. Front Synaptic Neurosci. 2014 Jul 8;6:15. doi: 10.3389/fnsyn.2014.00015. PMID: 25071549; PMCID: PMC4086023.

Grizzell JA, Iarkov A, Holmes R, Mori T, Echeverria V. Cotinine reduces depressive-like behavior, working memory deficits, and synaptic loss associated with chronic stress in mice. Behav Brain Res. 2014 Jul 15;268:55-65. doi: 10.1016/j.bbr.2014.03.047. Epub 2014 Apr 5. PMID: 24713149.

Grueter BA, Brasnjo G, Malenka RC. Postsynaptic TRPV1 triggers cell type-specific long-term depression in the nucleus accumbens. Nat Neurosci. 2010 Dec;13(12):1519-25. doi: 10.1038/nn.2685. Epub 2010 Nov 14. PMID: 21076424; PMCID: PMC3092590.

Haam J, Zhou J, Cui G, Yakel JL. Septal cholinergic neurons gate hippocampal output to entorhinal cortex via oriens lacunosum moleculare interneurons. Proc Natl Acad Sci U S A. 2018 Feb 20;115(8):E1886-E1895. doi: 10.1073/pnas.1712538115. Epub 2018 Feb 7. PMID: 29437952; PMCID: PMC5828580.

Hafting T, Fyhn M, Molden S, Moser MB, Moser EI. Microstructure of a spatial map in the entorhinal cortex. Nature. 2005 Aug 11;436(7052):801-6. doi: 10.1038/nature03721. Epub 2005 Jun 19. PMID: 15965463.

Hakimizadeh E, Oryan S, Hajizadeh Moghaddam A, Shamsizadeh A, Roohbakhsh A. Endocannabinoid System and TRPV1 Receptors in the Dorsal Hippocampus of the Rats Modulate Anxiety-like Behaviors. Iran J Basic Med Sci. 2012 May;15(3):795-802. PMID: 23493622; PMCID: PMC3586900.

Hall AM, Roberson ED. Mouse models of Alzheimer's disease. Brain Res Bull. 2012 May 1;88(1):3-12. doi: 10.1016/j.brainresbull.2011.11.017. Epub 2011 Nov 28. PMID: 22142973; PMCID: PMC3546481.

Hall C, Ballachey EL. A study of the rat's behavior in a field. A contribution to method in comparative psychology. University of California Publications in Psychology, 1932; 6, 1–12.

Hall CS. Emotional behavior in the rat: defecation and urination as measures of individual differences in emotionality. J. Comp. Psychol. 1934;18:385–403. [Google Scholar]

Hall J, Stewart ME. Basic psychology. In: Companion to Psychiatric Studies, edited by: Johnstone EC, Cunningham Owens DG, Lawrie SM, McIntosh AM, Sharpe M. Elsevier ltd, 2010; 95–108. doi:10.1016/b978-0-7020-3137-3.00005-x

Hammond C, Esclapez M. The chemical synapses. In: Cellular and Molecular Neurophysiology, edited by: Hammond C. Elsevier Ltd., 2015; 121–144. doi:10.1016/b978-0-12-397032-9.00006-6

Han Q, Kim YH, Wang X, Liu D, Zhang ZJ, Bey AL, Lay M, Chang W, Berta T, Zhang Y, Jiang YH, Ji RR. SHANK3 Deficiency Impairs Heat Hyperalgesia and TRPV1 Signaling in Primary Sensory Neurons. Neuron. 2016 Dec 21;92(6):1279-1293. doi: 10.1016/j.neuron.2016.11.007. Epub 2016 Dec 1. PMID: 27916453; PMCID: PMC5182147.

Hanack C, Moroni M, Lima WC, Wende H, Kirchner M, Adelfinger L, Schrenk-Siemens K, Tappe-Theodor A, Wetzel C, Kuich PH, Gassmann M, Roggenkamp D, Bettler B, Lewin GR, Selbach

M, Siemens J. GABA blocks pathological but not acute TRPV1 pain signals. Cell. 2015 Feb 12;160(4):759-770. doi: 10.1016/j.cell.2015.01.022. PMID: 25679765.

Hanson JE, La H, Plise E, Chen YH, Ding X, Hanania T, Sabath EV, Alexandrov V, Brunner D, Leahy E, Steiner P, Liu L, Scearce-Levie K, Zhou Q. SAHA enhances synaptic function and plasticity in vitro but has limited brain availability in vivo and does not impact cognition. PLoS One. 2013 Jul 26;8(7):e69964. doi: 10.1371/journal.pone.0069964. PMID: 23922875; PMCID: PMC3724849.

Harding EC, Franks NP, Wisden W. The Temperature Dependence of Sleep. Front Neurosci. 2019 Apr 24;13:336. doi: 10.3389/fnins.2019.00336. PMID: 31105512; PMCID: PMC6491889.

Harland B, Contreras M, Fellous JM. A Role for the Longitudinal Axis of the Hippocampus in Multiscale Representations of Large and Complex Spatial Environments and Mnemonic Hierarchies. In: The Hippocampus - Plasticity and Functions, edited by: Stuchlik A. IntechOpen, 2017, London. 10.5772/intechopen.71165.

Harmony T. The functional significance of delta oscillations in cognitive processing. Front Integr Neurosci. 2013 Dec 5;7:83. doi: 10.3389/fnint.2013.00083. PMID: 24367301; PMCID: PMC3851789.

Hasselmo ME, Stern CE. Theta rhythm and the encoding and retrieval of space and time. Neuroimage. 2014 Jan 15;85 Pt 2(0 2):656-66. doi: 10.1016/j.neuroimage.2013.06.022. Epub 2013 Jun 14. PMID: 23774394; PMCID: PMC3918488.

Hasselmo ME. Neuromodulation: acetylcholine and memory consolidation. Trends Cogn Sci. 1999 Sep;3(9):351-359. doi: 10.1016/s1364-6613(99)01365-0. PMID: 10461198.

Hayes P, Meadows HJ, Gunthorpe MJ, Harries MH, Duckworth MD, Cairns W, Harrison DC, Clarke CE, Ellington K, Prinjha RK, Barton AJL, Medhurst AD, Smith GD, Topp S, Murdock P, Sanger GJ, Terrett J, Jenkins O, Benham CD, Randall AD, Gloger IS, Davis JB. Cloning and functional expression of a human orthologue of rat vanilloid receptor-1. Pain. 2000 Nov;88(2):205-215. doi: 10.1016/S0304-3959(00)00353-5. PMID: 11050376.

Hebb DO. The organization of behavior: A neuropsychological theory. John Wiley & Sons. Inc. 1949.

Helliwell RJA, McLatchie LM, Clarke M, Winter J, Bevan S, McIntyre P (1998) Capsaicin sensitivity is associated with the expression of the vanilloid (capsaicin) receptor (VR1) mRNA in adult rat sensory ganglia. Neurosci Lett 250(3):177–180. http://dx.doi.org/10.1016/S0304-3940(98)00475-3

Heng LJ, Huang B, Guo H, Ma LT, Yuan WX, Song J, Wang P, Xu GZ, Gao GD. Blocking TRPV1 in nucleus accumbens inhibits persistent morphine conditioned place preference expression in rats. PLoS One. 2014 Aug 13;9(8):e104546. doi: 10.1371/journal.pone.0104546. Retraction in: PLoS One. 2020 Mar 6;15(3):e0230396. PMID: 25118895; PMCID: PMC4131889.

Henley JM, Wilkinson KA. Synaptic AMPA receptor composition in development, plasticity and disease. Nat Rev Neurosci. 2016 Jun;17(6):337-50. doi: 10.1038/nrn.2016.37. Epub 2016 Apr 15. PMID: 27080385.

Herbst MR, Twining RC, Gilmartin MR. Ventral hippocampal shock encoding modulates the expression of trace cued fear. Neurobiol Learn Mem. 2022 Apr;190:107610. doi: 10.1016/j.nlm.2022.107610. Epub 2022 Mar 14. PMID: 35302040.

Herweg NA, Solomon EA, Kahana MJ. Theta Oscillations in Human Memory. Trends Cogn Sci. 2020 Mar;24(3):208-227. doi: 10.1016/j.tics.2019.12.006. Epub 2020 Feb 3. PMID: 32029359; PMCID: PMC8310425.

Ho KW, Ward NJ, Calkins DJ. TRPV1: a stress response protein in the central nervous system. Am J Neurodegener Dis. 2012;1(1):1-14. Epub 2012 Apr 1. PMID: 22737633; PMCID: PMC3560445.

Hochmair J, Exner C, Franck M, Dominguez-Baquero A, Diez L, Brognaro H, Kraushar ML, Mielke T, Radbruch H, Kaniyappan S, Falke S, Mandelkow E, Betzel C, Wegmann S. Molecular crowding and RNA synergize to promote phase separation, microtubule interaction, and seeding of Tau condensates. EMBO J. 2022 Jun 1;41(11):e108882. doi: 10.15252/embj.2021108882. Epub 2022 Mar 17. PMID: 35298090; PMCID: PMC9156969.

Hodgkin AL, Katz B. The effect of temperature on the electrical activity of the giant axon of the squid. J Physiol. 1949 Aug;109(1-2):240-9. doi: 10.1113/jphysiol.1949.sp004388. PMID: 15394322; PMCID: PMC1392577.

Holmes A, Wrenn CC, Harris AP, Thayer KE, Crawley JN. Behavioral profiles of inbred strains on novel olfactory, spatial and emotional tests for reference memory in mice. Genes Brain Behav. 2002 Jan;1(1):55-69. doi: 10.1046/j.1601-1848.2001.00005.x. PMID: 12886950.

Holmes GL, Lenck-Santini PP. Role of interictal epileptiform abnormalities in cognitive impairment. Epilepsy Behav. 2006 May;8(3):504-15. doi: 10.1016/j.yebeh.2005.11.014. Epub 2006 Mar 15. PMID: 16540376.

Honson NS, Kuret J. Tau aggregation and toxicity in tauopathic neurodegenerative diseases. J Alzheimers Dis. 2008 Aug;14(4):417-22. doi: 10.3233/jad-2008-14409. PMID: 18688092; PMCID: PMC2748882.

Hormuzdi SG, Pais I, LeBeau FE, Towers SK, Rozov A, Buhl EH, Whittington MA, Monyer H. Impaired electrical signaling disrupts gamma frequency oscillations in connexin 36-deficient mice. Neuron. 2001 Aug 16;31(3):487-95. doi: 10.1016/s0896-6273(01)00387-7. PMID: 11516404.

Huang WX, Yu F, Sanchez RM, Liu YQ, Min JW, Hu JJ, Bsoul NB, Han S, Yin J, Liu WH, He XH, Peng BW. TRPV1 promotes repetitive febrile seizures by pro-inflammatory cytokines in immature brain. Brain Behav Immun. 2015 Aug;48:68-77. doi: 10.1016/j.bbi.2015.01.017. Epub 2015 Mar 20. PMID: 25801060.

Huerta PT, Lisman JE. Bidirectional synaptic plasticity induced by a single burst during cholinergic theta oscillation in CA1 in vitro. Neuron. 1995 Nov;15(5):1053-63. doi: 10.1016/0896-6273(95)90094-2. PMID: 7576649.

Hurtado-Zavala JI, Ramachandran B, Ahmed S, Halder R, Bolleyer C, Awasthi A, Stahlberg MA, Wagener RJ, Anderson K, Drenan RM, Lester HA, Miwa JM, Staiger JF, Fischer A, Dean C. TRPV1 regulates excitatory innervation of OLM neurons in the hippocampus. Nat Commun. 2017 Jul 19;8:15878. doi: 10.1038/ncomms15878. PMID: 28722015; PMCID: PMC5524938.

Hutchison IC, Rathore S. The role of REM sleep theta activity in emotional memory. Front Psychol. 2015 Oct 1;6:1439. doi: 10.3389/fpsyg.2015.01439. PMID: 26483709; PMCID: PMC4589642.

Iaccarino HF, Singer AC, Martorell AJ, Rudenko A, Gao F, Gillingham TZ, Mathys H, Seo J, Kritskiy O, Abdurrob F, Adaikkan C, Canter RG, Rueda R, Brown EN, Boyden ES, Tsai LH. Gamma frequency entrainment attenuates amyloid load and modifies microglia. Nature. 2016 Dec 7;540(7632):230-235. doi: 10.1038/nature20587. Erratum in: Nature. 2018 Oct;562(7725):E1. PMID: 27929004; PMCID: PMC5656389.

Ishikawa D, Matsumoto N, Sakaguchi T, Matsuki N, Ikegaya Y. Operant conditioning of synaptic and spiking activity patterns in single hippocampal neurons. J Neurosci. 2014 Apr 2;34(14):5044-53. doi: 10.1523/JNEUROSCI.5298-13.2014. PMID: 24695722; PMCID: PMC6802715.

Ito M, Kano M. Long-lasting depression of parallel fiber-Purkinje cell transmission induced by conjunctive stimulation of parallel fibers and climbing fibers in the cerebellar cortex. Neurosci Lett. 1982 Dec 13;33(3):253-8. doi: 10.1016/0304-3940(82)90380-9. PMID: 6298664.

Jacobs J, Hwang G, Curran T, Kahana MJ. EEG oscillations and recognition memory: theta correlates of memory retrieval and decision making. Neuroimage. 2006 Aug 15;32(2):978-87. doi: 10.1016/j.neuroimage.2006.02.018. Epub 2006 Jul 12. PMID: 16843012.

Jacobs J, Staba R, Asano E, Otsubo H, Wu JY, Zijlmans M, Mohamed I, Kahane P, Dubeau F, Navarro V, Gotman J. High-frequency oscillations (HFOs) in clinical epilepsy. Prog Neurobiol. 2012 Sep;98(3):302-15. doi: 10.1016/j.pneurobio.2012.03.001. Epub 2012 Apr 3. PMID: 22480752; PMCID: PMC3674884.

Jadhav SP, Kemere C, German PW, Frank LM. Awake hippocampal sharp wave ripples support spatial memory. Science. 2012 Jun 15;336(6087):1454-8. doi: 10.1126/science.1217230. Epub 2012 May 3. PMID: 22555434; PMCID: PMC4441285.

Jamieson BB, Kim JS, Iremonger KJ. Cannabinoid and vanilloid pathways mediate opposing forms of synaptic plasticity in corticotropin-releasing hormone neurons. J Neuroendocrinol. 2022 Apr;34(4):e13084. doi: 10.1111/jne.13084. Epub 2022 Jan 17. PMID: 35034400.

Jankowski MM, Ronnqvist KC, Tsanov M, Vann SD, Wright NF, Erichsen JT, Aggleton JP, O'Mara SM. The anterior thalamus provides a subcortical circuit supporting memory and spatial

navigation. Front Syst Neurosci. 2013 Aug 30;7:45. doi: 10.3389/fnsys.2013.00045. PMID: 24009563; PMCID: PMC3757326.

Jeewajee A, Lever C, Burton S, O'Keefe J, Burgess N. Environmental novelty is signaled by reduction of the hippocampal theta frequency. Hippocampus. 2008;18(4):340-8. doi: 10.1002/hipo.20394. PMID: 18081172; PMCID: PMC2678674.

Jensen O, fftbandpass. 2000.

Jenuwein T, Allis CD. Translating the histone code. Science. 2001 Aug 10;293(5532):1074-80. doi: 10.1126/science.1063127. PMID: 11498575.

Ji RR, Samad TA, Jin SX, Schmoll R, Woolf CJ. p38 MAPK activation by NGF in primary sensory neurons after inflammation increases TRPV1 levels and maintains heat hyperalgesia. Neuron. 2002 Sep 26;36(1):57-68. doi: 10.1016/s0896-6273(02)00908-x. PMID: 12367506.

Jiang H, Liu S, Geng X, Caccavano A, Conant K, Vicini S, Wu J. Pacing Hippocampal Sharp Wave Ripples With Weak Electric Stimulation. Front Neurosci. 2018 Mar 15;12:164. doi: 10.3389/fnins.2018.00164. PMID: 29599704; PMCID: PMC5862867.

Jiang L, Zhao J, Cheng JX, Wolozin B. Tau Oligomers and Fibrils Exhibit Differential Patterns of Seeding and Association With RNA Binding Proteins. Front Neurol. 2020 Sep 30;11:579434. doi: 10.3389/fneur.2020.579434. PMID: 33101187; PMCID: PMC7554625.

Jimenez JC, Berry JE, Lim SC, Ong SK, Kheirbek MA, Hen R. Contextual fear memory retrieval by correlated ensembles of ventral CA1 neurons. Nat Commun. 2020 Jul 13;11(1):3492. doi: 10.1038/s41467-020-17270-w. PMID: 32661319; PMCID: PMC7359370.

Jin X, Morsy N, Winston J, Pasricha PJ, Garrett K, Akbarali HI. Modulation of TRPV1 by nonreceptor tyrosine kinase, c-Src kinase. Am J Physiol Cell Physiol. 2004 Aug;287(2):C558-63. doi: 10.1152/ajpcell.00113.2004. Epub 2004 Apr 14. PMID: 15084474.

Jiruska P, Finnerty GT, Powell AD, Lofti N, Cmejla R, Jefferys JG. Epileptic high-frequency network activity in a model of non-lesional temporal lobe epilepsy. Brain. 2010 May;133(Pt 5):1380-90. doi: 10.1093/brain/awq070. Epub 2010 Apr 16. PMID: 20400525; PMCID: PMC2859153.

Johnson JM, Durrant SJ. Commentary: SWS Brain-Wave Music May Improve the Quality of Sleep: An EEG Study. Front Neurosci. 2021 Feb 1;15:609169. doi: 10.3389/fnins.2021.609169. PMID: 33597842; PMCID: PMC7882482.

Jones EA, Gillespie AK, Yoon SY, Frank LM, Huang Y. Early Hippocampal Sharp Wave Ripple Deficits Predict Later Learning and Memory Impairments in an Alzheimer's Disease Mouse Model. Cell Rep. 2019 Nov 19;29(8):2123-2133.e4. doi: 10.1016/j.celrep.2019.10.056. PMID: 31747587; PMCID: PMC7437815.

Joo HR, Frank LM. The hippocampal sharp wave-ripple in memory retrieval for immediate use and consolidation. Nat Rev Neurosci. 2018 Dec;19(12):744-757. doi: 10.1038/s41583-018-0077-1. PMID: 30356103; PMCID: PMC6794196.

Jouvet M, Michel F. Corrélations électromyographique du sommeil chez le chat décortiqué et mésencéphalique chronique [Electromyographic correlations of sleep in the chronic decorticate & mesencephalic cat]. C R Seances Soc Biol Fil. 1959;153(3):422-5. French. PMID: 13663472.

Jun H, Bramian A, Soma S, Saito T, Saido TC, Igarashi KM. Disrupted Place Cell Remapping and Impaired Grid Cells in a Knockin Model of Alzheimer's Disease. Neuron. 2020 Sep 23;107(6):1095-1112.e6. doi: 10.1016/j.neuron.2020.06.023. Epub 2020 Jul 21. PMID: 32697942; PMCID: PMC7529950.

Jung MW, Wiener SI, McNaughton BL. Comparison of spatial firing characteristics of units in dorsal and ventral hippocampus of the rat. J Neurosci. 1994 Dec;14(12):7347-56. doi: 10.1523/JNEUROSCI.14-12-07347.1994. PMID: 7996180; PMCID: PMC6576902.

Kaplan R, Adhikari MH, Hindriks R, Mantini D, Murayama Y, Logothetis NK, Deco G. Hippocampal Sharp Wave Ripples Influence Selective Activation of the Default Mode Network. Curr Biol. 2016 Mar 7;26(5):686-91. doi: 10.1016/j.cub.2016.01.017. Epub 2016 Feb 18. PMID: 26898464; PMCID: PMC4791429.

Karlsson MP, Frank LM. Awake replay of remote experiences in the hippocampus. Nat Neurosci. 2009 Jul;12(7):913-8. doi: 10.1038/nn.2344. Epub 2009 Jun 14. PMID: 19525943; PMCID: PMC2750914.

Karnatovskaia LV, Wartenberg KE, Freeman WD. Therapeutic hypothermia for neuroprotection: history, mechanisms, risks, and clinical applications. Neurohospitalist. 2014 Jul;4(3):153-63. doi: 10.1177/1941874413519802. PMID: 24982721; PMCID: PMC4056415.

Keinath AT, Wang ME, Wann EG, Yuan RK, Dudman JT, Muzzio IA. Precise spatial coding is preserved along the longitudinal hippocampal axis. Hippocampus. 2014 Dec;24(12):1533-48. doi: 10.1002/hipo.22333. Epub 2014 Aug 1. PMID: 25045084; PMCID: PMC4447627.

Kennedy JP, Zhou Y, Qin Y, Lovett SD, Sheremet A, Burke SN, Maurer AP. A Direct Comparison of Theta Power and Frequency to Speed and Acceleration. J Neurosci. 2022 May 25;42(21):4326-4341. doi: 10.1523/JNEUROSCI.0987-21.2022. Epub 2022 Apr 27. PMID: 35477905; PMCID: PMC9145239.

Kensinger EA, Ullman MT, Corkin S. Bilateral medial temporal lobe damage does not affect lexical or grammatical processing: evidence from amnesic patient H.M. Hippocampus. 2001;11(4):347-60. doi: 10.1002/hipo.1049. PMID: 11530839.

Kesner RP, Farnsworth G, Kametani H. Role of parietal cortex and hippocampus in representing spatial information. Cereb Cortex. 1991 Sep-Oct;1(5):367-73. doi: 10.1093/cercor/1.5.367. PMID: 1822746.

Kim JJ, Fanselow MS. Modality-specific retrograde amnesia of fear. Science. 1992 May 1;256(5057):675-7. doi: 10.1126/science.1585183. PMID: 1585183.

Kim WB, Cho JH. Encoding of contextual fear memory in hippocampal-amygdala circuit. Nat Commun. 2020 Mar 13;11(1):1382. doi: 10.1038/s41467-020-15121-2. PMID: 32170133; PMCID: PMC7069961.

King C, Henze DA, Leinekugel X, Buzsáki G. Hebbian modification of a hippocampal population pattern in the rat. J Physiol. 1999 Nov 15;521 Pt 1(Pt 1):159-67. doi: 10.1111/j.1469-7793.1999.00159.x. PMID: 10562342; PMCID: PMC2269637.

Kiyatkin EA. Brain temperature and its role in physiology and pathophysiology: Lessons from 20 years of thermorecording. Temperature (Austin). 2019;6(4):271-333. Published 2019 Dec 3. doi:10.1080/23328940.2019.1691896

Klausberger T, Magill PJ, Márton LF, Roberts JD, Cobden PM, Buzsáki G, Somogyi P. Brain-state- and cell-type-specific firing of hippocampal interneurons in vivo. Nature. 2003 Feb 20;421(6925):844-8. doi: 10.1038/nature01374. Erratum in: Nature. 2006 Jun 15;441(7095):902. Dosage error in article text. PMID: 12594513.

Klausberger T, Márton LF, Baude A, Roberts JD, Magill PJ, Somogyi P. Spike timing of dendrite-targeting bistratified cells during hippocampal network oscillations in vivo. Nat Neurosci. 2004 Jan;7(1):41-7. doi: 10.1038/nn1159. Epub 2003 Nov 23. Erratum in: Nat Neurosci. 2006 Jul;9(7):979. PMID: 14634650.

Klausberger T, Marton LF, O'Neill J, Huck JH, Dalezios Y, Fuentealba P, Suen WY, Papp E, Kaneko T, Watanabe M, Csicsvari J, Somogyi P. Complementary roles of cholecystokinin- and parvalbumin-expressing GABAergic neurons in hippocampal network oscillations. J Neurosci. 2005 Oct 19;25(42):9782-93. doi: 10.1523/JNEUROSCI.3269-05.2005. PMID: 16237182; PMCID: PMC6725722.

Knierim JJ. The hippocampus. Curr Biol. 2015 Dec 7;25(23):R1116-21. doi: 10.1016/j.cub.2015.10.049. PMID: 26654366.

Kong W, Wang X, Yang X, Huang W, Han S, Yin J, Liu W, He X, Peng B. Activation of TRPV1 Contributes to Recurrent Febrile Seizures via Inhibiting the Microglial M2 Phenotype in the Immature Brain. Front Cell Neurosci. 2019 Oct 11;13:442. doi: 10.3389/fncel.2019.00442. PMID: 31680864; PMCID: PMC6798794.

Kovacs GG. Tauopathies. Handb Clin Neurol. 2017;145:355-368. doi: 10.1016/B978-0-12-802395-2.00025-0. PMID: 28987182.

Kramis R, Vanderwolf CH, Bland BH. Two types of hippocampal rhythmical slow activity in both the rabbit and the rat: relations to behavior and effects of atropine, diethyl ether, urethane, and pentobarbital. Exp Neurol. 1975 Oct;49(1 Pt 1):58-85. doi: 10.1016/0014-4886(75)90195-8. PMID: 1183532.

Kropff E, Carmichael JE, Moser MB, Moser EI. Speed cells in the medial entorhinal cortex. Nature. 2015 Jul 23;523(7561):419-24. doi: 10.1038/nature14622. Epub 2015 Jul 15. PMID: 26176924.

Kudrimoti HS, Barnes CA, McNaughton BL. Reactivation of hippocampal cell assemblies: effects of behavioral state, experience, and EEG dynamics. J Neurosci. 1999 May 15;19(10):4090-101. doi: 10.1523/JNEUROSCI.19-10-04090.1999. PMID: 10234037; PMCID: PMC6782694.

Laínez S, Valente P, Ontoria-Oviedo I, Estévez-Herrera J, Camprubí-Robles M, Ferrer-Montiel A, Planells-Cases R. GABAA receptor associated protein (GABARAP) modulates TRPV1 expression and channel function and desensitization. FASEB J. 2010 Jun;24(6):1958-70. doi: 10.1096/fj.09-151472. Epub 2010 Feb 23. PMID: 20179142.

Larsen BR, Stoica A, MacAulay N. Managing Brain Extracellular K(+) during Neuronal Activity: The Physiological Role of the Na(+)/K(+)-ATPase Subunit Isoforms. Front Physiol. 2016 Apr 22;7:141. doi: 10.3389/fphys.2016.00141. PMID: 27148079; PMCID: PMC4841311.

Lasztóczi B, Tukker JJ, Somogyi P, Klausberger T. Terminal field and firing selectivity of cholecystokinin-expressing interneurons in the hippocampal CA3 area. J Neurosci. 2011 Dec 7;31(49):18073-93. doi: 10.1523/JNEUROSCI.3573-11.2011. PMID: 22159120; PMCID: PMC4487823.

Leão RN, Mikulovic S, Leão KE, Munguba H, Gezelius H, Enjin A, Patra K, Eriksson A, Loew LM, Tort AB, Kullander K. OLM interneurons differentially modulate CA3 and entorhinal inputs to hippocampal CA1 neurons. Nat Neurosci. 2012 Nov;15(11):1524-30. doi: 10.1038/nn.3235. Epub 2012 Oct 7. PMID: 23042082; PMCID: PMC3483451.

Lee AK, Wilson MA. Memory of sequential experience in the hippocampus during slow wave sleep. Neuron. 2002 Dec 19;36(6):1183-94. doi: 10.1016/s0896-6273(02)01096-6. PMID: 12495631.

Lee CH, Lü W, Michel JC, Goehring A, Du J, Song X, Gouaux E. NMDA receptor structures reveal subunit arrangement and pore architecture. Nature. 2014 Jul 10;511(7508):191-7. doi: 10.1038/nature13548. Epub 2014 Jun 22. PMID: 25008524; PMCID: PMC4263351.

Lee TH, Lee JG, Yon JM, Oh KW, Baek IJ, Nahm SS, Lee BJ, Yun YW, Nam SY. Capsaicin prevents kainic acid-induced epileptogenesis in mice. Neurochem Int. 2011 May;58(6):634-40. doi: 10.1016/j.neuint.2011.01.027. Epub 2011 Feb 16. PMID: 21333704.

Leung AK, Hon KL, Leung TN. Febrile seizures: an overview. Drugs Context. 2018 Jul 16;7:212536. doi: 10.7573/dic.212536. PMID: 30038660; PMCID: PMC6052913.

Lever C, Burton S, Jeewajee A, O'Keefe J, Burgess N. Boundary vector cells in the subiculum of the hippocampal formation. J Neurosci. 2009 Aug 5;29(31):9771-7. doi: 10.1523/JNEUROSCI.1319-09.2009. PMID: 19657030; PMCID: PMC2736390.

Lévesque M, Salami P, Gotman J, Avoli M. Two seizure-onset types reveal specific patterns of high-frequency oscillations in a model of temporal lobe epilepsy. J Neurosci. 2012 Sep 19;32(38):13264-72. doi: 10.1523/JNEUROSCI.5086-11.2012. PMID: 22993442; PMCID: PMC4878898.

Lewis PA, Durrant SJ. Overlapping memory replay during sleep builds cognitive schemata. Trends Cogn Sci. 2011 Aug;15(8):343-51. doi: 10.1016/j.tics.2011.06.004. Epub 2011 Jul 20. PMID: 21764357.

Li G, Pleasure SJ. Migration in the Hippocampus. In: Comprehensive developmental neuroscience: Cellular Migration and Formation of Neuronal Connections, edited by: Rubenstein JLR, Rakic P. Elsevier Inc, 2013; 331–343. doi:10.1016/B978-0-12-397266-8.00029-6

Li HB, Mao RR, Zhang JC, Yang Y, Cao J, Xu L. Antistress effect of TRPV1 channel on synaptic plasticity and spatial memory. Biol Psychiatry. 2008 Aug 15;64(4):286-92. doi: 10.1016/j.biopsych.2008.02.020. Epub 2008 Apr 11. PMID: 18405883.

Li S, Cullen WK, Anwyl R, Rowan MJ. Dopamine-dependent facilitation of LTP induction in hippocampal CA1 by exposure to spatial novelty. Nat Neurosci. 2003 May;6(5):526-31. doi: 10.1038/nn1049. PMID: 12704392.

Li Y, Chen X, Nie Y, Tian Y, Xiao X, Yang F. Endocannabinoid activation of the TRPV1 ion channel is distinct from activation by capsaicin. J Biol Chem. 2021 Sep;297(3):101022. doi: 10.1016/j.jbc.2021.101022. Epub 2021 Jul 30. PMID: 34332978; PMCID: PMC8387766.

Liao M, Cao E, Julius D, Cheng Y. Structure of the TRPV1 ion channel determined by electron cryo-microscopy. Nature. 2013 Dec 5;504(7478):107-12. doi: 10.1038/nature12822. PMID: 24305160; PMCID: PMC4078027.

Lishko PV, Procko E, Jin X, Phelps CB, Gaudet R. The ankyrin repeats of TRPV1 bind multiple ligands and modulate channel sensitivity. Neuron. 2007 Jun 21;54(6):905-18. doi: 10.1016/j.neuron.2007.05.027. PMID: 17582331.

Lisman JE, Jensen O. The θ-γ neural code. Neuron. 2013 Mar 20;77(6):1002-16. doi: 10.1016/j.neuron.2013.03.007. PMID: 23522038; PMCID: PMC3648857.

Liu L, Zhou X, Wu JY. Preparing Viable Hippocampal Slices from Adult Mice for the Study of Sharp Wave-ripples. Bio Protoc. 2020 Oct 5;10(19):e3771. doi: 10.21769/BioProtoc.3771. PMID: 33659429; PMCID: PMC7842787.

Liu X, Ramirez S, Pang PT, Puryear CB, Govindarajan A, Deisseroth K, Tonegawa S. Optogenetic stimulation of a hippocampal engram activates fear memory recall. Nature. 2012 Mar 22;484(7394):381-5. doi: 10.1038/nature11028. PMID: 22441246; PMCID: PMC3331914.

Llano Lopez L, Hauser J, Feldon J, Gargiulo PA, Yee BK. Evaluating spatial memory function in mice: a within-subjects comparison between the water maze test and its adaptation to dry land. Behav Brain Res. 2010 May 1;209(1):85-92. doi: 10.1016/j.bbr.2010.01.020. Epub 2010 Jan 25. PMID: 20097231.

López-Madrona VJ, Pérez-Montoyo E, Álvarez-Salvado E, Moratal D, Herreras O, Pereda E, Mirasso CR, Canals S. Different theta frameworks coexist in the rat hippocampus and are

coordinated during memory-guided and novelty tasks. Elife. 2020 Jul 20;9:e57313. doi: 10.7554/eLife.57313. PMID: 32687054; PMCID: PMC7413668.

Lukasik KM, Waris O, Soveri A, Lehtonen M, Laine M. The Relationship of Anxiety and Stress With Working Memory Performance in a Large Non-depressed Sample. Front Psychol. 2019 Jan 23;10:4. doi: 10.3389/fpsyg.2019.00004. PMID: 30728790; PMCID: PMC6351483.

Lüscher C, Malenka RC. NMDA receptor-dependent long-term potentiation and long-term depression (LTP/LTD). Cold Spring Harb Perspect Biol. 2012 Jun 1;4(6):a005710. doi: 10.1101/cshperspect.a005710. PMID: 22510460; PMCID: PMC3367554.

Ma S, Olucha-Bordonau FE, Hossain MA, Lin F, Kuei C, Liu C, Wade JD, Sutton SW, Nuñez A, Gundlach AL. Modulation of hippocampal theta oscillations and spatial memory by relaxin-3 neurons of the nucleus incertus. Learn Mem. 2009 Oct 30;16(11):730-42. doi: 10.1101/lm.1438109. PMID: 19880588.

Ma SX, Kwon SH, Seo JY, Hwang JY, Hong SI, Kim HC, Lee SY, Jang CG. Impairment of opiate-mediated behaviors by the selective TRPV1 antagonist SB366791. Addict Biol. 2017 Nov;22(6):1817-1828. doi: 10.1111/adb.12460. Epub 2016 Oct 11. PMID: 27730727.

Mably AJ, Colgin LL. Gamma oscillations in cognitive disorders. Curr Opin Neurobiol. 2018 Oct;52:182-187. doi: 10.1016/j.conb.2018.07.009. Epub 2018 Aug 16. PMID: 30121451; PMCID: PMC6139067.

Maccaferri G, Roberts JD, Szucs P, Cottingham CA, Somogyi P. Cell surface domain specific postsynaptic currents evoked by identified GABAergic neurones in rat hippocampus in vitro. J Physiol. 2000 Apr 1;524 Pt 1(Pt 1):91-116. doi: 10.1111/j.1469-7793.2000.t01-3-00091.x. Erratum in: J Physiol 2000 Nov 1;528(Pt 3):669. PMID: 10747186; PMCID: PMC2269850.

Maier N, Güldenagel M, Söhl G, Siegmund H, Willecke K, Draguhn A. Reduction of high-frequency network oscillations (ripples) and pathological network discharges in hippocampal slices from connexin 36-deficient mice. J Physiol. 2002 Jun 1;541(Pt 2):521-8. doi: 10.1113/jphysiol.2002.017624. PMID: 12042356; PMCID: PMC2290340.

Maier N, Morris G, Johenning FW, Schmitz D. An approach for reliably investigating hippocampal sharp wave-ripples in vitro. PLoS One. 2009 Sep 7;4(9):e6925. doi: 10.1371/journal.pone.0006925. PMID: 19738897; PMCID: PMC2732900.

Maier N, Nimmrich V, Draguhn A. Cellular and network mechanisms underlying spontaneous sharp wave-ripple complexes in mouse hippocampal slices. J Physiol. 2003 Aug 1;550(Pt 3):873-87. doi: 10.1113/jphysiol.2003.044602. Epub 2003 Jun 13. PMID: 12807984; PMCID: PMC2343079.

Maione S, Cristino L, Migliozzi AL, Georgiou AL, Starowicz K, Salt TE, Di Marzo V. TRPV1 channels control synaptic plasticity in the developing superior colliculus. J Physiol. 2009 Jun 1;587(Pt 11):2521-35. doi: 10.1113/jphysiol.2009.171900. Epub 2009 Apr 30. PMID: 19406878; PMCID: PMC2714018.

Maione S, De Petrocellis L, de Novellis V, Moriello AS, Petrosino S, Palazzo E, Rossi FS, Woodward DF, Di Marzo V. Analgesic actions of N-arachidonoyl-serotonin, a fatty acid amide hydrolase inhibitor with antagonistic activity at vanilloid TRPV1 receptors. Br J Pharmacol. 2007 Mar;150(6):766-81. doi: 10.1038/sj.bjp.0707145. Epub 2007 Feb 5. PMID: 17279090; PMCID: PMC2013858.

Makeig S, Delorme A, Brunner C. eegfilt. 1997.

Malik AS, Amin HU. Designing an EEG Experiment. In: Designing EEG Experiments for Studying the Brain, edited by: Malik AS, Amin HU. Elsevier Inc., 2017; 1–30. doi:10.1016/B978-0-12-811140-6.00001-1

Malin SA, Molliver DC, Koerber HR, Cornuet P, Frye R, Albers KM, Davis BM. Glial cell line-derived neurotrophic factor family members sensitize nociceptors in vitro and produce thermal hyperalgesia in vivo. J Neurosci. 2006 Aug 16;26(33):8588-99. doi: 10.1523/JNEUROSCI.1726-06.2006. PMID: 16914685; PMCID: PMC6674355.

Maloney EA, Sattizahn JR, Beilock SL. Anxiety and cognition. Wiley Interdiscip Rev Cogn Sci. 2014 Jul;5(4):403-411. doi: 10.1002/wcs.1299. PMID: 26308653.

Manchanda M, Leishman E, Sangani K, Alamri A, Bradshaw HB. Activation of TRPV1 by Capsaicin or Heat Drives Changes in 2-Acyl Glycerols and N-Acyl Ethanolamines in a Time, Dose, and Temperature Dependent Manner. Front Cell Dev Biol. 2021 Apr 16;9:611952. doi: 10.3389/fcell.2021.611952. PMID: 33937226; PMCID: PMC8085603.

Mandelkow EM, Mandelkow E. Biochemistry and cell biology of tau protein in neurofibrillary degeneration. Cold Spring Harb Perspect Med. 2012 Jul;2(7):a006247. doi: 10.1101/cshperspect.a006247. PMID: 22762014; PMCID: PMC3385935.

Manns JR, Eichenbaum H. Evolution of declarative memory. Hippocampus. 2006;16(9):795-808. doi: 10.1002/hipo.20205. PMID: 16881079.

Marinelli S, Pascucci T, Bernardi G, Puglisi-Allegra S, Mercuri NB. Activation of TRPV1 in the VTA excites dopaminergic neurons and increases chemical- and noxious-induced dopamine release in the nucleus accumbens. Neuropsychopharmacology. 2005 May;30(5):864-70. doi: 10.1038/sj.npp.1300615. PMID: 15562294.

Marinelli S, Vaughan CW, Christie MJ, Connor M. Capsaicin activation of glutamatergic synaptic transmission in the rat locus coeruleus in vitro. J Physiol. 2002 Sep 1;543(Pt 2):531-40. doi: 10.1113/jphysiol.2002.022863. PMID: 12205187; PMCID: PMC2290516.

Marrone MC, Morabito A, Giustizieri M, Chiurchiù V, Leuti A, Mattioli M, Marinelli S, Riganti L, Lombardi M, Murana E, Totaro A, Piomelli D, Ragozzino D, Oddi S, Maccarrone M, Verderio C, Marinelli S. TRPV1 channels are critical brain inflammation detectors and neuropathic pain biomarkers in mice. Nat Commun. 2017 May 10;8:15292. doi: 10.1038/ncomms15292. PMID: 28489079; PMCID: PMC5436240.

Marsch R, Foeller E, Rammes G, Bunck M, Kössl M, Holsboer F, Zieglgänsberger W, Landgraf R, Lutz B, Wotjak CT. Reduced anxiety, conditioned fear, and hippocampal long-term potentiation in transient receptor potential vanilloid type 1 receptor-deficient mice. J Neurosci. 2007 Jan 24;27(4):832-9. doi: 10.1523/JNEUROSCI.3303-06.2007. PMID: 17251423; PMCID: PMC6672910.

Mathis A, Mamidanna P, Cury KM, Abe T, Murthy VN, Mathis MW, Bethge M. DeepLabCut: markerless pose estimation of user-defined body parts with deep learning. Nat Neurosci. 2018 Sep;21(9):1281-1289. doi: 10.1038/s41593-018-0209-y. Epub 2018 Aug 20. PMID: 30127430.

Matsuo N, Takao K, Nakanishi K, Yamasaki N, Tanda K, Miyakawa T. Behavioral profiles of three C57BL/6 substrains. Front Behav Neurosci. 2010 Jun 14;4:29. doi: 10.3389/fnbeh.2010.00029. PMID: 20676234; PMCID: PMC2912075.

Matta JA, Miyares RL, Ahern GP. TRPV1 is a novel target for omega-3 polyunsaturated fatty acids. J Physiol. 2007 Jan 15;578(Pt 2):397-411. doi: 10.1113/jphysiol.2006.121988. Epub 2006 Oct 12. PMID: 17038422; PMCID: PMC2075157.

McGinty D, Szymusiak R. Keeping cool: a hypothesis about the mechanisms and functions of slow-wave sleep. Trends Neurosci. 1990 Dec;13(12):480-7. doi: 10.1016/0166-2236(90)90081-k. PMID: 1703678.

McHugh SB, Deacon RM, Rawlins JN, Bannerman DM. Amygdala and ventral hippocampus contribute differentially to mechanisms of fear and anxiety. Behav Neurosci. 2004 Feb;118(1):63-78. doi: 10.1037/0735-7044.118.1.63. PMID: 14979783.

Mezey E, Tóth ZE, Cortright DN, Arzubi MK, Krause JE, Elde R, Guo A, Blumberg PM, Szallasi A. Distribution of mRNA for vanilloid receptor subtype 1 (VR1), and VR1-like immunoreactivity, in the central nervous system of the rat and human. Proc Natl Acad Sci U S A. 2000 Mar 28;97(7):3655-60. doi: 10.1073/pnas.97.7.3655. PMID: 10725386; PMCID: PMC16295.

Michael GJ, Priestley JV. Differential expression of the mRNA for the vanilloid receptor subtype 1 in cells of the adult rat dorsal root and nodose ganglia and its downregulation by axotomy. J Neurosci. 1999 Mar 1;19(5):1844-54. doi: 10.1523/JNEUROSCI.19-05-01844.1999. PMID: 10024368; PMCID: PMC6782176.

Mikulovic S, Restrepo CE, Siwani S, Bauer P, Pupe S, Tort ABL, Kullander K, Leão RN. Ventral hippocampal OLM cells control type 2 theta oscillations and response to predator odor. Nat Commun. 2018 Sep 7;9(1):3638. doi: 10.1038/s41467-018-05907-w. PMID: 30194386; PMCID: PMC6128904.

Miller JF, Neufang M, Solway A, Brandt A, Trippel M, Mader I, Hefft S, Merkow M, Polyn SM, Jacobs J, Kahana MJ, Schulze-Bonhage A. Neural activity in human hippocampal formation reveals the spatial context of retrieved memories. Science. 2013 Nov 29;342(6162):1111-4. doi: 10.1126/science.1244056. PMID: 24288336; PMCID: PMC4669102.

Montoya CP, Sainsbury RS. The effects of entorhinal cortex lesions on type 1 and type 2 theta. Physiol Behav. 1985 Jul;35(1):121-6. doi: 10.1016/0031-9384(85)90183-0. PMID: 4059392.

Morales-Lázaro SL, Llorente I, Sierra-Ramírez F, López-Romero AE, Ortíz-Rentería M, Serrano-Flores B, Simon SA, Islas LD, Rosenbaum T. Inhibition of TRPV1 channels by a naturally occurring omega-9 fatty acid reduces pain and itch. Nat Commun. 2016 Oct 10;7:13092. doi: 10.1038/ncomms13092. PMID: 27721373; PMCID: PMC5062500.

Moreno A. Molecular mechanisms of forgetting. Eur J Neurosci. 2021 Oct;54(8):6912-6932. doi: 10.1111/ejn.14839. Epub 2020 Jun 14. PMID: 32464703.

Moroni F, Nobili L, Curcio G, De Carli F, Tempesta D, Marzano C, De Gennaro L, Mai R, Francione S, Lo Russo G, Ferrara M. Procedural learning and sleep hippocampal low frequencies in humans. Neuroimage. 2008 Aug 15;42(2):911-8. doi: 10.1016/j.neuroimage.2008.05.027. Epub 2008 May 27. PMID: 18593645.

Morris RGM. Spatial localization does not require the presence of local cues. Learning and Motivation. 1981, 12(2): 239–260. doi:10.1016/0023-9690(81)90020-5

Moscovitch M, Rosenbaum RS, Gilboa A, Addis DR, Westmacott R, Grady C, McAndrews MP, Levine B, Black S, Winocur G, Nadel L. Functional neuroanatomy of remote episodic, semantic and spatial memory: a unified account based on multiple trace theory. J Anat. 2005 Jul;207(1):35-66. doi: 10.1111/j.1469-7580.2005.00421.x. PMID: 16011544; PMCID: PMC1571502.

Moser E, Moser MB, Andersen P. Spatial learning impairment parallels the magnitude of dorsal hippocampal lesions, but is hardly present following ventral lesions. J Neurosci. 1993 Sep;13(9):3916-25. doi: 10.1523/JNEUROSCI.13-09-03916.1993. PMID: 8366351; PMCID: PMC6576447.

Müller C, Remy S. Dendritic inhibition mediated by O-LM and bistratified interneurons in the hippocampus. Front Synaptic Neurosci. 2014 Sep 30;6:23. doi: 10.3389/fnsyn.2014.00023. PMID: 25324774; PMCID: PMC4179767.

Mullis KB. The unusual origin of the polymerase chain reaction. Sci Am. 1990 Apr;262(4):56-61, 64-5. doi: 10.1038/scientificamerican0490-56. PMID: 2315679.

Musella A, De Chiara V, Rossi S, Prosperetti C, Bernardi G, Maccarrone M, Centonze D. TRPV1 channels facilitate glutamate transmission in the striatum. Mol Cell Neurosci. 2009 Jan;40(1):89-97. doi: 10.1016/j.mcn.2008.09.001. Epub 2008 Sep 30. PMID: 18930149.

Myers A, McGonigle P. Overview of Transgenic Mouse Models for Alzheimer's Disease. Curr Protoc Neurosci. 2019 Sep;89(1):e81. doi: 10.1002/cpns.81. PMID: 31532917.

Myers KM, Davis M. Mechanisms of fear extinction. Mol Psychiatry. 2007 Feb;12(2):120-50. doi: 10.1038/sj.mp.4001939. Epub 2006 Dec 12. PMID: 17160066.

Nakashiba T, Buhl DL, McHugh TJ, Tonegawa S. Hippocampal CA3 output is crucial for ripple-associated reactivation and consolidation of memory. Neuron. 2009 Jun 25;62(6):781-7. doi: 10.1016/j.neuron.2009.05.013. PMID: 19555647; PMCID: PMC2728553.

Nguyen TL, Kwon SH, Hong SI, Ma SX, Jung YH, Hwang JY, Kim HC, Lee SY, Jang CG. Transient receptor potential vanilloid type 1 channel may modulate opioid reward. Neuropsychopharmacology. 2014 Sep;39(10):2414-22. doi: 10.1038/npp.2014.90. Epub 2014 Apr 15. PMID: 24732880; PMCID: PMC4138752.

Nicholls RE, Alarcon JM, Malleret G, Carroll RC, Grody M, Vronskaya S, Kandel ER. Transgenic mice lacking NMDAR-dependent LTD exhibit deficits in behavioral flexibility. Neuron. 2008 Apr 10;58(1):104-17. doi: 10.1016/j.neuron.2008.01.039. PMID: 18400167.

Nicole O, Hadzibegovic S, Gajda J, Bontempi B, Bem T, Meyrand P. Soluble amyloid beta oligomers block the learning-induced increase in hippocampal sharp wave-ripple rate and impair spatial memory formation. Sci Rep. 2016 Mar 7;6:22728. doi: 10.1038/srep22728. PMID: 26947247; PMCID: PMC4779992.

Norimoto H, Makino K, Gao M, Shikano Y, Okamoto K, Ishikawa T, Sasaki T, Hioki H, Fujisawa S, Ikegaya Y. Hippocampal ripples down-regulate synapses. Science. 2018 Mar 30;359(6383):1524-1527. doi: 10.1126/science.aao0702. Epub 2018 Feb 8. PMID: 29439023.

Norimoto H, Mizunuma M, Ishikawa D, Matsuki N, Ikegaya Y. Muscarinic receptor activation disrupts hippocampal sharp wave-ripples. Brain Res. 2012 Jun 21;1461:1-9. doi: 10.1016/j.brainres.2012.04.037. Epub 2012 Apr 26. PMID: 22608077.

Nuñez A, Buño W. The Theta Rhythm of the Hippocampus: From Neuronal and Circuit Mechanisms to Behavior. Front Cell Neurosci. 2021 Mar 4;15:649262. doi: 10.3389/fncel.2021.649262. PMID: 33746716; PMCID: PMC7970048.

O'Keefe J, Dostrovsky J. The hippocampus as a spatial map. Preliminary evidence from unit activity in the freely-moving rat. Brain Res. 1971 Nov;34(1):171-5. doi: 10.1016/0006-8993(71)90358-1. PMID: 5124915.

O'Keefe J, Nadel L. The Hippocampus as a Cognitive Map, 1978, Oxford University Press.

Ólafsdóttir HF, Bush D, Barry C. The Role of Hippocampal Replay in Memory and Planning. Curr Biol. 2018 Jan 8;28(1):R37-R50. doi: 10.1016/j.cub.2017.10.073. PMID: 29316421; PMCID: PMC5847173.

Oliva A, Fernández-Ruiz A, Fermino de Oliveira E, Buzsáki G. Origin of Gamma Frequency Power during Hippocampal Sharp Wave Ripples. Cell Rep. 2018 Nov 13;25(7):1693-1700.e4. doi: 10.1016/j.celrep.2018.10.066. PMID: 30428340; PMCID: PMC6310484.

Oliva A, Fernández-Ruiz A, Leroy F, Siegelbaum SA. Hippocampal CA2 sharp wave ripples reactivate and promote social memory. Nature. 2020 Nov;587(7833):264-269. doi: 10.1038/s41586-020-2758-y. Epub 2020 Sep 23. PMID: 32968277; PMCID: PMC7666067.

O'Mara SM, Commins S, Anderson M, Gigg J. The subiculum: a review of form, physiology and function. Prog Neurobiol. 2001 Jun;64(2):129-55. doi: 10.1016/s0301-0082(00)00054-x. PMID: 11240210.

O'Neill J, Senior TJ, Allen K, Huxter JR, Csicsvari J. Reactivation of experience-dependent cell assembly patterns in the hippocampus. Nat Neurosci. 2008 Feb;11(2):209-15. doi: 10.1038/nn2037. Epub 2008 Jan 13. PMID: 18193040.

Ormond J, McNaughton BL. Place field expansion after focal MEC inactivations is consistent with loss of Fourier components and path integrator gain reduction. Proc Natl Acad Sci U S A. 2015 Mar 31;112(13):4116-21. doi: 10.1073/pnas.1421963112. Epub 2015 Mar 2. PMID: 25733884; PMCID: PMC4386360.

Ortega-de San Luis C, Ryan TJ. Understanding the physical basis of memory: Molecular mechanisms of the engram. J Biol Chem. 2022 May;298(5):101866. doi: 10.1016/j.jbc.2022.101866. Epub 2022 Mar 26. PMID: 35346687; PMCID: PMC9065729.

Pan WX, McNaughton N. The medial supramammillary nucleus, spatial learning and the frequency of hippocampal theta activity. Brain Res. 1997 Aug 1;764(1-2):101-8. doi: 10.1016/s0006-8993(97)00431-9. PMID: 9295198.

Pangalos M, Donoso JR, Winterer J, Zivkovic AR, Kempter R, Maier N, Schmitz D. Recruitment of oriens-lacunosum-moleculare interneurons during hippocampal ripples. Proc Natl Acad Sci U S A. 2013 Mar 12;110(11):4398-403. doi: 10.1073/pnas.1215496110. Epub 2013 Feb 25. PMID: 23440221; PMCID: PMC3600450.

Papatheodoropoulos C, Kostopoulos G. Spontaneous, low frequency (approximately 2-3 Hz) field activity generated in rat ventral hippocampal slices perfused with normal medium. Brain Res Bull. 2002 Jan 15;57(2):187-93. doi: 10.1016/s0361-9230(01)00738-9. PMID: 11849825.

Papatheodoropoulos C, Sotiriou E, Kotzadimitriou D, Drimala P. At clinically relevant concentrations the anaesthetic/amnesic thiopental but not the anticonvulsant phenobarbital interferes with hippocampal sharp wave-ripple complexes. BMC Neurosci. 2007 Jul 31;8:60. doi: 10.1186/1471-2202-8-60. PMID: 17672909; PMCID: PMC1950312.

Papatheodoropoulos C. Patterned activation of hippocampal network (approximately 10 Hz) during in vitro sharp wave-ripples. Neuroscience. 2010 Jun 30;168(2):429-42. doi: 10.1016/j.neuroscience.2010.03.058. Epub 2010 Apr 3. PMID: 20371272.

Park H, Choi Y, Jung H, Kim S, Lee S, Han H, Kweon H, Kang S, Sim WS, Koopmans F, Yang E, Kim H, Smit AB, Bae YC, Kim E. Splice-dependent trans-synaptic PTPδ-IL1RAPL1 interaction regulates synapse formation and non-REM sleep. EMBO J. 2020 Jun 2;39(11):e104150. doi: 10.15252/embj.2019104150. Epub 2020 Apr 29. PMID: 32347567; PMCID: PMC7265247.

Park P, Volianskis A, Sanderson TM, Bortolotto ZA, Jane DE, Zhuo M, Kaang BK, Collingridge GL. NMDA receptor-dependent long-term potentiation comprises a family of temporally overlapping forms of synaptic plasticity that are induced by different patterns of stimulation. Philos Trans R Soc Lond B Biol Sci. 2013 Dec 2;369(1633):20130131. doi: 10.1098/rstb.2013.0131. PMID: 24298134; PMCID: PMC3843864.

Paterno R, Marafiga JR, Ramsay H, Li T, Salvati KA, Baraban SC. Hippocampal gamma and sharp wave ripple oscillations are altered in a Cntnap2 mouse model of autism spectrum disorder. Cell Rep. 2021 Nov 9;37(6):109970. doi: 10.1016/j.celrep.2021.109970. PMID: 34758298; PMCID: PMC8783641.

Peça J, Feliciano C, Ting JT, Wang W, Wells MF, Venkatraman TN, Lascola CD, Fu Z, Feng G. Shank3 mutant mice display autistic-like behaviours and striatal dysfunction. Nature. 2011 Apr 28;472(7344):437-42. doi: 10.1038/nature09965. Epub 2011 Mar 20. PMID: 21423165; PMCID: PMC3090611.

Pedrosa V, Clopath C. The interplay between somatic and dendritic inhibition promotes the emergence and stabilization of place fields. PLoS Comput Biol. 2020 Jul 10;16(7):e1007955. doi: 10.1371/journal.pcbi.1007955. PMID: 32649658; PMCID: PMC7386595.

Pelkey KA, Chittajallu R, Craig MT, Tricoire L, Wester JC, McBain CJ. Hippocampal GABAergic Inhibitory Interneurons. Physiol Rev. 2017 Oct 1;97(4):1619-1747. doi: 10.1152/physrev.00007.2017. PMID: 28954853; PMCID: PMC6151493.

Peñagarikano O, Abrahams BS, Herman EI, Winden KD, Gdalyahu A, Dong H, Sonnenblick LI, Gruver R, Almajano J, Bragin A, Golshani P, Trachtenberg JT, Peles E, Geschwind DH. Absence of CNTNAP2 leads to epilepsy, neuronal migration abnormalities, and core autism-related deficits. Cell. 2011 Sep 30;147(1):235-46. doi: 10.1016/j.cell.2011.08.040. PMID: 21962519; PMCID: PMC3390029.

Penfield W, Milner B. Memory deficit produced by bilateral lesions in the hippocampal zone. AMA Arch Neurol Psychiatry. 1958 May;79(5):475-97. doi: 10.1001/archneurpsyc.1958.02340050003001. PMID: 13519951.

Pereda AE. Electrical synapses and their functional interactions with chemical synapses. Nat Rev Neurosci. 2014 Apr;15(4):250-63. doi: 10.1038/nrn3708. Epub 2014 Mar 12. PMID: 24619342; PMCID: PMC4091911.

Petersen PC, Buzsáki G. Cooling of Medial Septum Reveals Theta Phase Lag Coordination of Hippocampal Cell Assemblies. Neuron. 2020 Aug 19;107(4):731-744.e3. doi: 10.1016/j.neuron.2020.05.023. Epub 2020 Jun 10. PMID: 32526196; PMCID: PMC7442698.

Pfeiffer BE, Foster DJ. Hippocampal place-cell sequences depict future paths to remembered goals. Nature. 2013 May 2;497(7447):74-9. doi: 10.1038/nature12112. Epub 2013 Apr 17. PMID: 23594744; PMCID: PMC3990408.

Phillips KG, Bartsch U, McCarthy AP, Edgar DM, Tricklebank MD, Wafford KA, Jones MW. Decoupling of sleep-dependent cortical and hippocampal interactions in a neurodevelopmental model of schizophrenia. Neuron. 2012 Nov 8;76(3):526-33. doi: 10.1016/j.neuron.2012.09.016. PMID: 23141065; PMCID: PMC3898840.

Philpot BD, Cho KK, Bear MF. Obligatory role of NR2A for metaplasticity in visual cortex. Neuron. 2007 Feb 15;53(4):495-502. doi: 10.1016/j.neuron.2007.01.027. PMID: 17296552; PMCID: PMC1847797.

Ponomarenko AA, Li JS, Korotkova TM, Huston JP, Haas HL. Frequency of network synchronization in the hippocampus marks learning. Eur J Neurosci. 2008 Jun;27(11):3035-42. doi: 10.1111/j.1460-9568.2008.06232.x. PMID: 18588541.

Prescott ED, Julius D. A modular PIP2 binding site as a determinant of capsaicin receptor sensitivity. Science. 2003 May 23;300(5623):1284-8. doi: 10.1126/science.1083646. PMID: 12764195.

Prince SM, Paulson AL, Jeong N, Zhang L, Amigues S, Singer AC. Alzheimer's pathology causes impaired inhibitory connections and reactivation of spatial codes during spatial navigation. Cell Rep. 2021 Apr 20;35(3):109008. doi: 10.1016/j.celrep.2021.109008. PMID: 33882308; PMCID: PMC8139125.

Puente N, Cui Y, Lassalle O, Lafourcade M, Georges F, Venance L, Grandes P, Manzoni OJ. Polymodal activation of the endocannabinoid system in the extended amygdala. Nat Neurosci. 2011 Nov 6;14(12):1542-7. doi: 10.1038/nn.2974. PMID: 22057189.

Quirk CR, Zutshi I, Srikanth S, Fu ML, Devico Marciano N, Wright MK, Parsey DF, Liu S, Siretskiy RE, Huynh TL, Leutgeb JK, Leutgeb S. Precisely timed theta oscillations are selectively required during the encoding phase of memory. Nat Neurosci. 2021 Nov;24(11):1614-1627. doi: 10.1038/s41593-021-00919-0. Epub 2021 Oct 4. PMID: 34608335; PMCID: PMC8556344.

Rácz A, Ponomarenko AA, Fuchs EC, Monyer H. Augmented hippocampal ripple oscillations in mice with reduced fast excitation onto parvalbumin-positive cells. J Neurosci. 2009 Feb 25;29(8):2563-8. doi: 10.1523/JNEUROSCI.5036-08.2009. PMID: 19244531; PMCID: PMC6666231.

Rajasethupathy P, Sankaran S, Marshel JH, Kim CK, Ferenczi E, Lee SY, Berndt A, Ramakrishnan C, Jaffe A, Lo M, Liston C, Deisseroth K. Projections from neocortex mediate top-down control of memory retrieval. Nature. 2015 Oct 29;526(7575):653-9. doi: 10.1038/nature15389. Epub 2015 Oct 5. PMID: 26436451; PMCID: PMC4825678.

Ramadan W, Eschenko O, Sara SJ. Hippocampal sharp wave/ripples during sleep for consolidation of associative memory. PLoS One. 2009 Aug 20;4(8):e6697. doi: 10.1371/journal.pone.0006697. PMID: 19693273; PMCID: PMC2725314.

Ramirez DM, Kavalali ET. Differential regulation of spontaneous and evoked neurotransmitter release at central synapses. Curr Opin Neurobiol. 2011 Apr;21(2):275-82. doi: 10.1016/j.conb.2011.01.007. Epub 2011 Feb 18. PMID: 21334193; PMCID: PMC3092808.

Ramirez S, Liu X, Lin PA, Suh J, Pignatelli M, Redondo RL, Ryan TJ, Tonegawa S. Creating a false memory in the hippocampus. Science. 2013 Jul 26;341(6144):387-91. doi: 10.1126/science.1239073. PMID: 23888038.

Rao-Ruiz P, Visser E, Mitrić M, Smit AB, van den Oever MC. A Synaptic Framework for the Persistence of Memory Engrams. Front Synaptic Neurosci. 2021 Mar 24;13:661476. doi: 10.3389/fnsyn.2021.661476. PMID: 33841124; PMCID: PMC8024575.

Raymann RJ, Swaab DF, Van Someren EJ. Cutaneous warming promotes sleep onset. Am J Physiol Regul Integr Comp Physiol. 2005 Jun;288(6):R1589-97. doi: 10.1152/ajpregu.00492.2004. Epub 2005 Jan 27. PMID: 15677527.

Raymann RJ, Swaab DF, Van Someren EJ. Skin deep: enhanced sleep depth by cutaneous temperature manipulation. Brain. 2008 Feb;131(Pt 2):500-13. doi: 10.1093/brain/awm315. Epub 2008 Jan 11. PMID: 18192289.

Raymond CR. LTP forms 1, 2 and 3: different mechanisms for the "long" in long-term potentiation. Trends Neurosci. 2007 Apr;30(4):167-75. doi: 10.1016/j.tins.2007.01.007. Epub 2007 Feb 9. PMID: 17292975.

Riera CE, Huising MO, Follett P, Leblanc M, Halloran J, Van Andel R, de Magalhaes Filho CD, Merkwirth C, Dillin A. TRPV1 pain receptors regulate longevity and metabolism by neuropeptide signaling. Cell. 2014 May 22;157(5):1023-36. doi: 10.1016/j.cell.2014.03.051. PMID: 24855942.

Robert V, Therreau L, Chevaleyre V, Lepicard E, Viollet C, Cognet J, Huang AJ, Boehringer R, Polygalov D, McHugh TJ, Piskorowski RA. Local circuit allowing hypothalamic control of hippocampal area CA2 activity and consequences for CA1. Elife. 2021 May 18;10:e63352. doi: 10.7554/eLife.63352. PMID: 34003113; PMCID: PMC8154026.

Roumis DK, Frank LM. Hippocampal sharp wave ripples in waking and sleeping states. Curr Opin Neurobiol. 2015 Dec;35:6-12. doi: 10.1016/j.conb.2015.05.001. Epub 2015 May 23. PMID: 26011627; PMCID: PMC4641767.

Roux L, Hu B, Eichler R, Stark E, Buzsáki G. Sharp wave ripples during learning stabilize the hippocampal spatial map. Nat Neurosci. 2017 Jun;20(6):845-853. doi: 10.1038/nn.4543. Epub 2017 Apr 10. PMID: 28394323; PMCID: PMC5446786.

Rubin A, Yartsev MM, Ulanovsky N. Encoding of head direction by hippocampal place cells in bats. J Neurosci. 2014 Jan 15;34(3):1067-80. doi: 10.1523/JNEUROSCI.5393-12.2014. PMID: 24431464; PMCID: PMC6608343.

Ryan TJ, Frankland PW. Forgetting as a form of adaptive engram cell plasticity. Nat Rev Neurosci. 2022 Mar;23(3):173-186. doi: 10.1038/s41583-021-00548-3. Epub 2022 Jan 13. PMID: 35027710.

Ryu S, Liu B, Qin F. Low pH potentiates both capsaicin binding and channel gating of VR1 receptors. J Gen Physiol. 2003 Jul;122(1):45-61. doi: 10.1085/jgp.200308847. PMID: 12835470; PMCID: PMC2234467.

Sadowski JH, Jones MW, Mellor JR. Sharp Wave Ripples Orchestrate the Induction of Synaptic Plasticity during Reactivation of Place Cell Firing Patterns in the Hippocampus. Cell Rep. 2016;14(8):1916-1929. doi:10.1016/j.celrep.2016.01.061

Saito S, Tominaga M. Evolutionary tuning of TRPA1 and TRPV1 thermal and chemical sensitivity in vertebrates. Temperature (Austin). 2017 Apr 7;4(2):141-152. doi: 10.1080/23328940.2017.1315478. PMID: 28680930; PMCID: PMC5489018.

Sánchez-Moreno A, Guevara-Hernández E, Contreras-Cervera R, Rangel-Yescas G, Ladrón-de-Guevara E, Rosenbaum T, Islas LD. Irreversible temperature gating in trpv1 sheds light on channel activation. Elife. 2018 Jun 5;7:e36372. doi: 10.7554/eLife.36372. PMID: 29869983; PMCID: PMC5999395.

Sandi C. Stress and cognition. Wiley Interdiscip Rev Cogn Sci. 2013 May;4(3):245-261. doi: 10.1002/wcs.1222. Epub 2013 Jan 22. PMID: 26304203.

Santos CJ, Stern CA, Bertoglio LJ. Attenuation of anxiety-related behaviour after the antagonism of transient receptor potential vanilloid type 1 channels in the rat ventral hippocampus. Behav Pharmacol. 2008 Jul;19(4):357-60. doi: 10.1097/FBP.0b013e3283095234. PMID: 18622185.

Santschi LA, Stanton PK. A paired-pulse facilitation analysis of long-term synaptic depression at excitatory synapses in rat hippocampal CA1 and CA3 regions. Brain Res. 2003 Feb 7;962(1-2):78-91. doi: 10.1016/s0006-8993(02)03846-5. PMID: 12543458.

Sanz-Salvador L, Andrés-Borderia A, Ferrer-Montiel A, Planells-Cases R. Agonist- and Ca2+-dependent desensitization of TRPV1 channel targets the receptor to lysosomes for degradation. J Biol Chem. 2012 Jun 1;287(23):19462-71. doi: 10.1074/jbc.M111.289751. Epub 2012 Apr 6. PMID: 22493457; PMCID: PMC3365984.

Schacter DL, Addis DR, Buckner RL. Episodic simulation of future events: concepts, data, and applications. Ann N Y Acad Sci. 2008 Mar;1124:39-60. doi: 10.1196/annals.1440.001. PMID: 18400923.

Scherma M, Masia P, Satta V, Fratta W, Fadda P, Tanda G. Brain activity of anandamide: a rewarding bliss? Acta Pharmacol Sin. 2019 Mar;40(3):309-323. doi: 10.1038/s41401-018-0075-x. Epub 2018 Jul 26. PMID: 30050084; PMCID: PMC6460372.

Schindelin J, Arganda-Carreras I, Frise E, Kaynig V, Longair M, Pietzsch T, Preibisch S, Rueden C, Saalfeld S, Schmid B, Tinevez JY, White DJ, Hartenstein V, Eliceiri K, Tomancak P, Cardona A. Fiji: an open-source platform for biological-image analysis. Nat Methods. 2012 Jun 28;9(7):676-82. doi: 10.1038/nmeth.2019. PMID: 22743772; PMCID: PMC3855844.

Schlingloff D, Káli S, Freund TF, Hájos N, Gulyás AI. Mechanisms of sharp wave initiation and ripple generation. J Neurosci. 2014 Aug 20;34(34):11385-98. doi: 10.1523/JNEUROSCI.0867-14.2014. PMID: 25143618; PMCID: PMC6615505.

Schmid LC, Mittag M, Poll S, Steffen J, Wagner J, Geis HR, Schwarz I, Schmidt B, Schwarz MK, Remy S, Fuhrmann M. Dysfunction of Somatostatin-Positive Interneurons Associated with Memory Deficits in an Alzheimer's Disease Model. Neuron. 2016 Oct 5;92(1):114-125. doi: 10.1016/j.neuron.2016.08.034. Epub 2016 Sep 15. PMID: 27641495.

Schneiderman JH. Low concentrations of penicillin reveal rhythmic, synchronous synaptic potentials in hippocampal slice. Brain Res. 1986 Nov 29;398(2):231-41. doi: 10.1016/0006-8993(86)91482-4. PMID: 3026566.

Schomburg EW, Anastassiou CA, Buzsáki G, Koch C. The spiking component of oscillatory extracellular potentials in the rat hippocampus. J Neurosci. 2012 Aug 22;32(34):11798-811. doi: 10.1523/JNEUROSCI.0656-12.2012. PMID: 22915121; PMCID: PMC3459239.

Schuchmann S, Schmitz D, Rivera C, Vanhatalo S, Salmen B, Mackie K, Sipilä ST, Voipio J, Kaila K. Experimental febrile seizures are precipitated by a hyperthermia-induced respiratory alkalosis. Nat Med. 2006 Jul;12(7):817-23. doi: 10.1038/nm1422. Epub 2006 Jul 2. PMID: 16819552; PMCID: PMC1698875.

Schultheiss NW, Schlecht M, Jayachandran M, Brooks DR, McGlothan JL, Guilarte TR, Allen TA. Awake delta and theta-rhythmic hippocampal network modes during intermittent locomotor behaviors in the rat. Behav Neurosci. 2020 Dec;134(6):529-546. doi: 10.1037/bne0000409. Epub 2020 Jul 16. PMID: 32672989; PMCID: PMC8193833.

Schulz PE. Long-term potentiation involves increases in the probability of neurotransmitter release. Proc Natl Acad Sci U S A. 1997 May 27;94(11):5888-93. doi: 10.1073/pnas.94.11.5888. Erratum in: Proc Natl Acad Sci U S A 1997 Oct 28;94(22):12241. PMID: 9159170; PMCID: PMC20876.

Schüz A, Palm G. Density of neurons and synapses in the cerebral cortex of the mouse. J Comp Neurol. 1989 Aug 22;286(4):442-55. doi: 10.1002/cne.902860404. PMID: 2778101.

Schwartz ES, Christianson JA, Chen X, La JH, Davis BM, Albers KM, Gebhart GF. Synergistic role of TRPV1 and TRPA1 in pancreatic pain and inflammation. Gastroenterology. 2011 Apr;140(4):1283-1291.e1-2. doi: 10.1053/j.gastro.2010.12.033. Epub 2010 Dec 24. PMID: 21185837; PMCID: PMC3066263.

Scopinho AA, Lisboa SF, Guimarães FS, Corrêa FM, Resstel LB, Joca SR. Dorsal and ventral hippocampus modulate autonomic responses but not behavioral consequences associated to acute restraint stress in rats. PLoS One. 2013 Oct 17;8(10):e77750. doi: 10.1371/journal.pone.0077750. PMID: 24147071; PMCID: PMC3798415.

Seibenhener ML, Wooten MC. Use of the Open Field Maze to measure locomotor and anxiety-like behavior in mice. J Vis Exp. 2015 Feb 6;(96):e52434. doi: 10.3791/52434. PMID: 25742564; PMCID: PMC4354627.

Sela Y, Hoekstra MM, Franken P. Sub-minute prediction of brain temperature based on sleep-wake state in the mouse. Elife. 2021 Mar 8;10:e62073. doi: 10.7554/eLife.62073. PMID: 33683202; PMCID: PMC7939547.

Shafiei SS, Guerrero-Muñoz MJ, Castillo-Carranza DL. Tau Oligomers: Cytotoxicity, Propagation, and Mitochondrial Damage. Front Aging Neurosci. 2017 Apr 4;9:83. doi: 10.3389/fnagi.2017.00083. PMID: 28420982; PMCID: PMC5378766.

Shehadul Islam M, Aryasomayajula A, Selvaganapathy PR. A Review on Macroscale and Microscale Cell Lysis Methods. Micromachines (Basel). 2017 Mar 8;8(3):83. doi: 10.3390/mi8030083. PMCID: PMC6190294.

Shein-Idelson M, Ondracek JM, Liaw HP, Reiter S, Laurent G. Slow waves, sharp waves, ripples, and REM in sleeping dragons. Science. 2016 Apr 29;352(6285):590-5. doi: 10.1126/science.aaf3621. PMID: 27126045.

Sheridan GK, Moeendarbary E, Pickering M, O'Connor JJ, Murphy KJ. Theta-burst stimulation of hippocampal slices induces network-level calcium oscillations and activates analogous gene transcription to spatial learning. PLoS One. 2014 Jun 20;9(6):e100546. doi: 10.1371/journal.pone.0100546. PMID: 24950243; PMCID: PMC4065069.

Shewmon DA, Erwin RJ. The effect of focal interictal spikes on perception and reaction time. I. General considerations. Electroencephalogr Clin Neurophysiol. 1988.

Shirazi M, Izadi M, Amin M, Rezvani ME, Roohbakhsh A, Shamsizadeh A. Involvement of central TRPV1 receptors in pentylenetetrazole and amygdala-induced kindling in male rats. Neurol Sci. 2014 Aug;35(8):1235-41. doi: 10.1007/s10072-014-1689-5. Epub 2014 Feb 28. PMID: 24577898.

Shoji H, Miyakawa T. Age-related behavioral changes from young to old age in male mice of a C57BL/6J strain maintained under a genetic stability program. Neuropsychopharmacol Rep. 2019 Jun;39(2):100-118. doi: 10.1002/npr2.12052. Epub 2019 Feb 27. PMID: 30816023; PMCID: PMC7292274.

Shuba YM. Beyond Neuronal Heat Sensing: Diversity of TRPV1 Heat-Capsaicin Receptor-Channel Functions. Front Cell Neurosci. 2021 Feb 5;14:612480. doi: 10.3389/fncel.2020.612480. PMID: 33613196; PMCID: PMC7892457.

Siapas AG, Wilson MA. Coordinated interactions between hippocampal ripples and cortical spindles during slow-wave sleep. Neuron. 1998 Nov;21(5):1123-8. doi: 10.1016/s0896-6273(00)80629-7. PMID: 9856467.

Sierra RO, Pedraza LK, Barcsai L, Pejin A, Kozák G, Takeuchi Y, Lőrincz ML, Devinsky O, Buzsáki G, Berényi A, 2022, Closed-loop brain stimulation to reduce pathologic fear, bioRxiv 2022.07.24.501314; doi: https://doi.org/10.1101/2022.07.24.501314

Sik A, Penttonen M, Ylinen A, Buzsáki G. Hippocampal CA1 interneurons: an in vivo intracellular labeling study. J Neurosci. 1995 Oct;15(10):6651-65. doi: 10.1523/JNEUROSCI.15-10-06651.1995. PMID: 7472426; PMCID: PMC6577981.

Siwani S, França ASC, Mikulovic S, Reis A, Hilscher MM, Edwards SJ, Leão RN, Tort ABL, Kullander K. OLMα2 Cells Bidirectionally Modulate Learning. Neuron. 2018 Jul 25;99(2):404-412.e3. doi: 10.1016/j.neuron.2018.06.022. Epub 2018 Jul 5. PMID: 29983324.

Skaggs WE, McNaughton BL, Gothard KM. An Information-Theoretic Approach to Deciphering the Hippocampal Code. NIPS, 1992

Smith PK, Krohn RI, Hermanson GT, Mallia AK, Gartner FH, Provenzano MD, Fujimoto EK, Goeke NM, Olson BJ, Klenk DC. Measurement of protein using bicinchoninic acid. Anal Biochem. 1985 Oct;150(1):76-85. doi: 10.1016/0003-2697(85)90442-7. Erratum in: Anal Biochem 1987 May 15;163(1):279. PMID: 3843705.

Socała K, Nieoczym D, Pieróg M, Wlaź P. α-Spinasterol, a TRPV1 receptor antagonist, elevates the seizure threshold in three acute seizure tests in mice. J Neural Transm (Vienna). 2015 Sep;122(9):1239-47. doi: 10.1007/s00702-015-1391-7. Epub 2015 Mar 13. PMID: 25764210; PMCID: PMC4540766.

Spange S, Wagner T, Heinzel T, Krämer OH. Acetylation of non-histone proteins modulates cellular signalling at multiple levels. Int J Biochem Cell Biol. 2009 Jan;41(1):185-98. doi: 10.1016/j.biocel.2008.08.027. Epub 2008 Sep 2. PMID: 18804549.

Squire LR, Clark RE, Knowlton BJ. Retrograde amnesia. Hippocampus. 2001;11(1):50-5. doi: 10.1002/1098-1063(2001)11:1<50::AID-HIPO1019>3.0.CO;2-GPMID: 11261772.

Stangor C, Walinga J. Introduction to Psychology – 1st Canadian Edition. Victoria, B.C.: BCcampus, 2014; Retrieved from https://opentextbc.ca/introductiontopsychology/.

Stark E, Roux L, Eichler R, Senzai Y, Royer S, Buzsáki G. Pyramidal cell-interneuron interactions underlie hippocampal ripple oscillations. Neuron. 2014 Jul 16;83(2):467-480. doi: 10.1016/j.neuron.2014.06.023. PMID: 25033186; PMCID: PMC4393648.

Storozhuk MV, Moroz OF, Zholos AV. Multifunctional TRPV1 Ion Channels in Physiology and Pathology with Focus on the Brain, Vasculature, and Some Visceral Systems. Biomed Res Int. 2019 May 27;2019:5806321. doi: 10.1155/2019/5806321. PMID: 31263706; PMCID: PMC6556840.

Suemaru K, Yoshikawa M, Aso H, Watanabe M. TRPV1 mediates the anticonvulsant effects of acetaminophen in mice. Epilepsy Res. 2018 Sep;145:153-159. doi: 10.1016/j.eplepsyres.2018.06.016. Epub 2018 Jul 3. PMID: 30007240.

Suh J, Foster DJ, Davoudi H, Wilson MA, Tonegawa S. Impaired hippocampal ripple-associated replay in a mouse model of schizophrenia. Neuron. 2013 Oct 16;80(2):484-93. doi: 10.1016/j.neuron.2013.09.014. PMID: 24139046; PMCID: PMC3871857.

Sullivan D, Csicsvari J, Mizuseki K, Montgomery S, Diba K, Buzsáki G. Relationships between hippocampal sharp waves, ripples, and fast gamma oscillation: influence of dentate and entorhinal cortical activity. J Neurosci. 2011 Jun 8;31(23):8605-16. doi: 10.1523/JNEUROSCI.0294-11.2011. PMID: 21653864; PMCID: PMC3134187.

Sun FJ, Guo W, Zheng DH, Zhang CQ, Li S, Liu SY, Yin Q, Yang H, Shu HF. Increased expression of TRPV1 in the cortex and hippocampus from patients with mesial temporal lobe epilepsy. J Mol Neurosci. 2013 Jan;49(1):182-93. doi: 10.1007/s12031-012-9878-2. Epub 2012 Aug 31. PMID: 22936245.

Sun X, Zakharian E. Regulation of the temperature-dependent activation of transient receptor potential vanilloid 1 (TRPV1) by phospholipids in planar lipid bilayers. J Biol Chem. 2015 Feb 20;290(8):4741-4747. doi: 10.1074/jbc.M114.611459. Epub 2015 Jan 5. PMID: 25561742; PMCID: PMC4335212.

Szallasi A, Blumberg PM. Characterization of vanilloid receptors in the dorsal horn of pig spinal cord. Brain Res. 1991 May 3;547(2):335-8. doi: 10.1016/0006-8993(91)90982-2. PMID: 1884211.

Tancredi V, D'Arcangelo G, Zona C, Siniscalchi A, Avoli M. Induction of epileptiform activity by temperature elevation in hippocampal slices from young rats: an in vitro model for febrile seizures? Epilepsia. 1992 Mar-Apr;33(2):228-34. doi: 10.1111/j.1528-1157.1992.tb02311.x. PMID: 1547752.

Tao K, Chung M, Watarai A, Huang Z, Wang MY, Okuyama T. Disrupted social memory ensembles in the ventral hippocampus underlie social amnesia in autism-associated Shank3 mutant mice. Mol Psychiatry. 2022 Apr;27(4):2095-2105. doi: 10.1038/s41380-021-01430-5. Epub 2022 Feb 4. PMID: 35115700; PMCID: PMC9126818.

Tao S, Wang Y, Peng J, Zhao Y, He X, Yu X, Liu Q, Jin S, Xu F. Whole-Brain Mapping the Direct Inputs of Dorsal and Ventral CA1 Projection Neurons. Front Neural Circuits. 2021 Apr 14;15:643230. doi: 10.3389/fncir.2021.643230. PMID: 33935658; PMCID: PMC8079783.

Taylor MM. The problem of stimulus structure in the behavioural theory of perception. South African Journal of Psychology, 1973; 3:23–45.

Thaler F, Mercurio C. Towards selective inhibition of histone deacetylase isoforms: what has been achieved, where we are and what will be next. ChemMedChem. 2014 Mar;9(3):523-6. doi: 10.1002/cmdc.201300413. PMID: 24730063.

Thompson SM, Masukawa LM, Prince DA. Temperature dependence of intrinsic membrane properties and synaptic potentials in hippocampal CA1 neurons in vitro. J Neurosci. 1985 Mar;5(3):817-24. doi: 10.1523/JNEUROSCI.05-03-00817.1985. PMID: 3973697; PMCID: PMC6565032.

Tian YH, Lee SY, Kim HC, Jang CG. Repeated methamphetamine treatment increases expression of TRPV1 mRNA in the frontal cortex but not in the striatum or hippocampus of mice. Neurosci Lett. 2010 Mar 12;472(1):61-4. doi: 10.1016/j.neulet.2010.01.058. Epub 2010 Feb 1. PMID: 20122992.

Todorova R, Zugaro M. Isolated cortical computations during delta waves support memory consolidation. Science. 2019 Oct 18;366(6463):377-381. doi: 10.1126/science.aay0616. PMID: 31624215.

Tognetto M, Amadesi S, Harrison S, Creminon C, Trevisani M, Carreras M, Matera M, Geppetti P, Bianchi A. Anandamide excites central terminals of dorsal root ganglion neurons via vanilloid receptor-1 activation. J Neurosci. 2001 Feb 15;21(4):1104-9. doi: 10.1523/JNEUROSCI.21-04-01104.2001. PMID: 11160380; PMCID: PMC6762236.

Tomar A, Polygalov D, Chattarji S, McHugh TJ. Stress enhances hippocampal neuronal synchrony and alters ripple-spike interaction. Neurobiol Stress. 2021 Apr 13;14:100327. doi: 10.1016/j.ynstr.2021.100327. PMID: 33937446; PMCID: PMC8079661.

Tominaga M, Caterina MJ, Malmberg AB, Rosen TA, Gilbert H, Skinner K, Raumann BE, Basbaum AI, Julius D. The cloned capsaicin receptor integrates multiple pain-producing stimuli. Neuron. 1998 Sep;21(3):531-43. doi: 10.1016/s0896-6273(00)80564-4. PMID: 9768840.

Torrence C, Compo GP. A Practical Guide to Wavelet Analysis. Bull. Am. Meteorol. Soc. 1998; 79, 61–78.

Tóth A, Boczán J, Kedei N, Lizanecz E, Bagi Z, Papp Z, Edes I, Csiba L, Blumberg PM. Expression and distribution of vanilloid receptor 1 (TRPV1) in the adult rat brain. Brain Res Mol Brain Res. 2005 Apr 27;135(1-2):162-8. doi: 10.1016/j.molbrainres.2004.12.003. Epub 2005 Jan 22. PMID: 15857679.

Tovote P, Fadok JP, Lüthi A. Neuronal circuits for fear and anxiety. Nat Rev Neurosci. 2015 Jun;16(6):317-31. doi: 10.1038/nrn3945. Erratum in: Nat Rev Neurosci. 2015 Jul;16(7):439. PMID: 25991441.

Traynelis SF, Wollmuth LP, McBain CJ, Menniti FS, Vance KM, Ogden KK, Hansen KB, Yuan H, Myers SJ, Dingledine R. Glutamate receptor ion channels: structure, regulation, and function. Pharmacol Rev. 2010 Sep;62(3):405-96. doi: 10.1124/pr.109.002451. Erratum in: Pharmacol Rev. 2014 Oct;66(4):1141. PMID: 20716669; PMCID: PMC2964903.

Turi GF, Li WK, Chavlis S, Pandi I, O'Hare J, Priestley JB, Grosmark AD, Liao Z, Ladow M, Zhang JF, Zemelman BV, Poirazi P, Losonczy A. Vasoactive Intestinal Polypeptide-Expressing Interneurons in the Hippocampus Support Goal-Oriented Spatial Learning. Neuron. 2019 Mar 20;101(6):1150-1165.e8. doi: 10.1016/j.neuron.2019.01.009. Epub 2019 Jan 31. PMID: 30713030; PMCID: PMC6428605.

van de Ven GM, Trouche S, McNamara CG, Allen K, Dupret D. Hippocampal Offline Reactivation Consolidates Recently Formed Cell Assembly Patterns during Sharp Wave-Ripples. Neuron. 2016 Dec 7;92(5):968-974. doi: 10.1016/j.neuron.2016.10.020. Epub 2016 Nov 10. PMID: 27840002; PMCID: PMC5158132.

Van Der Stelt M, Di Marzo V. Endovanilloids. Putative endogenous ligands of transient receptor potential vanilloid 1 channels. Eur J Biochem. 2004 May;271(10):1827-34. doi: 10.1111/j.1432-1033.2004.04081.x. PMID: 15128293.

van Groen T, Wyss JM. Extrinsic projections from area CA1 of the rat hippocampus: olfactory, cortical, subcortical, and bilateral hippocampal formation projections. J Comp Neurol. 1990 Dec 15;302(3):515-28. doi: 10.1002/cne.903020308. PMID: 1702115.

van Strien NM, Cappaert NL, Witter MP. The anatomy of memory: an interactive overview of the parahippocampal-hippocampal network. Nat Rev Neurosci. 2009 Apr;10(4):272-82. doi: 10.1038/nrn2614. PMID: 19300446.

Vandal M, White PJ, Tournissac M, Tremblay C, St-Amour I, Drouin-Ouellet J, Bousquet M, Traversy MT, Planel E, Marette A, Calon F. Impaired thermoregulation and beneficial effects of thermoneutrality in the 3×Tg-AD model of Alzheimer's disease. Neurobiol Aging. 2016 Jul;43:47-57. doi: 10.1016/j.neurobiolaging.2016.03.024. Epub 2016 Mar 30. PMID: 27255814.

Vandecasteele M, Varga V, Berényi A, Papp E, Barthó P, Venance L, Freund TF, Buzsáki G. Optogenetic activation of septal cholinergic neurons suppresses sharp wave ripples and enhances theta oscillations in the hippocampus. Proc Natl Acad Sci U S A. 2014 Sep 16;111(37):13535-40. doi: 10.1073/pnas.1411233111. Epub 2014 Sep 2. PMID: 25197052; PMCID: PMC4169920.

Vanderwolf CH. Hippocampal electrical activity and voluntary movement in the rat. Electroencephalogr Clin Neurophysiol. 1969 Apr;26(4):407-18. doi: 10.1016/0013-4694(69)90092-3. PMID: 4183562.

Varga C, Golshani P, Soltesz I. Frequency-invariant temporal ordering of interneuronal discharges during hippocampal oscillations in awake mice. Proc Natl Acad Sci U S A. 2012 Oct 2;109(40):E2726-34. doi: 10.1073/pnas.1210929109. Epub 2012 Sep 10. PMID: 23010933; PMCID: PMC3479571.

Vargas R, Thorsteinsson H, Karlsson KA. Spontaneous neural activity of the anterodorsal lobe and entopeduncular nucleus in adult zebrafish: a putative homologue of hippocampal sharp waves. Behav Brain Res. 2012 Apr 1;229(1):10-20. doi: 10.1016/j.bbr.2011.12.025. Epub 2011 Dec 22. PMID: 22207154.

Vécsei L, Bollók I, Penke B, Telegdy G. Somatostatin and (D-Trp8, D-Cys14)-somatostatin delay extinction and reverse electroconvulsive shock induced amnesia in rats. Psychoneuroendocrinology. 1986;11(1):111-5. doi: 10.1016/0306-4530(86)90037-5. PMID: 2871576.

Verma M, Vats A, Taneja V. Toxic species in amyloid disorders: Oligomers or mature fibrils. Ann Indian Acad Neurol. 2015 Apr-Jun;18(2):138-45. doi: 10.4103/0972-2327.144284. PMID: 26019408; PMCID: PMC4445186.

Villers A, Ris L. Improved preparation and preservation of hippocampal mouse slices for a very stable and reproducible recording of long-term potentiation. J Vis Exp. 2013 Jun 26;(76):50483. doi: 10.3791/50483. PMID: 23851639; PMCID: PMC3729182.

Viney TJ, Lasztoczi B, Katona L, Crump MG, Tukker JJ, Klausberger T, Somogyi P. Network state-dependent inhibition of identified hippocampal CA3 axo-axonic cells in vivo. Nat Neurosci. 2013 Dec;16(12):1802-1811. doi: 10.1038/nn.3550. Epub 2013 Oct 20. PMID: 24141313; PMCID: PMC4471148.

Vorhees CV, Williams MT. Morris water maze: procedures for assessing spatial and related forms of learning and memory. Nat Protoc. 2006;1(2):848-58. doi: 10.1038/nprot.2006.116. PMID: 17406317; PMCID: PMC2895266.

Vorster AP, Born J. Sleep and memory in mammals, birds and invertebrates. Neurosci Biobehav Rev. 2015 Mar;50:103-19. doi: 10.1016/j.neubiorev.2014.09.020. Epub 2014 Oct 7. PMID: 25305058.

Weller J, Budson A. Current understanding of Alzheimer's disease diagnosis and treatment. F1000Res. 2018 Jul 31;7:F1000 Faculty Rev-1161. doi: 10.12688/f1000research.14506.1. PMID: 30135715; PMCID: PMC6073093.

Wiegand JP, Gray DT, Schimanski LA, Lipa P, Barnes CA, Cowen SL. Age Is Associated with Reduced Sharp Wave Ripple Frequency and Altered Patterns of Neuronal Variability. J Neurosci. 2016 May 18;36(20):5650-60. doi: 10.1523/JNEUROSCI.3069-15.2016. PMID: 27194342; PMCID: PMC5696526.

Wikenheiser AM, Redish AD. The balance of forward and backward hippocampal sequences shifts across behavioral states. Hippocampus. 2013 Jan;23(1):22-9. doi: 10.1002/hipo.22049. Epub 2012 Jun 27. PMID: 22736562; PMCID: PMC3774294.

Wilson MA, McNaughton BL. Reactivation of hippocampal ensemble memories during sleep. Science. 1994 Jul 29;265(5172):676-9. doi: 10.1126/science.8036517. PMID: 8036517.

Wirt RA, Crew LA, Ortiz AA, McNeela AM, Flores E, Kinney JW, Hyman JM. Altered theta rhythm and hippocampal-cortical interactions underlie working memory deficits in a hyperglycemia risk factor model of Alzheimer's disease. Commun Biol. 2021 Sep 3;4(1):1036. doi: 10.1038/s42003-021-02558-4. PMID: 34480097; PMCID: PMC8417282.

Wittner L, Miles R. Factors defining a pacemaker region for synchrony in the hippocampus. J Physiol. 2007 Nov 1;584(Pt 3):867-83. doi: 10.1113/jphysiol.2007.138131. Epub 2007 Sep 6. PMID: 17823211; PMCID: PMC2276992.

Witton J, Staniaszek LE, Bartsch U, Randall AD, Jones MW, Brown JT. Disrupted hippocampal sharp wave ripple-associated spike dynamics in a transgenic mouse model of dementia. J Physiol. 2016 Aug 15;594(16):4615-30. doi: 10.1113/jphysiol.2014.282889. Epub 2015 Jan 2. PMID: 25480798; PMCID: PMC4983632.

Wright KP Jr, Hull JT, Czeisler CA. Relationship between alertness, performance, and body temperature in humans. Am J Physiol Regul Integr Comp Physiol. 2002 Dec;283(6):R1370-7. doi: 10.1152/ajpregu.00205.2002. Epub 2002 Aug 15. PMID: 12388468.

Wu L, Rosa-Neto P, Hsiung GY, Sadovnick AD, Masellis M, Black SE, Jia J, Gauthier S. Early-onset familial Alzheimer's disease (EOFAD). Can J Neurol Sci. 2012 Jul;39(4):436-45. doi: 10.1017/s0317167100013949. PMID: 22728850.

Wyss JM, van Groen T. Connections between the retrosplenial cortex and the hippocampal formation in the rat: a review. Hippocampus. 1992 Jan;2(1):1-11. doi: 10.1002/hipo.450020102. PMID: 1308170.

Yamazaki Y, Fujii S, Goto J, Sugihara T, Sugita M, Fujiwara H, Kaneko K, Aihara T, Mikoshiba K. Suppressive effect of preconditioning low-frequency stimulation on subsequent induction of long-term potentiation by high frequency stimulation in hippocampal CA3 neurons. Brain Res. 2012 Apr 17;1449:15-23. doi: 10.1016/j.brainres.2012.02.025. Epub 2012 Feb 18. PMID: 22405691.

Ylinen A, Bragin A, Nádasdy Z, Jandó G, Szabó I, Sik A, Buzsáki G. Sharp wave-associated high-frequency oscillation (200 Hz) in the intact hippocampus: network and intracellular mechanisms. J Neurosci. 1995 Jan;15(1 Pt 1):30-46. doi: 10.1523/JNEUROSCI.15-01-00030.1995. PMID: 7823136; PMCID: PMC6578299.

Yokoyama M, Kobayashi H, Tatsumi L, Tomita T. Mouse Models of Alzheimer's Disease. Front Mol Neurosci. 2022 Jun 21;15:912995. doi: 10.3389/fnmol.2022.912995. PMID: 35799899; PMCID: PMC9254908.

You IJ, Jung YH, Kim MJ, Kwon SH, Hong SI, Lee SY, Jang CG. Alterations in the emotional and memory behavioral phenotypes of transient receptor potential vanilloid type 1-deficient mice are mediated by changes in expression of 5-HT_1A, GABA(A), and NMDA receptors. Neuropharmacology. 2012 Feb;62(2):1034-43. doi: 10.1016/j.neuropharm.2011.10.013. Epub 2011 Nov 4. PMID: 22074644.

Yu JY, Frank LM. Hippocampal-cortical interaction in decision making. Neurobiol Learn Mem. 2015 Jan;117:34-41. doi: 10.1016/j.nlm.2014.02.002. Epub 2014 Feb 13. PMID: 24530374; PMCID: PMC4133322.

Zhang Q, Luo P, Xia F, Tang H, Chen J, Zhang J, Liu D, Zhu Y, Liu Y, Gu L, Zheng L, Li Z, Yang F, Dai L, Liao F, Xu C, Wang J. Capsaicin ameliorates inflammation in a TRPV1-independent mechanism by inhibiting PKM2-LDHA-mediated Warburg effect in sepsis. Cell Chem Biol. 2022a Aug 18;29(8):1248-1259.e6. doi: 10.1016/j.chembiol.2022.06.011. Epub 2022a Jul 19. PMID: 35858615.

Zhang Y, Wu KM, Yang L, Dong Q, Yu JT. Tauopathies: new perspectives and challenges. Mol Neurodegener. 2022b Apr 7;17(1):28. doi: 10.1186/s13024-022-00533-z. PMID: 35392986; PMCID: PMC8991707.

Zheng C, Bieri KW, Hwaun E, Colgin LL. Fast Gamma Rhythms in the Hippocampus Promote Encoding of Novel Object-Place Pairings. eNeuro. 2016 May 12;3(2):ENEURO.0001-16.2016. doi: 10.1523/ENEURO.0001-16.2016. PMID: 27257621; PMCID: PMC4874540.

Zhou Y, Danbolt NC. Glutamate as a neurotransmitter in the healthy brain. J Neural Transm (Vienna). 2014 Aug;121(8):799-817. doi: 10.1007/s00702-014-1180-8. Epub 2014 Mar 1. PMID: 24578174; PMCID: PMC4133642.

Zielinski MC, Shin JD, Jadhav SP, Hippocampal theta sequences in REM sleep during spatial learning, bioRxiv 2021.04.15.439854; doi: https://doi.org/10.1101/2021.04.15.439854

Zschenderlein C, Gebhardt C, von Bohlen Und Halbach O, Kulisch C, Albrecht D.
Capsaicin-induced changes in LTP in the lateral amygdala are mediated by TRPV1. PLoS One. 2011 Jan 13;6(1):e16116. doi: 10.1371/journal.pone.0016116. PMID: 21249195; PMCID: PMC3020947.

Acknowledgements

First and foremost, I would like to thank my supervisor, Camin Dean, for her continuous support and excellent mentorship. I was given freedom to develop my own ideas, guidance when I needed it, and was encouraged to initiate collaborations that were instrumental in this project. Thank you for all the late evening meetings, the quick feedback, and the patience when listening to the various problems I encountered. I can't imagine how I would have completed my thesis without your help.

I am sincerely grateful for my lab colleagues: Dmytro Nesterenko, Larissa Breuer, Hanna Dubrovska, Jeremy Krohn, John Carl Begley, Hana Sheldon, Shimon Jude Swer, and our technician Sarah Foss. I have learned so much from all of you, but most importantly, thank you for providing a stimulating, positive, and accepting work environment. A special thanks to Dmytro for helping me troubleshoot the numerous problems with noise in in vitro experiments and our excellent team work on the LTP and SWRs experiment, to John Carl for his input regarding analysis, and to Shimon for helping me build the microdrives. I would also like to thank Hermes Pofantis for teaching me how to record SWRs in slices, and Ana Carolina Odebrecht Vergne de Abreu, my lab rotation student, with whom we completed the ohtau40-heparin experiments.

This work would not have been possible without our collaborators. Firstly, the in vivo electrophysiology and behavioral experiments would not have taken place if not for Silvia Viana da Silva's group. Their support was not just intellectual, but also personal. To Rina Patel, thank you for teaching me how to build the drives (and helping me with them), how to do the surgeries, how to do the recordings, and so so many more things. And maybe more importantly, thank you for the hugs when things went wrong! I would like to thank Dejana Mitrovic and Can Tartanoglu for their help with analysis of the behavioral experiments and encouragement that everything will work out fine, as well as Silvia for teaching me cluster cutting, correcting me, supporting me, and being there to answer any questions I had. I am also indebted to Nikolaus Maier and Daniel Parthier from Dietmar Schmitz's lab for all the assistance they provided with analysis of in vitro data, thank you for teaching me and answering my numerous questions. Lastly, I would like to thank Susanne Wegmann's lab and especially Janine Hochmair for providing me with all the tau variants.

I would also like to express my gratitude to the IMPRS Neuroscience office for all the aid they provided through the years and to the program who provided part of my funding. For their financial support, I would also like to thank the Studienstiftung des deutschen Volkes and the DZNE.

Finally, to my friends and family, thank you for listening to all the issues I was facing in my experiments, even if it didn't make much sense to you, for bearing with me when I was stressed and nervous, for reminding me that there are more important things in life than a PhD, and most importantly, for making me feel loved and accepted. I hope this work is making you proud too.

Changes from submitted dissertation

Editorial changes have taken place in order to make the dissertation more clear and consistent.

Content changes are:
1. List of abbreviations: addition of ANOVA, APV, FWHM, H_2O_2, HSD, and PCR.

2. Methods:

a. Performed chi-square tests for analysis of data presented on Figures 38A and 46C (also added in results section).

b. Correction of units for the rate of bubbling of carbogen in aCSF for in vitro SWR recordings: from mmHg to L/h.

c. Correction of video tracking parameter for behavioral tests: from 30 fps to 15 fps.

d. Correction of the bandpass filter used for in vivo LFP recordings: from 0.1-900 Hz to 1-1000 Hz.

e. To better explain data analysis, added:

- "Ripple events were excluded from analysis of peak frequency and peak power if the time of the maximum power was more than 15 ms from the middle of the event and more than 15 ms from the maximum ripple peak of the event or if the event had a duration longer than 110ms".
- "The line of best fit for each genotype was determined using the mean daily performance per genotype" (also in Figure legends of relevant graphs).

3. Results:

a. Changed Figures 27A+B and 30A+B so that PSDs are depicted after analysis of filtered rather than raw data (to better represent following analysis).

b. Corrected Figure 34 title from "Delta peak frequency was higher in TRPV1 KOs" to "Delta peak frequency was lower in TRPV1 KOs".

c. Corrected Figure 15 legend, from " at the second time point of 36 ^{o}C" to "at the end of temperature steps".

d. Corrected Figure 18B title from "start" to "end" of temperature steps.

e. Corrected Figure 19 + 21 legends, from "At the start of the first exposure at 31 ^{o}C" and "At the first time point at 31 ^{o}C", to "At the initial minutes at each temperature step" and "When the initial minutes after each temperature step was reached were examined", respectively.

f. For more transparency, p-values from post-hoc analysis that before were only represented by the asterisks on the respective graphs were added in numerical form in text.

g. Added “However, if animals are used as experimental units, an opposite trend is seen with an increase in theta power in WT mice from r1 to r2” (also in Figure 32 legend and discussion section).

4. Discussion:

a. Added the last paragraph (with its references) on page 150, to discuss results from the open field test (paragraph was mistakenly deleted from the dissertation, but proof can be provided that it was there in earlier versions if needed).

b. Corrected the percentage of TRPV1 KO and WT slices with increased EA from ~ 30% to ~ 40%.

c. Because references were misunderstood, deleted:

- “Hippocampal delta waves share characteristics with cortical delta oscillations (Moroni et al., 2007), so it is possible that decreased delta frequency simply represents decreased wakefulness, similar to cortical delta oscillations (Erickson et al., 2019)” (and references).
- “ Alternatively, decreased delta power might lead to memory impairments, as delta power during post-learning sleep positively correlates with performance (Axmacher et al., 2008a)”.

d. Changed “It has been suggested that REM sleep and associated theta might be involved in memory consolidation (Zielinski et al., 2021) similar to SWRs and NREM sleep; an increase in theta frequency from rest before exploration to rest after exploration as seen in both WT and TRPV1 KO mice would support this” to “It has been suggested that REM sleep and associated theta might be involved in memory consolidation (Zielinski et al., 2021) similar to SWRs and NREM sleep; an increase in theta power from rest before exploration to rest after exploration as seen in both WT and TRPV1 KO mice after exploration of novel environments would support this”, because power would better support this claim.

e. Added “The difference could be attributed to TRPV1 expression outside the hippocampus”, to explain discrepancies of our results with others regarding susceptibility of TRPV1 KO mice to develop febrile seizures.